

**The Dissertation Committee for Ioannis Korkolis
certifies that this is the approved version of the following dissertation:**

**FORMABILITY AND HYDROFORMING OF
ANISOTROPIC ALUMINUM TUBES**

Committee:

Kyriakides, Stelios, Supervisor

Liechti, Kenneth M.

Mear, Mark

Ravi-Chandar, K.

Tassoulas, John L.

**FORMABILITY AND HYDROFORMING OF
ANISOTROPIC ALUMINUM TUBES**

by

Ioannis Korkolis, Dipl.-Ing; M.Sc

Dissertation

Presented to the Faculty of the Graduate School of

The University of Texas at Austin

in Partial Fulfillment

of the Requirements

for the Degree of

Doctor of Philosophy

The University of Texas at Austin

August, 2009

In the history of mechanical art two modes of progress may be distinguished - the *empirical* and the *scientific*. Not the *practical* and the *theoretic*, for that distinction is fallacious; all real progress in mechanical art, whether theoretical or not, must be practical. The true distinction is this: that the empirical mode of progress is purely and simply practical; the scientific mode of progress is at once practical and theoretic.

William J.M. Rankine
*A Manual of the Steam Engine
and Other Prime Movers,*
Richard Griffin & Co.,
London and Glasgow, 1859

Dedication

To my grandparents, Evangelos and Marika Venetaki.

Acknowledgements

I would like to thank my advisor, Professor Stelios Kyriakides, whom I consider my greatest intellectual benefactor to date. His unwavering trust in me has guided me through the years of my graduate studies. His method of work, his insistence on excellence and his solid work ethics I hope that will influence and attend me in the rest of my professional career.

I was fortunate to have been educated by an exceptional group of scholars, both in Athens and in Austin. Professors Ken Liechti, Mark Mear, K. Ravi-Chandar and Yannis Tassoulas served as members of my committee, reviewing my dissertation and offering me their constructive criticism. I have also profited significantly from Professors Frederick Barlat, Eric Becker, Edmundo Corona, Yannis Dafalias, Gregory Rodin and Ronald Stearman and I would like to thank them for these interactions. Frank Wise was an unlimited source of help in our experimental work. Jim Williams was also indispensable. Our project benefited from the expert machining work of Travis Crooks and David Gray. Mike Kripl of Henkel Surface Technologies generously provided the lubricants used in this study.

The hydroforming project was supported by the National Science Foundation through grant DMI-0140599. Supplementary funding was provided by General Motors with Robin Stevenson as coordinator. Initial seed funding for the project and the tubes

analyzed and tested were provided by Alcoa through Edmund Chu. Dr. Jeong-Whan Yoon of Alcoa graciously provided the subroutine for the Yld2004-3D model.

In my years in Austin, I was fortunate to have met and worked with a large number of talented and dedicated fellow graduate students and post-docs. I worked with Jorge Capeto in the initial phases of the project, when the hydroforming facility was being developed. Dr. Liang-Hai Lee was always available, knowledgeable and willing to help with practically anything that could be asked from him. Dr. Lixin Gong, Dr. Wen-Yea Jang, Josh Paquette, Julian Hallai, Pierre Hosate, Francois Bardi, Andre DaSilva, Ali Ok, Dr. Antonios Kotsos, Min Kyoo Kang, John Nacker, Ken Hunzicker, Federico Gallo, Maud Russo, Dr. Dewei Xu, William Hickey and of course, Maria Carka, Stavros Gaitanaros and Theofilos Giagmouris are to be thanked for both the scientific and the social interactions we have all, I hope, enjoyed.

I developed happy and long lasting – I hope again – bonds with many people outside UT in Austin, without whom I would not had succeeded in my studies. Dimi Culcer, Yorgos Klonaris and Vangelis Meintanis were among the first people I met here and whom I enjoy meeting to this day. So was Anna Marchi, whom I haven't seen since 2003, Nalini Belaramani whom I see every few days since 2003, Jason Brandt, Genevieve Frisch, Christine Vogel, Waqas Akram, Patricia Mosier, Rena Cornell, Henrietta Yang, Estibalitz Ukar, Nacho Gallardo, Angeliki Kasi, Yorgos Skretas, Yorgos, Terpsithea and Antonia Chimonidou, Louiza Fouli, Maxine Beach, Anne-Marie Thomas, Vijay Pasricha, Michalis Xyntarakis, Angela Bardo and Andeas Malisiovas. Last but not least, Saša Jonaš biked with me to every single street of this city and bore my presence for countless hours, relieving all the people above. To all of my friends, those mentioned above and those not, I wish happy rides.

I was fortunate to have been supported throughout my life by an outstanding family. My cousin Vassilis Giakoumis and his family, Eleni, Georgia, Billy, Maria, Nick and Foufi in Chicago have been the closest to immediate family that one could wish to have away from home. So was Arie Agniyadis, who incidentally was never at home, like me, either.

The last but not least thanks are reserved for my parents, Petros and Loukia, my brother Vangelis and my grandmother, Marika. Thank you for all you have done for me.

FORMABILITY AND HYDROFORMING OF ANISOTROPIC ALUMINUM TUBES

Publication No. _____

Ioannis Korkolis, PhD

The University of Texas at Austin, 2009

Supervisor: Stelios Kyriakides

The automotive industry is required to meet improved fuel efficiency standards and stricter emission controls. Aluminum tube hydroforming is particularly well suited in meeting the goals of lighter, more fuel-efficient and less polluting cars. Its wider use in industry is hindered however by the reduced ductility and more complex constitutive behavior of aluminum in comparison to the steels that it is meant to replace. This study aims to address these issues by improving the understanding of the limitations of the process as applied to aluminum alloys.

A series of hydroforming experiments were conducted in a custom testing facility, designed and constructed for the purposes of this project. At the same time, several levels of modeling of the process, of increasing complexity, were developed. A comparison of these models to the experiments revealed a serious deficiency in predicting burst, which was found experimentally to be one of the main limiting factors of the process. This discrepancy between theory and experiment was linked to the adoption of the von Mises yield function for the material at hand. This prompted a separate study, combining

experiments and analysis, to calibrate alternative, non-quadratic anisotropic yield functions and assess their performance in predicting burst. The experiments involved testing tubes under combined internal pressure and axial load to failure using various proportional and non-proportional loading paths (free inflation). A number of state of the art yield functions were then implemented in numerical models of these experiments and calibrated to reproduce the induced strain paths and failure strains.

The constitutive models were subsequently employed in the finite element models of the hydroforming experiments. The results demonstrate that localized wall thinning in the presence of contact, as it occurs in hydroforming as well as other sheet metal forming problems, is a fully 3D process requiring appropriate modeling with solid elements. This success also required the use of non-quadratic yield functions in the constitutive modeling, although the anisotropy present did not play as profound a role as it did in the simulation of the free inflation experiments. In addition, corresponding shell element calculations were deficient in capturing this type of localization that precipitates failure, irrespective of the sophistication of the constitutive model adopted. This finding contradicts current practice in modeling of sheet metal forming, where the thin-walled assumption is customarily adopted.

Table of Contents

Nomenclature	xiii
Chapter 1: Introduction	1
1.1 Automobile Design	2
1.2 The Tube Hydroforming Process (THF).....	4
1.2.1 Evolution of the Process	4
1.2.2 Process Extensions and Variants.....	5
1.2.3 Equipment	7
1.2.4 Applications	8
1.2.5 Hydroforming Process Envelope	10
1.3 Outline of the Thesis	11
Chapter 2: Tube Hydroforming Experiments	30
2.1 Hydroforming Facility	30
2.1.1 Hydroforming Machine	30
2.1.2 Pressurization System	32
2.1.3 Data Acquisition and Control System.....	33
a. Transducers	33
b. Computerized Control System.....	34
2.1.4 Summary of Specifications of Hydroforming Facility	36
2.2 Description of a Typical Experiment.....	37
2.2.1 Selection of the Loading Path	37
2.2.2 Tube Preparation.....	38
2.2.3 Experimental Procedure.....	38
2.3 Typical Results.....	39
Chapter 3: Tube Inflation and Burst Experiments	62
3.1 Test Specimens	62
3.2 Experimental Set-up and Testing Procedures	63
3.2.1 Radial (Proportional) Stress Paths	64

3.2.2 Corner Stress Paths	65
3.3 Material Testing	66
3.4 Experimental Results from the Radial Path Tests.....	68
3.4.1 Stress-Strain Responses	68
3.4.2 Strain Paths	71
3.4.3 Contours of Constant Plastic Work.....	72
3.5 Experimental Results from the Corner Path Tests.....	73
3.5.1 $x \rightarrow \theta$ Paths	74
3.5.2 $\theta \rightarrow x$ Path.....	75
3.5.3 Discussion of the Corner Path Test Results.....	76
Chapter 4: Constitutive and Numerical Modeling of Tube Bursting.....	102
4.1 Constitutive Modeling	102
4.1.1 Hosford's 1979 Anisotropic Yield Function	103
4.1.2 Karafillis and Boyce 1993 Anisotropic Yield Function	105
4.1.3 Barlat <i>et al.</i> 2003 Anisotropic Yield Function (Yld2000-2D)..	108
4.2 Finite Element Modeling of the Burst Experiments	110
4.2.1 Finite Element Models.....	110
4.2.2 Discussion of Representative Numerical Results for the Radial Paths	113
4.2.3 Cumulative Numerical Results for the Radial Paths	118
4.2.4 Numerical Results for the Corner Paths	125
a. $x \rightarrow \theta$ Paths	125
b. $\theta \rightarrow x$ Paths	129
Chapter 5: Numerical Modeling of Tube Hydroforming.....	175
5.1 Generalized Plane Strain Model (2D).....	175
5.1.1 Model Set-up.....	175
5.1.2 Design of the Hydroforming Experiments.....	177
5.1.3 Numerical Results	177
5.2 Shell Element Model (3D-Sh).....	178
5.2.1 Model Set-up.....	179

5.2.2 Numerical Results	180
5.3 Solid Element Model (3D-So)	183
5.3.1 Model Set-up.....	183
5.3.2 Numerical Results	183
5.4 Discussion	186
Chapter 6: Conclusions	225
6.1 Hydroforming Experiments	225
6.2 Tube Formability Study	226
6.3 Hydroforming Simulations	228
Appendix: Yld2004-3D Anisotropic Yield Function	230
References.....	234
Vita	238

Nomenclature

c	Weight of Karafillis-Boyce yield function
$c'_{ij}, c''_{ij}, i, j = 1,6$	Anisotropic parameters for Yld2004-3D
C', C''	Transformation matrices for Yld2000-2D and Yld2004-3D yield functions
D	Tube diameter (initial)
e_e^p	Equivalent logarithmic plastic strain
e_x^p, e_θ^p	Axial and hoop logarithmic plastic strains
f	Yield function
f_1, f_2	Components of Karafillis-Boyce yield function
F, F_{Spec}	Axial load on the specimen
F_{Tot}	Total load on hydraulic actuator
F_P	Load on hydraulic actuator due to internal pressure of specimen
F, G, H	Parameters for Hosford's yield function
k	Yield function exponent
L	Specimen length (hydroforming) or half-length (tube inflation)
L_1, s_1	Zone of refined mesh in tube bursting FE model
L_g, s_g	Reduced thickness groove dimensions in same model
L	Transformation matrix for Karafillis-Boyce yield function
L', L''	Transformation matrices for Yld2000-2D and Yld2004-3D yield functions
P	Internal pressure

P_{\max}	Limit pressure
R	Mid-surface radius of the tube
s	Deviatoric stress tensor
s_1, s_2, s_3	Principal values of s
S', S''	Linearly transformed stress tensors for Yld2000-2D and Yld2004-3D yield functions
S'_1, S'_2, S'_3	Principal values of S'
S''_1, S''_2, S''_3	Principal values of S''
S_θ, S_r	Anisotropic parameters for Hosford's yield function
t, t_o	Tube wall thickness (initial)
$t(\theta)$	Circumferential thickness distribution
T	Transformation matrix to convert the stress tensor to its deviator
w_g	Width of the reduced thickness groove in the tube bursting FE model
W^p	Plastic work
x, y, z and x, R, θ	Coordinate systems used
α	Stress biaxiality ratio
$\alpha_i, i = 1, 2$	Parameters of Karafillis-Boyce yield function
$\alpha_i, i = 1, 8$	Parameters of Yld2000-2D yield function
$\beta_i, i = 1, 3$	Parameters of Karafillis-Boyce yield function
Γ	Parameter of Karafillis-Boyce yield function
δ	Parameter of Karafillis-Boyce yield function, or Axial feed
ε_e^p	Equivalent engineering plastic strain
$\varepsilon_x, \varepsilon_\theta$	Axial and hoop engineering strains

$\bar{\varepsilon}_\theta$	Hoop strain averaged around the tube circumference
$\varepsilon_{xL}, \varepsilon_{\theta L}$	Axial and hoop strain at the limit load
$\varepsilon_{xf}, \varepsilon_{\theta f}$	Axial and hoop strain at failure, measured by the extensometers
$\varepsilon_{xf l}, \varepsilon_{\theta f l}$	Axial and hoop strain at failure, measured by the strain grid
$\dot{\delta}$	Strain rate
η	Wall thinning imperfection parameter
θ	Circumferential coordinate
μ	Coulomb friction coefficient
ξ	Wall eccentricity variable
Ξ_o	Eccentricity in tube wall thickness
σ	Stress tensor
$\sigma_\theta, \sigma_x, \sigma_r$	Circumferential, axial and hoop engineering stresses
$\sigma_{\theta \max}, \sigma_x \Big _{\sigma_{\theta \max}}$	Hoop stress at the limit load (max. pressure) and corresponding axial one
$\sigma_{x \max}, \sigma_\theta \Big _{\sigma_{x \max}}$	Axial stress at the limit load (max. load) and corresponding hoop one
$\sigma_{xf}, \sigma_{\theta f}$	Axial and hoop stress at the onset of failure
σ_e	Equivalent engineering stress
σ_o	Yield stress in the axial direction of the tube
$\sigma_{o\theta}$	Yield stress in the circumferential direction of the tube
σ_{or}	Yield stress in the radial direction of the tube
τ_e	Equivalent true stress
τ_x, τ_θ	Axial and hoop true stresses
ϕ	Yield function for Yld2000-2D and Yld2004-3D
ϕ', ϕ''	Components of Yld2000-2D yield function

Chapter 1: *Introduction*

The automotive industry is faced with very stringent controls, concerning first the fuel consumption and second the emissions. In addition the amount of energy used to manufacture the vehicles remains a concern. These challenges are amplified by the expectation of the consumer for safer and more comfortable automobiles and commercial vehicles.

To meet these demands of reduced emissions, improved performance and a more sustainable carbon footprint, it is generally accepted and even expected from the industry to develop more imaginative and more fuel efficient designs. A lighter vehicle structure is one way of meeting these targets, along with improved aerodynamics, more efficient engines based on new concepts, better rolling tires, etc. To achieve a lighter structure, an ever expanding variety of materials has been introduced; indeed, a modern automobile as the one shown in Fig. 1.1 has quite a different material mix from the all-steel-sheet car that was commonplace 40 years ago. Many of these new materials often require novel shaping techniques, as well.

Tube hydroforming has a history of more than 100 years, however it was introduced in the automotive industry only in the past two decades. Typical applications involve quite naturally the tubular components found in the engine and exhaust systems. In addition however, numerous structural parts of the chassis and the body as well as closings such as doors, hoods, etc. are also hydroformed. The main advantage that the process offers is the ability to optimize the structure for weight and strength, while often offering at the same time superior crashworthiness. Aluminum tube hydroforming is

particularly well suited in these roles, however its widespread use in the industry is hindered by, among other reasons, the reduced ductility and the more complex constitutive behavior of aluminum alloys in comparison to the steels that they are meant to replace.

This thesis presents an investigation into limit states of aluminum hydroforming, intrinsically coupled with the study of tube formability and of the appropriate constitutive modeling for the material at hand.

1.1 AUTOMOBILE DESIGN

Historically, the bodies of the first cars were fabricated using coachbuilding techniques and utilizing materials such as wood and fabric (Eckermann, 2001). Soon though (1910s), it was realized that such methods did not lend themselves to massive production, nor were they compatible with the improvements in automobile performance. By the mid 1920s, steel had emerged as the material of choice, combining strength, stiffness, formability and weldability. Still however the structural design of the car involved a frame, responsible for carrying the loads and an independent body attached to the frame and intended to protect the passengers from the elements (termed “body-on-chassis” technology). Both the frame and the body were manufactured from steel sheets, suitably formed to the desired shapes and riveted (initially) or welded. In the mid- to late-twenties, it was conceived that significant gains in strength and stiffness and reductions in weight could be accomplished with the *unibody* type of construction, manufactured with increasingly complex formed sheets. The first mass-production application (1934) derived from a patent of the Budd Company in Philadelphia, licensed to Citroën in France. In the unibody construction, the frame is merged with the floor of the passenger compartment, while the rest of the structure is also reinforced. In this way the loads are carried by the entire structure. It was also shown that a car body would be manufactured

more economically by welding together a relatively limited amount of large and complex formed panels, rather than a larger number of smaller and simpler ones. While the first bodies were made out of relatively thick (0.9 to 1 mm) steel sheets, this was reduced to 0.8 mm in the fifties/sixties to the current standard of 0.7 mm for external panels (Davies, 2007). With the advent of technology more advanced ferrous alloys were used in the construction of the body, such as aluminum killed (AK) and drawing quality (DQ) instead of plain carbon steel. In the eighties, high strength low alloy (HSLA), dual phase (DP), rephosphorized and zinc coated sheets came to prominence, while nowadays TRIP (transformation induced plasticity), High Strength and Advanced High Strength (HSS and AHSS) steels are commonly used. The stampings required for the unibody construction result in about 40 to 45% scrap, with the result that the material cost amounts to about 50% of the total body cost (Ludke, 1999).

As Fenton (1980) points out, the main drag force encountered by a vehicle at relatively low speeds is the tire rolling resistance, which is proportional to the mass of the vehicle. In addition, the inertia forces required for acceleration as well as the gradient resistance also scale with the mass. Ultimately, the chemical energy of the fuel is transformed into kinetic and potential energy of the moving vehicle, which are also proportional to the mass. For all these reasons, lightening up a vehicle leads to direct fuel savings.

The oil crises of the seventies brought into attention the issues of fuel economy, which in the United States were incorporated into legislation with the Energy Policy and Conservation Act of 1975. The Act introduced the concept of the Corporate Average Fuel Economy (CAFE), to be maintained by each manufacturer to a preset standard. Starting from 18 miles per gallon (mpg) in 1978, CAFE was ramped to 27.5 mpg in 1985 - however it has remained fluctuating to that level since then (recently updated to 30.2 mpg

for 2011). However, it has contributed to reducing the weight of an average automobile from 3,500 lb in the mid-seventies to 2,500 lb in the mid-nineties (Field & Clark, 1997).

1.2 THE TUBE HYDROFORMING PROCESS (THF)

The tube hydroforming process allows the fabrication of thin-walled structural members of rather complicated cross-sectional shape, which in addition can be varying along the length of the component. This is a major difference of the method in comparison to extrusion, where the cross-sectional shape can be quite complicated as well, but has to remain constant throughout the workpiece. The principle of tube hydroforming is quite simple (see Fig. 1.2). One usually starts with a circular cylindrical thin-walled tube, which is placed inside a cavity (die) of the desired final shape. The workpiece is engaged from the two ends by suitable actuators, providing sealing and axial feed. The tube is then inflated internally and thus it is forced to expand and conform to the shape of the surrounding die. Usually water with an anticorrosion additive is used as pressurizing medium, while a variant of the process uses hot gas. A typical process cycle is of 10-15 seconds, which classifies the method as slower than the typical stamping operations. However, considering that stamped parts require subsequently more extensive assembly and welding and often higher equipment and die capital costs, the method becomes economically competitive, especially for medium production volumes. Figure 1.3 shows a large variety of cross sectional shapes that can be hydroformed.

1.2.1 Evolution of the Process

Among the first applications of THF was the manufacturing of serpentine tubing for use in steam boilers (Park, 1903, see also Singh, 2003). In that specific application, molten lead was used as the pressurizing medium. Also among the earliest applications, that continue to date, is the manufacturing of wind instruments (Foster, 1917, Sachs,

1950). The instruments are made of conical 70-30 brass tubes, rolled from sheets and brazed along the seam. Typical examples include saxophone mouthpipes, trombone crooks and sousaphone and euphonium branches and elbows (Fig. 1.4). The tubes are first filled with a low temperature melting alloy (e.g., Wood's metal) and bent to the required shape. The filler metal is then melted away and the bent tube is expanded by hydroforming to the desired shape. In one such application (Sachs, 1950) the pressurization was performed by a special weighted accumulator at 3,000 psi (210 bar) while the expansion was achieved in a single operation. Careful design of the process is required to avoid local thinning, since even if that does not lead to bursting, it may affect the acoustical performance of the instrument.

Other early applications included the manufacture of T fittings for plumbing from wrought-metal (Gray, 1940) and copper (Ogura and Ueda, 1968) tubes, hollow aircraft propeller blades (Kearns, 1950), camshafts from steel tubing (Garvin, 1959), joints for bicycle frames and even artificial limbs from spun aluminum (Davies, 1932). The majority of these pieces are small in dimensions and/or made from relatively low-strength materials. In fact, up to the early nineties the main application of THF was in the manufacturing of Ts and other plumbing fittings. Only in the last 20 years have the advances in high pressure technology and in controls permitted the systematic manufacture of long steel components, such as those encountered in car body applications (Fig 1.5).

1.2.2 Process Extensions and Variants

A number of secondary processes can be performed in conjunction with THF to increase its flexibility and competitiveness. Perhaps the most common such process is hydropiercing, where a number of holes and other openings are pierced while the tube is still inside the hydroforming die and under pressure. Numerous such openings are shown

in Fig. 1.5 (several of these are laser cut after forming instead of hydropierced). Other operations include hydrobending, to eliminate the need for separate bending before hydroforming and localized cam forming to produce local features along the component.

Perhaps the most common variant of THF is Low Pressure Hydroforming (LPH, see Koc, 2008). In the classical THF (also called High Pressure Hydroforming), the periphery of the undeformed tube is usually smaller than that of the final product and the process is divided into two phases: inflation/axial feed and calibration. In the latter, the pressure is increased so that the tube will fill the die completely. This pressurization while the tube is in contact with the die often leads to bursting, since the tube-die friction impedes the material flow. LPH attempts to resolve this problem by starting with a tube of larger diameter, which is subsequently crushed in the die as the die closes. To support the tube against collapse, it is filled with water that is maintained at a relatively low pressure. The fact that the initial periphery of the tube is closer to that of the final desired shape helps limit the need of subsequent pressurization for expansion and hence the possibility of local wall thinning and of bursting.

A further extension of the LPH idea is the Liquid Impact Forming process (LIF), in which the tube is filled with water, capped and then crushed locally using a standard stamping press. This is a faster method than the previous two and one that also does not require special hydroforming equipment. However, the features that can be produced are also more limited.

Hot Forming (HF) involves an inert gas (Nitrogen or Argon) as the pressure medium. Both the workpiece and the die are heated. Often, the die is inductively heated to different temperatures along its length to aid with the material deformation and flow, as well as with end sealing. This last method can be used to achieve very large expansions or to form alloys with limited ductility at room temperature.

Lastly, other notable cases in industrial practice include the hydroforming of conical and of tailor-welded tubes (composed of tubes with different thicknesses), of double tubing and of entire tube assemblies that are simultaneously hydroformed in the die (see Koc, 2008).

1.2.3 Equipment

The standard equipment for THF usually involves a special hydroforming press and a set of dies. A laboratory facility that was designed and manufactured for the purposes of this study and that also includes a sophisticated data acquisition and control system is described in the next Chapter. Industrial THF facilities however tend to be grouped into complete forming cells, which receive bundles of tubular blanks and return ready to assemble components. These cells include, in sequence, a lubricating facility, a tube bender, possibly a preforming press, the actual hydroforming machine, a washing system, a shear cutting and trimming machine and perhaps a laser cutting machine, while the material handling is usually automated with robots. Such manufacturing cells are shown in Figs. 1.6 to 1.8 while a close up of the tooling is shown in Fig. 1.9.

The actual hydroforming machine consists of the hydraulic press, the pressurizing system, auxiliary cylinders and punches for clamping, piercing etc., controls and the forming dies (Koc, 2008). The forming press is designed to provide the required clamping force during forming. The tonnage is often in the order of 7000-8000 tons, with larger machines also in operation nowadays (notice that the machines shown in Figs 1.6 to 1.8 range from 5000 to 8500 tons). Alternatively, some manufacturers offer a special locking device which is activated at the bottom end of the piston stroke and hence provides the clamping instead of the actual hydraulic system of the press.

At the heart of the pressurizing system for the working medium is a pressure intensifier (booster) working on Pascal's principle. The system also includes filling

pumps, piping, valves, filters and a tank. Typical working pressures for THF are between 30 to 150 ksi (2 to 10 kbar). To facilitate short forming cycles, flow rates of the order of 50 lt/min are common, while in some applications multiple intensifiers are used for this reason, as well.

The hydroforming machine is also equipped with a variety of auxiliary hydraulic cylinders. These are used to engage the tubular blank and to provide sealing and perhaps axial feed during the operation. Such cylinders (termed “docking rods”) are shown in Fig. 1.9. Other cylinders can be used for secondary operations close to the end of the forming cycle, such as piercing of openings (hydropiercing) and localized cam forming.

The system is completed with suitable sensors and a controller. Closed-loop controllers are often opted for, since the loading paths used for THF are non linear and the forming conditions can well vary from specimen to specimen (e.g., due to die wear).

The present day hydroforming technology was developed in Germany in the eighties and nineties. Major suppliers of hydroforming equipment include Schuler, Siempelkamp (SPS) and Anton Bauer from Germany, AP&T from Sweden, Muraro from Italy, Kawasaki Hydromechanics from Japan and Interlaken from the United States.

1.2.4 Applications

Numerous applications of THF have been mentioned in Section 1.2.1 and are shown in Figs 1.4 and 1.5. The majority of applications nowadays come from the automotive sector. In Fig. 1.10, two all-aluminum Audi models, the A2 and the A8 are presented. Among modern manufacturers, Audi has pioneered the use of aluminum in mass produced cars (notable earlier applications include the BMW 328 of 1936, the Dyna Panhard of 1954 and the Land Rover family of vehicles starting from 1948). Audi’s efforts started with the model 100 all-aluminum concept car in 1985 and the Audi Space Frame in 1987, which was claimed to have the same behavior as an all steel body but

being 40% lighter (Davies, 2007). These matured into actual production vehicles, with the A8 (in 1994) designed to be manufactured at a rate of 15,000 per annum while the A2 (in 2000) at four to five times that rate.

The GM Kappa platform and a vehicle that is based on it (the 2007 Pontiac Solstice) are shown in Fig. 1.11. In this case the structure is made out of steel and can be seen to employ multiple hydroformed components. The Pontiac Solstice is remarkable also for using a large number of hydroformed sheet panels. Other automobiles that are using THF are the Ford Mondeo and Windstar, 1997 Malibu Cutlass, 1997 Buick Park Avenue and Pontiac Aztec, 2006 Corvette Z06, Honda Insight, Acura RL and NSX, Saab 9-3, Volvo 850, Audi A4 and A6, Mercedes-Benz S-Class, BMW 5 and 7 series, Jaguar XJ, Dodge Dakota and Ram, 2004 Ford F-150, GMC pick-up trucks and SUVs as well as a variety of high performance cars (Koc, 2008)

Naturally, automotive components that lend themselves to hydroforming are those encountered in the exhaust systems (Fig. 1.12), however as shown in Fig. 1.5 the automotive applications of THF are by no means limited to that area. A variety of structural components is shown in Fig. 1.13 and includes engine cradles, roll bars and suspension subframes, i.e., all high stress parts. Often, various machine elements are made by THF, such as metal bellows (used in couplings as in Fig. 1.14a but also in piping) and transmission drive shafts (notice the hydroformed body of the shaft in Fig. 1.14b). Another large area of application is in the bicycle (mainly) and the motorcycle industry (less so). Typical examples are included in Figs 1.15 and 1.16, showing bicycle frames that have distinctly varying cross sections along their length. This trend began in 2003 when Giant offered the first mass produced hydroformed bicycles and since then has undeniably become the industry standard. Hydroforming offers lighter and stiffer

frames, but not less importantly, it allows for greater design flexibility in the bicycle aesthetics.

Lastly, typical applications in plumbing fittings and domestic appliances are shown in Fig. 1.17, including a Tee fitting, branches and a variety of faucets, formed from copper, aluminum and brass alloys.

1.2.5 Hydroforming Process Envelope

During the THF process, the tube is loaded under internal pressure and axial load and is in partial contact with the surrounding die. Friction impedes the material flow. As a result of this, the tube may fail in a variety of ways, presented schematically as a working envelope graph in Fig. 1.18. Naturally it is of major interest to the user to be able to determine the working envelope for the material at hand, and it is in this direction that the present research aims to contribute.

Provided that the combination of internal pressure and axial load is such as to plastically deform the material, the lower bound of the working envelope in Fig. 1.18b is traced by the axial force that needs to be provided for any given pressure to ensure sealing. As the pressure increases however, the bursting limit of the tube is reached (see right hand specimen in Fig. 1.18a). On the other hand, if the axial load is excessive, then the tube will wrinkle (left specimen in Fig. 1.18a) or will experience overall buckling as a column.

The working envelope is also affected by the presence of the die. In general, the die will support the tube against buckling or wrinkling, however the friction associated with the tube/die contact will promote the bursting failure.

1.3 OUTLINE OF THE THESIS

This thesis presents an investigation of aluminum THF and its limit states. This includes the development of a custom hydroforming facility, the forming of tubular components and a parallel study dealing with tube formability and constitutive modeling. In Chapter 2, an experimental study of THF is described along with the extensive custom designed and fabricated facility. Originally, the bursting failures that were encountered experimentally in our work could not be predicted beforehand with standard analytical and numerical tools. This prompted a combined experimental and analytical study of tube formability with the aim, first to investigate the forming limits of the tubular specimens and second to establish appropriate constitutive frameworks for accurate predictions of localization and burst. The experimental component of the formability study is presented in Chapter 3, while the analytical and numerical effort is detailed in Chapter 4. Also included in that Chapter are details of the constitutive and of the finite element models employed. With the benefit of this improved understanding of the behavior of the material, the simulation of the THF experiments is revisited in Chapter 5. The predictions from the variety of constitutive models are critically evaluated against the hydroforming experiments and a set of firm guidelines for successful simulations of the process, including failure, are deduced. The main conclusions and findings are summarized in Chapter 6.

Audi TT Roadster

Rohkarosserie

Structure

11/06

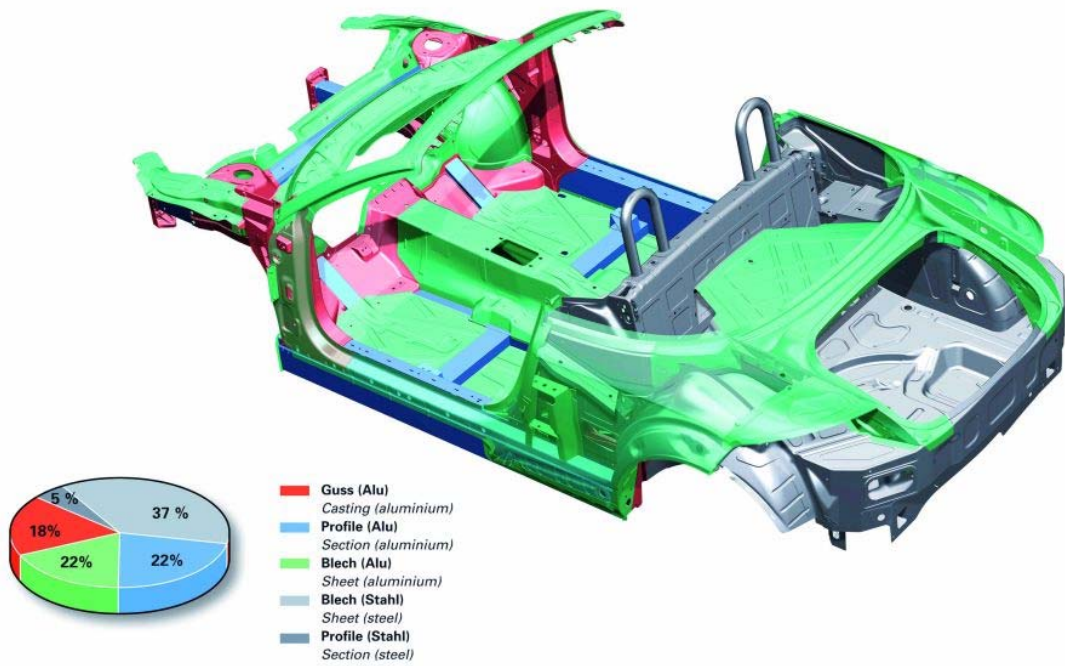


Fig 1.1 – Materials used in the body of a modern automobile.

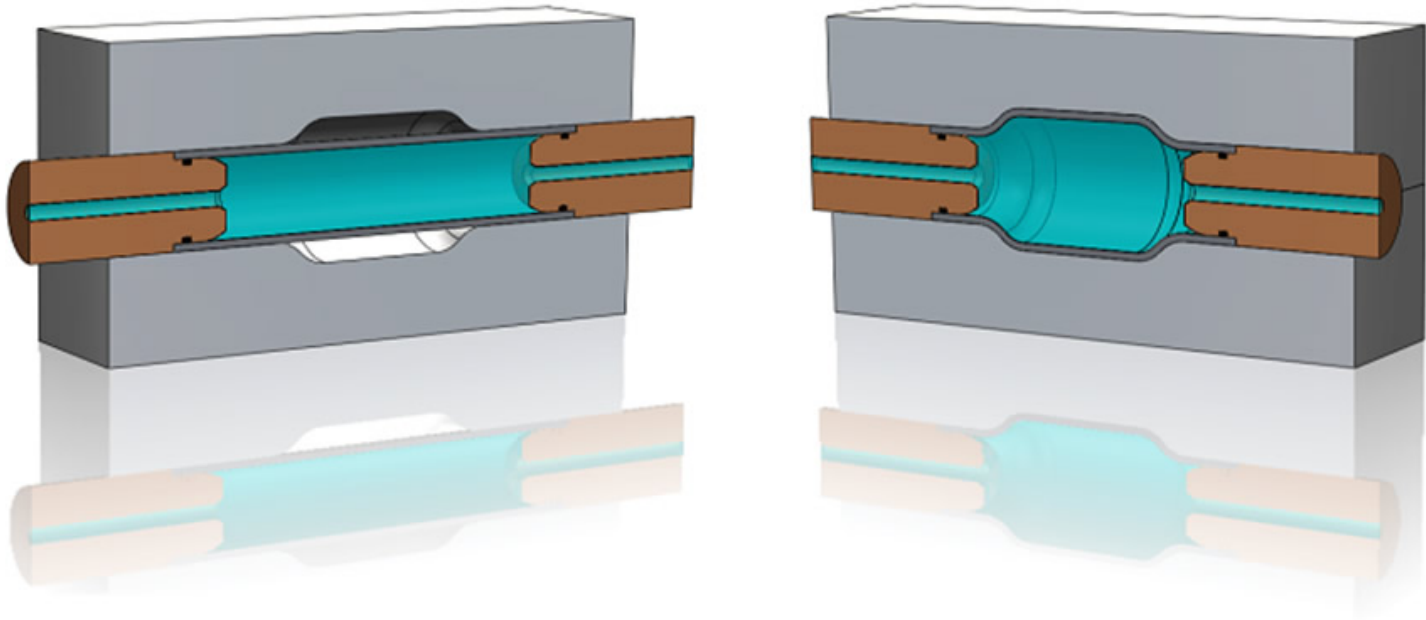


Fig 1.2 – Tube hydroforming (www.muraropresse.com).

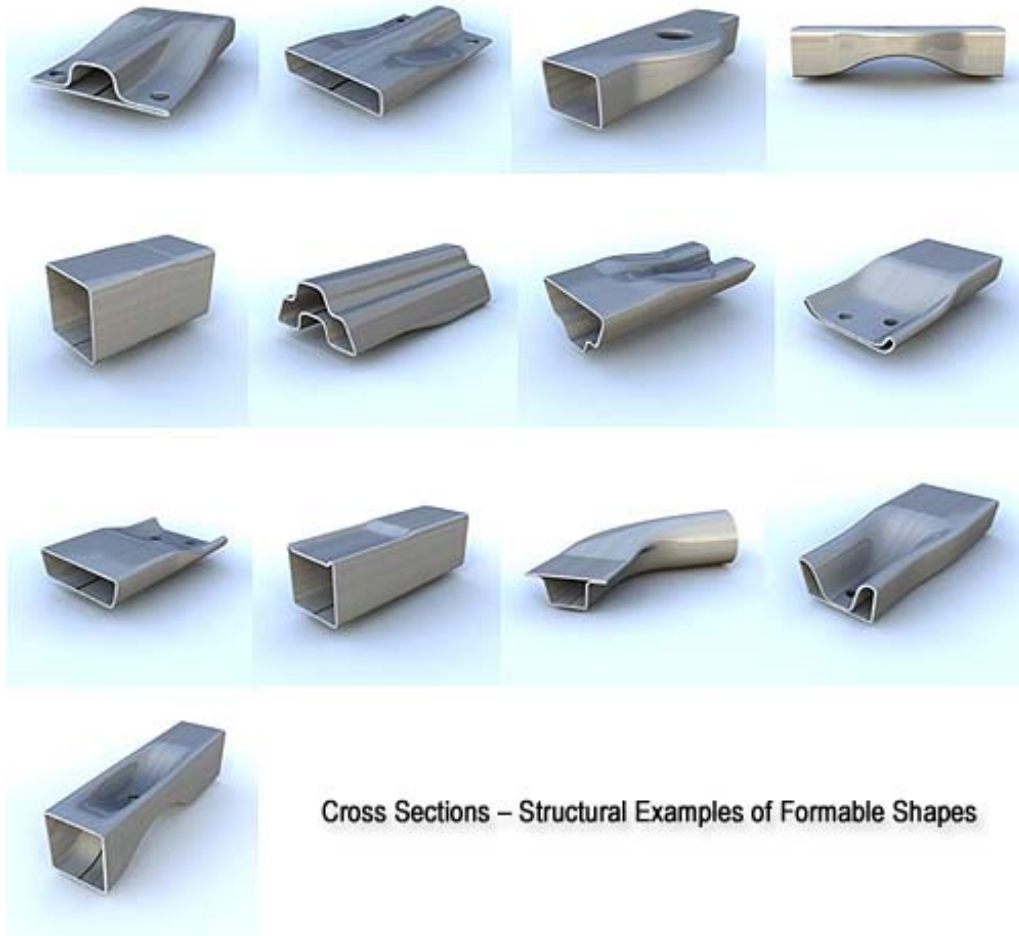


Fig 1.3 – Examples of shapes that can be hydroformed (www.excellatechnologies.com).



(a)



(b)

Fig 1.4 – Hydroformed musical instruments. (a) Euphonium and (b) Sousaphone.

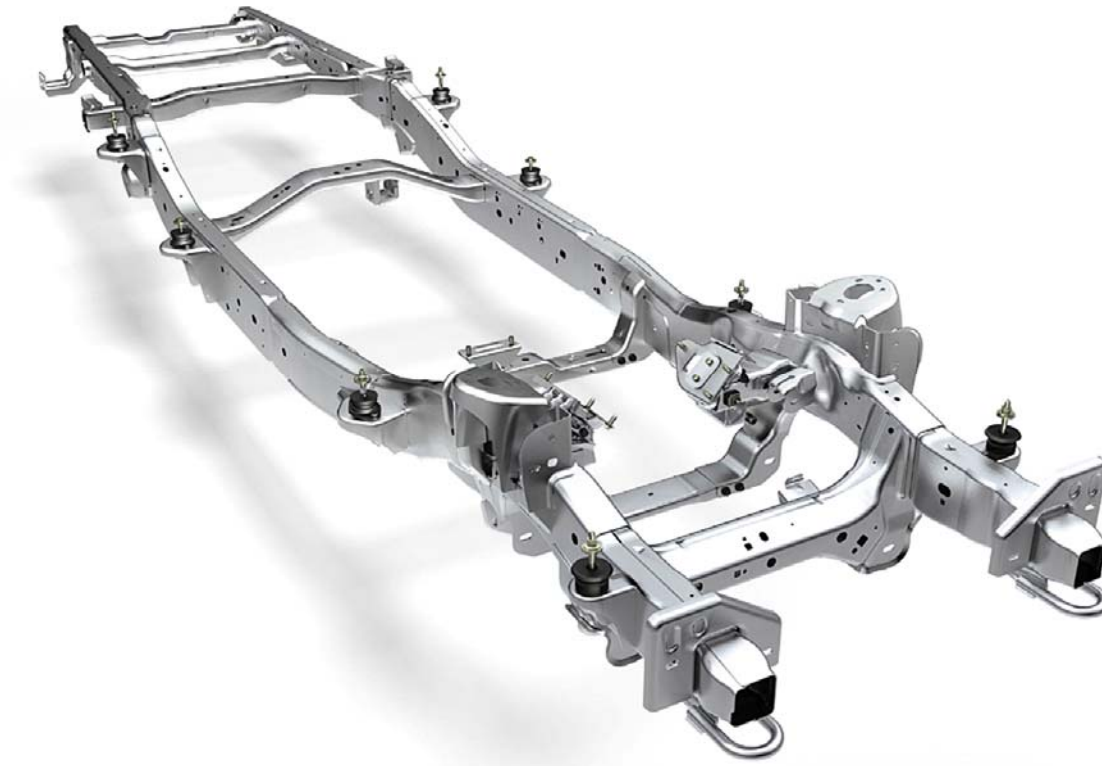


Fig 1.5 – Hydroformed frame for Ford F-150 pick-up truck (www.dana.com).



Fig 1.6 – 8,500 ton hydroforming press, including tube benders, performing press and shear cutting (www.schulergroup.com).



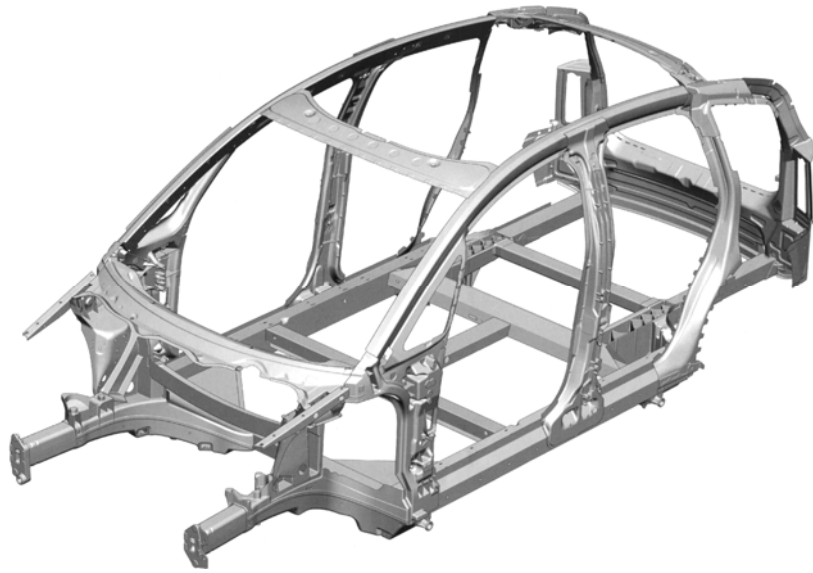
Fig 1.7 – 50 MN Hydroforming press (www.siempelkamp.de).



Fig 1.8 – 60 MN/3 kbar hydroforming press (www.muraropresse.com).



Fig 1.9 – Hydroforming an automobile component. Also visible are the two tube guides/docking rods (www.schulergroup.com).



(a)



(b)

Fig 1.10 – All-aluminum cars, employing the space frame with numerous hydroformed components. (a) Audi A2, and (b) Audi A8 (www.schulergroup.com).



(a)



(b)

Fig 1.11 – (a) GM Kappa architecture and (b) 2007 Pontiac Solstice that uses the Kappa architecture. The Solstice is notable for using extensively both tube and sheet hydroforming.



(a)

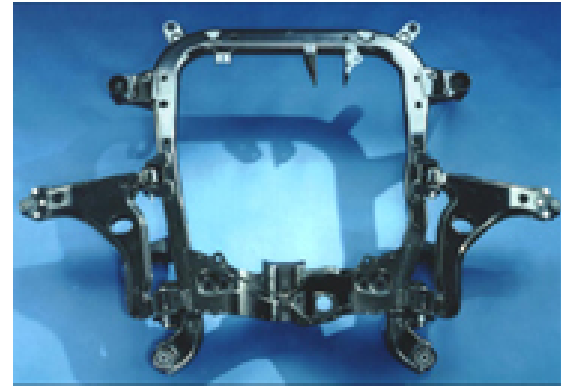


(b)

Fig 1.12 – Automotive exhaust components ((a) www.sapagroup.com and (b) www.muraropresse.com).



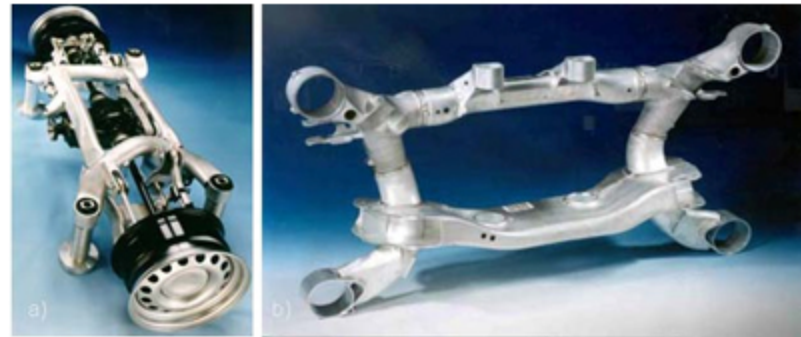
(a)



(b)



(c)



(d)

Fig 1.13 – Hydroformed automotive components. (a) and (b) engine cradle for Opel AG, (c) roll bar and (d) rear axle subframe assembly for BMW ((a) to (c) www.schulergroup.com, (d) Hydro Aluminum Deutschland GmbH)



(a)



(b)

Fig 1.14 – Hydroformed machine elements. (a) Coupling with hydroformed stainless steel bellows (www.couplingtips.com) and (b) hydroformed drive shaft (www.dana.com)



(a)



(b)

Fig 1.15 – Bicycles with hydroformed frames from aluminum alloys. (a) Giant Reign and (b) Giant Cityspeed



(a)

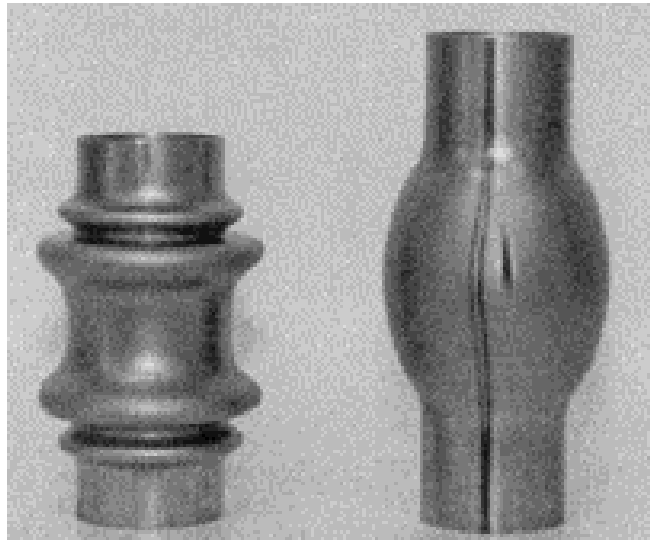


(b)

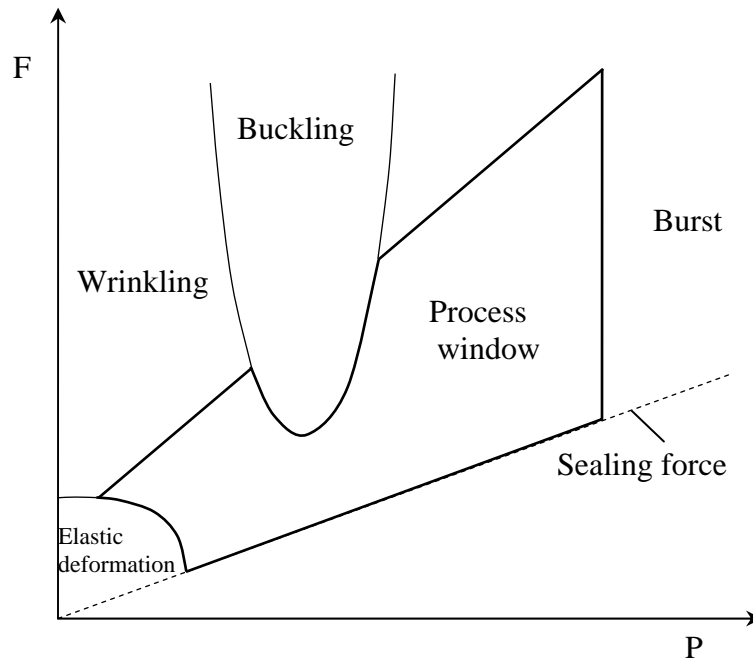
Fig 1.16 – Hydroformed bicycle frames from aluminum alloys. (a) Yeti 575 and (b) Scott Gambler FR 10



Fig 1.17 – Copper, brass and aluminum plumbing fittings, fixtures and faucets



(a)



(b)

Fig 1.18 – (a) Failure modes of tubes under internal pressure and axial load, after Asnafi and Skogsgårdh, 2000 and (b) THF process envelope.

Chapter 2: *Tube Hydroforming Experiments*

A custom facility was designed and constructed to study the hydroforming of relatively long, thin-walled tubes. The facility consists of a hydroforming machine, a pressurizing unit of 20,000 psi (1378 bar) capacity and a computerized data acquisition and control system. As will be described subsequently, most of this equipment was custom designed and fabricated for the purposes of this study. A more detailed presentation of the testing facility is given in the MS thesis by J. Capeto (2003).

2.1 HYDROFORMING FACILITY

2.1.1 Hydroforming Machine

We investigated one of the simplest forming operations, where an initially circular cross-section is formed into a rounded square of 2.4 in. (60.96 mm) side with a 0.5 in. (12.70 mm) radius at each corner (Fig. 2.1). For a tube of 2.357 in. (59.88 mm) initial diameter and under ideal forming conditions, this expansion imparts an average hoop strain of about 18%, which is close to the failure strain of Al-6260-T4 in uniaxial tension. The machine is designed to receive tube specimens of up to 34 in. (863.60 mm) in length. Thus for example using 24 in. (609.60 mm) long dies, the remaining 10 in. (254 mm) are available for end feeding.

The cross-section of the hydroforming machine is shown in Fig. 2.2 while a three-dimensional rendering and side and plan views are given in Fig. 2.3. A photograph of the facility is given in Fig. 2.4. The machine consists of two main members (top and bottom steel “shoes”) which enclose the forming die and provide support for the end-feed actuators. During forming, the shoes are held together by 14 high strength (1.25 in. /

31.75mm, Grade 8, 12 UNF) bolts (see Fig. 2.2) which are tightened using a pneumatic impact wrench. The closing operation lasts approximately 30 minutes. While clearly too slow for a production environment, this solution significantly reduced the cost of the lab facility. In industrial hydroforming machines, the opening, closing and clamping operations are facilitated by hydraulic actuators, allowing for a forming cycle of 1-2 minutes or less.

The forming dies are located in wide channels machined in the shoes for that purpose. Generous dimensional allowances were provided for these channels to allow for different cross-sections to be investigated (see Fig. 2.2). To hold each piece in place, the spacer plates (6) are bolted to the shoes (3 and 9). The clamping strips (7) are in turn bolted to the spacers 6 and thus hold the forming die (5 and 8) and the insert plates (4) in place. This allowed for the best possible clamping of the forming die, preventing distortions and localized loads.

The dies are made of P20 tool steel and have overall dimensions of $24 \times 5 \times 5.05$ in. ($609.60 \times 127 \times 128.27$ mm) as in Fig. 2.5a. They have been machined with precision (± 0.002 in. / 0.0508 mm and ± 0.005 / 0.127 mm for the inside and outside dimensions, respectively) and to a good surface finish (63 RMS) as is customary in such applications. The alignment of the dies, and in fact of the two shoes, is facilitated by two 0.5 in. (12.7 mm) dowel pins. As can be seen in Fig. 2.5a, the cross-section of the die at the two ends is circular to receive the yet undeformed tube, while the transition to the rounded square shape occurs gradually. A rendering of the transition zone is shown in Fig. 2.5b. Beyond each die end, hardened end-guides provide the necessary support to the remaining tube.

The required end-feed is provided by two 8 in. bore / 5 in. stroke (203.2 mm / 127 mm) hydraulic cylinders rated for 150 kips (667.2 kN) and operating on the standard

3,000 psi / 10.1 GPM (210 bar / 38.2 LPM) hydraulic pressure system available in the lab. The dimensions of the actuators have been decided using the graph in Fig. 2.6. An internal pressure of 20,000 psi (1,380 bar) results in 75 kips (333.6 kN) force on the load cell. Since a cylinder with 8 in. bore diameter and operating at 3,000 psi can develop 150 kips, the available load for forming (i.e., force on the specimen) when the internal pressure is 20,000 psi is 75 kips. Each actuator is mounted on a $12.5 \times 15 \times 2$ in. ($317.5 \times 381 \times 50.8$ mm) vertical plate which rests in suitable grooves in the top and bottom shoes (Fig. 2.3). In this manner, the axial loads are ultimately reacted by the shoes.

The whole machine has a footprint of $94.5 \times 28 \times 24$ in. ($2400 \times 711.2 \times 609.6$ mm) and weighs approximately 3,250 lbs (1474 kg). Each shoe weighs approximately 1,100 lb (500 kg) without the axial actuators assemblies. The machine rests on wooden blocks, about 12 in. (304.8 mm) off the floor, and is serviced by a 1 ton jib crane with a chain hoist.

2.1.2 Pressurization System

Pressurization is provided by a 20,000 psi (1,380 bar) pressure intensifier (“booster”) shown in Fig. 2.4. The booster operates on the standard 3,000 psi (210 bar) pressure available in the lab, while the available volume of high pressure fluid is 0.5 gallons (1.9 liters). For this reason and to conserve the booster stroke, the filling of the tube before each experiment was performed using a low-pressure water pump as shown in Fig. 2.7a. In Fig. 2.7b the detail of fluid passage through the axial actuator rams and the load cells is shown. These are connected to the pressurizing system using high-pressure flexible hoses, to facilitate their free axial movement. As a pressurizing medium, a compound of 95 parts water / 5 parts Multan 98-10 was selected. This substance is a standard, commercially available metalworking fluid supplied by Henkel Surface Technologies.

2.1.3 Data Acquisition and Control System

The facility is controlled via a six channel custom system shown schematically in Figs. 2.8 and 2.9. The same system is used both for feedback control and for data acquisition. It is based on an extensively modified MTS 458.20 control unit and is commanded by custom software running on a PC and created using LabView.

a. Transducers

Each axial feed actuator is equipped with a load cell and a displacement transducer. The load cells are custom designed to a rated capacity of 150 kips (667.2 kN) and are positioned between the actuator rams and the specimen (see Fig. 2.7b and Fig. 2.10). The material selected is AISI 4142 steel that was heat treated after machining, while the overall dimensions are chosen so as to prevent yielding. The end of the load cell, that engages the specimen, is suitably configured to ensure sealing using o-rings. The fluid passage through the load cell is facilitated by a coaxial high pressure tube (Fig. 2.10). Each load cell is provided with a pair of biaxial strain gages (CEA-06-062UT-350), suitably arranged in a Wheatstone bridge (providing both temperature and bending compensation). The bridge excitation is 10 V. The calibration of the load cells was performed using a standard servohydraulic testing machine with 220 kips (1 MN) capacity.

The actuator displacement is monitored using a Linear Variable Differential Transformer (LVDT) with a linear range of ± 3 in. (± 76.2 mm) and a linearity of $\pm 0.25\%$ full range (Schaevitz 3000 HR). Each hydraulic cylinder is equipped with a tail rod. This rod is connected to the core of the LVDT through an aluminum bracket and a non-conductive brass rod, thus transferring its motion to the sensor (Fig. 2.11). The LVDTs were calibrated using a standard electromechanical testing machine.

Also available are measurements of the internal pressure and of the volume of the pressurizing medium discharged in the specimen. The first is monitored by a 20,000 psi pressure transducer (Sensotec Z/1108-03), shown in Figs. 2.7a, 2.8 and 2.9. This transducer was calibrated using a dead-weight tester.

Because of the long stroke of the booster, a Magnetostrictive Linear Displacement Transducer was selected for monitoring the volume (= area \times stroke) (MagneRule MRU-3000-018). This instrument has a range of 18 in. (457.2 mm), maximum nonlinearity $\pm 0.05\%$ full range, resolution up to $\pm 0.002\%$ full range and maximum hysteresis of 0.001 in. The instrument was connected to the tail rod of the booster in a similar fashion as the LVDTs described earlier (see Fig. 2.12) and was calibrated using a standard electromechanical testing machine.

Since the MagneRule is an unconventional instrument, a description of its principle of operation is appropriate here. To measure the displacement, short electric pulses are emitted along a waveguide. When the accompanying magnetic field is disturbed by that of a permanent magnet, which is connected to the booster's tail rod (Fig. 2.12), magnetostriction generates a torsional wave that travels along the waveguide. As this wave is received by the instrument, it is converted back to an electric pulse. By measuring the time difference between the two pulses (original and reflected), the position of the permanent magnet can be precisely determined.

All transducers were suitably calibrated to the 10 V standard.

b. Computerized Control System

The controller of the facility is based on an extensively modified MTS 458.20 MicroConsole unit and a Personal Computer running a custom LabView application.

The MicroConsole is a microprocessor-based analog controller, also providing signal conditioning. In a biaxial materials testing setup, the MicroConsole is configured

to control two active actuators. In the present facility, it was initially aimed to use two control channels as well: one for the booster and the other for both of the axial feed actuators. However, it was discovered that due to asymmetries present in the system the two feed actuators did not have the same response to a common command signal. It was thus necessary to modify the MicroConsole to control three servovalves and to receive signals from six transducers. This resulted in using a total of six conditioner/controller channels (see Fig. 2.9). Depending on the particular transducer, these channels are either AC or DC (MTS 458.13 and 458.11, respectively) and perform conditioning of the transducers signals, as required. The outputs are directed to a PC-based system for plotting in real-time, storage and data reduction.

The computer system consists of a PC with 1.8 GHz Pentium 4 processor, 256 MB RAM and 40 GB Hard Drive, equipped with two NI PCI-6035E A/D cards. Each card has 8 differential input channels (A/D) with 16-bit resolution and 2 bipolar output channels (D/A) with 12-bit resolution. The maximum sampling rate when all six channels are active is 200 kS/s.

The software that is used to acquire the data and to generate the control commands was created in the LabView environment. During the experiment, the software acquires and plots the desired quantities in real-time and at the same time outputs the predetermined command signals. Special attention was paid to the fact that reading input from and writing output to the A/D-D/A card cannot be performed in LabView simultaneously by default. To overcome this difficulty, the input and the output functions were placed inside a “while loop” and executed in sequence. This loop was set to iterate every few milliseconds, thus allowing the nearly simultaneous input and output of signals. While this solution is perfectly adequate for the needs of these experiments, it

would be unsuitable for applications with more rapid events due to the execution time required for the loop to complete.

The LabView software developed for this facility can output arbitrary piece-wise linear commands. The A/D-D/A card converts the digital into analog signals, scaled from 0-10 V, before they are directed to the MTS MicroConsole. The MicroConsole performs the feedback control by comparing the output commands from the PC to the system response as monitored by the transducers, and issues the final command signals to the three servovalves (see Fig. 2.8).

Each function can run under either displacement (volume) or load (pressure) control. In our experimental work, we usually prescribed the axial feed displacements and the internal pressure.

2.1.4 Summary of Specifications of Hydroforming Facility

<i>Specimen dimensions</i>	
2.357 in. OD, 34 in. length (10 in. used for feeding)	
<i>Axial feed</i>	
8 in. bore / 5 in. stroke hydraulic cylinders, 150 kips capacity	
<i>Pressurization</i>	
20,000 psi pressure intensifier, 0.5 gals pressurizing medium	
<i>Physical dimensions of machine</i>	
Footprint	94.5 × 24 in.
Height	28 in.
Shoe weight	850 lbs
Top shoe with accessories weight	1,100 lbs

Total weight (excluding booster)	3,236 lbs
<i>Sensors</i>	
Axial load	Custom load cells (150 kips)
Axial feed	LVDT (Schaevitz 3000 HR, ± 3 in.)
Internal pressure	Pressure transducer (Sensotec, 20,000 psi)
Displaced volume	Magnetostrictive transducer (MagneRule MRU-3000-018, 18 in.)
<i>Data acquisition and control</i>	
Controller	MTS 458.20 MicroConsole with 458.11
PC	Dell Dimension 8200, 1.8 GHz Pentium 4, 256 MB RAM, 40 GB HDD
A/D-D/A card	NI PCI-6035E cards (8 input and 2 output channels).

1 in = 25.4 mm, 1 gal = 3.785 l, 1 psi = 0.06895 bar, 1 kips = 4448 N

2.2 DESCRIPTION OF A TYPICAL EXPERIMENT

2.2.1 Selection of the Loading Path

At first, it was considered to simply ramp both the pressure and the axial displacement to their target values. However, numerical simulations revealed that the induced compressive load on the specimen would then exhibit a limit load instability, which is customarily associated with buckling. This naturally led to the decision to select appropriate loading paths through simulation. The numerical models employed are described in detail in Chapter 5. Here it suffices to mention that two families of models were developed: generalized plane strain (2-D), and fully three dimensional (3-D). To

design a particular experiment, several runs of the fast 2-D models were performed given a target shape, and the required pressure and axial feed and their approximate histories were established. With the benefit of these results, a detailed 3-D calculation was conducted, to establish the final axial feed – internal pressure history. A typical path is shown in Fig. 2.13. It can be noticed that the axial feed is initially kept low, until the pressure has increased sufficiently to yield the tube and to bring it into contact with the surrounding die. With the additional stabilizing effect provided by the die and the danger of overall buckling of the specimen diminished, the material is then fed into the forming cavity. Finally, as is also customary in industrial practice, the axial feed is kept constant, while the internal pressure is increased further, to bring the shape of the formed tube closer to that of the surrounding die. The two main phases are referred to as “axial feeding” and “calibration”.

2.2.2 Tube Preparation

The specimen’s external surface is cleaned of various scratches by placing it in a lathe and scrubbing it with a Scotch Brite, while the ends are chamfered to facilitate the engagement of the load cells (Fig. 2.7b). An array of lines with a regular spacing of 1 in. (25.4 mm) is lightly scribed on the tube, to enable axial strain measurements after the test. Subsequently, the geometry of the specimens is documented by measurements with micrometers. Since the tubes tested were manufactured by extrusion and drawing, there was a slight thickness eccentricity (between 0.56% and 0.75%) in all of the stock tested.

The tube is then ready to be formed and is coated with the Henkel PTD-1424 BX lubricant. This is a special metal working lubricant with a viscosity of 3500 cPs.

2.2.3 Experimental Procedure

The lubricated specimen is placed in the machine and engaged from both ends by the load cells/axial feed actuators. This is a delicate operation, since at the end of it the

specimen must be centered in the machine, unloaded, while both load cells need to be in the appropriate place for forming to commence. The machine is then closed and the 14 bolts tightened. Time is of paramount importance here, since the lubricant slowly flows under gravity and collects in the bottom of the die, while leaving the top side of the tube unlubricated. The test then commences.

2.3 TYPICAL RESULTS

The forming was slow enough to be considered quasi-static, with the tests lasting between 20 and 30 minutes (see Fig. 2.13). Since the loading was applied in steps, with limited but finite time in between, some creep was evident. A major observation for the experiments is that as the machine was being closed and tightened, the tubes were pinched between the two semi-circular halves of the die ends. This restricted the flow of the material into the forming cavity and in addition resulted in axial loads much greater than anticipated from the simulations. In combination with a small clearance present between the tube and the end guides, the ends of the tube adjacent to the load cells had a markedly increased thickness after the forming operation.

Two hydroformed tubes are shown in Fig. 2.14, one of them having failed by bursting. Different views of a sectioned tube are given in Fig. 2.15. An interesting observation is that due to the relatively long specimens, friction has played a significant role in the final shapes of the two tubes. It can be noticed from Fig. 2.14 that the cross-sectional shape changes along the tube length: it is closer to the desired shape close to the two ends, while deviating increasingly from it as we approach the middle of the specimen. It would appear that as the material was fed into the forming cavity, the high friction encouraged local expansion instead of further axial displacement. This would be a serious shortcoming in an actual operation, but can be possibly remedied by a different transition zone in the dies and/or a different lubricant.

A number of specimens exhibited some mild wrinkling in the unsupported curved regions between the flat sides in contact with the die, as can be seen from Fig. 2.15a. It was not clarified however whether this developed during the actual forming, or during the unloading of the formed specimen.

The axial non-uniformity evident in these photographs has been quantified and is presented in Fig. 2.16. In this figure, the axial strain is plotted along the length of the tube. This is measured with the aid of the pre-scribed lines, using a pair of calipers. The striking feature is that the axial feed experienced at mid-span is significantly lower (1/3 to 1/2, depending on the loading path employed) than the one prescribed at the two ends. Hence, it can be concluded that the beneficial effect of axial feeding on delaying burst may in some cases be negated by the high friction encountered.

The circumferential thickness variation at mid-span for a quadrant of a formed tube is presented in Fig. 2.17. These data were acquired in a variety of ways. For the sectioned tubes, direct measurements were performed with a micrometer. Due to the relative softness of Al-6260-T4, as well as the fine scale nature of the thickness variation measured, these data were confirmed using a standard machine shop optical comparator with suitable magnification. For the non-sectioned tubes, an ultrasonic thickness gage (Panametrics 25 DL with an M 208 probe) was used, with glycerin as a coupling medium. This instrument has 0.0001 in. ($2.54 \mu m$) resolution and requires calibration for the material to be used on.

It can be noted from these thickness measurements that the maximum reduction in thickness on a given cross section occurs at the intersection of the flat and the curved sides. The pattern occurred in all of our experiments. It can be attributed to friction, since any part of the tube that comes into contact with the die is restrained to some degree in its further movement along the circumference.

As mentioned earlier, the tubes had an initial thickness eccentricity so that the corresponding final thickness measurements also vary around the circumference. This is shown in Fig. 2.18, where thickness measurements along the entire circumference are given for three axial locations along a particular tube (mid-span, 4 in. / 101.6mm and 8 in. / 203.2 mm away). The three sets of measurements are different, as is expected because of the friction. Interestingly, the section closest to the end of the die (8 in. / 203.2 mm from mid-span) has in fact become thicker than the original tube. One may also reasonably expect that had the loading continued, the deformation would have localized in the deepest groove (at about 250° at mid-span, Fig. 2.18) and the tube would have failed in much the same fashion as in Fig. 2.14b.

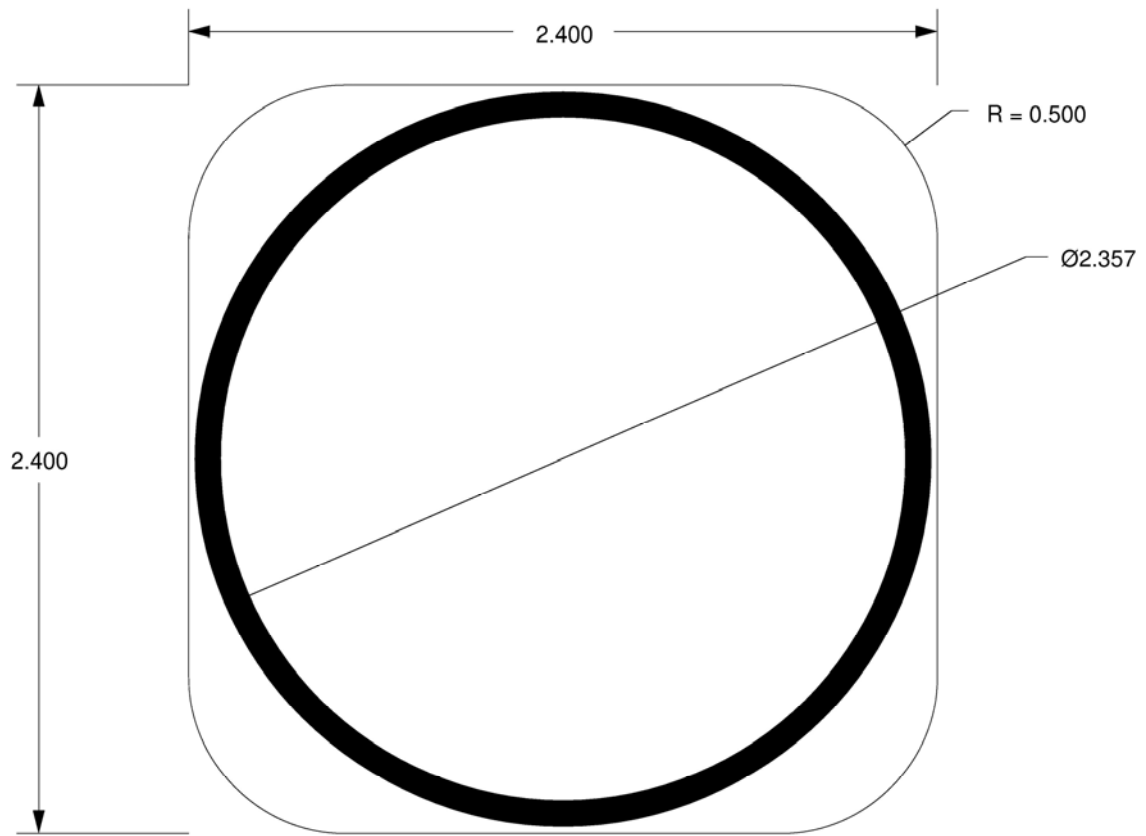


Fig 2.1 – Cross-sectional layout of the hydroforming experiment

- 1 : Tube
- 2 : Closing bolt
- 3 : Top shoe
- 4 : Insert plate
- 5 : Top die
- 6 : Spacers
- 7 : Clamping strip
- 8 : Bottom die
- 9 : Bottom shoe

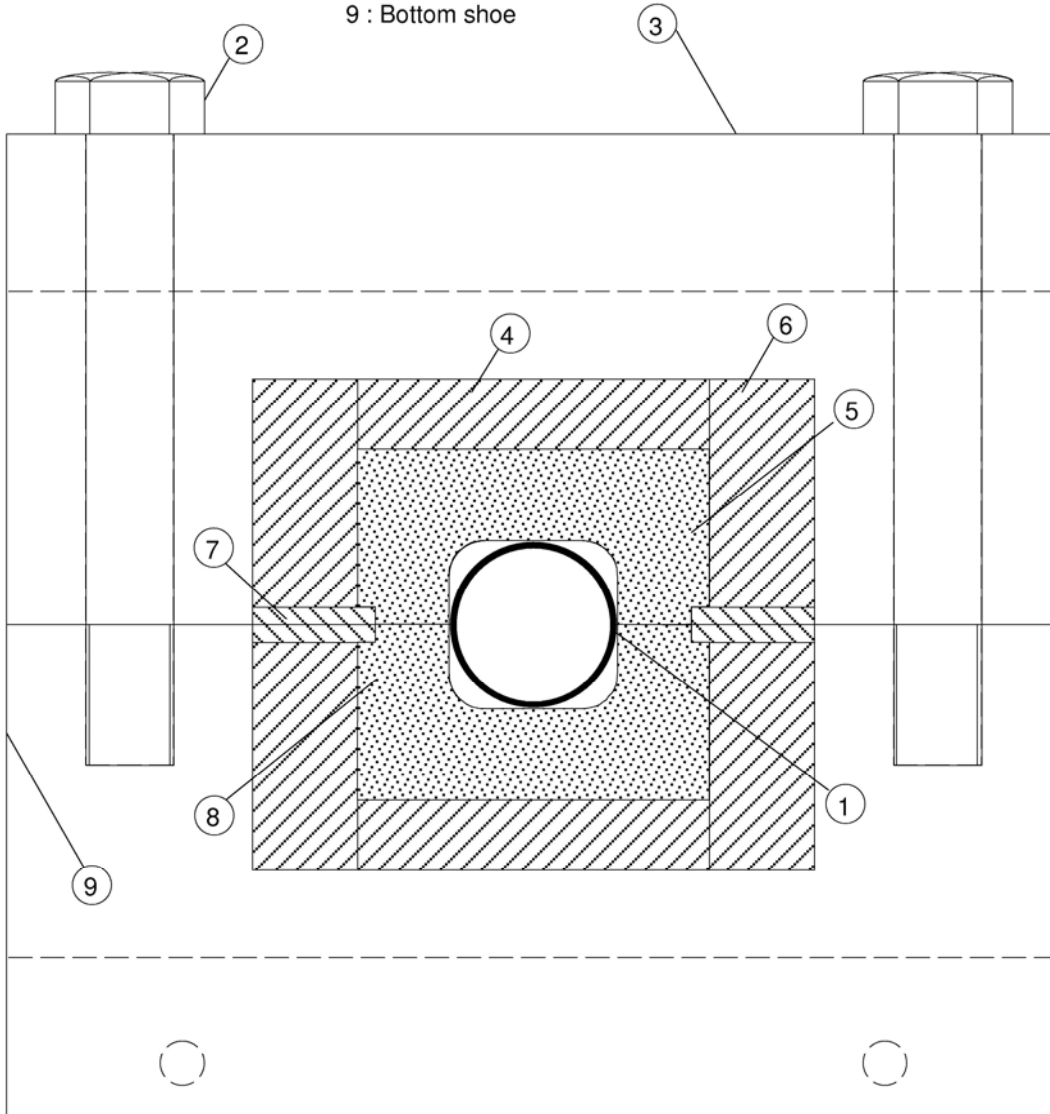
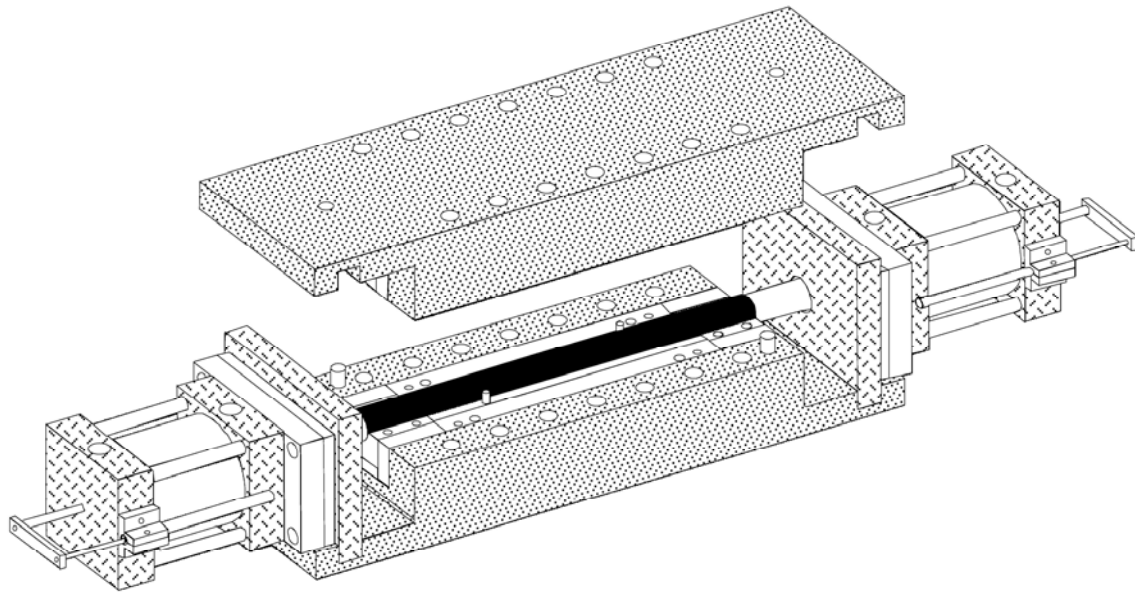
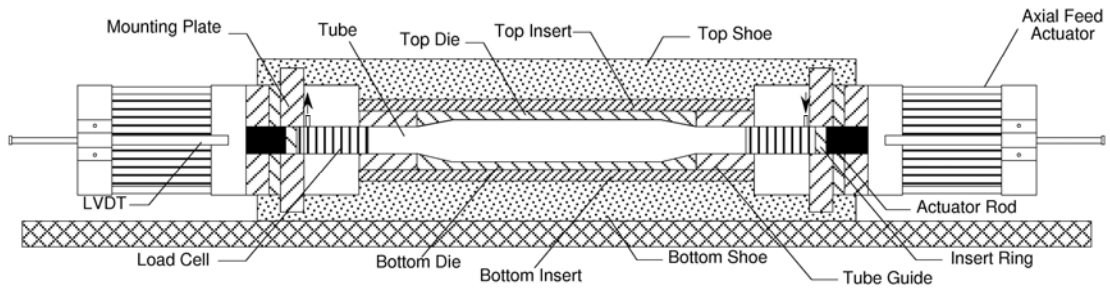


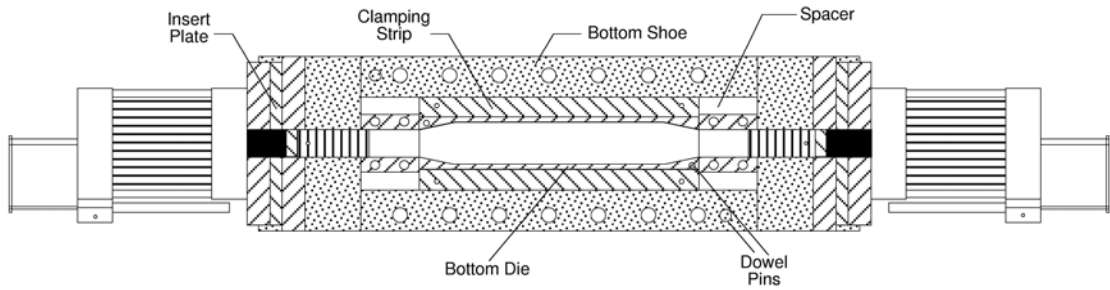
Fig 2.2 – Cross-section of the hydroforming machine



(a)



(b)



(c)

Fig 2.3 – Scaled drawings of the hydroforming machine
 (a) Assembly, (b) side view and (c) plan view

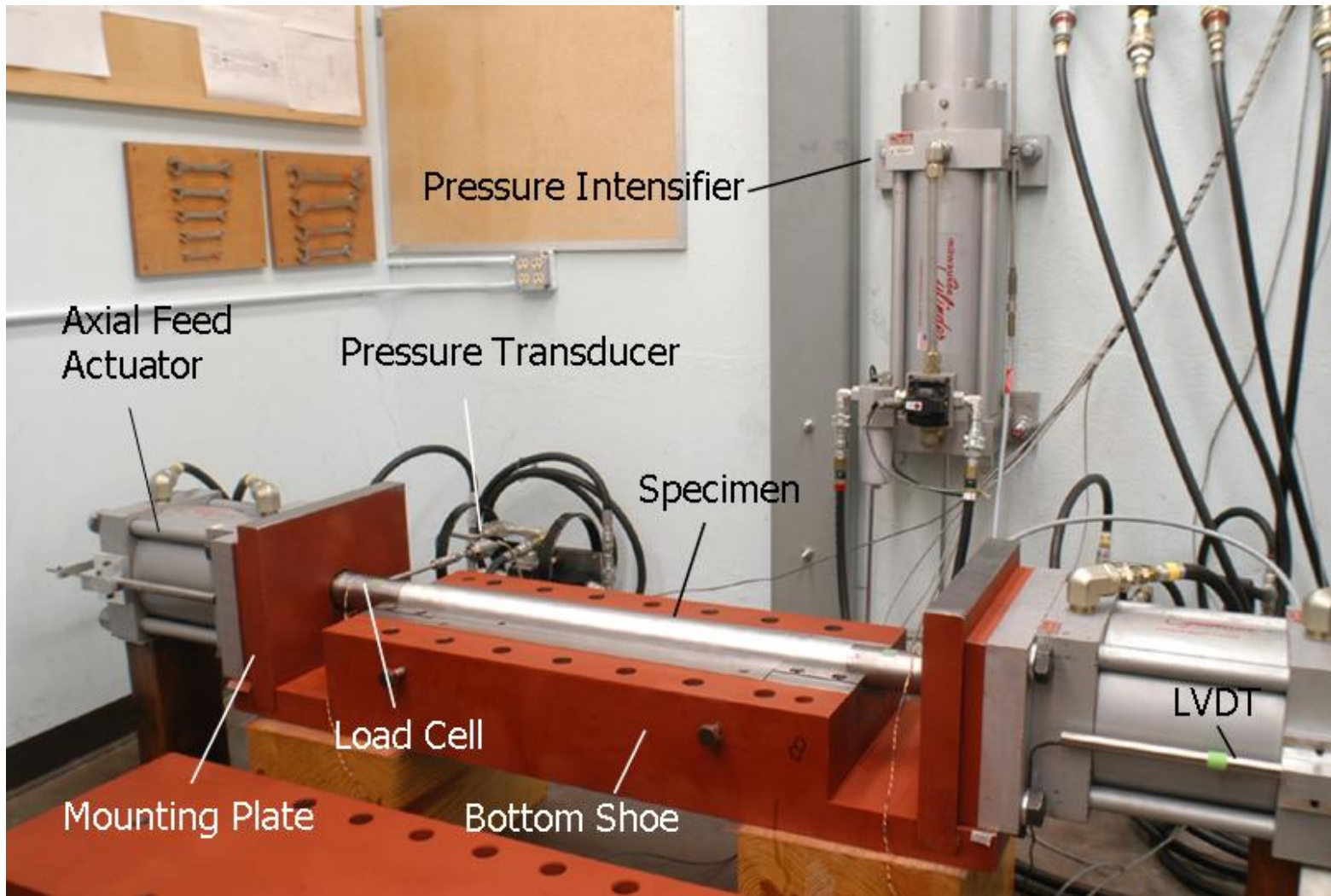


Fig 2.4 – Photograph of the hydroforming facility

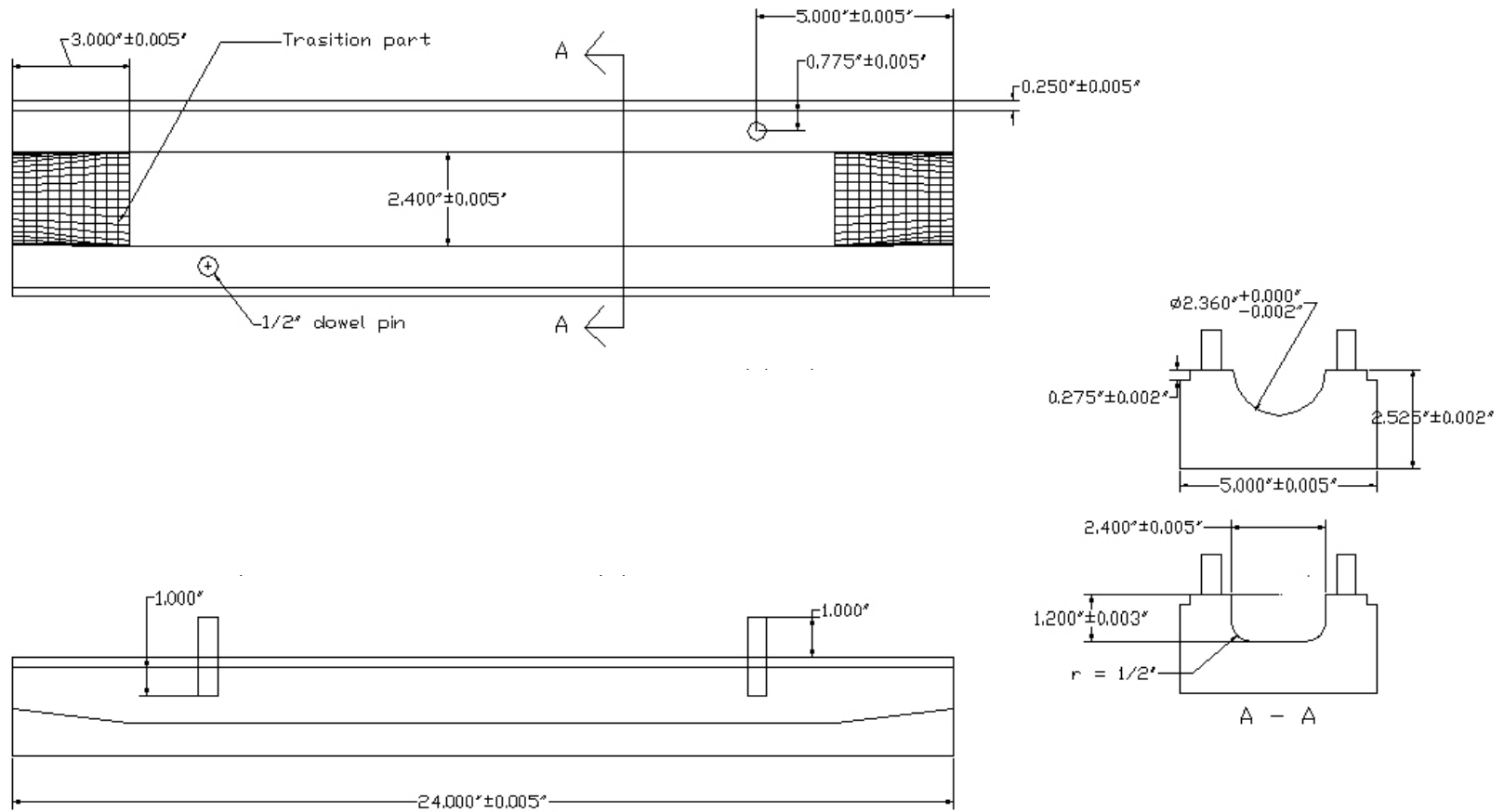
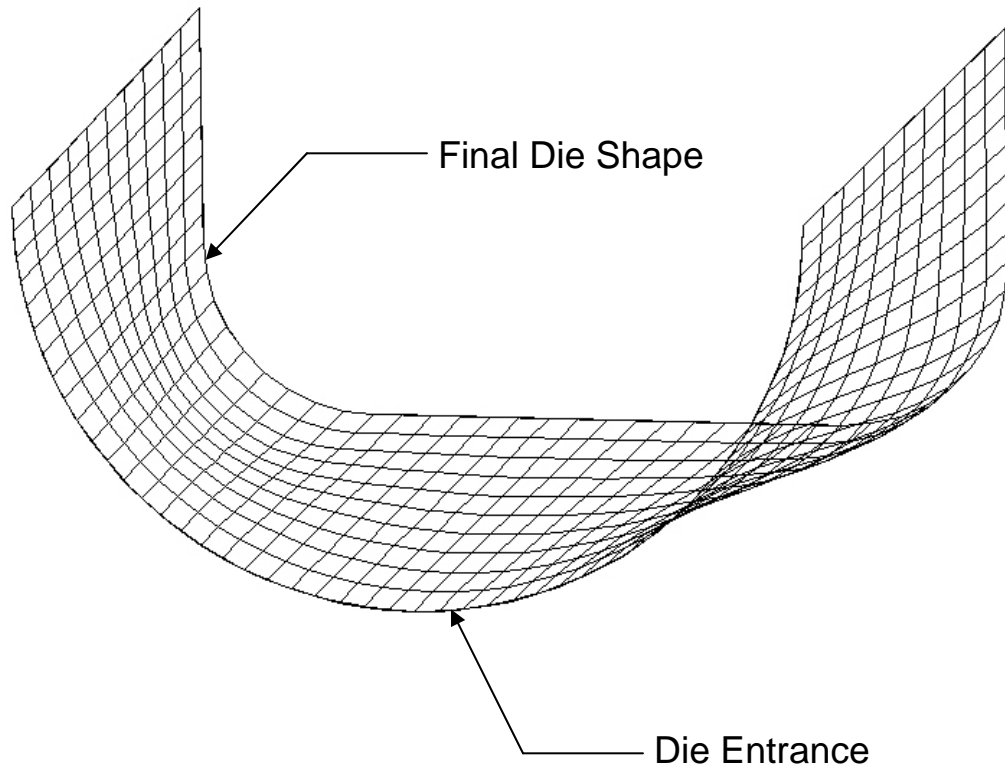


Fig 2.5 – (a) Scaled drawings of hydroforming die (plan, side and cross-sections)



(b)

Fig 2.5 – (b) Rendering of the die transition zone

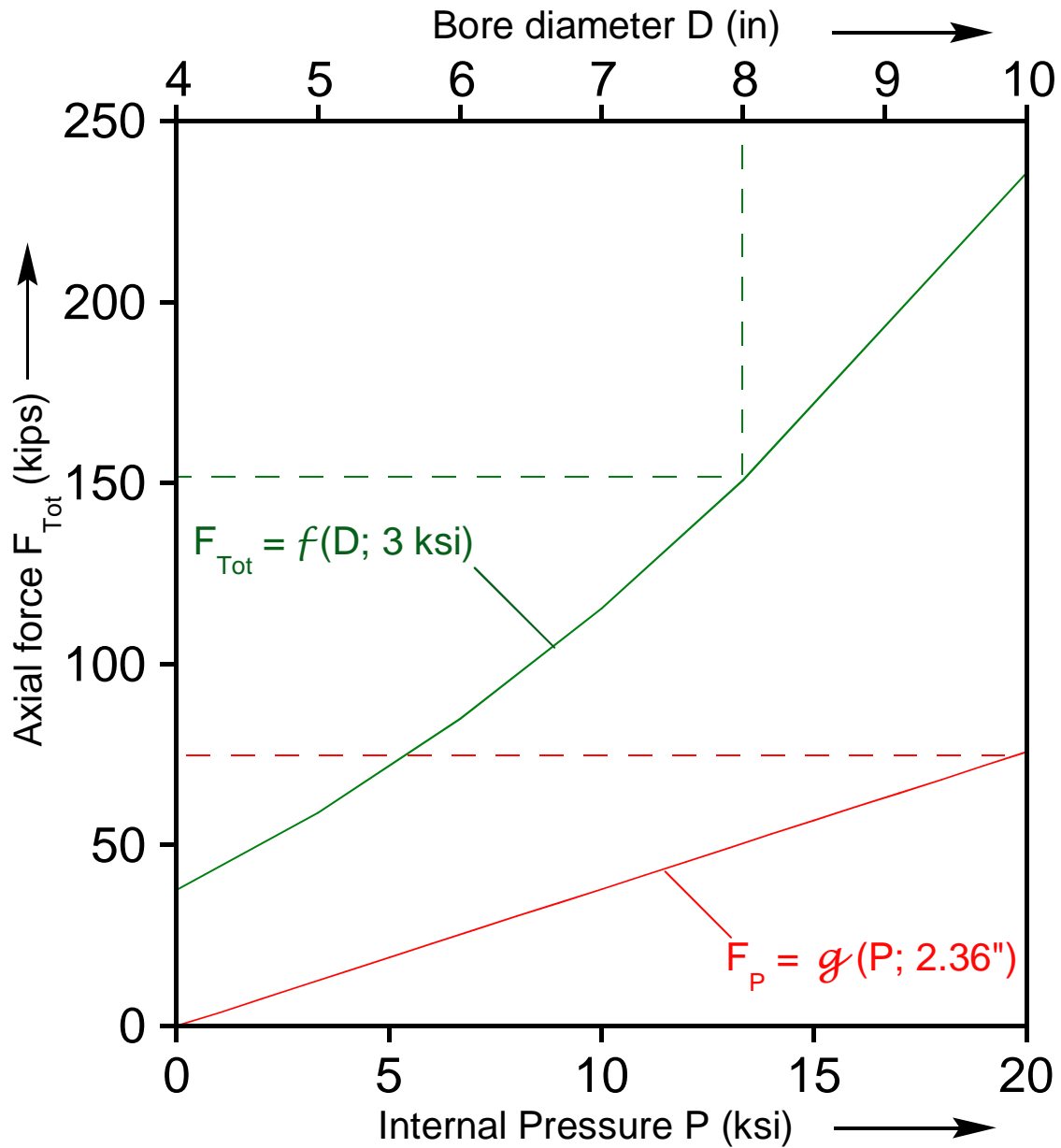
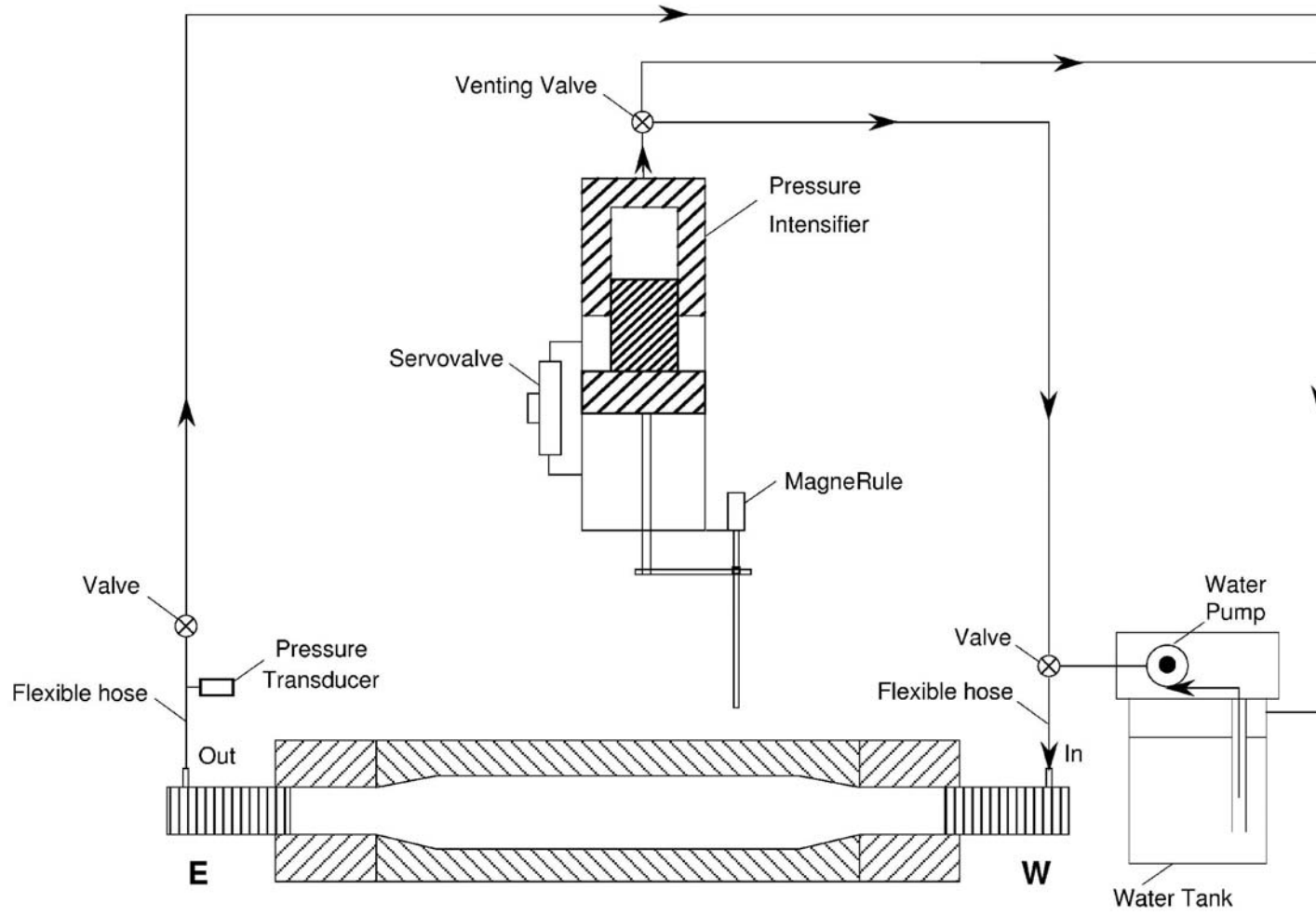
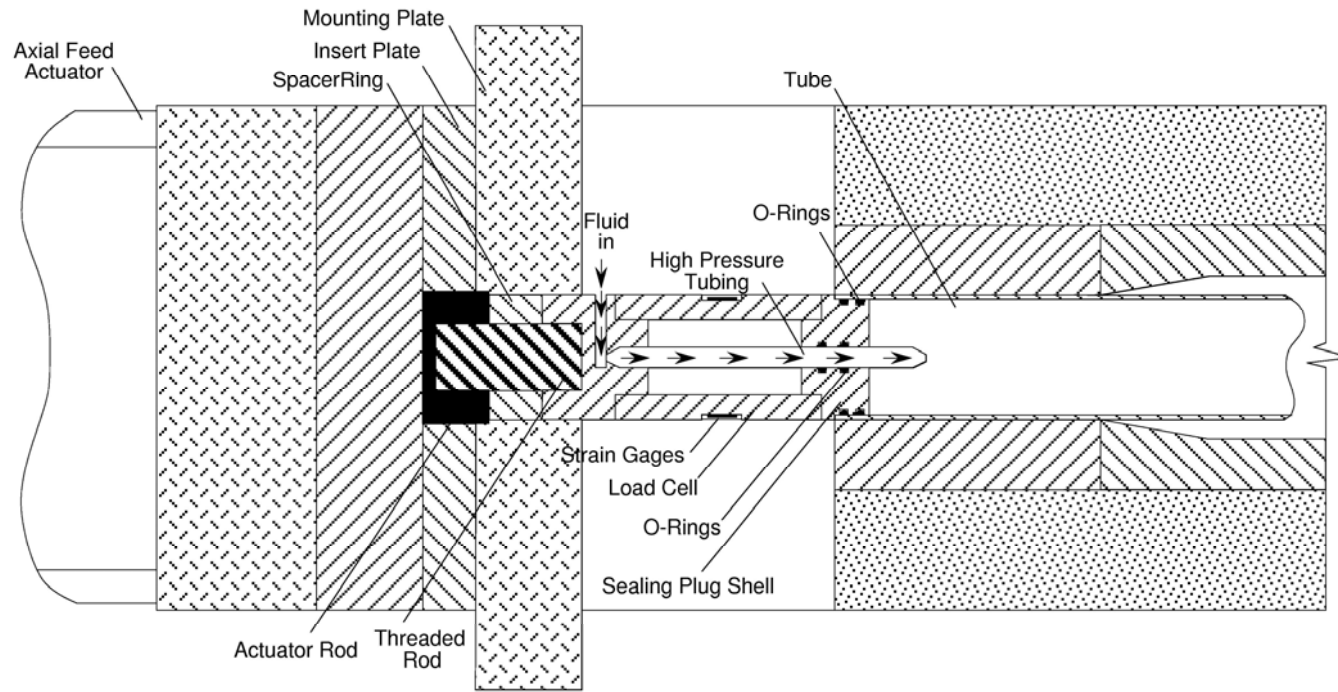


Fig 2.6 – Diagram relating the actuator load capacity as a function of cylinder bore diameter and internal pressure (F_{Tot} : total force that the actuator can develop at 3,000 psi, F_P : force on actuator due to internal pressure on specimen of ID=2.36’')



(a)



(b)

Fig 2.7 – (a) Inflation and pressurizing system and (b) detail of fluid passage

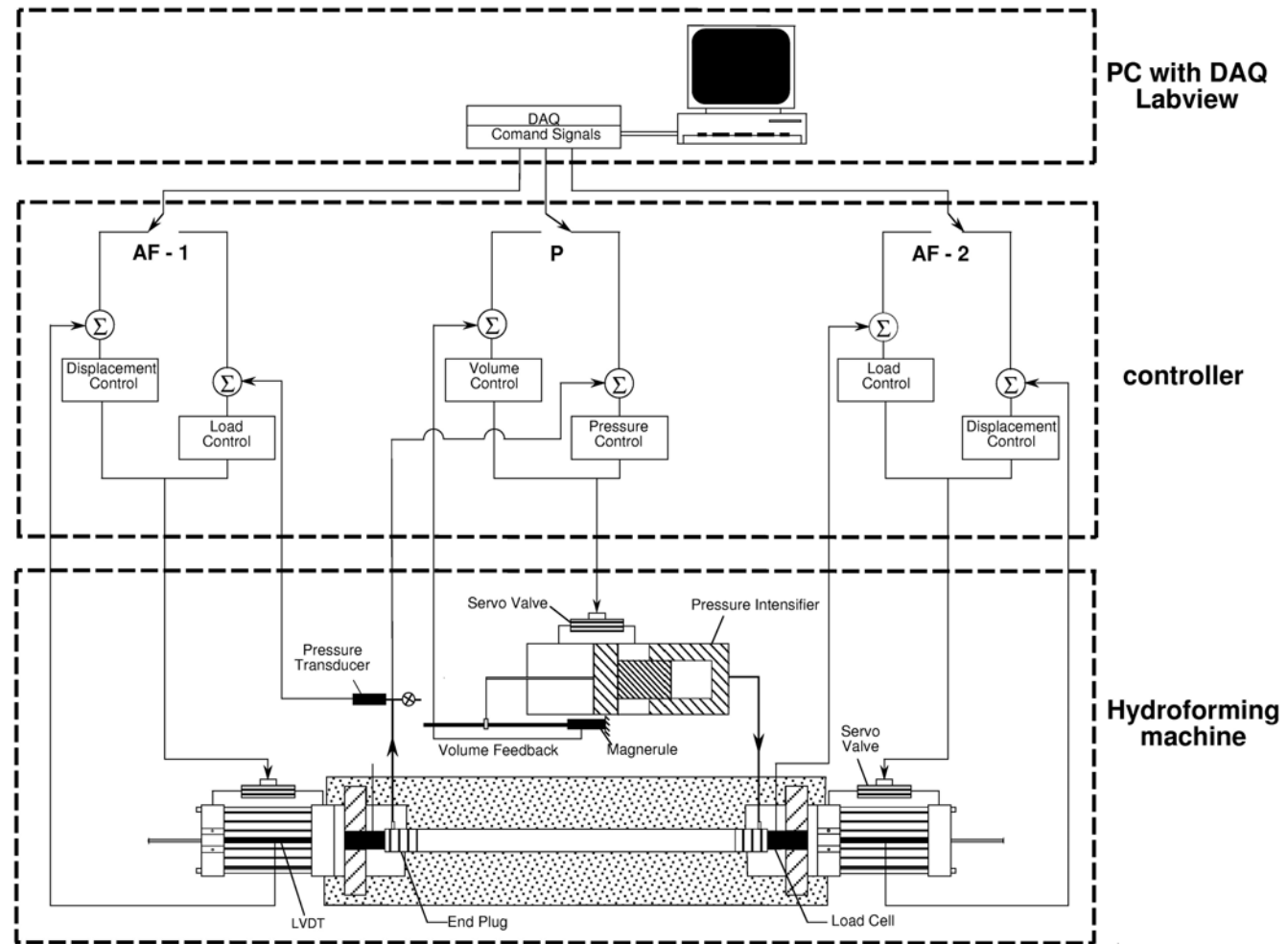


Fig 2.8 – Schematic of the pressurization and the data acquisition and control systems

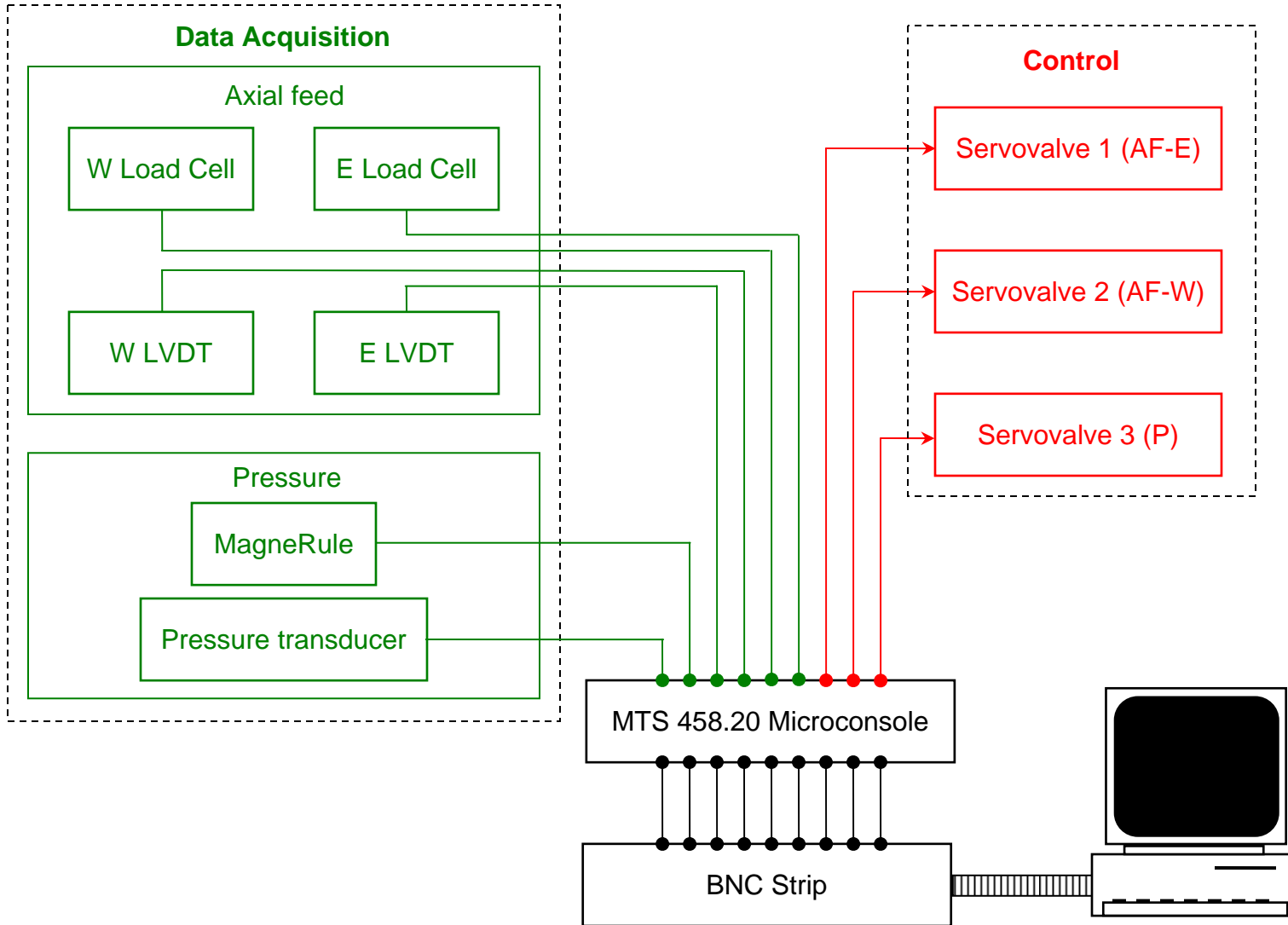


Fig 2.9 – Block diagram of the system transducers

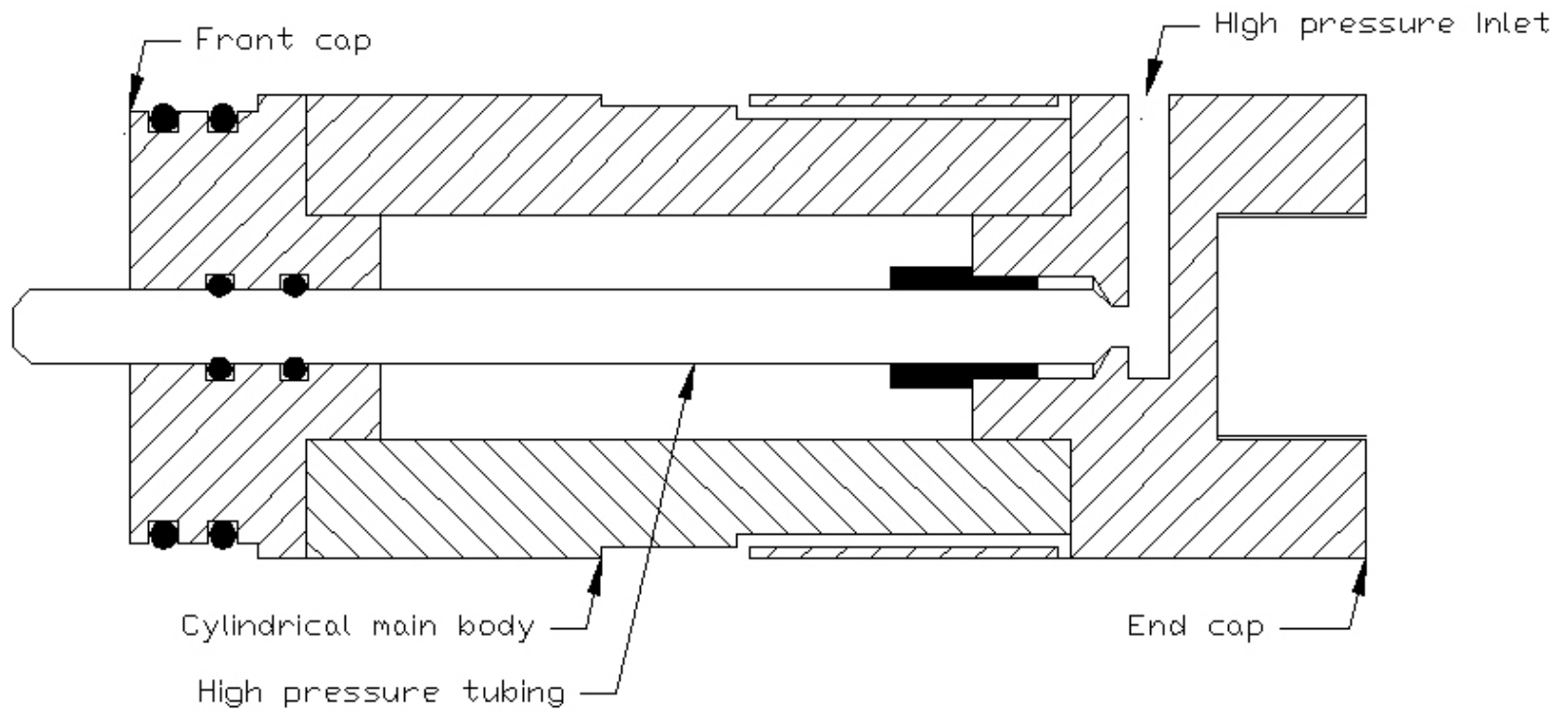


Fig 2.10 – Cross sectional view of a load cell

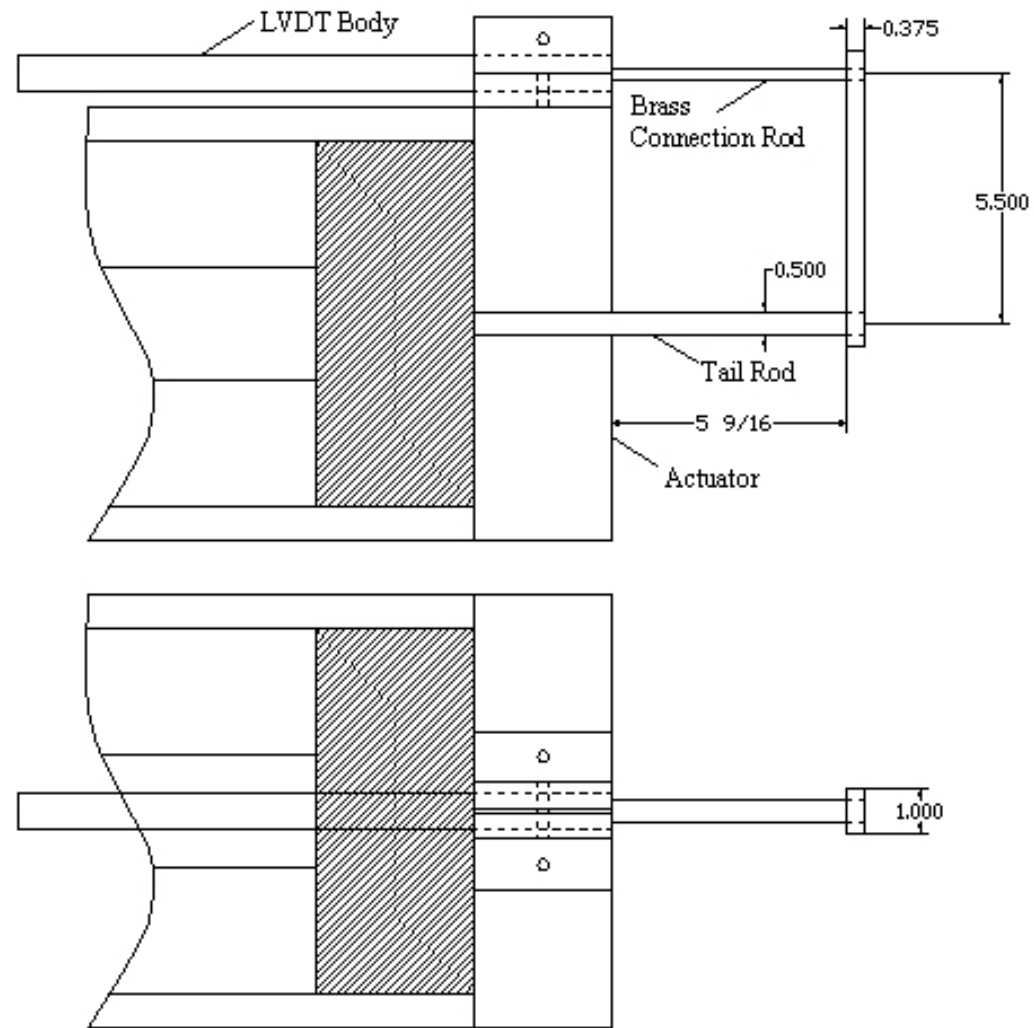


Fig 2.11 – Method of mounting the axial feed displacement transducer (LVDT)

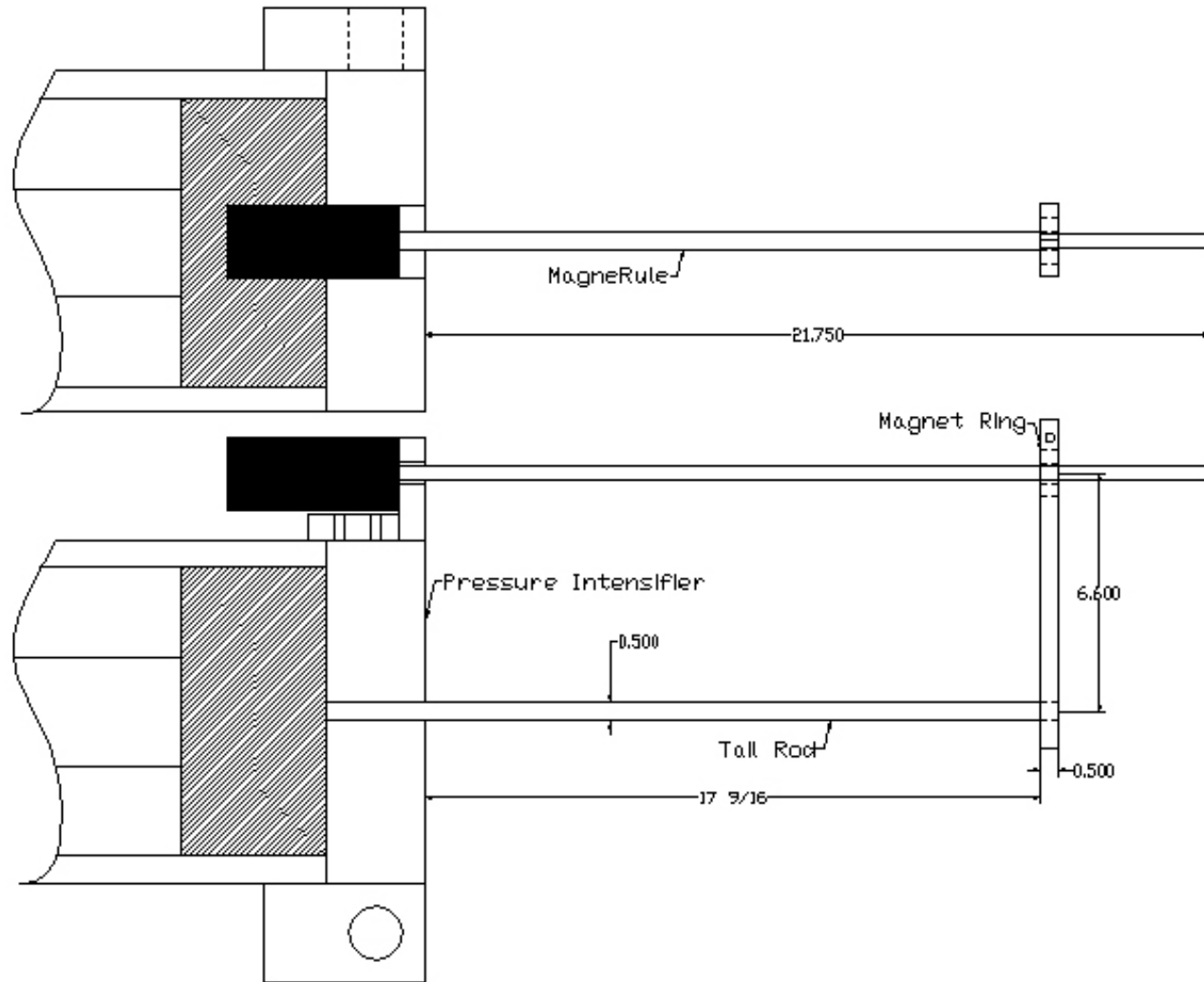


Fig 2.12 – Method of mounting the booster displacement transducer (MagneRule)

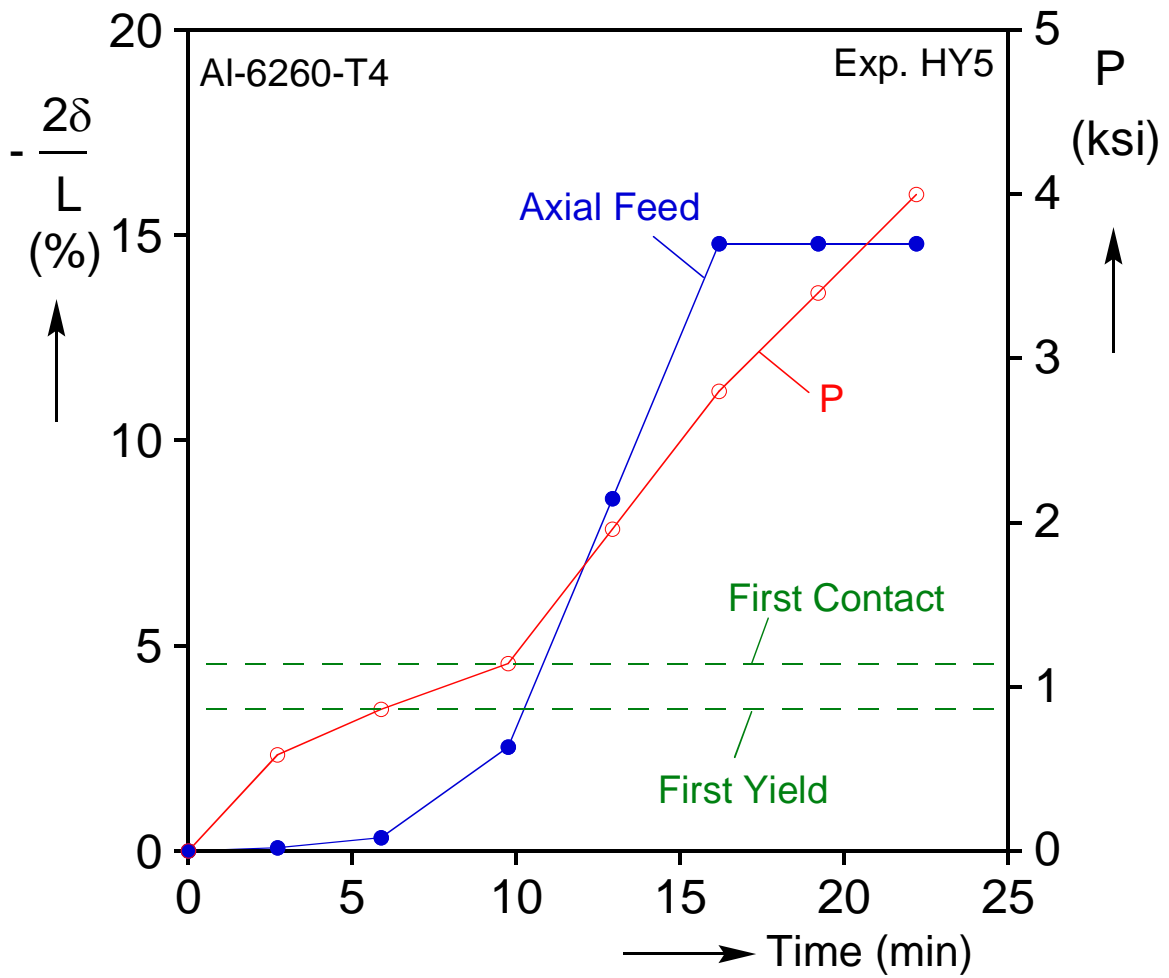
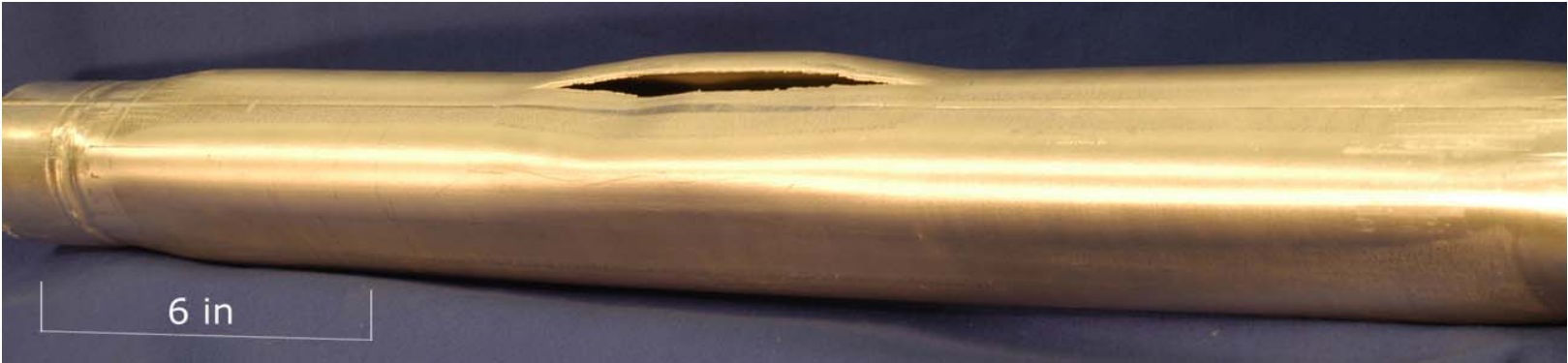


Fig 2.13 – Displacement and pressure histories prescribed in the experiment



(a)



(b)

Fig 2.14 – Hydroformed tubes. (a) Sound (HY7) and (b) Failed by bursting (HY1)



(a)



(b)

Fig 2.15 – Original and deformed cross sections of the hydroformed tube (HY8)

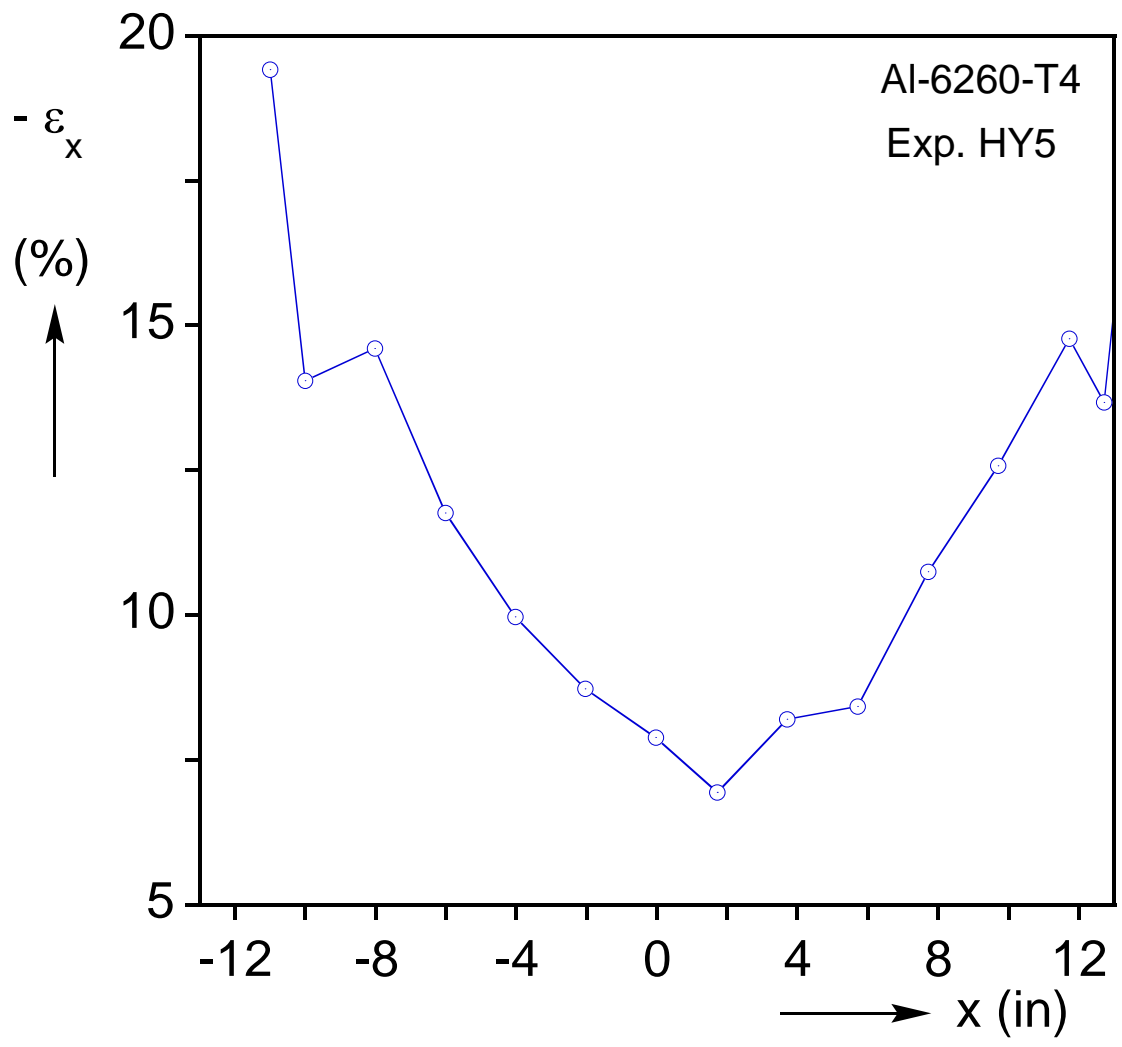


Fig 2.16 – Axial strain distribution in the tube after hydroforming (uncertainty is less than 0.1 % in strain)

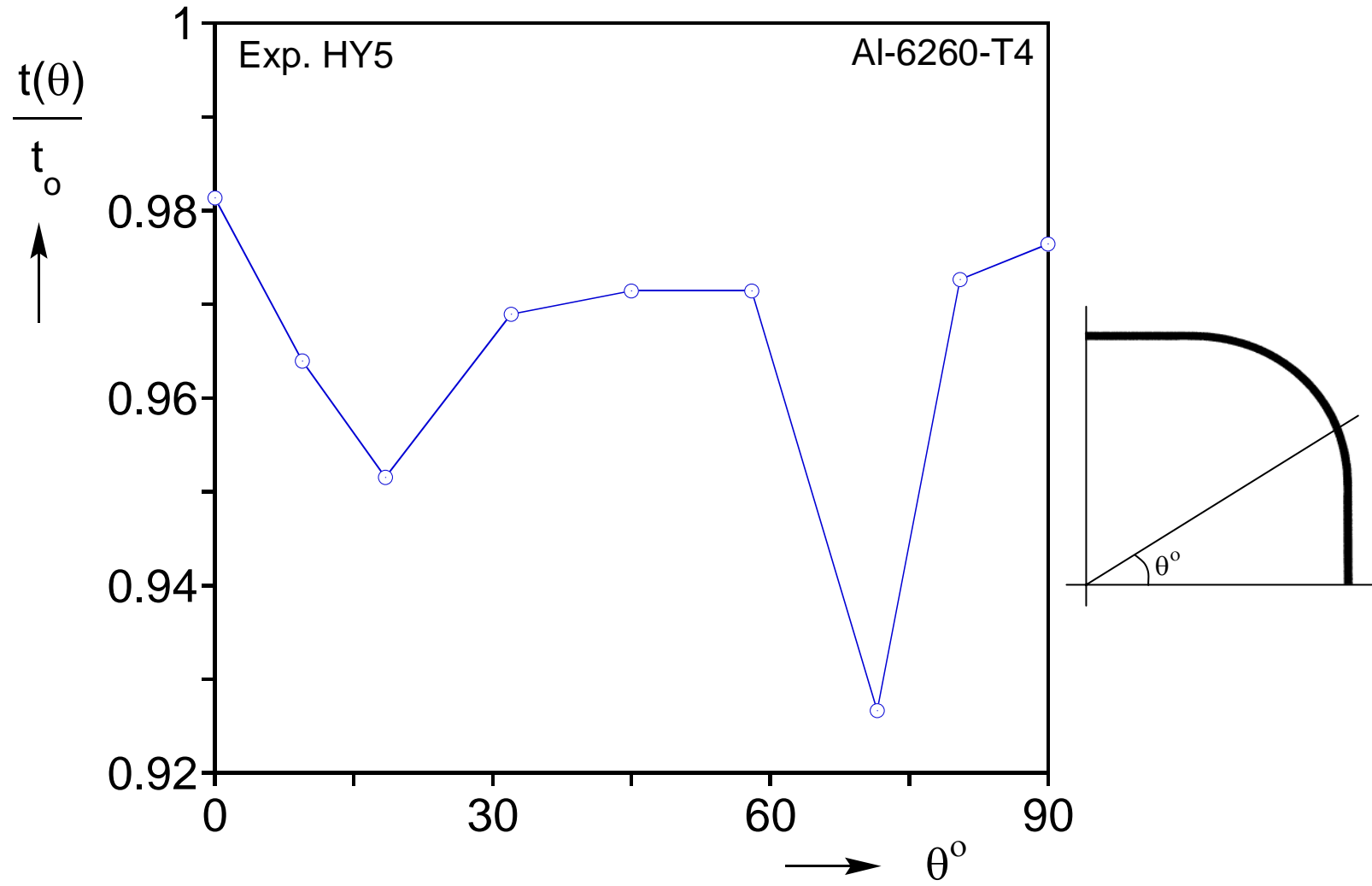


Fig 2.17 – Circumferential thickness distribution for a quadrant of the formed tube, at mid span (HY5)

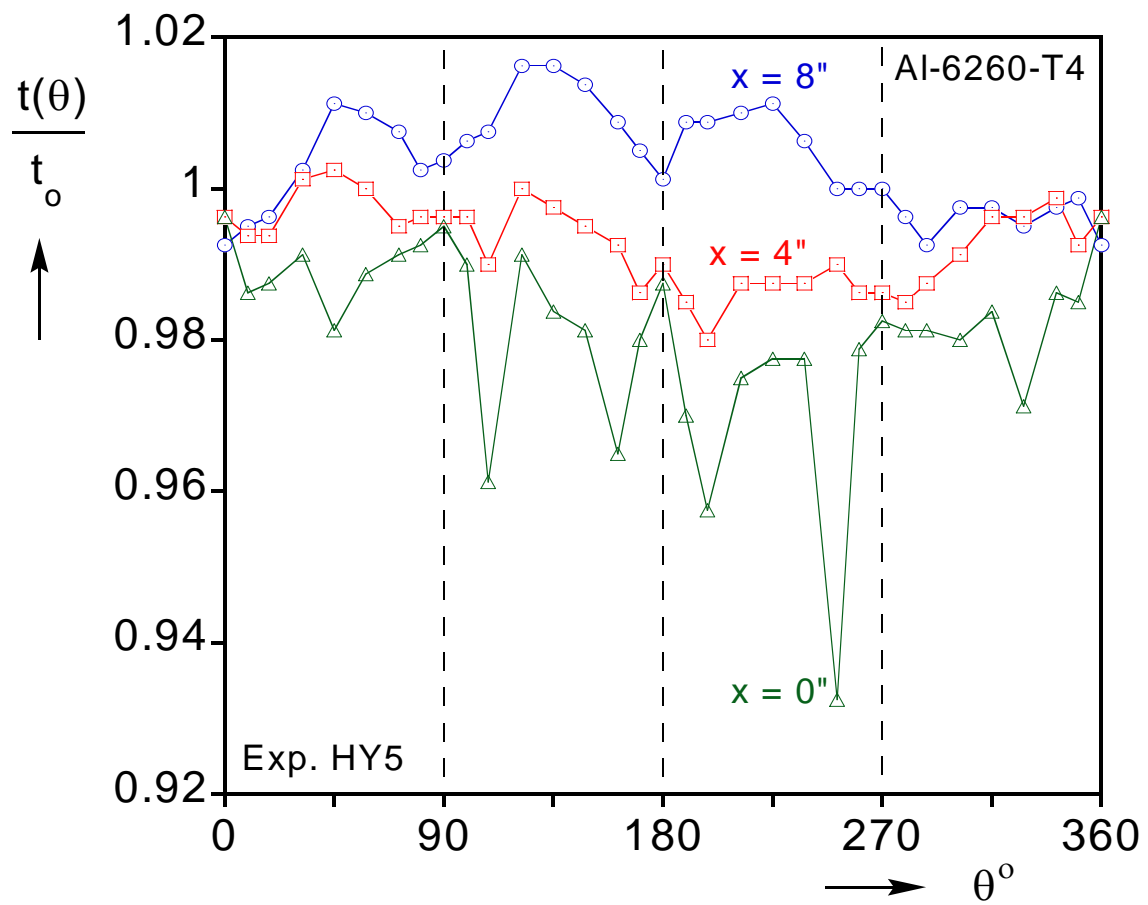


Fig 2.18 – Circumferential thickness distribution plotted at three axial locations for the entire circumference

Chapter 3: *Tube Inflation and Burst Experiments*

As it was demonstrated in the hydroforming experiments (Chapter 2), burst is a major mode of failure of aluminum tubes formed by this method. Clearly, accurate prediction of this limit state is essential for establishing a reliable working envelope for the process. Motivated by this, a separate study was undertaken to establish forming limits in the “free hydroforming” set up (i.e., tube inflation without a die). The problem was tackled using a combination of experiments and analysis. The simpler setting of this problem will enable evaluation of appropriate constitutive models to be used in numerical simulations of the hydroforming process, as well as establish the related failure limits. This chapter describes in detail the testing facilities used, the procedures followed and the experimental results.

3.1 TEST SPECIMENS

The test specimens used were seamless Al-6260-T4 tubes with a diameter (D) of approximately 2.36 in. (60 mm) and a wall thickness (t) of about 0.080 in. (2 mm). The material at hand is an aluminum-silicon-magnesium alloy (including multiple other elements) that is solution but not precipitation heat treated. This combination of alloying and temper results in a material with relatively low yield stress, significant work hardening and above average ductility (compared to other Al-alloys). It is these characteristics that make this alloy attractive for manufacturing.

The tubes were supplied by Alcoa in about 6 ft lengths. The tubes had a mild circumferential non-uniformity in the thickness in the form of an eccentricity between the

inner and outer diameters. This is a result of the extrusion process used to manufacture the tubes. The eccentricity is quantified by the following variable:

$$\bar{\varepsilon}_o = \frac{t_{\max} - t_{\min}}{t_{\max} + t_{\min}} \quad (3.1)$$

The eccentricity was of the order of 0.75% but this was sufficient to cause the specimens to rupture systematically on the thinner side.

The specimens had an overall length ($2L$) of about $5.5D$ when cut from the mother tubes. The geometric characteristics including the eccentricity of the tubes tested appear in Table 3.1.

3.2 EXPERIMENTAL SET-UP AND TESTING PROCEDURES

The tubular specimens were loaded under combined axial tension/compression and internal pressure along radial and along corner paths in the engineering stress space. The custom experimental facility consisted of a 50 kips (222 kN) servohydraulic testing machine that can operate in conjunction with a 10,000 psi (690 bar) pressurizing unit (Fig. 3.1). The pressurization unit has an independent closed-loop control system shown schematically inside the dashed boundary in Fig. 3.1. The pressurizing medium used was a white mineral oil. By connecting the two systems through feedback, tests can be performed under displacement (volume) or load (pressure) control. Typical strain rates during these experiments were of the order of 10^{-4} s^{-1} .

The tubes were held in the testing machine using *Ringfeder* axisymmetric locking devices leaving a test section that ranged in length between 7.625 and 8.5 in. (194-216 mm). A solid rod was placed inside the tube cavity, in order to reduce the energy stored in the system and thus to avoid an extended disintegration of the specimen during burst. During each test, transducers were recording the axial load, internal pressure and the

strains that developed in the specimen. Thus for example the strains were measured with strain gages mounted in the test section as well as with extensometers. Two pairs of strain gages (one pair in the axial and the other in the circumferential direction) recorded the strains up to about 4% while an axial and a hoop (chain) extensometer (MTS 632.11B-20 and 632.21A-01, respectively) were used for the entire response. The axial extensometer had a 1 in. gage length and a range of 30%, whereas the chain extensometer was modified to have a range of about 17%. This instrument consists of a chain that wraps around the tube, and hence measures the average hoop strain that the specimen experiences. Of course, since the deformation is anticipated to be axisymmetric for the most part of the experiment such a measurement is quite adequate. All signals were recorded in a computer operated data acquisition system using LabView.

To facilitate local strain measurements around the zone of failure, each specimen was equipped with a square strain grid of 0.25 in (6.4 mm) spacing, as shown in Fig. 3.2. Due to the wall thickness eccentricity mentioned earlier, the neighborhood of failure was known. Hence only half of the circumference was lightly scribed over a length of about $1.5D$ around the mid-span. For better accuracy, the pattern was scribed in a lathe.

In addition to the strain grid, the thickness around the failure zone was measured with an ultrasonic thickness gage. Since the localization is experienced only in one direction (axial or hoop), the strain in that direction and adjacent to the rupture can then be determined by knowing the strains in the two orthogonal directions and invoking the incompressibility of the plastic deformations. These results compare favorably to the grid measurements.

3.2.1 Radial (Proportional) Stress Paths

Initially, the tubes were loaded along radial stress paths such that:

$$\sigma_x = \alpha \sigma_\theta \tag{3.2}$$

where α is the stress biaxiality ratio (path denoted as “R” in Fig. 3.3). In turn, if the force measured by the load cell of the machine is F and the internal pressure is P , the axial and circumferential engineering stresses are:

$$\sigma_x = \frac{F}{2\pi R t} + \frac{P R}{2t} \quad \text{and} \quad \sigma_\theta = \frac{P R}{t} \quad (3.3)$$

where R and t are the initial mid-surface radius and wall thickness of the tube, respectively. Using (3.2) and (3.3) one can find a relationship between F and P for a constant stress biaxiality ratio.

To perform the radial tests, the pressurizing unit was run under volume control supplying fluid at a constant flow rate to the tube. A pressure transducer was measuring the induced internal pressure in the specimen. The axial actuator was run under load control, and through feedback it was made to follow the induced pressure at a prescribed ratio. Thus by keeping the load to pressure ratio constant, the stress biaxiality ratio α was also maintained constant.

3.2.2 Corner Stress Paths

The radial paths were used to extract the formability information for the material at hand and to establish the appropriate constitutive framework for accurate numerical predictions of the rupture (see following chapter). Since however plastic deformations are path-dependent, one may suspect that the results associated with the radial paths might only be applicable to forming operations with similar loading histories. Hence the investigation was expanded by considering highly non-proportional paths, involving sharp corners in the engineering stress space. These paths can also be considered to be closer to the loading experienced by the tube in an actual hydroforming operation.

Two families of corners were examined: $x \rightarrow \theta$ and $\theta \rightarrow x$, each set associated with a corresponding radial path (Fig. 3.3). The $x \rightarrow \theta$ paths were designed so that the

tube was first loaded axially in tension (branch OB in Fig 3.3), until the stress reached the axial stress at the onset of failure in the corresponding radial path. Then, by holding that stress constant, biaxial loading commenced by inflating the tube until rupture (branch BC). In the associated $\theta \rightarrow x$ path, the tube was loaded in uniaxial tension in the hoop direction first, until the stress reached the hoop stress at failure of the corresponding radial path (branch OD). The tube then was pulled to failure, while keeping the hoop stress constant (branch DE).

To implement the $x \rightarrow \theta$ paths, the testing machine was first run in displacement control (branch OB). On reaching point B, the machine was switched to load control and the tube was inflated under volume control, with the induced pressure serving as the command signal for the axial loading (branch BC). In this way, as the pressure increased, the machine force was reduced in accordance with Eq. (3), to keep the axial stress in the specimen constant.

For the $\theta \rightarrow x$ paths, the two systems were initially coupled as for the radial paths, with the axial load servocontrolled to exactly balance the end-cap loading due to the internal pressure (branch OD). This way no axial stress developed in the specimen (also see Section 3.3). On arriving at point D, the two systems were decoupled and pressurization was switched to pressure control. By keeping the pressure constant in this fashion, the tube was loaded axially under displacement control and taken to failure (branch DE).

3.3 MATERIAL TESTING

A series of tests to extract the basic mechanical properties of the tubes was conducted before the biaxial experiments. The first test was a uniaxial tension test performed on a strip extracted along the axial direction of the tube (see Fig. 3.4a). The test was conducted in a universal electromechanical testing machine. The maximum

stress occurred at a strain of 19.5%, soon after which the strip developed a diffuse and then a localized inclined neck. The failure strain measured by the extensometer (1 in. gage length) was about 25%.

The tensile tests on the strips were repeated for strain rates ranging from 10^{-5} to 10^{-3} s^{-1} . These tests were performed in the same electromechanical testing machine and the results are presented in Fig. 3.5, with the curves truncated just before the maximum load. It can be concluded that for the range of rates investigated, the material response appears to be insensitive to the strain rate.

The stress-strain response was also measured in the circumferential direction, using a tube which was inflated in the biaxial facility described in the previous section. The path chosen was such that the axial actuator balanced exactly the end-cap load due to the internal pressure in the specimen, so that the axial stress in the specimen remained zero. A very different sequence of events was observed during this test, in comparison to the strip. At first, the inflation lead to uniform deformation of the specimen, which maintained its circular cylindrical geometry except of course at the ends. After some deformation, a limit load in the form of a pressure maximum was attained, which was soon followed by a mild axisymmetric bulge at mid-span. This is seen to occur in Fig. 3.4a at about 11% hoop strain. The bulge quickly evolved into a non-axisymmetric one which led to localization of the deformation and rapid failure of the specimen in the form of an axial rupture. The failure of this specimen is seen in Fig. 3.7 to extend over a length of approximately one tube diameter (this is a function of the energy stored in the test system as a whole). It should be noted however that despite the “stiff” testing system used, the localization of plastic deformation occurs suddenly and dynamically at a location not exactly known a priori.

It is quite apparent by comparing the two responses in Fig. 3.4a that the overall deformations and the strains that correspond to the limit loads are significantly different, with the strip specimen having failed at more than twice the strain of the tubular one. This is a striking difference considering that both specimens are in a uniaxial stress state, at least up to their respective limit loads. A similar observation was reported earlier by Stout and Hecker (1983). While naturally one may attribute this to anisotropy, the difference in the failure strains is too large to be caused only by this. It is thus postulated that it should be largely attributed to the different geometries of the two specimens, which favor different necking instabilities and different localization patterns. In the context of tube hydroforming, this observation leads to the conclusion that the formability information should be extracted from tests performed directly on tubes, rather than be extrapolated from tests on sheets or other geometries.

A third material test was performed by twisting a tubular specimen to establish any shear anisotropy present. This experiment was performed on the same servohydraulic machine, which also possesses a rotational actuator. The resulting equivalent stress – equivalent plastic strain response using the von Mises yield function is compared to the two uniaxial responses in Fig. 3.4b. The results show significant shear anisotropy thus revealing a more complex constitutive behavior of the material at hand.

3.4 EXPERIMENTAL RESULTS FROM THE RADIAL PATH TESTS

3.4.1 Stress – Strain Responses

Nine biaxial radial experiments were conducted for ratios in the range $-0.2 \leq \alpha \leq 1.25$. The nine stress paths traced are shown in Fig. 3.6a and b (engineering and true, respectively), including the uniaxial response from the strip specimen. The engineering paths are exactly linear, as prescribed, while the true paths are also close to

linear. For the true paths, the same equations were used to convert the engineering to the true quantities even after the limit load, which is of course only an approximation.

A sample of tested specimens is presented in Fig. 3.7 where it can be noted that as the biaxiality ratio changes, the mode of failure switches from an axial to a circumferential rupture. Because of the way the experiments are performed, where care is taken to limit the amount of energy stored in the system, the extent of the rupture was limited thereby enabling local post-failure measurements.

The corresponding stress-strain responses in the axial and in the circumferential direction are given in Figs. 3.8a and b and the stresses and strains at the limit load and at failure are also included in Table 3.1.

All tubes developed a limit load instability and in several cases significant deformation well past this point was recorded. This indicates that a purely stress-controlled loading (e.g., as used by Kuwabara *et al.*, 2005) is not the best option if capturing the failure is a goal of the tests. In the case of the seven paths with $-0.2 \leq \alpha \leq 0.9$, the tubes developed some bulging followed by localized thinning along a generator of the cylinder that resulted in ductile rupture. This sequence of events was described earlier in Section 3.3 (three failed specimens from this group are shown in Fig. 3.7). For the other two cases, corresponding to $\alpha = 1.0$ and 1.25, the specimens developed a mild bulge at mid-span and failed by localized thinning in the circumferential direction as illustrated in Fig. 3.7 for $\alpha = 1.0$ (similar failure modes were reported in Davies *et al.*, 2000 and Yoshida *et al.*, 2005). Figure 3.9 shows thickness profiles along the lengths of these two tubes, measured with an ultrasonic thickness gage after the tests. The profiles demonstrate that the localization at mid-span extended over approximately a length of one tube diameter.

Results from two representative experiments corresponding to $\alpha = 0.75$ and -0.2 and shown in Figs. 3.10-3.12, will be used to describe some of the measurements made as well as some of the observed trends. In the case of $\alpha = 0.75$, shown in Fig. 3.10a and b, both the axial and circumferential stresses increase monotonically until a pressure maximum develops. The stress at the pressure maximum ($\sigma_{\theta_{\max}}$) is 34.03 ksi (235.7 MPa) and the corresponding strain ($\varepsilon_{\theta L}$) is 5.8% (see Table 3.1). The corresponding axial stress and strain are respectively 25.50 ksi (175.9 MPa) and 1.8%. Failure occurred at a decreasing pressure so the maximum strain recorded by the circumferential extensometer ($\varepsilon_{\theta f}$) was somewhat higher, 6.1%. Following the response past the limit load is possible because of the volume-controlled pressurization scheme adopted. Notice that because of the live pressure present and despite our efforts to limit the amount of energy stored in the system, failure occurred suddenly and dynamically at a location not exactly known a priori. Hence the stresses and strains that can be recorded and thus reported dependably stop at the onset of failure.

Included in Table 3.1 are strain values measured locally, adjacent to the failure zone, using the grid and verified by the ultrasonic thickness gage. For this experiment the local values were $\varepsilon_{\theta f|l} = 18.3\%$ and $\varepsilon_{x f|l} = 11.0\%$. These values are significantly larger than the average strains at failure illustrating the local nature of the failure. Figure 3.11 shows thickness contours around the circumference, taken after the completion of the test at the three axial locations indicated in the inset. The contours illustrate that wall thinning is localized circumferentially around the tube mid-span.

Results for $\alpha = -0.2$ are shown in Fig. 3.12a and b. In this case the tube was compressed as it was pressurized. The circumferential stress level is lower than the previous case, reaching a maximum of 31.21 ksi (215.2 MPa). Compression has however the beneficial effect of delaying burst as the circumferential strain at failure is now 22.1%

and the corresponding axial strain is -14.4%. In this case the capacity of the circumferential extensometer was exceeded and thus the last part of the $\sigma_\theta - \varepsilon_\theta$ response was constructed from the grid measurements (drawn in dashed line). In accord with the observations on the rest of the tests, this specimen (included in Fig. 3.7) also developed a bulge and failed by localized wall thinning along a generator of the cylinder.

3.4.2 Strain Paths

The stress-strain responses in Figs. 3.8a and b reveal that as α decreases from 1.0 to -0.2 the maximum circumferential stress sustained is reduced but more importantly the circumferential strain at the limit load increases. This is illustrated in Fig. 3.13a and b where plots of the engineering ($\varepsilon_x - \varepsilon_\theta$) and of the logarithmic ($e_x - e_\theta$) strain paths recorded appear. Also included in the two plots is the response from the uniaxial strip (see Section 3.3).

The strain paths remain nearly radial up to the limit load instability marked in these plots with the symbol (●). Values of the stresses and strains at the limit load are listed in Table 3.1. Because of space constraints, the axial extensometer was mounted just above the chain of the circumferential one, in other words above the axial centerline of the specimen. For this reason, in some cases where failure involved bulging followed by localization around the mid-span, the axial extensometer did not record accurately the axial strain past the limit load, causing the abrupt nonlinearity seen in one of the strain paths. The maximum average strains recorded by the extensometers are listed in Table 3.1 and are marked in the figure with the symbol (▲). Finally, the local strains in the zones of failure were measured from the grid and verified by local thickness measurements using the ultrasonic thickness gage. These strains are listed under ($\varepsilon_{x|l}$, $\varepsilon_{\theta|l}$) in Table 3.1 and are marked with an open circle symbol (○) in Fig. 3.13a and b. They follow a similar trend as the average strains at failure but have much higher values.

The strain path results illustrate that the local strains in the proximity of the failure zone are significantly higher than the values measured by the extensometers at the onset of failure. Furthermore, by comparing the uniaxial response to $\alpha = 0$, it can be concluded again that the onset of instability, as indicated by the attainment of a load maximum, is influenced by the cylindrical geometry of the specimens. The magnitude and trend of the failure strains is similar to those reported by Davies *et al.* (2000) for the same material (Al-6260-T4).

3.4.3 Contours of Constant Plastic Work

It has been long realized that deformation can induce anisotropy to materials. To evaluate this effect for our material, we use the experimental results to construct contours of constant plastic work in the spirit of Hill (Hill, 1991; Hill and Hutchinson, 1992; Hill *et al.*, 1994). Each contour consists of 10 points of equal plastic work plotted in the true stress (τ_x, τ_θ) plane in Fig. 3.14 (the points are joined by straight construction lines). The innermost contour is essentially equivalent to the initial yield surface. Subsequent ones are not related to yield surfaces except through the fact that the local normal at a point on the contour is in the direction of the plastic strain increment. In other words, at any stress state, the current yield surface is tangent to the plastic work contour. In that sense, for each level of plastic work the contour can be considered as the envelope of the current yield surfaces.

It is apparent from Fig. 3.14 that the shapes of successive contours gradually change, with the sides becoming flatter and the rounded zone around equibiaxial tension changing curvature. This indicates that deformation-induced anisotropy, due to microstructural evolution, has taken place. Since the plastic strain increment is in effect normal to the plastic work contours, such distortions can be expected to affect the strains that develop.

The plastic work contours will be shown in Chapter 4 to be very useful in developing an appropriate constitutive framework for the material in hand and thus in predicting the deformation of the inflated tubes.

3.5 EXPERIMENTAL RESULTS FROM THE CORNER PATH TESTS

The radial path experiments were used to assess the forming limits of the Al-6260-T4 tubes and to establish the appropriate constitutive framework for accurate predictions of this mode of failure (also see following Chapter). However, since plastic deformations are path-dependent, evaluation of the performance of the constitutive models that will be developed in more challenging, non-proportional paths is desirable. This was investigated by considering rather extreme corner paths. Two families of paths were examined, $x \rightarrow \theta$ and $\theta \rightarrow x$. Each pair of paths is associated with a specific radial path (see Fig. 3.3) while the implementation details in our biaxial testing facility were discussed in Section 3.2.2.

Clearly, it would be desirable to examine as many such combinations of corner and radial paths as possible. It was only feasible however to perform the tests shown in Fig. 3.15a on Al-6260-T4 for the following reason. Considering for example the $\theta \rightarrow x$ case, the preloading essentially follows the $\alpha = 0$ path. Referring now to Fig. 3.6a, it can be seen that there is only a limited number of radial paths that have hoop failure stresses less than that of the $\alpha = 0$ path. Hence a $\theta \rightarrow x$ corner path can be associated to only a few of the radial paths. Similar difficulties were encountered for the $x \rightarrow \theta$ paths, bearing in mind that the preloading should deform the material plastically (the uniaxial yield stress is approximately 18 ksi / 125 MPa, see Fig. 3.4a). However, despite the relatively limited number of corner path experiments that could be performed, this work unearthed a number of significant findings and trends.

3.5.1 $x \rightarrow \theta$ Paths

Three $x \rightarrow \theta$ corner path tests were performed and are included in Figs. 3.15a and b (engineering and true stresses, respectively). The geometric characteristics of the tubes tested are included in Table 3.2. Each corner path is characterized by a number that corresponds to the associated radial path (also included in the figures). The engineering stress paths are forming sharp corners, as prescribed. The true paths are quite similar in shape and value, which is a result of the relatively limited deformations that developed in the specimens (see below).

The strain paths traced are given in Figs. 3.16a and b (engineering and logarithmic versions). These paths are seen to consist of two distinct branches, like the stress paths did. The first branch corresponds to the uniaxial preloading (branch OB in Fig. 3.3), so that the hoop strain that is seen to develop is purely due to the Poisson effect. The path then exhibits a tight knee, which marks the commencement of the biaxial loading. Typically, only limited deformation follows the knee, before failure.

By comparing a $x \rightarrow \theta$ corner path to the associated radial one, one can notice that both the strain path and the strains at failure are distinctly path-dependent (see also Table 3.2). For example, while the strains at the onset of failure for the R0.9 path were $\{\varepsilon_{xL}, \varepsilon_{\theta L}\} = \{7.39\%, 7.54\%\}$, the strains of the corresponding $x \rightarrow \theta$ corner path were $\{6.61\%, 0.88\%\}$. This path dependence is quite visible in the actual specimens, as well (Fig. 3.17). In one experiment, a failure mode change was observed (Fig. 3.18). Notice how the corner specimens' (ones on the RHS) gage sections seem identical in diameter to the gripped ends, indicating the very limited deformation that preceded failure. The failure mode change in this experiment can be explained easily with reference to Fig. 3.15a, where it can be noted that for the radial path (R1.25) the axial stress at failure was

greater than the hoop (hence the circumferential rupture mode), whereas in the $x \rightarrow \theta$ path the hoop stress was greater than the axial (hence the axial rupture mode).

The axial and circumferential stress-strain responses in the three $x \rightarrow \theta$ corner tests are given in Figs. 3.19a and b. The axial responses replicate the initial uniaxial behavior, until the beginning of the biaxial loading, where the axial stress is held constant (of course, the axial strain continues to accumulate, so that the responses exhibit a plateau). The corresponding initial part of the hoop responses (Fig. 3.19b) is not visible since the hoop stress is kept at zero. With the commencement of the biaxiality, the tube responds at first elastically as one would expect, re-yields and failure occurs after limited deformation. Also to be noted is the limit load instability in each of the three paths tested. Furthermore, it can be seen from Fig. 3.19b that as the preloading increases ($x \rightarrow \theta$ 0.75 to 1.25), the subsequent re-yielding of the tube is significantly delayed, indicating that for the material at hand isotropic hardening seems to be dominating the evolution of the yield surface.

3.5.2 $\theta \rightarrow x$ Path

In addition one $\theta \rightarrow x$ path test was performed that corresponds to R1.25 following the loading procedure described in Section 3.2.2 (see Fig. 3.3). The results are included in Figs. 3.15 and 3.16 and in Table 3.2. The first leg (OD in Fig. 3.3) represents in essence uniaxial loading in the hoop direction, which results in nearly uniform expansion of the tube diameter and axial contraction (see Fig. 3.16a). During the axial loading leg (DE in Fig. 3.3), the presence of the constant pressure causes simultaneous growth of ε_θ and ε_x as illustrated in Fig. 3.16a. Unfortunately this specimen failed at the grips, perhaps prematurely. Consequently comparison of failure stresses and strains to those of the radial path is not possible but the new stress-strain results are a welcome

addition to the data set. It is of interest however that the axial stress reached before failure exceeds the value at failure of the corresponding R path.

3.5.3 Discussion of the Corner Path Test Results

The observed path dependence of the strains at the onset of failure (Fig. 3.16a) is in concert with similar results in the literature (e.g., see Hosford and Caddell, 2007) and follows quite naturally from the path-dependent nature of the plastic deformation. On the other hand, strain based forming limits have been generated experimentally without regard for the path followed and then used to design actual operations with drastically different loading paths. Only recently has the strong path dependence of these results been appreciated and a search for more intrinsic limits to ductility has began.

Recently, it has been postulated that despite the strains at failure being path dependent, the corresponding stresses at the onset of failure are not, and hence can be used as a measure of forming severity. In this context, the experimental results included in Figs. 3.15a and b indicate that in the case of paths with limited plastic prestraining, the stresses at failure are indeed close for the corner and radial paths. By contrast, when the prestraining is large the difference between the corner and radial paths becomes quite significant. This is in variance with the current prevailing thinking that the stresses at the onset of failure are path independent. A possible explanation of this fact is that as shown in Fig. 3.19b, the corner paths chosen introduced significant prestraining to the Al-6260-T4 specimens. This tended to expand the yield surface of this material, which in turn delayed re-yielding during the second legs of the corner paths (see also similar results in Fig. 6b in Wu *et al.*, 2005).

Table 3.1a Geometric characteristics of the tubes tested under radial paths.

Exp No.	D in	t in	$2L$ in	$\bar{\varepsilon}_o$ %
A17-4	2.359	0.0800	13.38	0.69
A17-3	2.359	0.0800	13.50	0.63
A19-3	2.358	0.0800	13.38	0.69
A17-1	2.359	0.0801	13.38	0.63
A20-1	2.358	0.0800	12.63	0.56
A19-1	2.356	0.0800	13.00	0.63
A20-2	2.359	0.0800	12.63	0.75
A19-2	2.358	0.0800	13.25	0.69
A17-2	2.359	0.0800	13.38	0.69
A18-3 [†]	-	-	-	-

1 in = 25.4 mm

77

Table 3.1b Summary of biaxial burst test results. Included are the stresses and strains at the limit load instability and at failure.

Exp No.	α	$\sigma_{\theta \max}$ ksi	$\sigma_x \sigma_{\theta \max}$ ksi	$\sigma_{\theta} \sigma_{x \max}$ ksi	$\sigma_{x \max}$ ksi	$\varepsilon_{\theta L}$ (%)	ε_{xL} (%)	$\varepsilon_{\theta f}$ (%)	ε_{xf} (%)	$\varepsilon_{\theta f} l$ (%)	$\varepsilon_{xf} l$ (%)
A17-4	-0.2	31.21	-6.19	-	-	18.1	-11.9	22.1	-14.4	44.0	-14.4
A17-3	-0.1	32.07	-3.02	-	-	18.0	-11.0	19.1	-11.0	35.3	-11.0
A19-3	0	32.87	0.185	-	-	11.8	-5.7	12.6	-5.7	29.7	-5.7
A17-1	0.25	33.58	8.58	-	-	9.3	-2.2	9.7	-2.2	25.5	-3.6
A20-1	0.5	33.68	16.87	-	-	7.0	-0.2	7.4	-0.2	19.4	0.0
A19-1	0.75	34.03	25.50	-	-	5.8	1.8	6.1	1.8	21.6	1.8
A20-2	0.9	33.88	30.49	-	-	6.7	7.4	7.5	7.9	18.3	11.0
A19-2	1.0	-	-	32.27	32.40	5.0	10.6	9.8	12.8	11.9	27.7
A17-2	1.25	-	-	26.95	33.61	2.2	15.1	3.3	19.4	3.3	29.5
A18-3 [†]	-	-	-	0	32.55	-	19.5	-	24.7	-	-

1 ksi = 6.897 MPa

[†] uniaxial test on an axial strip of the material

Table 3.2a Geometric characteristics of the tubes tested under the corner paths and the corresponding radial ones.

Exp No.	D in	t in	$2L$ in	$\bar{\varepsilon}_o$ %
A17-2	2.359	0.0800	13.38	0.69
A19-1	2.356	0.0800	13.00	0.63
A20-2	2.359	0.0800	12.63	0.75
A20-4	2.360	0.0796	13.50	0.82
A20-5	2.359	0.0797	12.75	0.75
A21-1	2.359	0.0795	13.50	0.70
A21-3	2.359	0.0800	13.50	0.88

1 in = 25.4 mm

Table 3.2b Summary of radial and corner path test results. Included are the stresses and strains at the limit load instability and at failure, and the mode of failure (A: axial and C: circumferential as per Fig. 3.18).

Exp No.	R α	$x \rightarrow \theta$	$\theta \rightarrow x$	$\sigma_{\theta max}$ ksi	$\sigma_x _{\sigma_{\theta max}}$ ksi	$\sigma_{\theta} _{\sigma_{x max}}$ ksi	$\sigma_{x max}$ ksi	$\sigma_{\theta f}$ ksi	σ_{xf} ksi	$\varepsilon_{\theta L}$ (%)	ε_{xL} (%)	$\varepsilon_{\theta f}$ (%)	ε_{xf} (%)	$\varepsilon_{\theta f} l$ (%)	$\varepsilon_{xf} l$ (%)	Mode of failure
A19-1	0.75	-	-	34.03	25.50	-	-	33.31	25.00	5.86	1.80	6.08	1.80	21.6	1.8	A
A20-4	-	0.75	-	36.77	24.56	-	-	35.77	24.56	2.79	3.49	3.08	3.49	11.5	4.6	A
A20-2	0.9	-	-	33.88	30.49	-	-	33.31	30.02	6.73	7.39	7.54	7.85	18.3	11.0	A
A20-5	-	0.9	-	38.44	29.78	-	-	37.33	29.78	0.58	6.61	0.88	6.61	5.3	6.7	A
A17-2	1.25	-	-	-	-	26.95	33.61	25.63	31.98	2.19	15.12	3.26	19.38	3.3	29.5	C
A21-1	-	1.25	-	39.33	31.89	-	-	38.33	31.89	-0.79	8.98	-0.25	9.27	2.4	10.0	A
A21-3	-	-	1.25	n/a	n/a	n/a	n/a	n/a	n/a	n/a	n/a	n/a	n/a	n/a	n/a	n/a

1 ksi = 6.897 MPa.

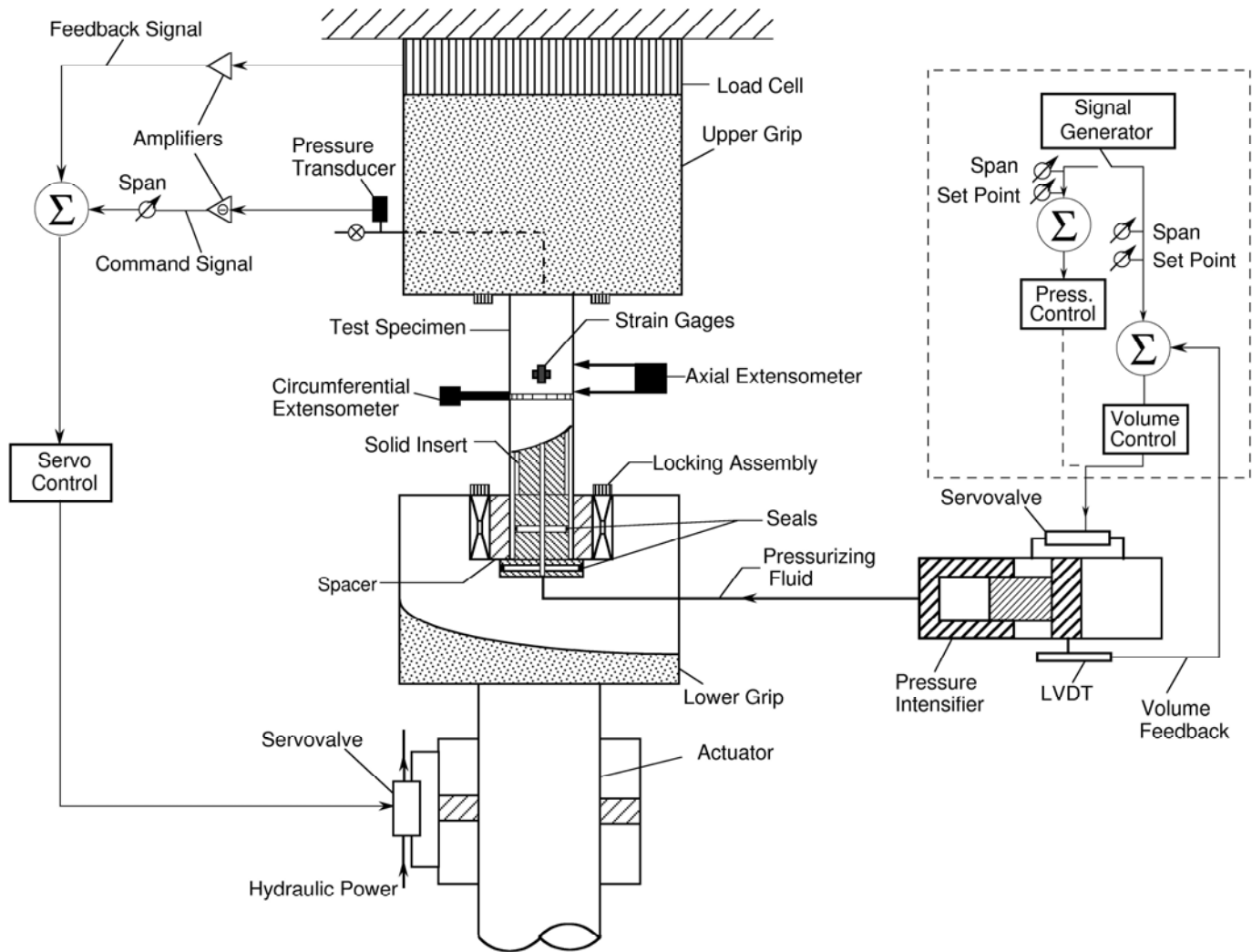


Fig. 3.1 – Experimental set-up used to load tubes under internal pressure and axial load

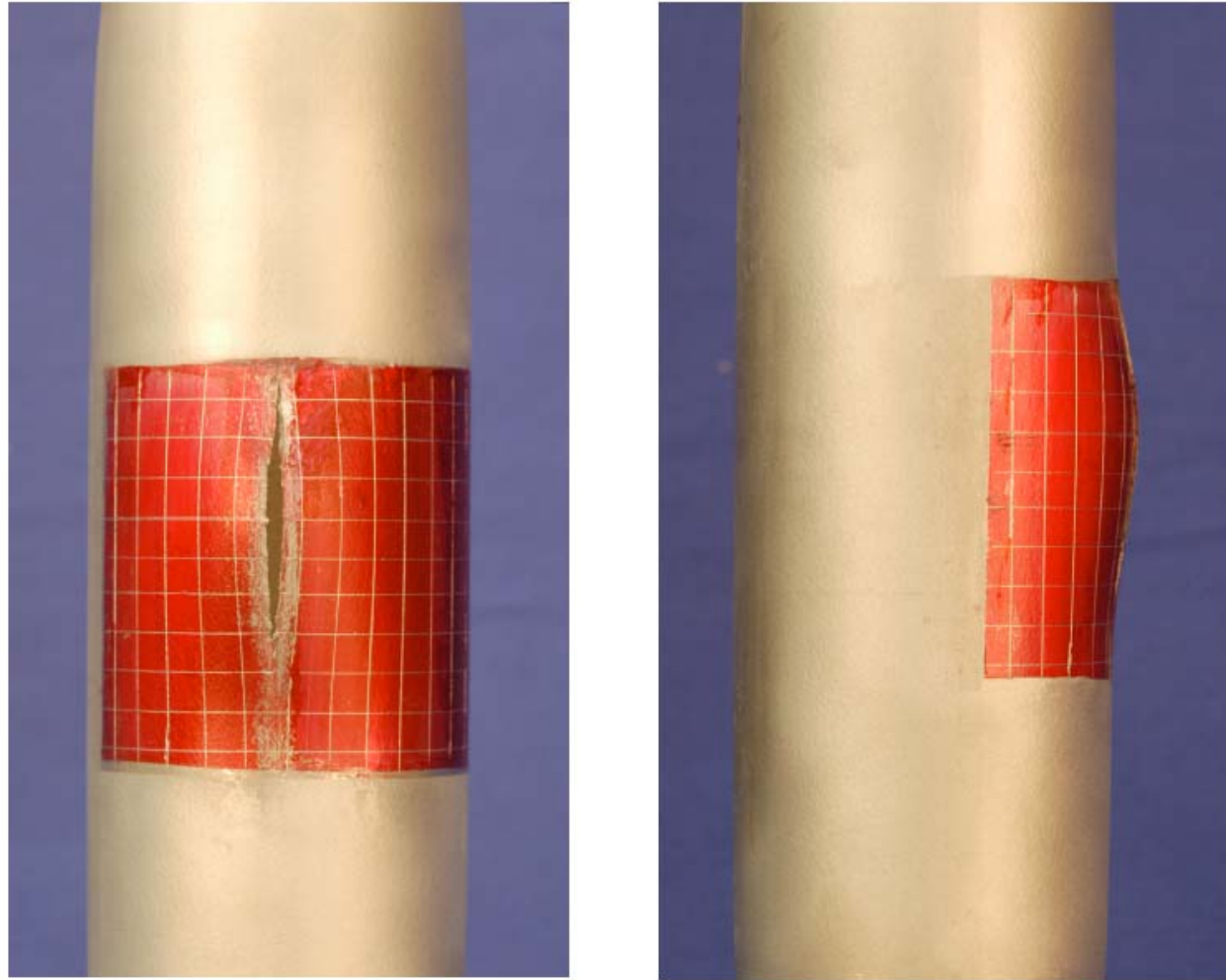


Fig. 3.2 – Tube ductile rupture from Exp. A20-1 ($\alpha=0.5$), also showing the strain grid employed

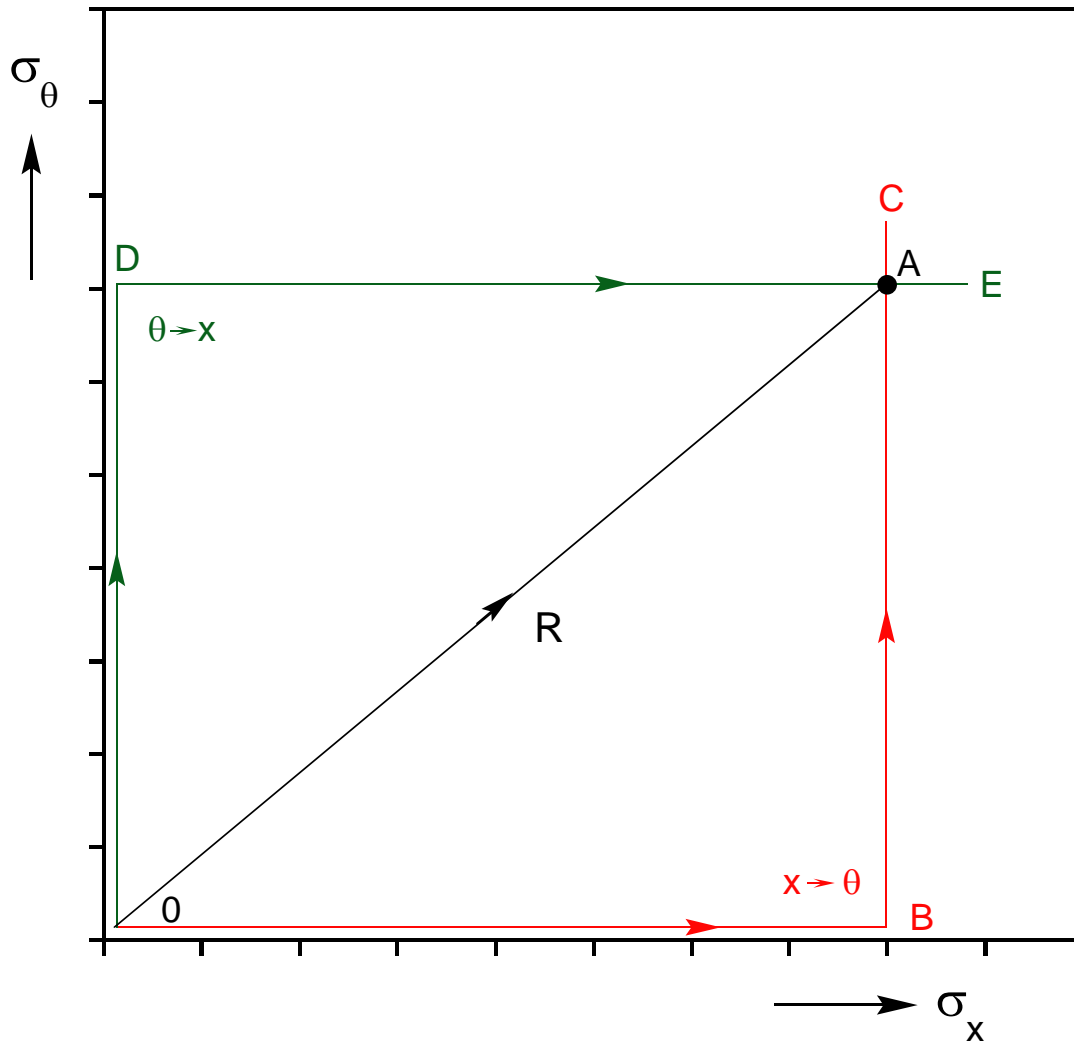
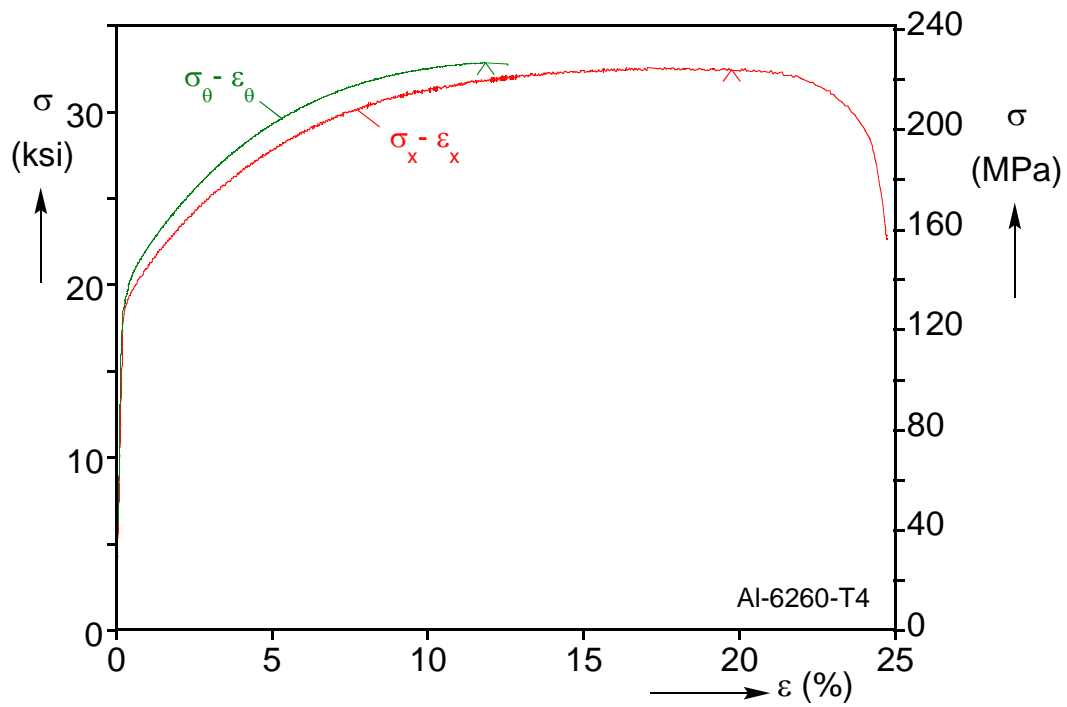
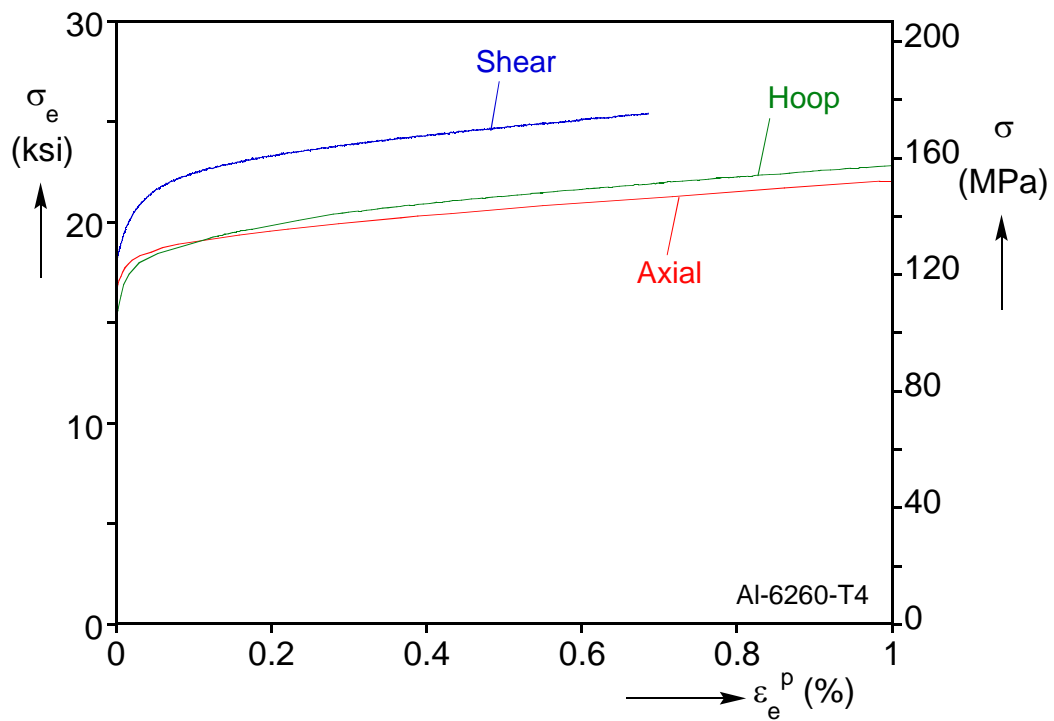


Fig. 3.3 – Definition of the radial and corner loading paths prescribed in the engineering stress space.



(a)



(b)

Fig. 3.4 – (a) Axial and circumferential stress-strain responses of Al-6260-T4 tubes tested to failure. (b) Axial, circumferential and shear equivalent plastic stress-strain responses.

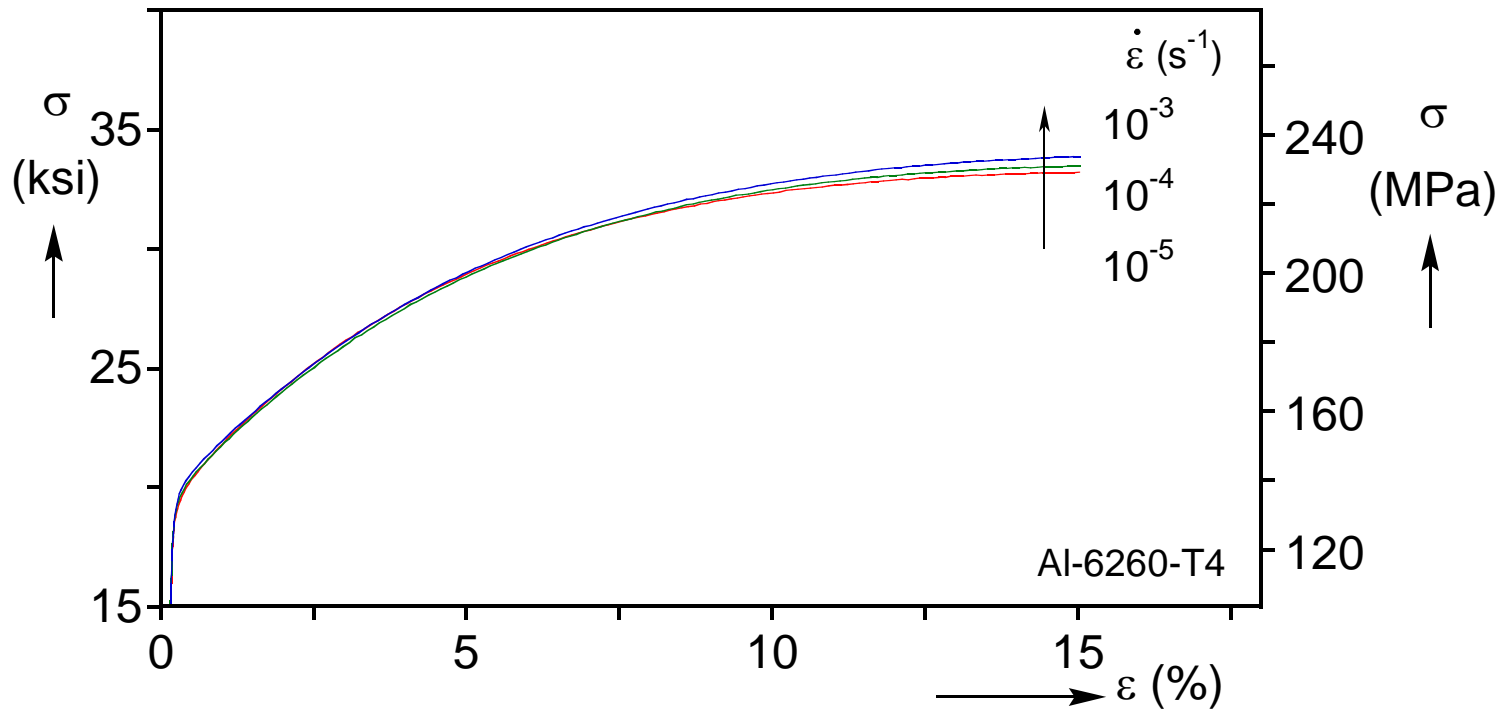


Fig. 3.5 – Effect of strain rate on the uniaxial response.

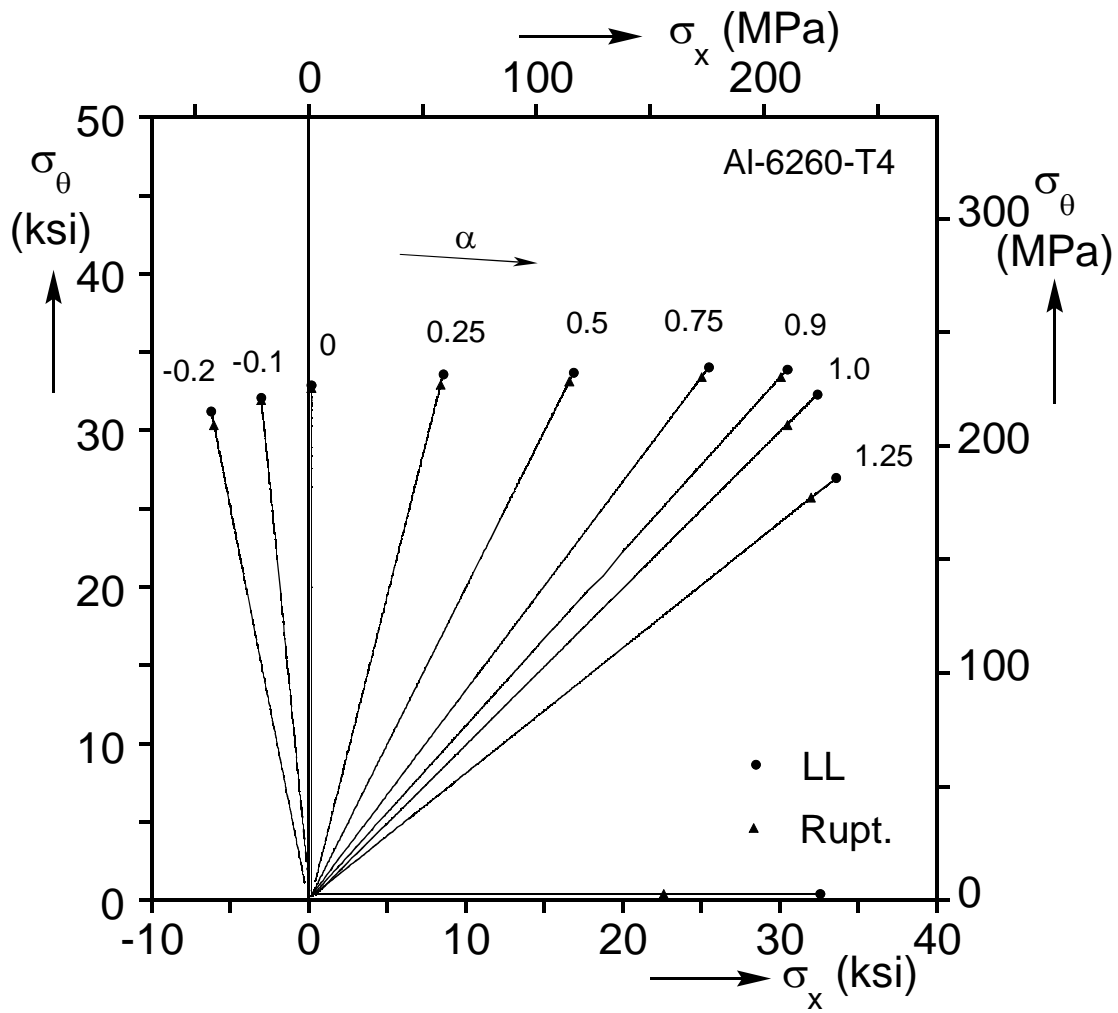


Fig. 3.6(a)– Radial engineering stress paths prescribed. Marked are the limit and the failure stresses

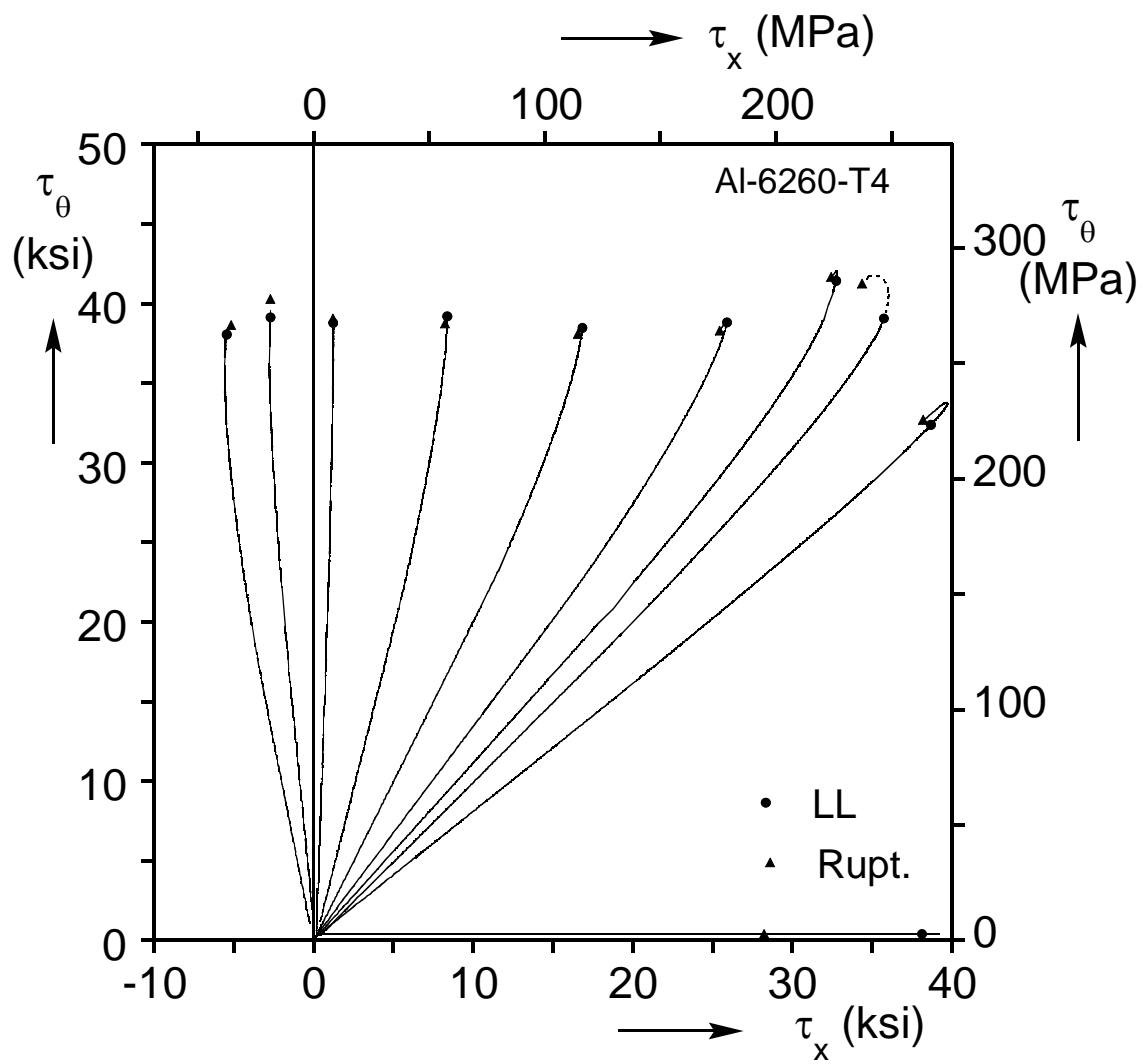
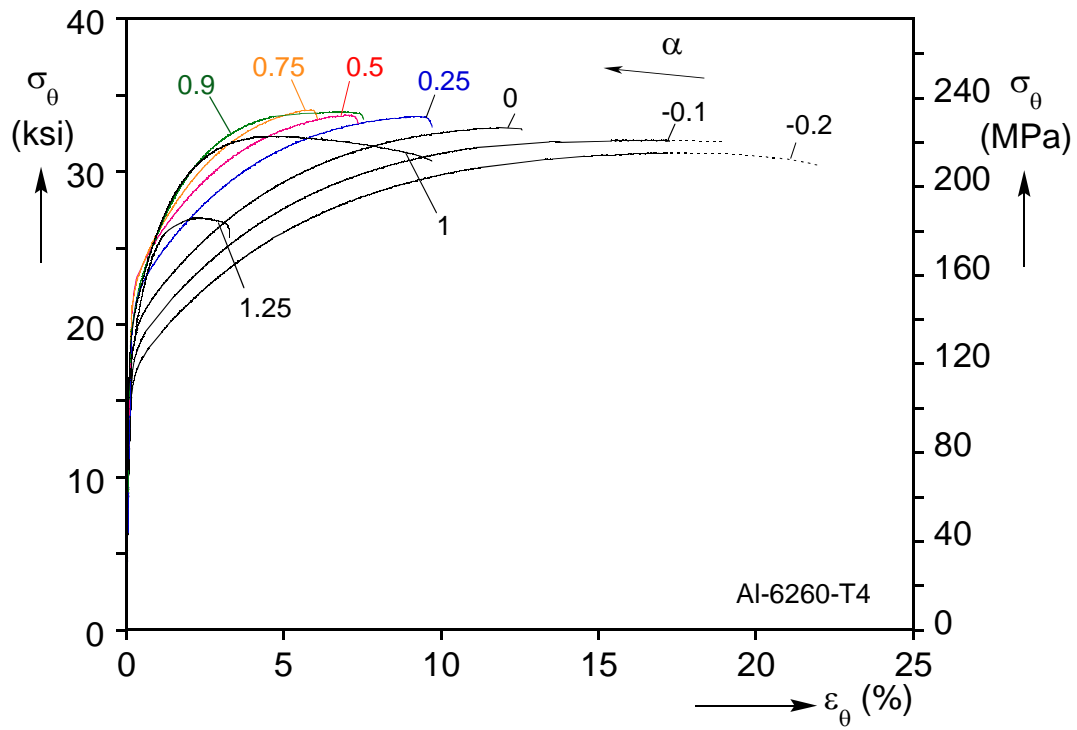


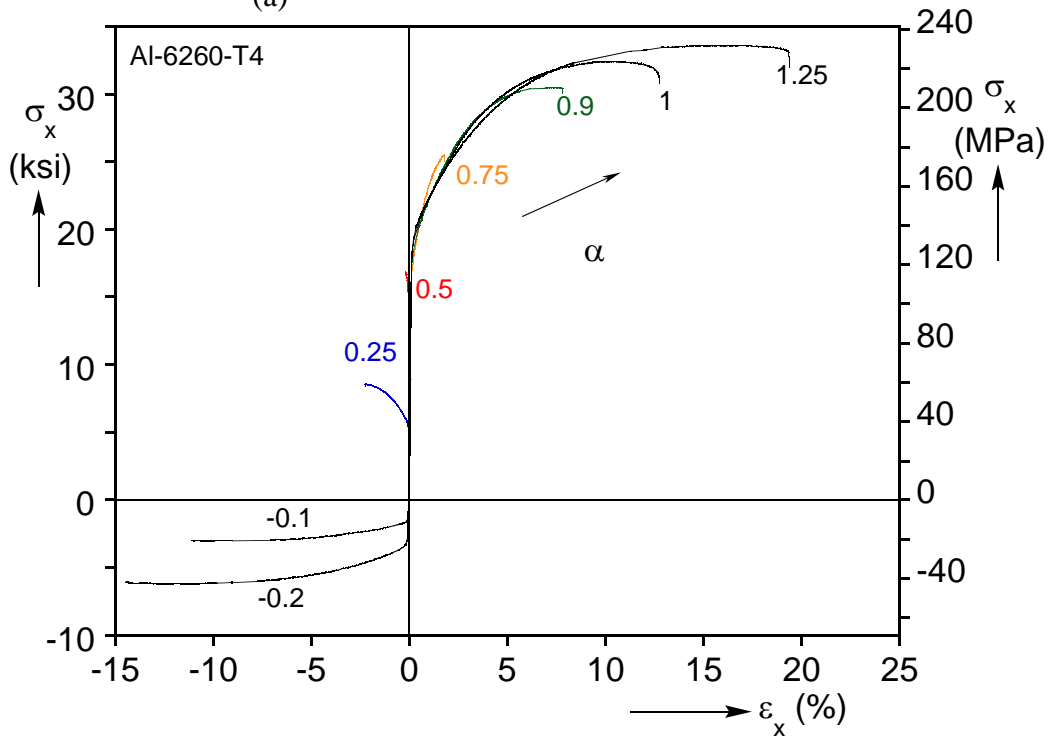
Fig. 3.6(b) – Radial true stress paths induced. Marked are the limit and the failure stresses



Fig. 3.7 – A set of failed specimens tested at different biaxiality ratios:
from left to right, $\alpha = -0.2, 0, 0.75, 1.0$



(a)



(b)

Fig. 3.8 – (a) Circumferential and (b) axial stress-strain responses recorded in nine experiments

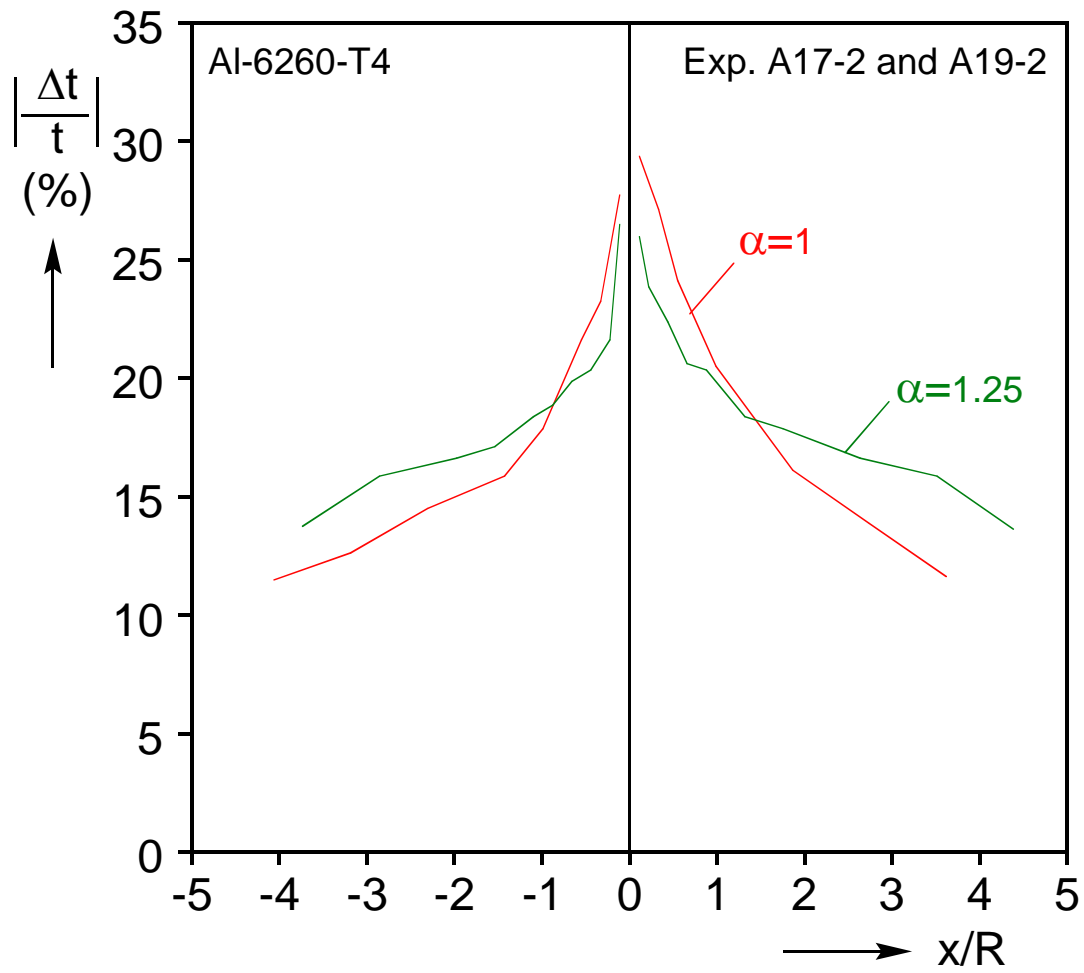
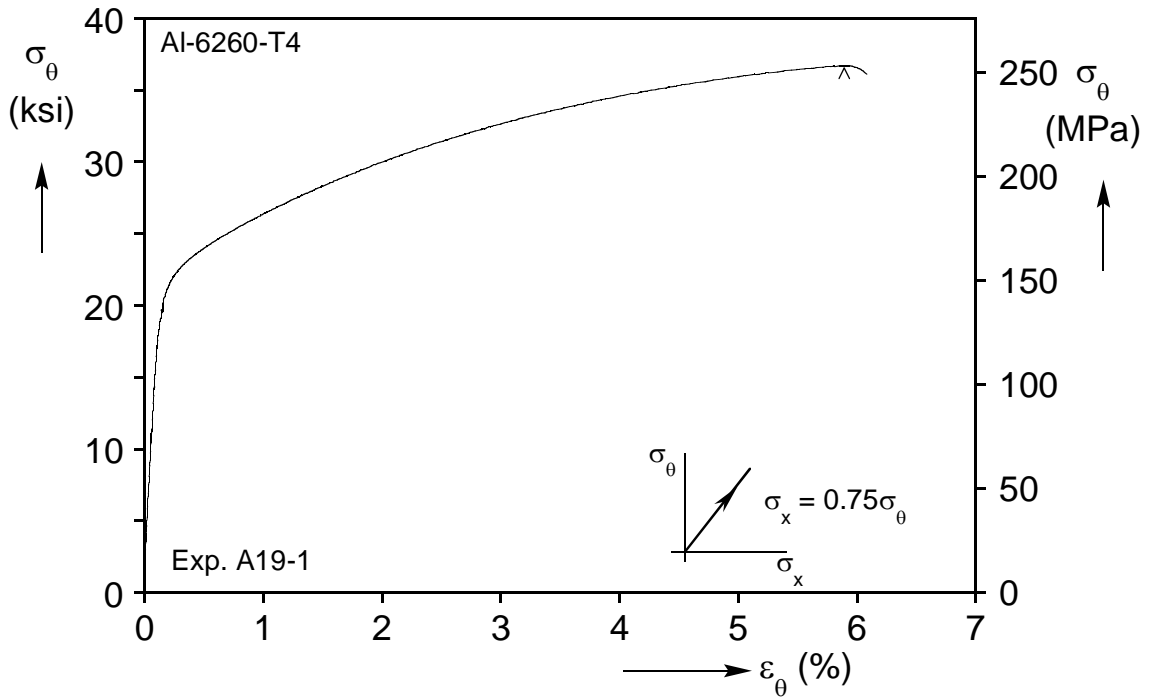
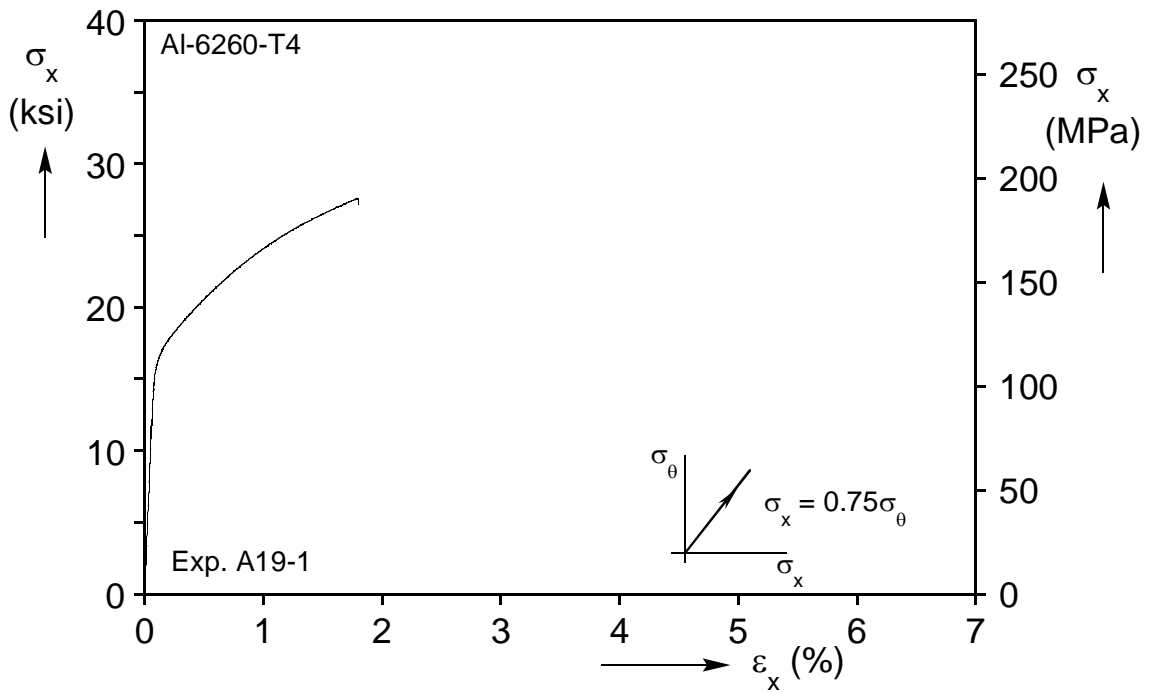


Fig. 3.9 – Axial thickness reduction profiles from two experiments that exhibited circumferential rupture. Both illustrate localized wall-thinning.



(a)



(b)

Fig. 3.10 – (a) Circumferential and (b) axial stress-strain responses recorded in experiment with $\alpha=0.75$

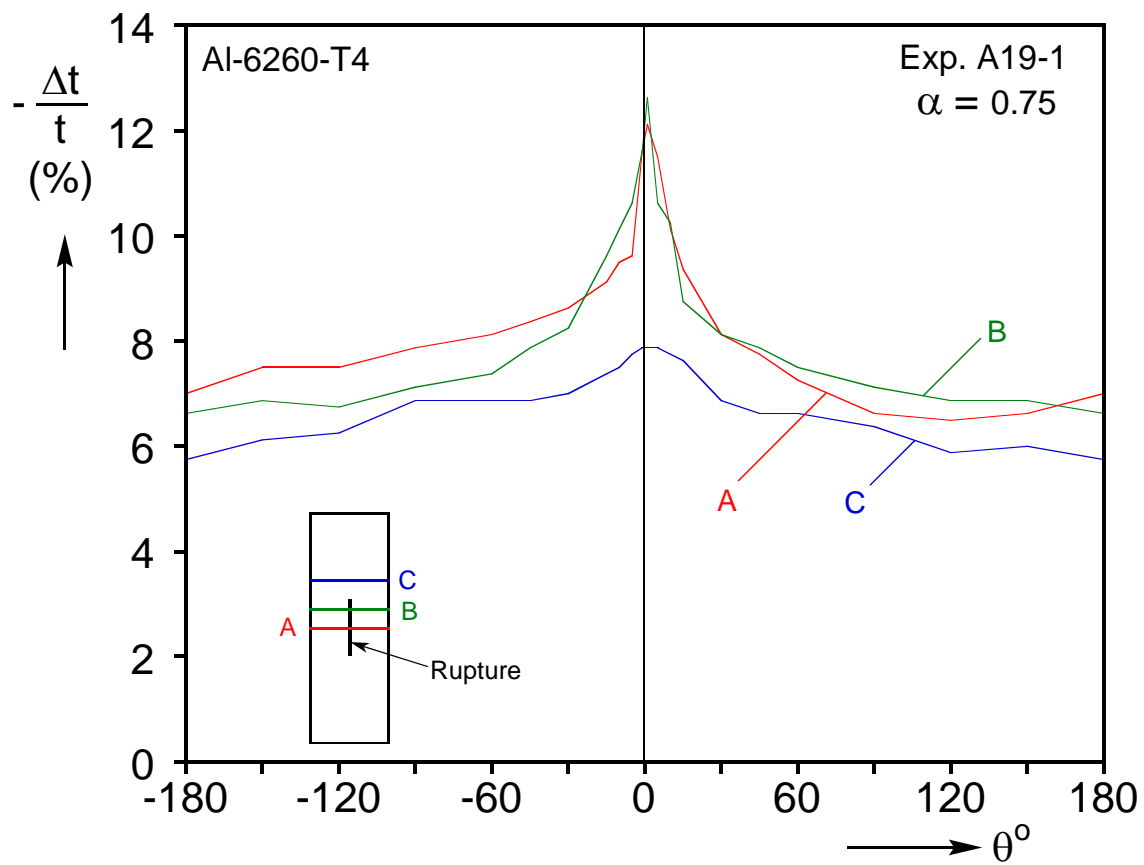
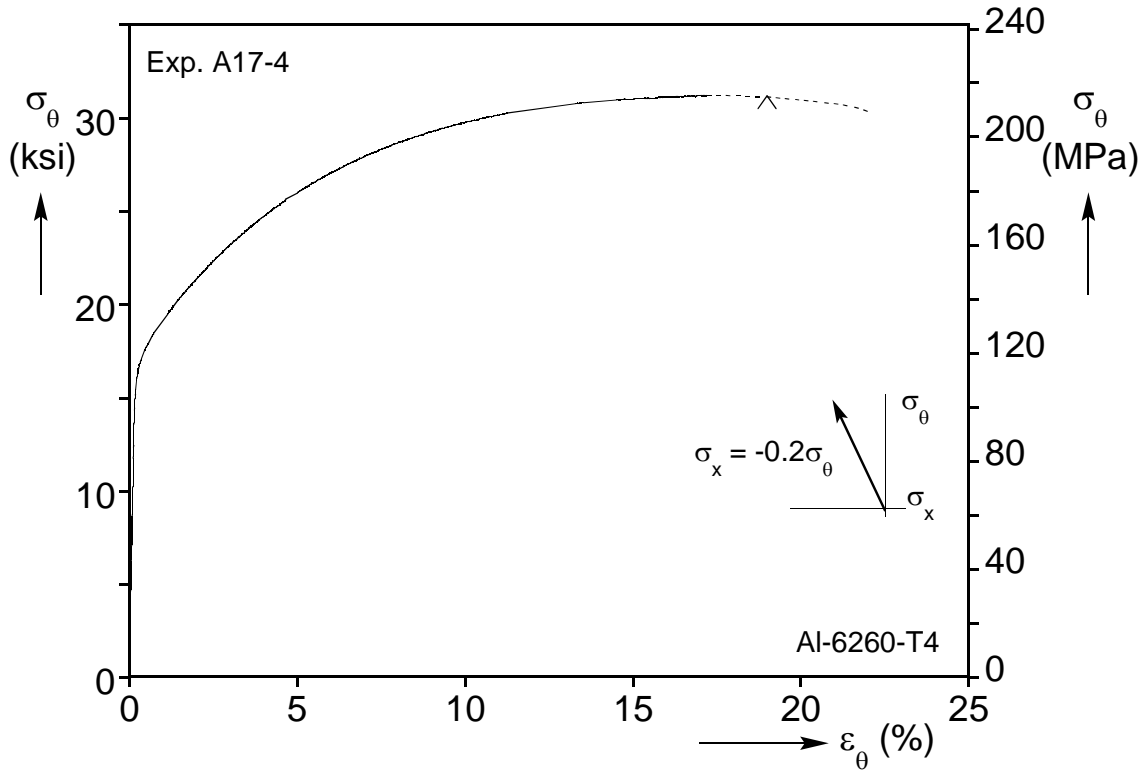
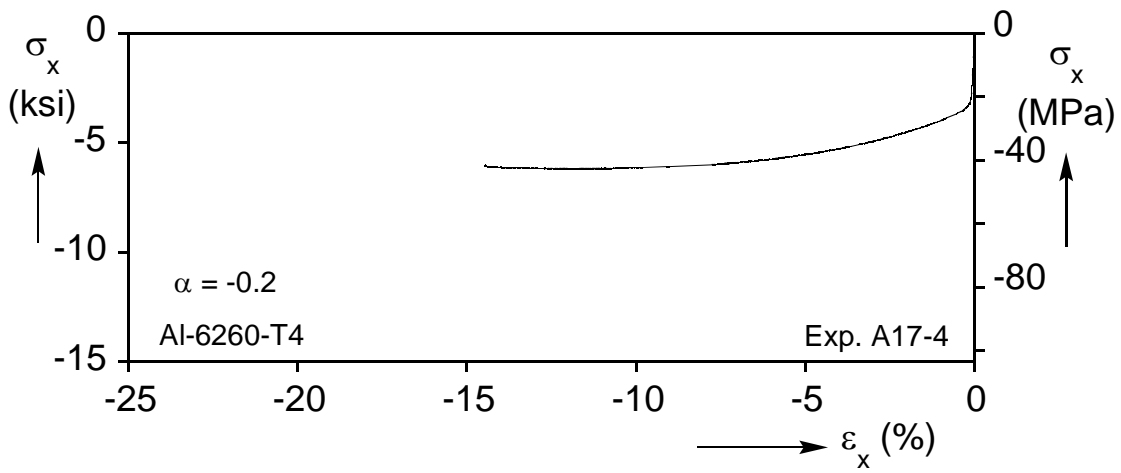


Fig. 3.11 – Thickness reduction profiles at three locations around the circumference of a burst tube, illustrating localization of wall thinning.



(a)



(b)

Fig. 3.12 – (a) Circumferential and (b) axial stress-strain responses recorded in experiment with $\alpha = -0.2$

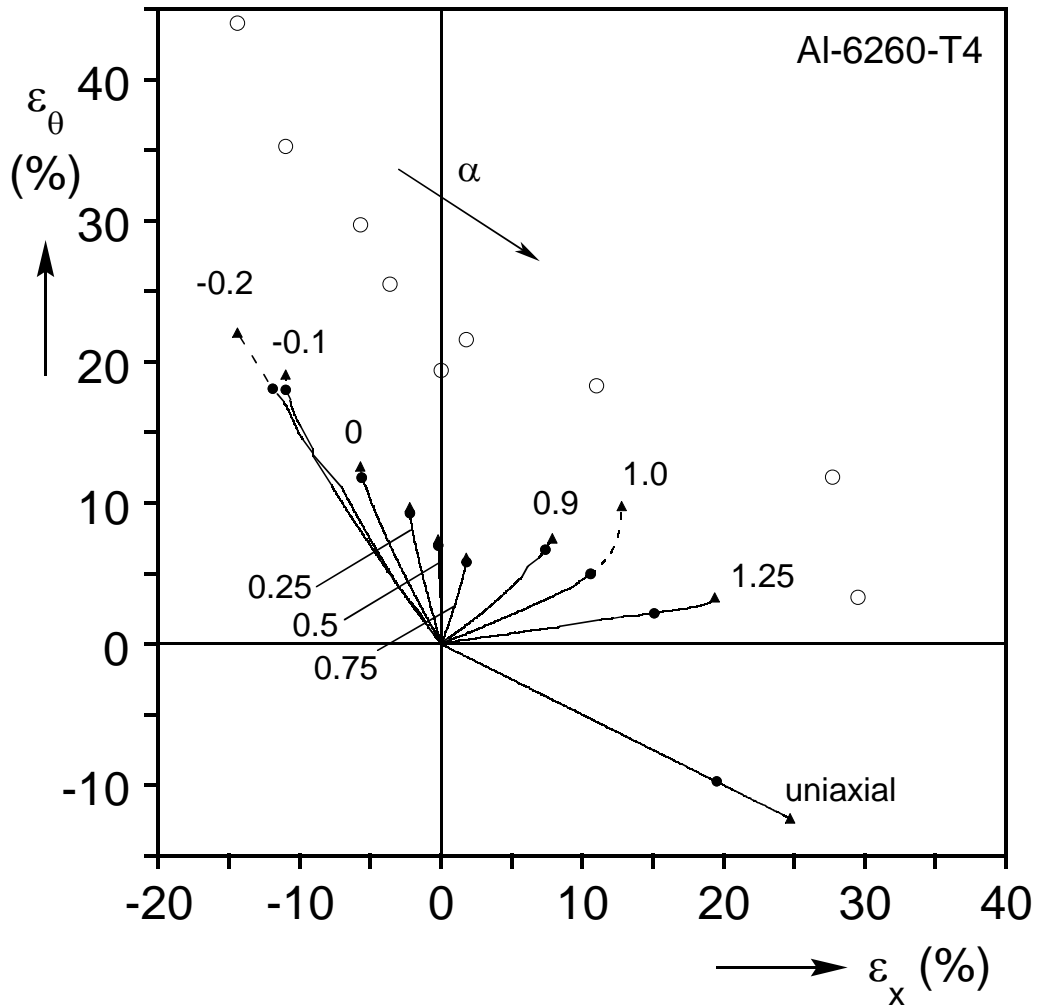


Fig. 3.13(a) – Strain paths traced in the experiments (●, average strains at the limit load; ▲, average strains at rupture; ○, local strains in zone of rupture).

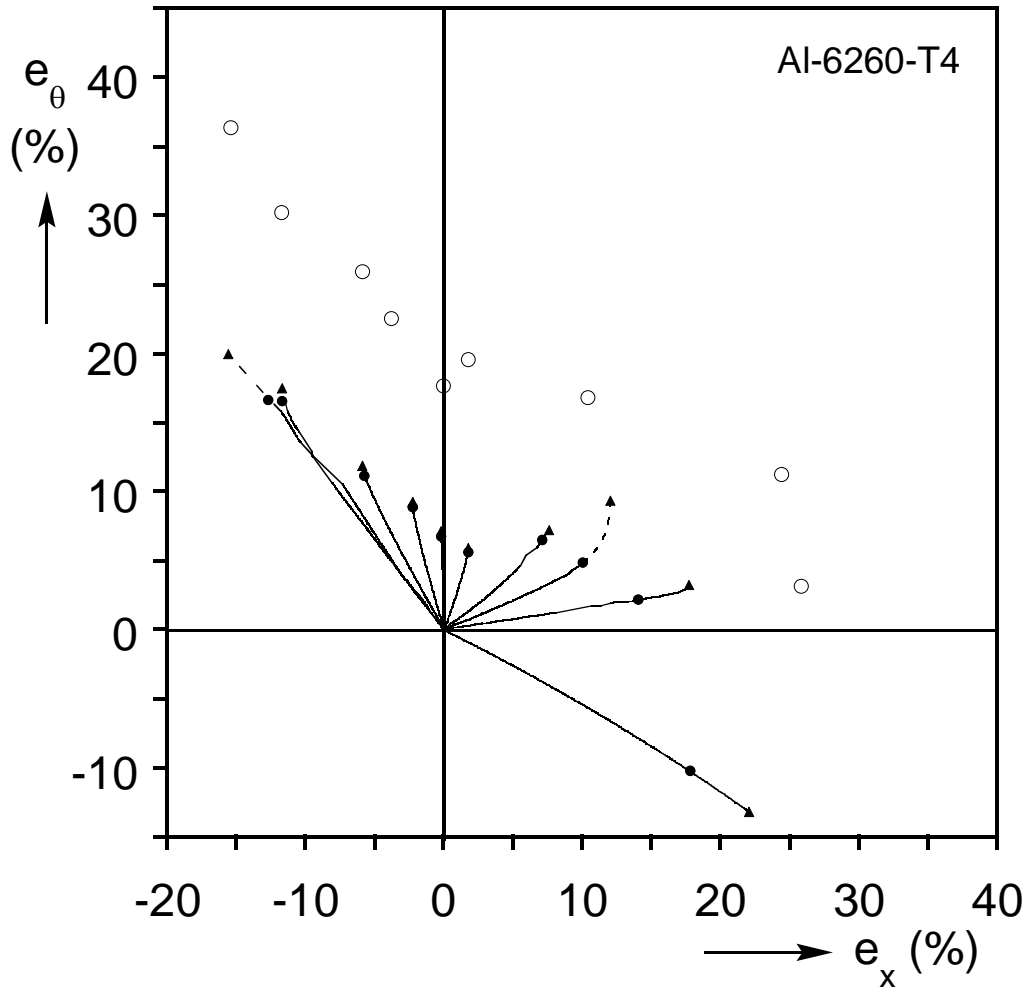


Fig. 3.13(b)– Figure 3.13(a) replotted for the logarithmic strains.

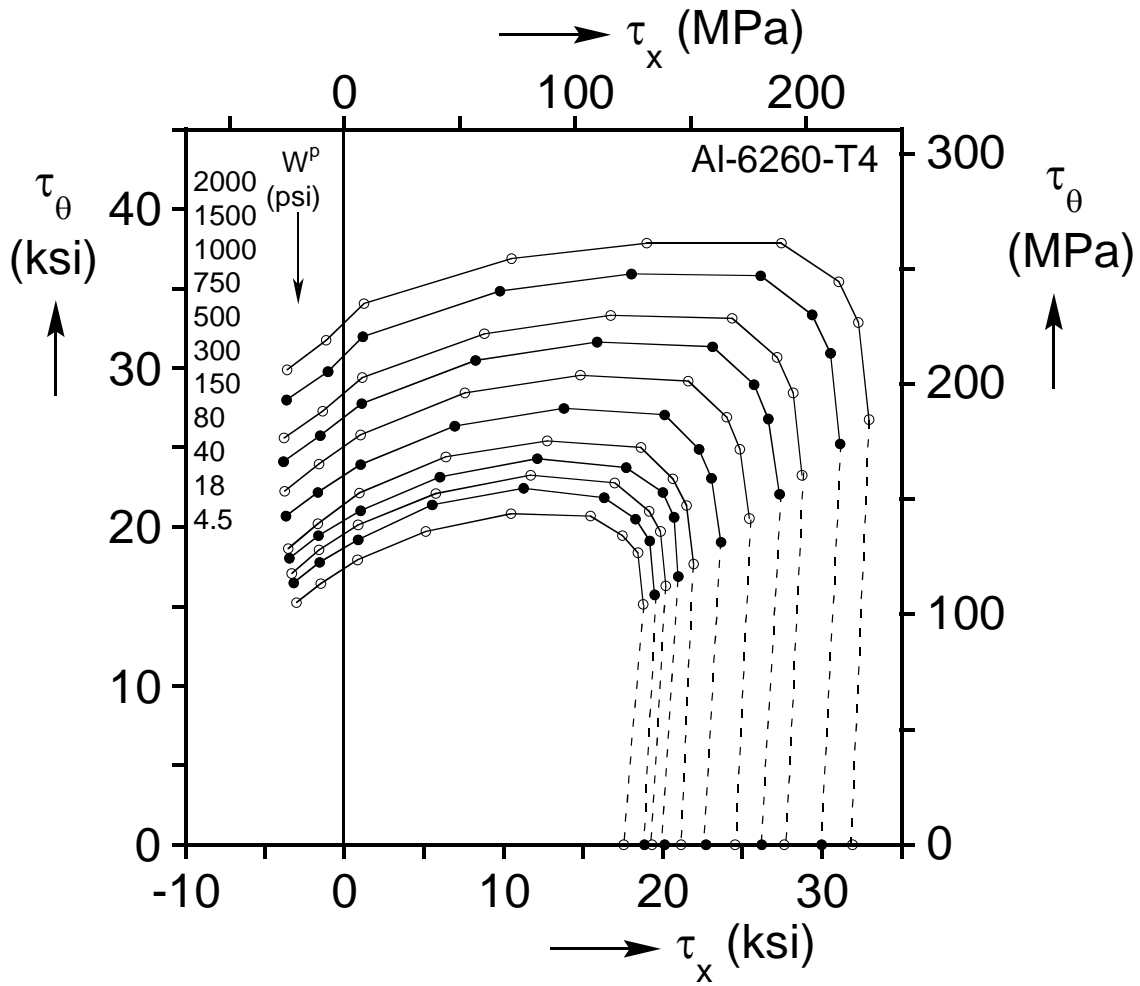


Fig. 3.14 – Loci of experimental points representing various levels of constant plastic work

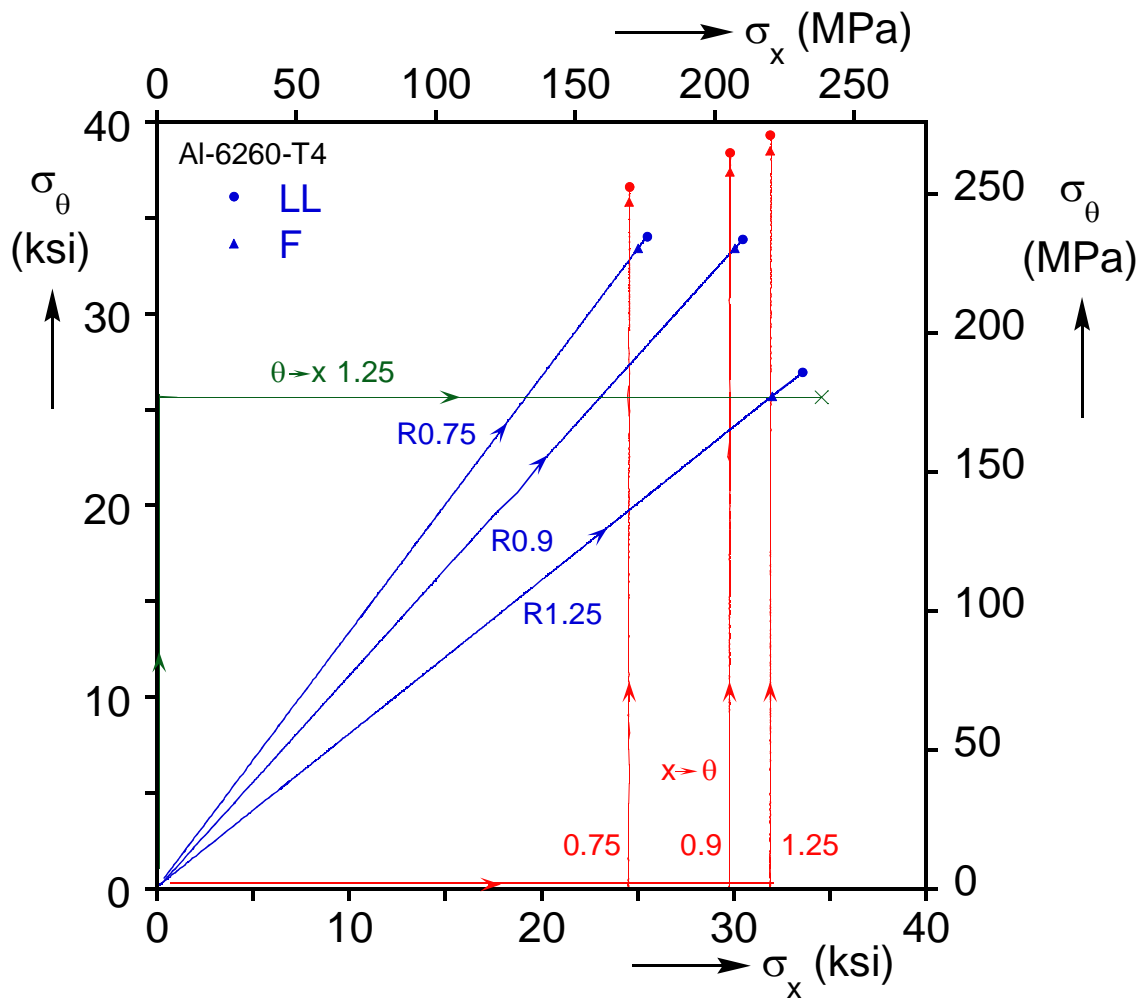


Fig. 3.15(a) – Corner paths prescribed in the experiments and the corresponding radial paths, plotted in the engineering stress space. Marked are the limit (●) and the failure stresses (▲).

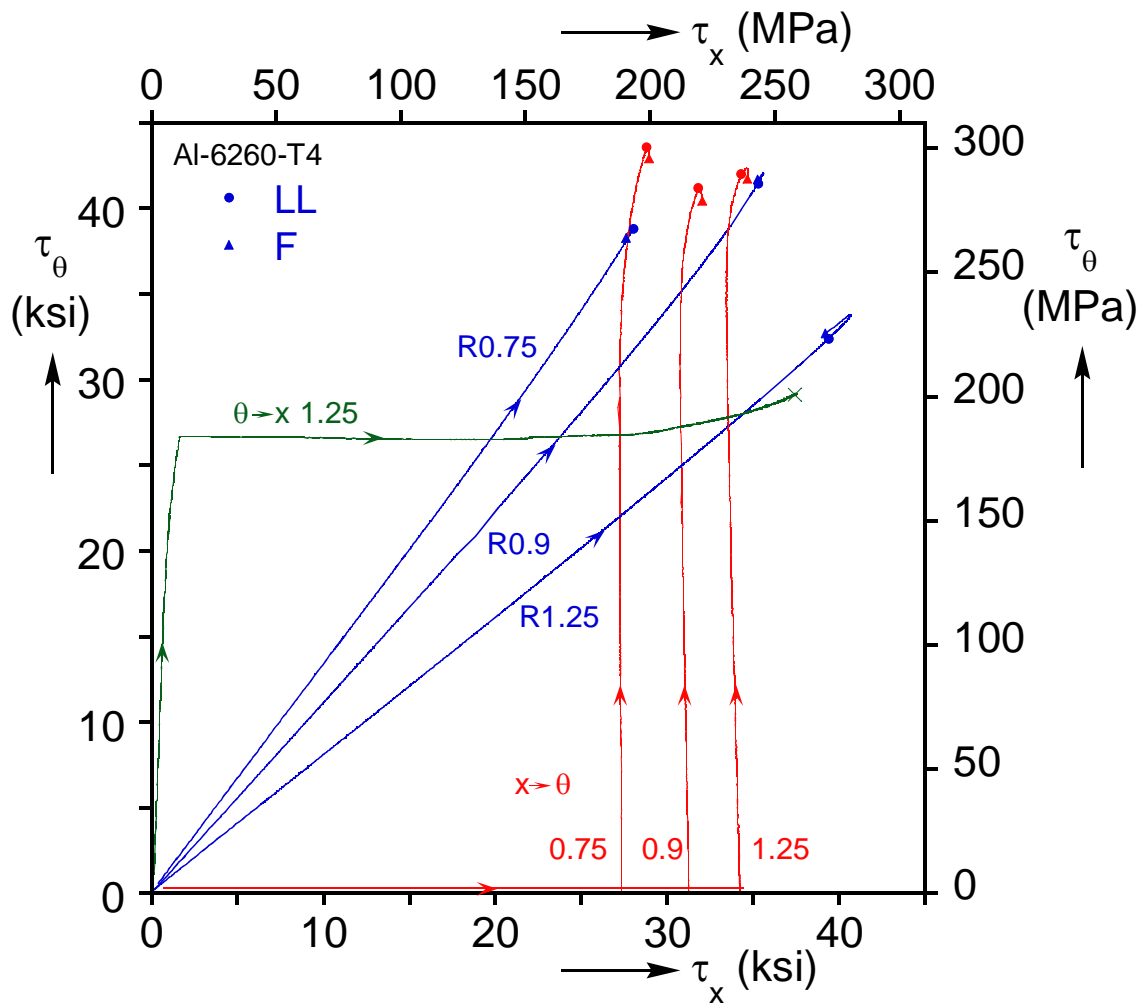


Fig. 3.15(b) – Figure 3.15(a) replotted for the true stresses.

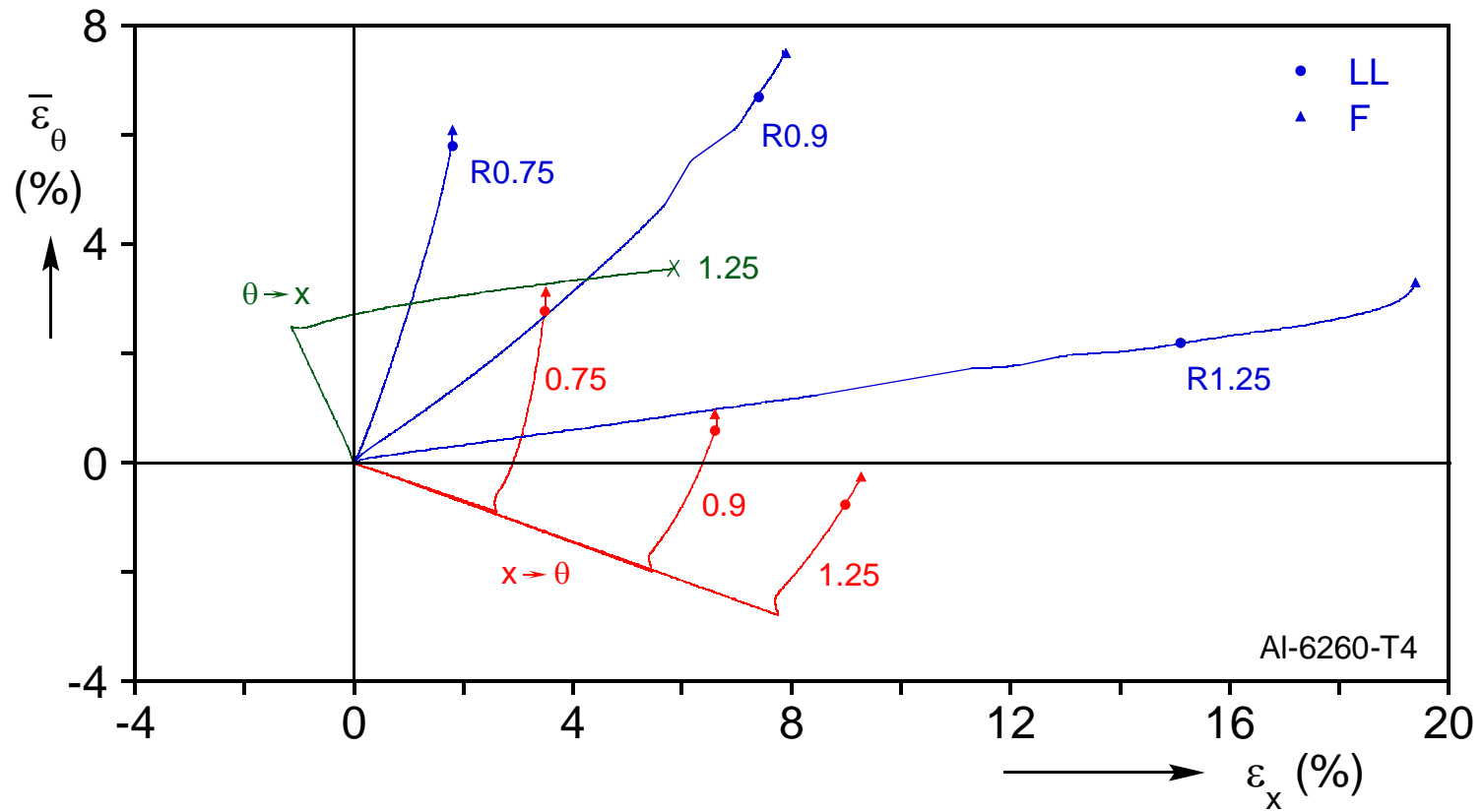


Fig. 3.16(a) – Engineering strain paths traced in the corner experiments, and the corresponding paths for radial loadings. Marked are the average strains at the limit load (●) and at failure (▲).

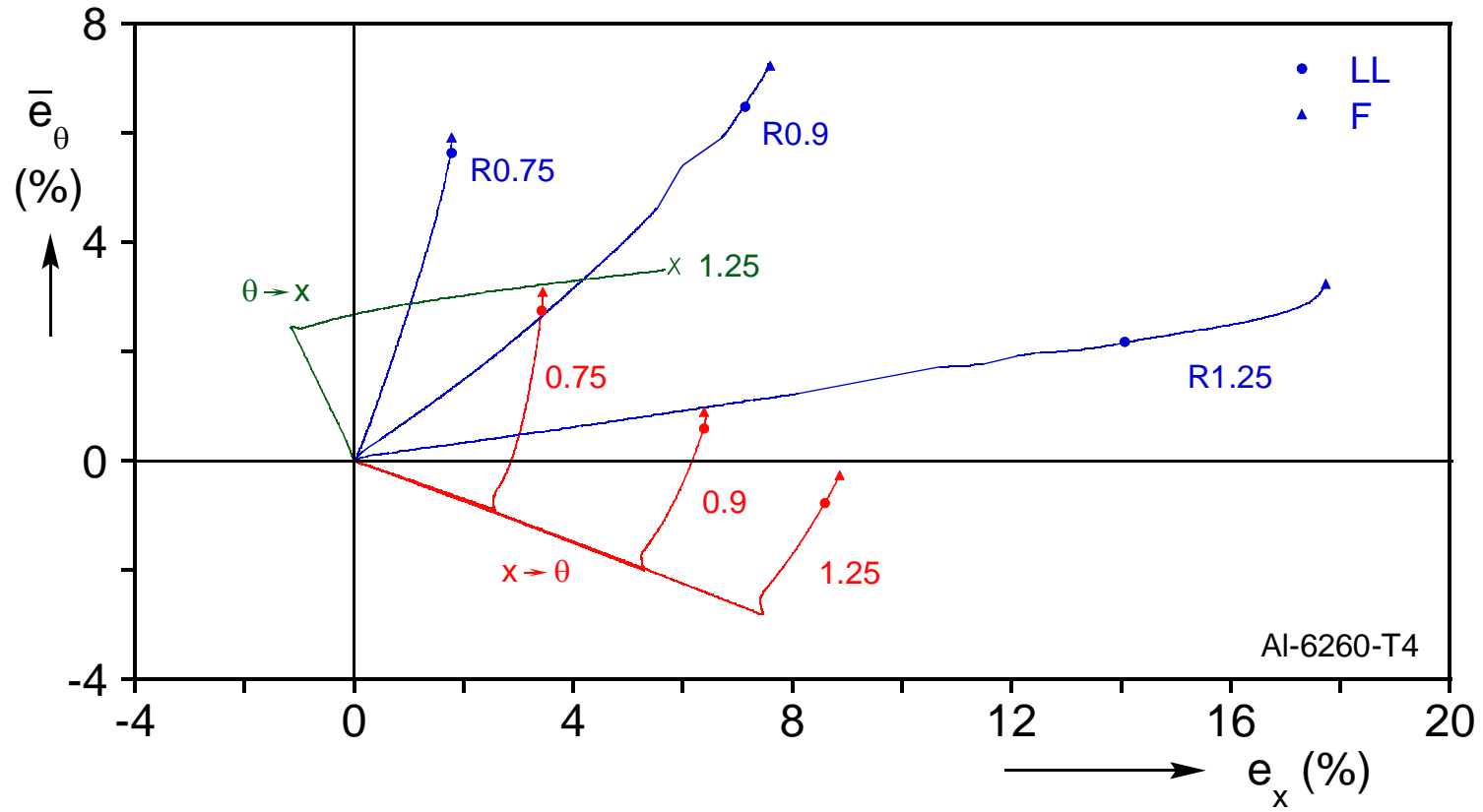


Fig. 3.16(b) – Figure 3.16(a) replotted for the logarithmic strains.

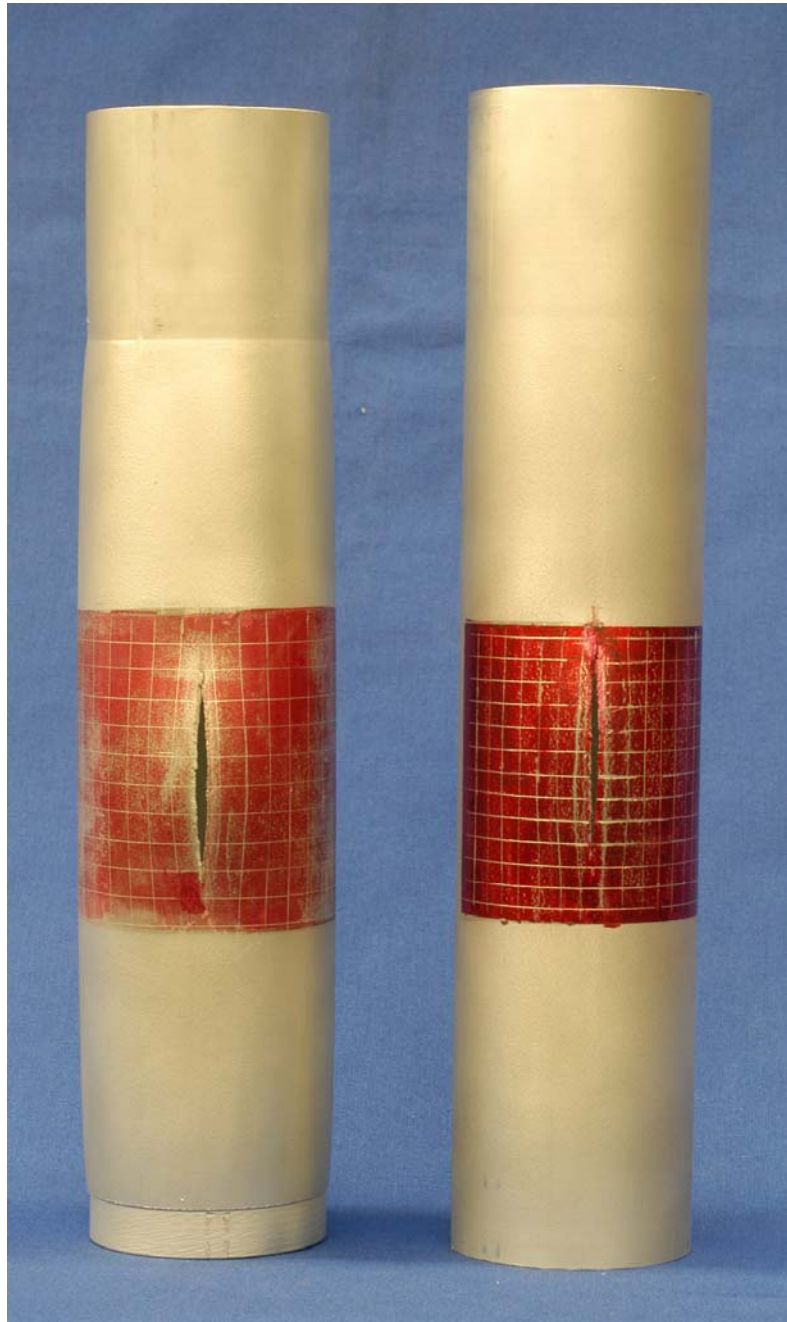


Fig. 3.17 – Comparison of failed test specimens for R0.75 (left) and $x \rightarrow \theta$ 0.75 (right). Notice the remarkably different hoop strain.

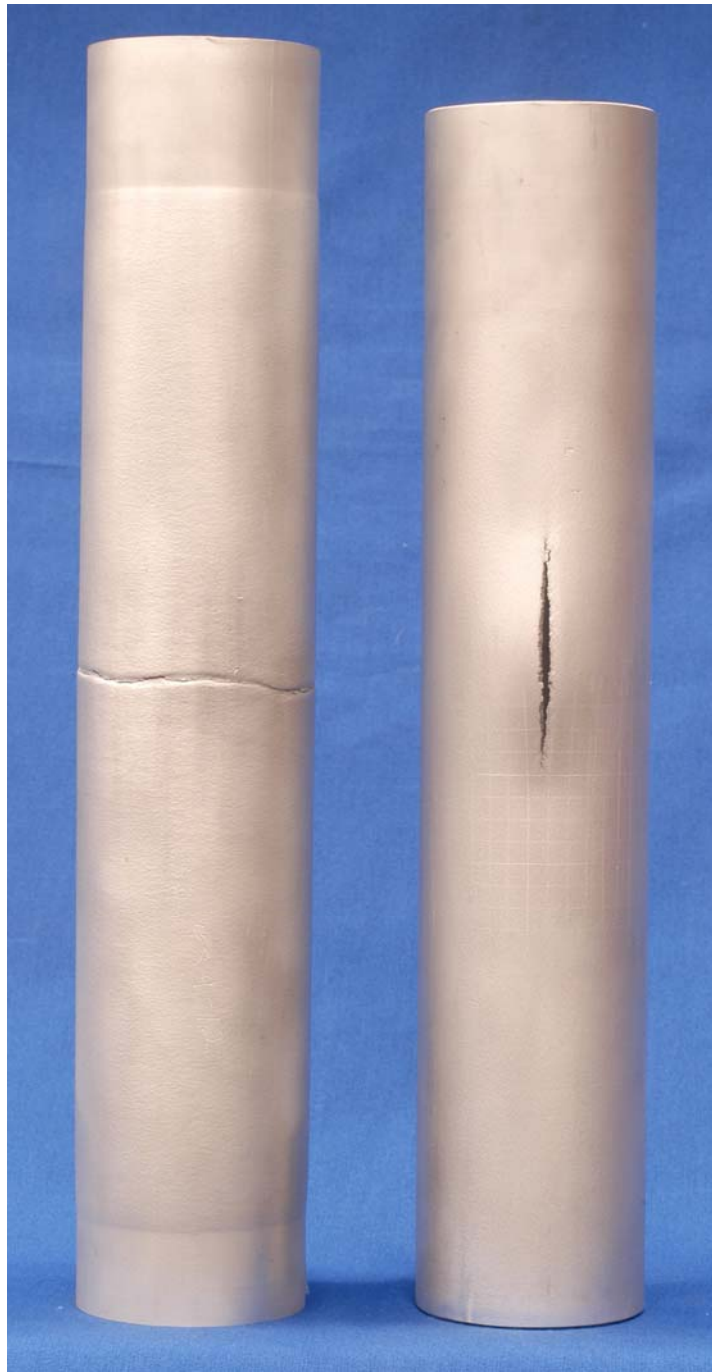
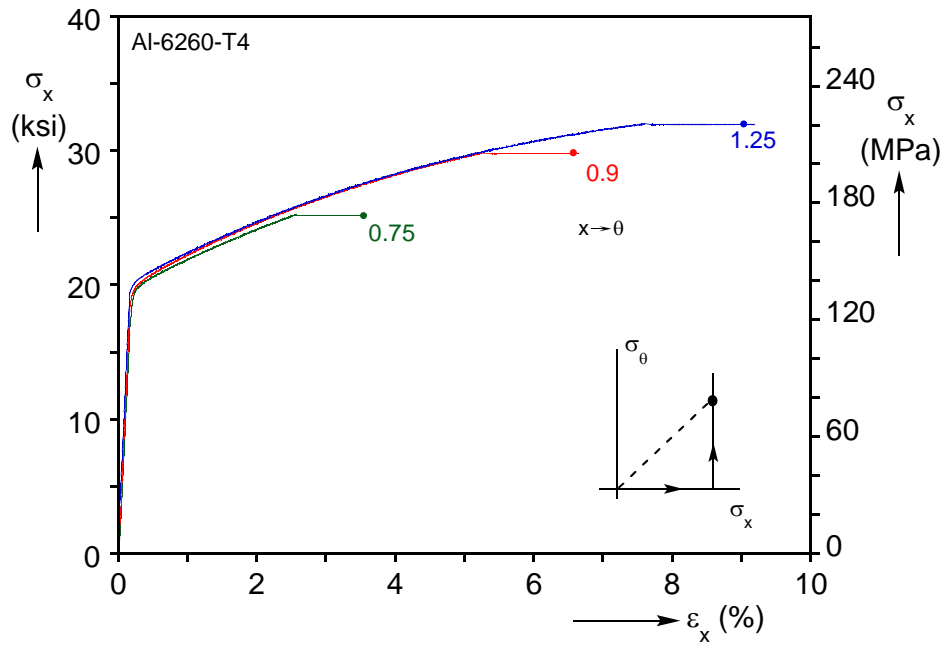
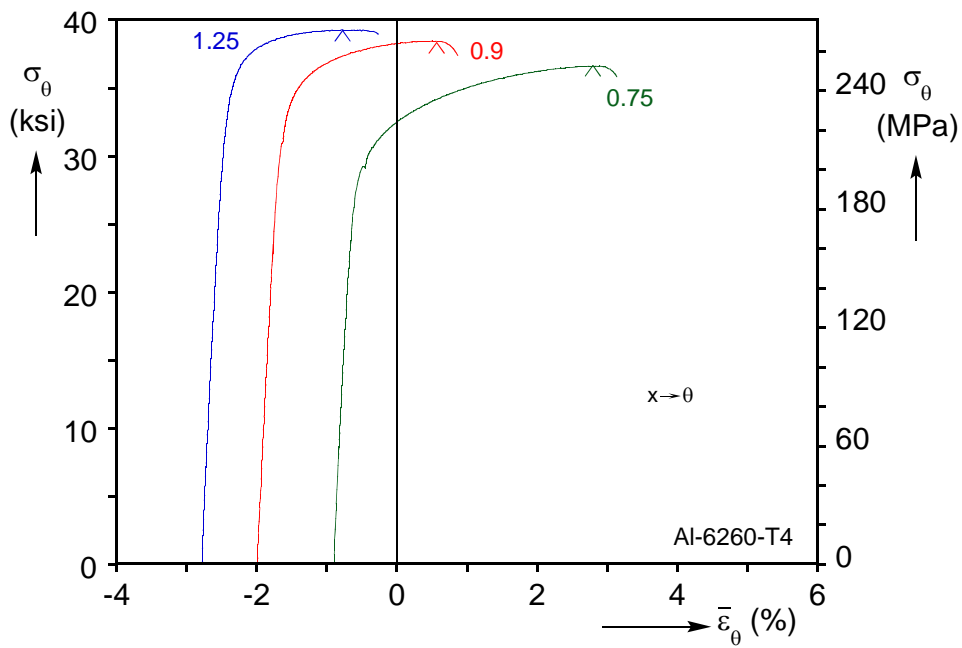


Fig. 3.18 – Comparison of failed test specimens for R1.25 (left) and for the corresponding corner path $x \rightarrow \theta$ 1.25 (right). Of interest is the failure mode change, and the very limited hoop strain the developed in the right tube before rupture.



(a)



(b)

Fig. 3.19 – (a) Axial, and (b) circumferential stress-strain responses recorded in the three $x \rightarrow \theta$ corner path experiments. The symbol (●) in (a) corresponds to the limit pressure marked in (b).

Chapter 4: *Constitutive and Numerical Modeling*

of Tube Bursting

The major aims of the experimental study on the formability of Al-6260-T4 tubes described in the previous Chapter were, first, to establish the forming limits for this material and in tubular form; and second, to generate enough data to calibrate an appropriate constitutive framework for accurate numerical predictions of burst. This mode of failure was seen in Chapter 2 to be a dominant factor that limited the performance of Al-6260-T4 in the tube hydroforming experiments. With the aid of these data then, we expand here in detail on the constitutive and numerical modeling appropriate for this class of problems.

4.1 CONSTITUTIVE MODELING

The inelastic behavior of our material will be modeled through an associated flow rule that is based on an anisotropic yield function. It is clear from the plastic work contours of Fig. 3.14 that the as-received tubes exhibited initial anisotropy induced by the manufacturing process. Furthermore, that the anisotropy evolves as plastic deformation accumulates. Isotropic hardening will be adopted, in the sense that the center of any subsequent yield surface will always remain at the origin. Also, as is currently well accepted, aluminum alloys require the use of non-quadratic yield functions (Hosford 1972, 1979, Hill 1979, 1990, Barlat and Lian 1989, Barlat *et al.* 1991, Barlat *et al.* 1997, Barlat *et al.* 2003, Miller and Kyriakides, 2003; Kyriakides *et al.*, 2004 and others).

In the free hydroforming experiments conducted (radial as well as corner paths), the tubes deformed homogeneously over a significant part of their loading histories, with bulging and localization that precipitate rupture only occurring in the latter parts of the histories. Thus, for the most part of the life of the specimen, a principal state of stress $(\sigma_x, \sigma_\theta)$ existed (the third component being negligible). Consequently we begin by examining Hosford's principal stress anisotropic yield function (Hosford, 1972, 1979) as it is relatively easy to calibrate and manipulate. By contrast, at the onset of rupture the state of stress is no longer axisymmetric and thus the more general anisotropic yield functions put forward by Karafillis and Boyce (1993) and Barlat *et al.* (2003) are more appropriate.

4.1.1 Hosford's 1979 Anisotropic Yield Function

A variety of materials, including aluminum alloys, exhibit initial, plane stress yield loci that lie between the von Mises ellipse and the Tresca hexagon. In an attempt to model this behavior, Hosford (1972) at first suggested an isotropic non-quadratic yield function in terms of the principal stresses:

$$|\sigma_\theta - \sigma_x|^k + |\sigma_x - \sigma_r|^k + |\sigma_r - \sigma_\theta|^k = 2\sigma_o^k \quad (4.1)$$

Later, this yield function was extended by Hosford (1979) to the anisotropic case to read:

$$\frac{1}{2} \left\{ F |\sigma_\theta - \sigma_x|^k + G |\sigma_x - \sigma_r|^k + H |\sigma_r - \sigma_\theta|^k \right\} = \sigma_o^k \quad (4.2)$$

Introducing now the dimensionless parameters $S_\theta = \frac{\sigma_{o\theta}}{\sigma_o}$ and $S_r = \frac{\sigma_{or}}{\sigma_o}$, where σ_o , $\sigma_{o\theta}$, σ_{or} are the yield stresses in the axial, circumferential and radial directions respectively, Eq. (4.2) can be written in a form more suitable for our problem:

$$\frac{1}{2} \left\{ \left(1 + \frac{1}{S_\theta^k} - \frac{1}{S_r^k} \right) |\sigma_\theta - \sigma_x|^k + \left(1 + \frac{1}{S_r^k} - \frac{1}{S_\theta^k} \right) |\sigma_x - \sigma_r|^k + \left(\frac{1}{S_r^k} + \frac{1}{S_\theta^k} - 1 \right) |\sigma_r - \sigma_\theta|^k \right\} = \sigma_o^k \quad (4.3)$$

This constitutive model allows for two parameters to be adjusted to match the yield behavior of any specific material. The exponent k can be calculated with the aid of crystal plasticity, and was shown to be equal to 8 for FCC materials such as aluminum alloys (Logan and Hosford, 1980). Notice that for $k = 2$, Eq. (4.3) reduces to the classical Hill (1948) yield function. For the two anisotropy parameters, $S_\theta = 1.04$ was found to bring together the early parts of the two uniaxial stress-strain responses shown in Fig. 3.4b. The value of S_r was then chosen for optimal matching of the structural response of the finite element models of the biaxial tests (to be described in Section 4.2.1) to the actual experiments. Observe that since the tubes deformed essentially uniformly up until at least the limit load a homogeneous state of stress can be assumed, which greatly simplifies this calibration procedure.

The resulting initial yield surface in the $(\sigma_x - \sigma_\theta)$ plane is shown in Fig. 4.1. It has a sharper curvature along the equibiaxial tension direction and flatter sides than the von Mises yield criterion. Included in the figure are two sets of experimental points, for two different definitions of yielding. The first set corresponds to a strain offset of 0.05% and the second to a plastic work of 9.2 psi (63 kPa). The two sets of points are seen to agree quite well with each other, indicating the near equivalence of the two methods of establishing yielding. The data is also in good agreement with Hosford's yield function as calibrated.

The true stress version of the yield function was used to generate an associative flow rule. The flow rule was subsequently used to calculate the equivalent true stress-equivalent logarithmic plastic strain $(\tau_e - de_e^P)$ response for the early part of each of the

nine biaxial experiments performed (radial paths). The equivalent logarithmic plastic strain is calculated by requiring that these stress and strain measures are work conjugate, or that:

$$\tau_e de_e^p = \tau_\theta de_\theta^p + \tau_x de_x^p. \quad (4.4)$$

The results for the nine radial path experiments performed are shown in Fig. 4.2. The yield function bundles the responses around the uniaxial one to a reasonable degree, while the spreading between the responses is an indication of the limitations of this yield function. The flow rule was also used to calculate contours of equal plastic work for the values for which the experimental contours in Fig. 3.14 were generated. The calculated and the experimental contours are compared in Fig. 4.3. The calculated work contours do not match perfectly the experimental points, which is another indication of the limitations of this yield function. Of course, it should also be considered that the isotropic hardening assumed is only an approximation that may not represent the material behavior perfectly.

4.1.2 Karafillis and Boyce 1993 Anisotropic Yield Function

A more elaborate description of the yielding behavior in comparison to that offered by Hosford was proposed by Karafillis and Boyce (1993) - abbreviated henceforth as K-B. The K-B yield function offers more flexibility than Hosford's model in fitting experimental work contours like the ones in Fig. 3.14. Even more importantly, since it can be related to the actual stress tensor and not only its principal values, it can be more naturally used for the incorporation of shear anisotropy. Recall that as shown in Fig. 3.4b, the material at hand exhibits significant anisotropy in shear.

The isotropic version of this yield criterion is a combination of two distinct yield surfaces. The first is Hosford's isotropic yield criterion (Eq. (4.1)) which in terms of the principal deviatoric stresses, s_i ($i=1,3$), is given by:

$$f_1 = \frac{1}{2} \left[(s_1 - s_2)^{2k} + (s_2 - s_3)^{2k} + (s_3 - s_1)^{2k} \right] = \sigma_o^{2k} \quad (4.5)$$

where σ_o is the yield stress in a uniaxial test. Yield surfaces bounded by the von Mises ($k = 1$) and Tresca ($k = \infty$) surfaces can be generated by selecting the exponent to be an integer $k \in [1, \infty)$. The second yield criterion, expressed again in terms of s_i , is written as:

$$f_2 = \frac{3^{2k}}{2^{2k} + 2} \left[s_1^{2k} + s_2^{2k} + s_3^{2k} \right] = \sigma_o^{2k} \quad (4.6)$$

with k once more having the same range. Equation (4.6) represents surfaces that lie between the von Mises and the outer bound for isotropic convex surfaces (Mendelson, 1968). Karafillis and Boyce combined f_1 and f_2 to form the following convex yield function:

$$f = [(1-c)f_1 + cf_2]^{1/2k}, \quad c \in [0,1]. \quad (4.7)$$

Anisotropy was introduced by evaluating the *isotropic plasticity equivalent deviatoric stress tensors*, related to the stress tensor $\boldsymbol{\sigma}$ acting on the anisotropic material point through a linear operator as follows:

$$\mathbf{s} = \mathbf{L}\boldsymbol{\sigma}. \quad (4.8)$$

Adopting the symmetries for \mathbf{L} appropriate for orthotropy, and limiting attention to plane stress states of interest to our tube problems, (4.8) can be written as:

$$\begin{Bmatrix} s_x \\ s_\theta \\ s_r \\ s_{r\theta} \end{Bmatrix} = \mathbf{L} \begin{Bmatrix} 1 & \beta_1 & \beta_2 & 0 \\ \beta_1 & \alpha_1 & \beta_3 & 0 \\ \beta_2 & \beta_3 & \alpha_2 & 0 \\ 0 & 0 & 0 & \delta \end{Bmatrix} \begin{Bmatrix} \sigma_x \\ \sigma_\theta \\ 0 \\ \sigma_{r\theta} \end{Bmatrix} \quad (4.9)$$

where $\beta_1 = \frac{1}{2}(\alpha_2 - \alpha_1 - 1)$, $\beta_2 = \frac{1}{2}(\alpha_1 - \alpha_2 - 1)$, and $\beta_3 = \frac{1}{2}(1 - \alpha_1 - \alpha_2)$.

Thus, the anisotropy is defined by four parameters, $\{\Gamma, \alpha_1, \alpha_2, \delta\}$ in addition to the exponent that controls the curvature. (Contrast this with the two parameters available for the anisotropic Hosford yield function.) The principal deviatoric stress components s_i ($i = 1, 3$) are evaluated from s_{ij} in (4.9) in the usual manner and are substituted in (4.7) to complete the anisotropic yield function. For sheet metal forming applications, the parameters $\{\Gamma, \alpha_1, \alpha_2\}$ can be determined as discussed in Appendix 2 of K-B (1993). The value of δ then becomes:

$$\delta = \frac{\sigma_o}{\Gamma \sigma_{xyo}} \left[(1-c)(2^{2k-1} + 1) + c \frac{3^{2k}}{2^{2k-1} + 1} \right]^{1/2k}. \quad (4.10)$$

Two versions of this model will be considered. In the first version $c = 0$, which reduces f in (4.7) to Hosford's yield function where however s_i are evaluated through (4.9). In this case, $2k$ was selected to be 8 as in the principal stress version of the anisotropic Hosford function. Since the procedure for determining the constants $\{\Gamma, \alpha_1, \alpha_2\}$ described in K-B is better suited for sheet metal, it was found more convenient in the present case to follow a different calibration approach. The constants were selected for optimal agreement of the initial yield surface with the experimental data, as well as for best performance in bringing together the structural response of the finite element models (Section 4.2.1) to those observed in the experiments. Notice again that a simple numerical model is sufficient for this trial-and-error procedure, as before. The parameters chosen are $\{\Gamma, \alpha_1, \alpha_2\} = \{0.68, 0.94, 0.97\}$. The resulting initial yield surface is compared to the experimental data that correspond to the two different definitions of yielding discussed earlier, in Fig. 4.4. The shape is seen to be in reasonable agreement with the data. The performance of the model with regards to the equivalent true stress-equivalent plastic strain responses from the biaxial experiments is comparable to the corresponding results from Hosford's model shown in Fig. 4.2.

Constant plastic work contours were generated with this yield function and are compared to the experimental ones in Fig. 4.5. The calculated contours underpredict the experimental values to some degree, most prominently for values of α between 0.5 and 1.0. Recall that the plastic strain increment vector at a point is normal to the contour. Then, this deviation between the experimental and the predicted work contours is expected to have an impact in the numerical simulations of the burst experiments that follow (see Section 4.2).

The performance of the full version of the K-B yield function was also investigated. The model was calibrated following a similar procedure. In this case, the presence of f_2 dictates that a much higher exponent be employed, $2k = 24$ in accord with K-B findings (Miller and Kyriakides (2003) used $2k = 30$). The parameters arrived at are $\{c, F, \alpha_1, \alpha_2\} = \{0.8, 0.6665, 0.96, 0.99\}$. The corresponding initial yield surface is shown in Fig. 4.6. In general, the shape is very close to the one in Fig. 4.4 with $c = 0$. The performance in pulling together the measured equivalent true stress-equivalent logarithmic plastic strain responses is once more of similar quality as that of the Hosford yield function shown in Fig. 4.2.

4.1.3 Barlat *et al.* 2003 Anisotropic Yield Function (Yld2000-2D)

An even more elaborate and flexible description of the constitutive behavior of a given material is afforded by the model suggested by Barlat *et al.* (2003). This is again based (as the K-B model) in the non-quadratic isotropic yield function of Hosford (1972), written now in terms of the principal stress deviators as:

$$|s_1 - s_2|^k + |2s_1 + s_2|^k + |s_1 + 2s_2|^k = 2\sigma_o^k \quad (4.11)$$

derived from (4.5) by using $s_{ii} = 0$. To allow for the inclusion of even more anisotropic parameters and hence improved flexibility of the model, Barlat *et al.* introduced

anisotropy by two linear transformations, one applied to the first term (ϕ') and the other to the second and third terms (ϕ''):

$$\phi = \phi' + \phi'' = |S'_1 - S'_2|^k + |2S''_1 + S''_2|^k + |S''_1 + 2S''_2|^k = 2\sigma_o^k \quad (4.12)$$

Here (S'_1, S'_2) and (S''_1, S''_2) are the principal values of the linearly transformed stress tensors S' and S'' , respectively, obtained from the stress deviator s and the stress tensor σ by:

$$S' = C's = C'T\sigma = L'\sigma \quad \text{and} \quad S'' = C''s = C''T\sigma = L''\sigma \quad (4.13)$$

where C', C'', T, L' and L'' are appropriate transformation tensors that allow introduction of the anisotropy (Barlat *et al.*, 2003). Thus, for our 2-D stress state:

$$\begin{Bmatrix} S'_x \\ S'_y \\ S'_{xy} \end{Bmatrix} = \begin{bmatrix} L'_{11} & L'_{12} & 0 \\ L'_{21} & L'_{22} & 0 \\ 0 & 0 & L'_{66} \end{bmatrix} \begin{Bmatrix} \sigma_x \\ \sigma_y \\ \sigma_{xy} \end{Bmatrix} \quad \text{and} \quad \begin{Bmatrix} S''_x \\ S''_y \\ S''_{xy} \end{Bmatrix} = \begin{bmatrix} L''_{11} & L''_{12} & 0 \\ L''_{21} & L''_{22} & 0 \\ 0 & 0 & L''_{66} \end{bmatrix} \begin{Bmatrix} \sigma_x \\ \sigma_y \\ \sigma_{xy} \end{Bmatrix} \quad (4.14a)$$

where L' and L'' are related to parameters α_i ($i=1,8$) as follows:

$$\begin{Bmatrix} L'_{11} \\ L'_{12} \\ L'_{21} \\ L'_{22} \\ L'_{66} \end{Bmatrix} = \begin{bmatrix} 2/3 & 0 & 0 \\ -1/3 & 0 & 0 \\ 0 & -1/3 & 0 \\ 0 & 2/3 & 0 \\ 0 & 0 & 1 \end{bmatrix} \begin{Bmatrix} \alpha_1 \\ \alpha_2 \\ \alpha_7 \end{Bmatrix} \quad \text{and} \quad \begin{Bmatrix} L''_{11} \\ L''_{12} \\ L''_{21} \\ L''_{22} \\ L''_{66} \end{Bmatrix} = \frac{1}{9} \begin{bmatrix} -2 & 2 & 8 & -2 & 0 \\ 1 & -4 & -4 & 4 & 0 \\ 4 & -4 & -4 & 1 & 0 \\ -2 & 8 & 2 & -2 & 0 \\ 0 & 0 & 0 & 0 & 9 \end{bmatrix} \begin{Bmatrix} \alpha_3 \\ \alpha_4 \\ \alpha_5 \\ \alpha_6 \\ \alpha_8 \end{Bmatrix}. \quad (4.14b)$$

(The first and second derivatives of the yield function with respect to the stress components, required for the flow rule and its numerical implementation, appear in Barlat *et al.*, 2003, and Yoon *et al.*, 2004).

The exponent k is again assigned the value of 8 as is typical for aluminum alloys. The model is then calibrated by fitting the parameters α_i ($i=1,8$) to the experimental work contours. Of these α_7 and α_8 are related to the shear stresses. As will be demonstrated in Section 4.2.2, shear anisotropy does not influence the predictions of this set of biaxial burst experiments and as a result it will be neglected here too (i.e., $\alpha_7 = \alpha_8 = 1$). Three different calibration schemes were attempted, leading to different performance first in predicting the strain paths traced and second in identifying the onset of rupture. As each of these calibration schemes was prompted by the performance of the previous one, the detailed discussion of them is postponed until Section 4.2.3 where they can be motivated and introduced more naturally than here. At this point it suffices to present the initial yield surface and work contour predictions for the three schemes (Figs. 4.7-4.10). It can be noted that the added flexibility of the Yld2000-2D model is reflected in the much better overall agreement between the experimental and the calculated plastic work contours in relation to either Hosford or K-B models (compare Figs. 4.8-4.10 to Figs. 4.3 and 4.5).

4.2 FINITE ELEMENT MODELING OF THE BURST EXPERIMENTS

4.2.1 Finite Element Models

The inflation experiments were simulated numerically using finite element models developed in the nonlinear code ABAQUS/Standard. The models are used in conjunction with the constitutive equations described in the previous section to reproduce the inflation experiments (radial and corner paths), including the onset of localization and burst. Because of the two distinctly different failure modes observed in the experiments, two different FE models have been developed. Model I is tailored to simulate rupture along a generator that was observed in seven of the radial and three of the corner

experiments. In this case, symmetry allows consideration of one quarter of the tube as shown in Fig. 4.11, with the origin of the coordinate system used being at the mid-span of the tube (i.e., the planes $x=0$ and $\theta=[0-\pi]$ are planes of symmetry). In each simulation the model is assigned the length ($2L$), mid-surface radius (R) and wall thickness (t) corresponding to the actual values of the tubes given in Tables 3.1 and 3.2. The wall thickness is assumed to be uniform except that a local imperfection in the form of an axial groove of reduced thickness (t_g) is added as shown in Fig. 4.11 (shaded band). Observe that this resembles a Marciniak-Kuczynski (1967) type of analysis, common in necking studies in sheet metal forming. The domain is discretized using linear, 4-node shell elements with reduced integration (S4R). These elements allow for large strains and large rotations, both required for the problem at hand. A mainly isotropic mesh is used, with a refinement in the zone surrounding the groove. The main mesh has 45 elements along the length and 45 around the half circumference. The zone around the groove ($L_1 \times s_1$) has double the mesh density in both directions and the groove itself is two elements wide and 25 elements long ($L_g = R$ and $s_g \cong t$ arrived at from convergence studies). The wall thinning imperfection is defined by:

$$\eta = \frac{t - t_g}{t} \geq 0. \quad (4.15)$$

The value of $\eta = 0.05$ is used in all cases analyzed.

Model II is customized to model circumferential rupture that was observed in two radial experiments with high biaxiality ratio ($\alpha = 1.0$ and 1.25). Again symmetries allow consideration of just one quarter of the tube. In this case the model is discretized with 61 elements along the half-length and 60 around the half-circumference. A groove of width $w_g \cong t$ is placed along the circumference at the plane of symmetry at $x=0$ as shown in

Fig. 4.12. The groove is two elements wide and has a wall thickness $t_g(\theta)$ with a wall thinning imperfection of $\eta = 0.05$. In order to allow for the possibility of non-axisymmetric localization to develop, t_g was given a small perturbation described by:

$$t_g(\theta) = \bar{t}_g \left(1 + \frac{\xi}{\bar{t}_g} \cos \theta \right), \quad (4.16)$$

where ξ/\bar{t}_g is a wall eccentricity variable that was assigned the value of 0.0105.

The boundary at $x = L$ is fixed radially and constrained to remain plane. To simulate the radial path experiments, each model is loaded by prescribing incrementally both the internal pressure and the axial load. The internal cavity of the tube is meshed with ABAQUS' hydrostatic elements F3D3 and F3D4 (removed from the figures for clarity), which allowed the pressure to be applied. In order to allow for the anticipated limit load to develop, Riks' path-following procedure is employed. The external axial force is prescribed at a reference node at $(x, r, \theta) = (L, 0, 0)$. All nodes in the plane $x = L$ (i.e., those of the tube as well as those of the cavity) were constrained to follow the reference node. Because of the kinematic coupling of the nodes, the axial load is shared between the specimen and the pressurized cavity, thus corresponding to the load measured by the load cell in our experimental setup. In this way the proportional loading histories prescribed in our radial experiments are reproduced exactly. Thus, for example, when the external axial force is set to remain zero throughout the simulation, the response of the model matches that of a hydrostatic pressure loading test (closed ends tube inflation, where the axial stress that develops is due to the end cap pressure loading only). Similarly, when the external load/pressure ratio is set at $-\pi R^2$, a purely lateral pressure loading is reproduced (zero engineering axial stress, in other words in the experiment the axial load due to the pressure on the end caps is reacted by the servohydraulic machine).

The $x \rightarrow \theta$ and $\theta \rightarrow x$ corner path tests were simulated in analogous ways, corresponding to the actual experimental procedures. Notice that for the corner test simulations, the “*RESTART” option was used in ABAQUS to allow for Riks’ method to be used throughout the calculation.

The FE models use any one of the three constitutive models described in the previous section, through user defined material subroutines (UMATs). The anisotropy parameters of the three constitutive models discussed earlier are summarized in Tables 4.1 – 4.3. In the two K-B models, the experimentally recorded shear anisotropy was also included. For each case the appropriate values of δ evaluated using Eq. (4.10) are listed in Table 4.2.

4.2.2 Discussion of Representative Numerical Results for the Radial Paths

We will discuss the main characteristics of the numerical responses through two representative examples. Figure 4.13a shows the calculated pressure-average circumferential strain response ($P - \bar{\varepsilon}_\theta$) for the radial loading case with $\alpha = 0.9$. Figure 4.13b shows the corresponding axial stress-strain response ($\sigma_x - \varepsilon_x$). Two sets of numerical results are presented, using the K-B and the Yld2000-2D-III constitutive models respectively, with the parameters given in Tables 4.2 and 4.3c. In an attempt to present results in a manner similar to the experimental ones, the circumferential deformation measure ($\bar{\varepsilon}_\theta$) adopted is the change in circumference/initial circumference at $x = 0$. By contrast, the axial strain (ε_x) is based on the change in length/original length of a 0.5-inch gage length in the imperfection at $(x, \theta) = (0, \pi)$. Included in the two figures are the corresponding experimental responses based on the average strain measured by the chain extensometer at the specimen mid-span and the strain measured by the axial extensometer. The predicted $P - \bar{\varepsilon}_\theta$ response using the K-B model is seen to track the

experimental one fairly well, under-predicting the pressure to some extent but over-predicting the corresponding strains significantly. The corresponding $\sigma_x - \varepsilon_x$ response from the K-B model also under-predicts the experimental one, but to a lesser extent. However, for both responses, the improvement in the performance offered by the Yld2000-2D-III model is quite drastic. It can be noticed that the responses predicted with this model lie now very closely to the experimental ones, both in terms of pressure or stress and of strain. This conclusion is true for all the other paths simulated, as well.

The numerical model reproduces very faithfully the array of events observed in the experiments. Inflation leads to uniform deformation, except of course at the ends where the tube is clamped. The stiffness of the model is gradually reduced, until a maximum pressure is reached. Observe that for the Yld2000-2D-III model, the predicted strain at the maximum pressure is $\bar{\varepsilon}_\theta = 7.99\%$ which compares favorably with the corresponding experimental strain of 6.76%. The simulation can of course continue past that instability since Riks' method is used to increment the "loading"; hence reproducing the effect of volume controlled-inflation used in the experiments. Soon after the maximum pressure, an axisymmetric bulge that extends for about one tube diameter appears at mid-span. Depending on the loading path, the deformation can continue for quite a while. At some point however, the deformation starts to localize in the neighborhood of the thickness imperfection where non-axisymmetric bulging develops. The growth of this bulge is rapid, as in the experiments. At approximately $\bar{\varepsilon}_\theta = 9.03\%$ (Yld2000-2D-III model), the wall in the local imperfection starts to undergo precipitous thinning while simultaneously the pressure drops sharply. This sharp drop is exactly associated with the onset of the non-axisymmetric bulge, as will be illustrated.

To better understand the events associated with the non-axisymmetric bulging, the reader is referred to Figures 4.13c and d. The first figure shows a view of the deformed

mesh at a point well past the sharp pressure drop, in the descending parts of the responses, with the color contours representing the current wall thickness (compare with corresponding experimental configurations in Fig. 3.7). The localized bulging is evident, as is the significant stretching and thinning of the elements spanning the imperfection. In the second figure, the localization of wall thinning is illustrated by plotting the reduction in wall thickness ($-\Delta t/t$) at two locations (A and B) against the mean circumferential strain at mid-span (same horizontal scale as Fig. 4.13a). Point A is located in the imperfection at $(x,\theta)=(0,\pi)$ whereas point B is located outside the imperfection at $(x,\theta)=(0.6L,\pi)$. Initially the thickness changes at a similar rate at the two points. Around a strain of 5% the two trajectories are already increasingly diverging, with the rate of thinning somewhat decelerating at point B. As the strain corresponding to the pressure maximum in Fig. 4.13a is approached, the rate of thinning at A is continuing to increase, while at B it is decelerating further. The kink on the response at A corresponds to the sharp downward trend in pressure in Fig. 4.13a at about 9% strain. The model does not include a rupture criterion and as a result the thickness at the crown point of the bulge is down to about 35% of its original value in the configuration of Fig. 4.13c. The material cannot sustain such large strains, and consequently rupture can be expected to take place in the very early parts of the descending response, as indeed occurred in the corresponding experimental response. The average strain at failure in the experiment was $\bar{\epsilon}_\theta = 7.5\%$ which compares favorably with $\bar{\epsilon}_\theta = 8.97\%$ from the calculation at the point where the precipitous localization commenced.

A similar calculation was performed using the constitutive model K-B_C, with the parameters listed in Table 4.2. The calculated $P - \bar{\epsilon}_\theta$ response is shown in Fig. 4.14 for the radial case $\alpha = -0.1$. The response is essentially identical to the one based on the K-B model, with the localization now occurring at the somewhat larger strain of

approximately $\bar{\epsilon}_\theta = 20\%$ instead of 19% for the reference K-B model. All other aspects of the simulation are essentially identical to those described above.

As stated earlier, the problems considered in this study remain essentially axisymmetric until the pressure maximum is reached, when non-axisymmetric localized bulging that precipitates wall thinning and rupture commences. In other words, in the latter part of the response in-plane shear cannot be precluded. At the same time, a certain amount of shear anisotropy was recorded in the pure shear test performed on a section of our tube (Fig. 3.4b), which for completeness should be incorporated in the constitutive model. This prompted the adoption of the K-B constitutive framework in our modeling efforts in the first place. The role of this shear anisotropy on the problem at hand was evaluated by running simulations of all experiments using the K-B model with and without the shear anisotropy (shear anisotropy is precluded when $\delta=1/\Gamma$ in Eq. (4.9)). Interestingly, in all cases the two simulations ended up being very close to each other. This is illustrated in Fig. 4.15, which shows the $P-\bar{\epsilon}_\theta$ responses from the two simulations for the loading case $\alpha=-0.1$ (K-B₁ does not include the shear anisotropy). Having reached the conclusion that the shear anisotropy does not influence the bursting response in any tangible manner, it became apparent that Hosford's principal stress anisotropic yield function could also serve the purposes of this class of problems. Included in Fig. 4.15 is the $P-\bar{\epsilon}_\theta$ response calculated with this constitutive model (H) using the anisotropy constants listed in Table 4.1. The response is very close to the two in which the K-B model was implemented, with the pressure maximum and the onset of localization being slightly delayed.

Figure 4.16 shows predictions for the radial loading case $\alpha = 1$. In the experiment, rupture was around the circumference (see Fig. 3.7) and as a result the FE model II with a circumferential imperfection at the plane of symmetry ($x=0$) was

adopted. Figure 4.16a shows the calculated engineering stress-average axial strain response ($\sigma_x - \bar{\epsilon}_x$) and Fig. 4.16b the $P - \bar{\epsilon}_\theta$ response, using this time only the Yld2000-2D-III model. The corresponding experimental results are included in both plots. Using the numerical results we evaluated $\bar{\epsilon}_x$ based on the change in length/original length using two different 0.5 in gage lengths (GL1 and GL2 shown in Fig. 4.12). GL1 starts at $x = 0$ so that it includes the imperfection. In this manner it is anticipated that it will capture the localized deformation expected to develop in the imperfection band. GL2 spans several elements immediately next to the imperfection and may not sense the localization. In each case, results from three locations, 0° , 90° and 180° from the position of the thinnest wall ($\theta = \pi$, see Eq. (4.16)), were then averaged to generate $\bar{\epsilon}_x$. The circumferential strain $\bar{\epsilon}_\theta$ was evaluated in the manner described earlier.

The axial responses are initially very close, following the experimental one quite well. Their small deviation is caused by the small difference in thickness in part of GL1. The responses attain a stress maximum at somewhat different strain levels, $\bar{\epsilon}_x = 9.63\%$ for GL2 and 10.67% for GL1. These values compare favorably with the 10.6% value recorded in the experiment by the 1-inch axial extensometer that was adjacent to the rupture zone. The circumferential response is seen to agree with the experimental one up to the limit load quite well.

The loading causes simultaneous circumferential expansion and axial stretching. In contrast to the “bottleneck” deformation of the tube seen in Fig. 4.13c for $\alpha = 0.9$ loading, in this case the radial fixity condition at $x = L$ results in the frustum-like deformed shape shown in Fig. 4.16c (compare these to the test specimens in Fig. 3.7). On reaching the axial stress maximum, deformation starts to localize in the imperfection band and its neighborhood. This is illustrated by the increasingly larger strain recorded by GL1. Concurrently, GL2 is registering unloading, something that is typical of localization

problems. At some point, the thinning becomes precipitous while the load is decreasing. The wall thinning is mainly axial but with a circumferential bias towards the initially thinner side. This bias results in loss of the essential axisymmetry (see Fig. 4.16c) that prevailed before the load maximum. As before, the model does not include a rupture criterion and as a result it is not possible to pinpoint the failure, but one can consider the strain regimes inside the construction ellipse (see Fig. 4.16a) to be reasonable estimates of rupture strains.

4.2.3 Cumulative Numerical Results for Radial Paths

Simulations were conducted for all nine radial and four corner path experiments performed, using subsequently all the constitutive models detailed in Section 4.1. The calculated limit loads and the resultant failure strains are influenced by the shape of the yield surface adopted, as it plays a decisive role in the induced strain path. In addition, they are influenced by the evolution of the yield surface, by the shape of the stress-strain response adopted, and by the amplitude of the imperfection introduced in the model. The stress-strain response adopted is the one measured in uniaxial tension tests on axial strips extracted from the tubes used in this study (true stress-logarithmic plastic strain version of the one shown in Fig. 3.4a). It is a fact that small changes in tangent modulus at higher strains can influence the calculation of the strains at which the limit load instabilities occur. In addition, since the uniaxial stress-strain curve needs to be extrapolated to be used in the numerical simulations, the way that this is performed affects the predictions drastically. We opted to use an extrapolated stress-strain curve that yielded close agreement with the experiments. The imperfection amplitude used was selected through a parametric study as the one that best represents actual thickness variations and other small imperfections unavoidably present in the test setup used. The complement of the results will now be presented in summary form.

Figures 4.17a and b show respectively the circumferential and axial engineering stress-strain responses calculated for each of the nine radial loading paths, using the K-B constitutive model. For the seven cases with $-0.2 \leq \alpha \leq 0.9$ the average circumferential strain ($\bar{\varepsilon}_\theta$) is based on the change in circumference/initial circumference at the symmetry plane $x = 0$ and the axial strain (ε_x) is based on the change in length of a 0.5 in gage length at $(x, \theta) = (0, \pi)$. For the cases with $\alpha = 1$ and 1.25 the circumferential strain is evaluated in the same manner but the axial strain is based on the average value of the change in length in three 0.5 in gage lengths located at $\theta = (0, \pi/2, \pi)$ and $x = 0$. All responses exhibit a limit load instability that leads to localized wall thinning and rupture. The onset of rupture is associated with the sharp downturn in the calculated responses, as explained in the previous section (see also Fig. 4.13). As was the case in the experiments, in seven cases rupture is axial and in two circumferential. The trends of the responses follow reasonably well those of the experimental results, while the quantitative comparison exposes some interesting differences (see below).

Figure 4.18 shows a plot of the engineering stress paths traced, with the simulations again performed with the K-B model. Since these were prescribed, they are identical to the corresponding experimental ones. Marked on the responses are the positions of the limit loads (●, at the end of each trajectory) and the corresponding experimental values (●). Also marked are the experimental (▲) and numerical (▲) points of rupture. The predicted limit load and rupture stresses with the K-B model are in very good agreement with the experiment.

A different perspective of the performance of the constitutive models can be obtained from Fig. 4.19, which shows plots of the engineering strain paths followed in the experiments and in the corresponding simulations using the Hosford (1979) model (presented in Section 4.1.1). Each path has been truncated at the pressure/load maximum.

The calculated paths follow the experimental ones quite well only for four paths, deviating from the experiments to a greater or lesser extent for the other five. The agreement is found to be particularly deficient for the $\alpha = 0.9$ and 1.0 cases. In other words, the main discrepancy is in the neighborhood of equibiaxial tension. In isotropic hardening plasticity, the high curvature of the yield surface in this regime (see Figs. 4.1 and 4.3) implies that even a small local deviation between the actual and fitted shapes can result in significant difference in the orientation of the local normal, with corresponding differences in the predicted strains. We believe that such differences are the main contributors for the strain path deviations for $\alpha = 0.9$ and 1.0 , as well as for the much milder disagreements observed for $\alpha = -0.1, 0$ and 0.25 .

The ends of the trajectories in Fig. 4.19 correspond to the load maximum that precipitates localization. With one exception (i.e. for $\alpha = 1.25$), the general trend is that the predicted limit loads occur at higher strains than in the experiments.

The calculated average strains at rupture, as defined above and using Hosford's (1979) model, are compared to the ones measured by the extensometers in the experiments in Fig. 4.20. Here the agreement is good for $\alpha = -0.2, -0.1, 0$ and 0.25 , deteriorating somewhat for $\alpha \geq 0.5$. The calculated results generally overpredict the experimental ones for $\alpha = 0, 0.25, 0.5, 0.75$ and 0.9 , and underpredict the failure strain for $\alpha = 1.25$. The case of $\alpha = 1$ presents some special interest, since it engages the yield surface in the region of its highest curvature. Hence, it is a rather difficult situation to achieve experimentally with accuracy and then to reproduce numerically. Despite this, the agreement of the predicted rupture strains with the experimental ones is not worse than for the rest of the radial paths.

The radial path experiments were subsequently simulated using the K-B yield function (see Section 4.1.2). The material is assumed to be isotropic in shear, since the

significant shear anisotropy present does not affect the failure predictions (Fig. 4.15). The agreement between the experimental and the predicted work contours is now only slightly better than with Hosford's model (compare Fig. 4.5 to Fig. 4.3). Thus the deficiency of the K-B model in the high curvature, equibiaxial tension region is still comparable to that of Hosford. As expected, this led to a similar overall behavior, shown in Figs. 4.21 and 4.22. The paths are slightly different from those in Fig. 4.19, being in some cases a bit closer to the measured paths while in others somewhat further apart. The strains at the limit loads and at the onset of failure were once more generally larger than the experimental values. As before, the strain paths for $\alpha = 0.9$ and 1.0 are not realistically predicted, which leads to poor estimations of the failure strains for these paths, as well. It is interesting to note however that the corresponding stresses at the limit load and at the onset of failure appear to be much less sensitive to details of the constitutive model employed (see Fig. 4.18).

These results clearly show that the two yield functions adopted are not capable of reproducing all the strain paths and consequently the failure strains recorded in the experiments. This deficiency is related to the small disagreements between the experimental and the predicted work contours, since it is the local normal to the yield surface that determines the amount of plastic deformation that can develop in the two directions (axial and hoop). This prompted the adoption of an even more powerful constitutive model, i.e. the one suggested by Barlat *et al.* and described in Section 4.1.3. As shown previously in Figs. 4.7 and 4.8, the added flexibility afforded by the 8 anisotropy parameters available in this model lead to a closer representation of the experimental contours than that of either Hosford (2 parameters) or K-B (4).

Three different calibration schemes of the Yld2000-2D model were attempted and are described in what follows. In the first case (I), in view of the experimentally observed

evolution of the plastic work contours, it was found convenient to choose the anisotropy variables from a subsequent contour, $W^P = 2$ ksi (13.8 MPa). The anisotropy parameters α_i are chosen for best fit of the experimental data and are given in Table 4.3a. The comparison of the resulting predicted work contour to the experimental one ($W^P = 2$ ksi -- 13.8 MPa) can be seen in Fig. 4.7 to be quite favorable, while the agreement is somewhat more adverse for other contours, but better than the corresponding results with the two previous models.

Figure 4.23 shows the calculated engineering strain paths, in each case truncated at the related limit load. By comparison to the corresponding results in Figs. 4.19 and 4.21, the paths are now uniformly much closer to the experimental ones, although the paths predicted for $\alpha = 0.9, 1.0$ and 1.25 continue to differ somewhat from the experimental ones. This improvement in performance can be linked to the better agreement between the calibrated and measured work contours, particularly true for the shapes, if not for the absolute values of the contours. Despite this improvement, the onset of limit states is further delayed and the corresponding strains (ends of trajectories) are much larger than the experimental ones. Consequently, the calculated onsets of rupture are similarly delayed as seen in Fig. 4.24 for the failure strains.

In a second attempt (Case II) the coefficients α_i are allowed to change with increasing plastic deformation (Plunkett *et al.*, 2006). This is done in order to also account for the experimentally observed deformation-induced anisotropy. The calibration was performed as follows. For six of the experimental work contours (9.2, 150, 500, 1000, 2000 and 3000 psi--63.5 kPa, 1.03, 3.45, 6.9, 13.8, 20.7 MPa) the anisotropy parameters were selected for best fit of each contour. The resulting α_i are given in Table 4.3b while the fitted contours were presented in Fig. 4.9, where it can be noted that the agreement to the experimental data is superior to that in Fig. 4.8.

In the FE implementation of this model, for each value of the plastic work the corresponding parameters are determined by linear interpolation between two neighboring contours. The calculated strain paths are compared to the measured ones in Fig. 4.25. The computed results in general follow the experiments with small deviations in the equibiaxial region. It is quite possible that additional data may be required in this high curvature area for further improvement of these predictions. It is interesting to observe that the results in Fig. 4.25 do not differ significantly from those of the previous calibration scheme (Fig. 4.23). This is partly due to the fact that the evolution of anisotropy is mild for this material, and partly due to the fitting of the previous case to a subsequent work contour rather than to the initial one. Unfortunately, the predicted limit states (ends of paths) are delayed essentially to the same extent as for the previous case. The same is true for the failure strains plotted with the corresponding experimental values in Fig. 4.26. This state of affairs confirms that matching of the work contours closely is not by itself sufficient to ensure accurate prediction of failure.

In an effort to understand the extent to which the calibrated yield functions used in the previous two cases need to be modified for the model predictions of the failure strains to approach the measured values, the following “hybrid” calibration approach was employed. The parameters given in Table 4.3b were considered as an initial guess for an iterative procedure where they were re-adjusted until an acceptable structural performance was achieved. The main structural performance criteria used were the loads and strains at which the limit load was attained. In Fig. 4.27, the axial (a) and circumferential (b) strains at the limit loads measured in the radial experiments are plotted as a function of the loading parameter α . Included are the corresponding values predicted using the two calibrations of Yld2000-2D described earlier (Cases I and II).

Both are seen to deviate from the experimental values by a certain degree. The two models also overpredict the corresponding limit pressures (P_{\max}) shown in Fig. 4.27c.

To improve this performance, the parameters were iteratively readjusted by performing a number of structural runs (using again the axisymmetric model), in each case modifying the anisotropy parameters α_i to approach the experimental data at the limit load. The values of α_i found to produce optimal overall results are given in Table 4.3c. The calculated strains and pressures that correspond to the limit loads are included in Fig. 4.27 as Case III and are seen to be in much better agreement with the experimental values than Cases I or II. Even though the predicted work contours of Case III shown in Fig. 4.10 now deviate somewhat from the experimental values, the induced strain paths shown in Fig. 4.28 are uniformly better predicted. Furthermore, the limit load states (ends of trajectories) are quite close to the actual ones. Indeed, they are much closer than any of the results described previously. This uniformly improved performance also carries over to the calculated failure strains, shown in Fig. 4.29. For completeness, the calculated and experimental engineering stress paths prescribed are shown in Fig. 4.30 for this case. Marked on the trajectories are the predicted stresses at the limit loads (\bullet) and at the onset of rupture (\blacktriangle) and the corresponding experimental values (red color). Both envelopes are seen to agree well with the experimental ones (compare this with the K-B predictions in Fig. 4.18).

It is interesting to observe that the work contours produced by this hybrid calibration scheme (Fig. 4.10) do not seem markedly different from those of Cases I and II (Figs. 4.8 and 4.9). However, the small shape changes introduced were sufficient to improve the predictions of failure. A detailed example of this improved performance was shown in Fig. 4.13 where the measured and calculated responses for the case with $\sigma_x = 0.9\sigma_\theta$ are compared. Included in the figure are the predictions obtained using the

K-B yield function. The first observation is that the Yld2000-2D-III responses are in better agreement with the measured ones than those yielded by K-B. The second is that the limit pressure and the onset of localized thinning are both attained at strains that are closer to the experimental values and simultaneously smaller than those of the K-B predictions. This carries over to most of the nine loading paths examined.

Clearly, the added flexibility provided by the 8 parameters of the Yld2000-2D model enables better fitting of the initial yielding and its evolution. This in turn is responsible for the overall better prediction of the strain paths compared to previously used models with fewer parameters. Nevertheless, this was not by itself sufficient for a corresponding improvement in the predicted rupture strains. A hybrid calibration procedure in which the yield function constants were also iteratively updated by monitoring the structural response had to be implemented for best overall performance. However, despite this procedure yielding very accurate predictions of failure, it is admittedly too cumbersome for implementation in more general settings.

4.2.4 Numerical Results for the Corner Paths

The FE models are now used to simulate the corner path experiments and their performance is evaluated by direct comparisons of the two sets of results. Since it was established in the previous section that the Yld2000-2D, Case III model gave the best predictions of failure, it will be used to generate all the results to be reported for the corner paths. Additional runs are subsequently performed in order to span more broadly the biaxial stress and strain spaces examined and help extract more general trends.

a. $x \rightarrow \theta$ Paths

We will discuss the main characteristics of the $x \rightarrow \theta$ path simulations by comparing experimental and predicted results from the 1.25 test. Figure 4.31 shows

comparisons of the measured and calculated axial and circumferential stresses and strains at mid-span. The prescribed stress path is included in Fig. 4.32 and the induced strain paths are compared to the experimental ones in Fig. 4.33. The first branch of this test involves pure uniaxial loading and as expected the numerical results replicate this exactly (see Fig. 4.31a). Figure 4.33 shows that the induced hoop strain follows a slightly different trajectory than the measured one, apparently because of some minor deficiency in the anisotropic yield function adopted in the neighborhood of the σ_x axis (this section of the stress space was not probed sufficiently in our original radial path tests used to calibrate the Yld2000 function -- see Fig. 4.7. This however, should not have a significant impact on the discussion that follows). Because of this small difference, the calculated $\sigma_\theta - \varepsilon_\theta$ response in Fig. 4.31b starts at a slightly smaller value of ε_θ but follows a similar trajectory to that of the experimental one. Indeed, the position of yielding is reproduced well as is the limited hardening that follows. The tube experiences some mild circumferential expansion but a limit load instability develops at a strain of about 1.5%, a value that is somewhat larger than the corresponding experimental one (see also Fig. 4.33). Beyond this point, the tube starts to develop some mild non-axisymmetric bulging that precipitates localized wall thinning in the axial groove. This is responsible for the sharp drop in pressure that is seen to occur at a strain of about 2.4%. As was done in the radial paths, we identify this point with the onset of rupture. The increasing circumferential strain in the descending part of the response, drawn in dashed line, is driven by the localizing deformation in the grooved zone illustrated in the similarly deformed configuration shown in Fig. 4.13c. In other words, the axial rupture observed in the corresponding experiment is reproduced by the model. The stresses and strains at the limit load and at rupture are listed in Table 4.4 and are marked in Figs. 4.32 and 4.33 with red bullets (●, ▲). It is important to note that the limit and rupture stresses are both close

to the experimental ones (see Table 3.2b and blue bullets -- ●, ▲ -- in Fig. 4.32). In other words, the analysis reproduces the path-dependence of the failure stresses observed in the experiment quite faithfully.

The other two $x \rightarrow \theta$ path experiments (0.75 and 0.9) were simulated in a similar fashion. The prescribed stress paths are included in Fig. 4.32, the induced strain paths in Fig. 4.33 while the $\sigma_x - \varepsilon_x$ and $\sigma_\theta - \varepsilon_\theta$ trajectories appear in Figs. 4.34a and 4.34b respectively. The general trends of the predictions follow those of the experimental results. Both cases ruptured along a generator, which is in agreement with the experiments. The delay in yielding during the pressurization phase of the response observed in the experiments is reproduced by the simulations. So also is the relatively low rate of hardening of the inelastic part of this branch. Consequently, the stresses at the limit loads and at the points of rupture are in close agreement with the measured values (see Tables 3.2b and 4.4 and Fig. 4.32). Furthermore, both the experimental and numerical results indicate that re-yielding in the circumferential direction is delayed until a stress level develops that approximately corresponds to the maximum value reached during the axial stressing phase of the path. This “delayed” re-yielding is at least partly responsible for the much higher failure stresses of the $x \rightarrow \theta$ paths compared to the corresponding radial ones.

Incidentally, we observe that since our calculations are based on pure isotropic hardening plasticity, the level of agreement between the measured and calculated stress-strain trajectories achieved in these simulations would indicate that for this particular Al alloy isotropic hardening must be dominant. This is said realizing that any deformation-induced shape changes of the yield surface, such as those purported to take place in the direction of loading, that may affect other performance criteria of the model (e.g., the onset of instability), are obviously not accounted for by this constitutive model.

The calculated strain paths are seen in Fig. 4.33 to follow the experimental ones quite well. However, as was the case for the 1.25 experiment, both the onset of the limit loads and the points of rupture are delayed somewhat compared to the experiments. It is reasonable to assume that this disagreement may be related to local changes in the yield surface shape not captured by our isotropic hardening plasticity model. This is suggested despite the deformation-induced adjustment of the anisotropy and the additional corrections to the yield functions described earlier (see Section 4.2.3), as such effects are most probably path dependent.

In summary then, the performance of the $x \rightarrow \theta$ path simulations and of the constitutive model as calibrated can be declared quite satisfactory as they support both qualitatively and quantitatively the experimental observations that for this type of corner paths the strains are strongly path dependent and the stresses of the limit states can also be so, especially as the prestrain increases.

For completeness, two additional pairs of cases were run numerically and will be discussed: R1.75 and R0.5 along with the corresponding $x \rightarrow \theta$ paths. The results from the $x \rightarrow \theta$ cases are included in Figs. 4.32-4.34. Both sets of results fall in line with the other three cases. Thus, for 1.75 the axial strain induced in the first branch of the path is larger than for 1.25 as is the corresponding contraction of the circumference (Fig. 4.33). A similar delay in yielding observed for the other cases during the pressurization phase of the path is seen to take place again (Fig. 4.34). The specimen develops a limit load instability close to 1% average ε_θ and ruptures along a generator. The stress and strain trajectories are compared to those of the corresponding radial path in Figs. 4.35 and 4.36. Once again a very significant difference between the limit and failure stresses from the two paths is observed in Fig. 4.35. Interestingly, Fig. 4.36 shows that R1.75 induced a nearly pure axial straining that led to circumferential rupture at $(\varepsilon_{xf}, \varepsilon_{\theta f})$ of (9.19%, 0)

(see Table 4.4). These values compare with $(\varepsilon_{xf}, \varepsilon_{\theta f})$ of (11.7%, 1.91%) for the $x \rightarrow \theta$ path. In other words, in the radial path rupture occurs at smaller strains reversing the trend seen in the other cases (0.75, 0.9 and 1.25).

The case of $x \rightarrow \theta$ 0.5 develops no plastic strain during the axial phase of the path. Furthermore, this path engages the yield surface in the zone of relatively small curvature (see Fig. 4.10) as does the corresponding R path. (We note that experimental results for R0.5 presented in Section 4.2.3 are in good agreement with the present simulation). Consequently, during the pressurization phase an essentially purely hoop strain trajectory is traced that is nearly congruent to that of the R path (Fig. 4.36). The values of the limit and rupture strains from the two cases are also almost coincident, which indicates that the strain path plays a decisive role in influencing rupture. The corresponding stress values from the two paths (Fig. 4.35 and Table 4.4) differ slightly but the difference is by far the smallest amongst the five cases compared in this set.

b. $\theta \rightarrow x$ Paths

The $\theta \rightarrow x$ 1.25 experiment was also simulated numerically and the induced stress and strain paths are included in Figs. 4.32, 4.33, 4.35 and 4.36. In addition, the axial and circumferential stress-strain results are compared to the corresponding measurements in Fig. 4.37. The calculated stress-strain paths are very close to those measured. The end of the experimental strain path in Fig. 4.33 represents the point at which the specimen failed prematurely at the grips. In the simulation, rupture was circumferential and occurred at strains that are slightly lower than those of the end of the experimental trajectory. From this we conclude that in the experiment the tube must have been very close to rupture before the test was terminated by end-failure. The deformed configuration, illustrating circumferential localization at mid-span of the specimen is similar to that shown in Fig. 4.16c. The stresses at rupture in the simulation are seen in

Fig. 4.32 to be in good agreement to those of the experiment also. Included in Figs. 4.35 and 4.36 are the stress and strain paths for the corresponding R path. The critical stresses of the $\theta \rightarrow x$ path are close to those of the R path but the strains differ considerably (as indeed was also the case in the experimental results in Figs. 3.15 and 3.16).

One additional pair of cases was run numerically comparing R1.75 and the corresponding $\theta \rightarrow x$ path. The calculated stress and strain paths are compared in Figs. 4.35 and 4.36 while the axial and circumferential stress-strain responses for the $\theta \rightarrow x$ run are included in Fig. 4.37. This particular radial path results in almost no plastic hoop strain and consequently the strain path is along the ε_x axis or, in other words, plastic deformation is essentially limited to the axial direction. The axial response develops a limit load at a strain of 8.87% and ruptures circumferentially at a strain of 9.19%. These values are of course significantly smaller than the failure strains for the 1.75 $x \rightarrow \theta$ path included in Figs. 4.35 and 4.36 as are the failure stresses.

Interestingly, the $\theta \rightarrow x$ path induces a strain trajectory that is very similar to that of the R path. Apparently, despite the different stresses the model develops very limited plastic circumferential deformation during the pressurization phase. During the σ_x branch of the path the material is initially elastic and plastic deformation, when it occurs, is limited to the axial strain. The axial response develops a limit load at $\varepsilon_{xL} = 8.63\%$ and ruptures circumferentially at a strain of 8.91%. Both of these values are very close to those of the R1.75 path while the maximum axial stress achieved is slightly higher than that of the R path. This supports once more the premise that the strain path is a major factor in deciding rupture. Surprisingly, the two rupture strains are also very close to the corresponding ε_θ values of the R0.5 and $x \rightarrow \theta$ 0.5 paths, which ruptured along a generator. In other words, despite the difference in the mode of rupture, the critical strains in the two pairs of calculations are similar.

Finally, it is also worth noting the significant difference between the critical stress levels of the 1.25 and 1.75 $\theta \rightarrow x$ and $x \rightarrow \theta$ paths observed in Fig. 4.35. As mentioned above, the critical stresses of the former paths are close to those of the R paths while the ones for the $x \rightarrow \theta$ paths are significantly higher. One contributor to this difference may be the fact that the stress levels of the initial σ_θ branches of the $\theta \rightarrow x$ paths are significantly lower than the axial stresses achieved during the σ_x branches of the $x \rightarrow \theta$ paths. Consequently, the induced σ_θ stresses did not cause significant expansion of the yield surfaces whereas, as observed earlier, the σ_x branches did. Accordingly, during the axial stressing branches of the $\theta \rightarrow x$ paths plastic deformation recommences earlier and apparently this also leads to failure at lower stresses levels.

Table 4.1 Anisotropy variables for the Hosford 1979 model

Model	$2k$	S_r	S_θ
H	8	1.01	1.04

Table 4.2 Anisotropy variables for two K-B models

Model	c	$2k$	Γ	α_1	α_2	δ
K-B	0	8	0.680	0.94	0.97	1.249
K-B _c	0.8	24	0.6665	0.96	0.99	1.287

Table 4.3a Anisotropy parameters for Yld2000-2D, Case I ($k=8$)

W^p	α_1	α_2	α_3	α_4	α_5	α_6	α_7	α_8
2 ksi	0.78	1.15	0.85	0.89	1.06	1.03	1.0	1.0

Table 4.3b Anisotropy parameters for Yld2000-2D, Case II ($k=8$)

W^p	α_1	α_2	α_3	α_4	α_5	α_6	α_7	α_8
9.2 psi	0.88	1.15	0.87	0.91	1.03	1.01	1.0	1.0
150 psi	0.8	1.15	0.92	0.88	1.05	1.03	1.0	1.0
500 psi	0.83	1.12	0.85	0.87	1.05	1.03	1.0	1.0
1 ksi	0.83	1.15	0.85	0.88	1.05	1.03	1.0	1.0
2 ksi	0.78	1.15	0.85	0.89	1.06	1.03	1.0	1.0
3 ksi	0.74	1.18	0.85	0.89	1.06	1.03	1.0	1.0

Table 4.3c Anisotropy parameters for Yld2000-2D, Case III ($k=8$)

W^p	α_1	α_2	α_3	α_4	α_5	α_6	α_7	α_8
9.2 psi	0.917	1.066	0.92	0.935	1.018	0.993	1.0	1.0
150 psi	0.87	1.066	0.92	0.91	1.05	1.03	1.0	1.0
500 psi	0.87	1.066	0.85	0.92	1.05	1.03	1.0	1.0
1 ksi	0.88	1.066	0.91	0.91	1.035	1.01	1.0	1.0
2 ksi	0.88	1.066	0.94	0.94	1.04	1.01	1.0	1.0
3 ksi	0.88	1.05	0.92	0.97	1.05	1.06	1.0	1.0

Table 4.4 Summary of radial and corner path results from numerical simulation. Included are the stresses and strains at the limit load instability and at failure, and the mode of failure (A: axial, and C: circumferential rupture)

R α	$x \rightarrow \theta$	$\theta \rightarrow x$	$\sigma_{\theta \max}$ ksi	$\sigma_x _{\sigma_{\theta \max}}$ ksi	$\sigma_{\theta} _{\sigma_{x \max}}$ ksi	$\sigma_{x \max}$ ksi	$\sigma_{\theta f}$ ksi	$\sigma_{x f}$ ksi	$\varepsilon_{\theta L}$ (%)	$\varepsilon_{x L}$ (%)	$\varepsilon_{\theta f}$ (%)	$\varepsilon_{x f}$ (%)	Mode of failure
0.5	-	-	34.12	17.08	-	-	33.57	16.81	8.55	-0.14	9.03	-0.34	A
-	0.5	-	35.65	16.56	-	-	34.76	16.56	8.63	-0.18	9.20	-0.34	A
0.75	-	-	33.84	25.42	-	-	33.57	25.28	7.91	1.89	8.72	2.05	A
-	0.75	-	36.55	25.51	-	-	36.12	25.51	4.77	3.41	4.93	3.37	A
0.9	-	-	33.15	29.86	-	-	33.00	29.72	7.91	6.78	8.83	7.15	A
-	0.9	-	37.21	29.67	-	-	36.55	29.67	2.76	7.49	3.08	7.54	A
1.25	-	-	-	-	26.04	32.50	25.21	31.53	1.11	13.44	1.23	14.35	C
-	1.25	-	38.20	31.85	-	-	38.20	31.88	1.47	10.00	2.36	10.36	A
-	-	1.25	-	-	25.34	33.27	25.34	31.61	3.39	4.62	3.51	4.93	C
1.75	-	-	-	-	18.72	32.56	18.05	31.44	0.10	8.87	0.10	9.19	C
-	1.75	-	37.66	32.11	-	-	37.10	32.11	0.55	10.97	1.91	11.70	A
-	-	1.75	-	-	18.49	33.89	18.49	31.89	0.26	8.63	0.26	8.91	C

1 ksi = 6.897 MPa.

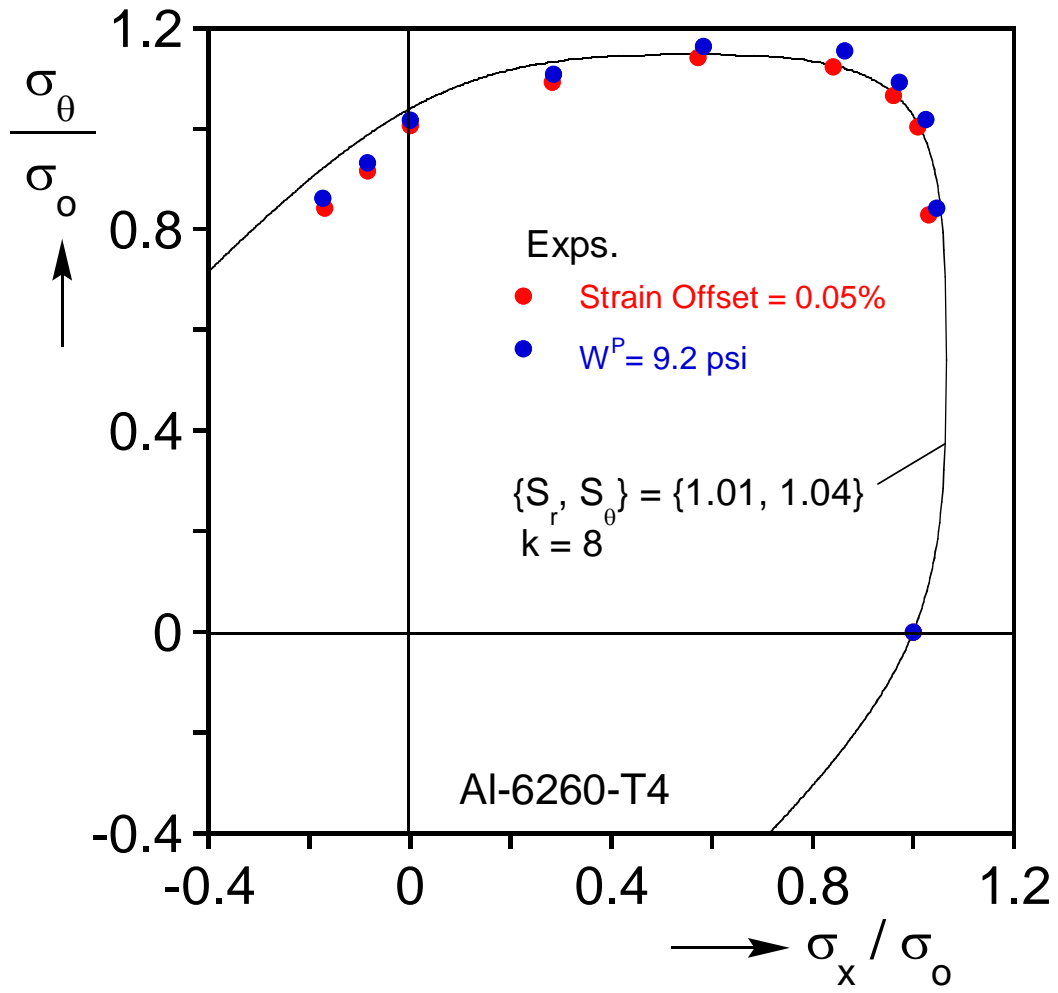


Fig. 4.1 – Experimental data representing the initial yield surface according to two different definitions of yielding and Hosford’s anisotropic yield function.

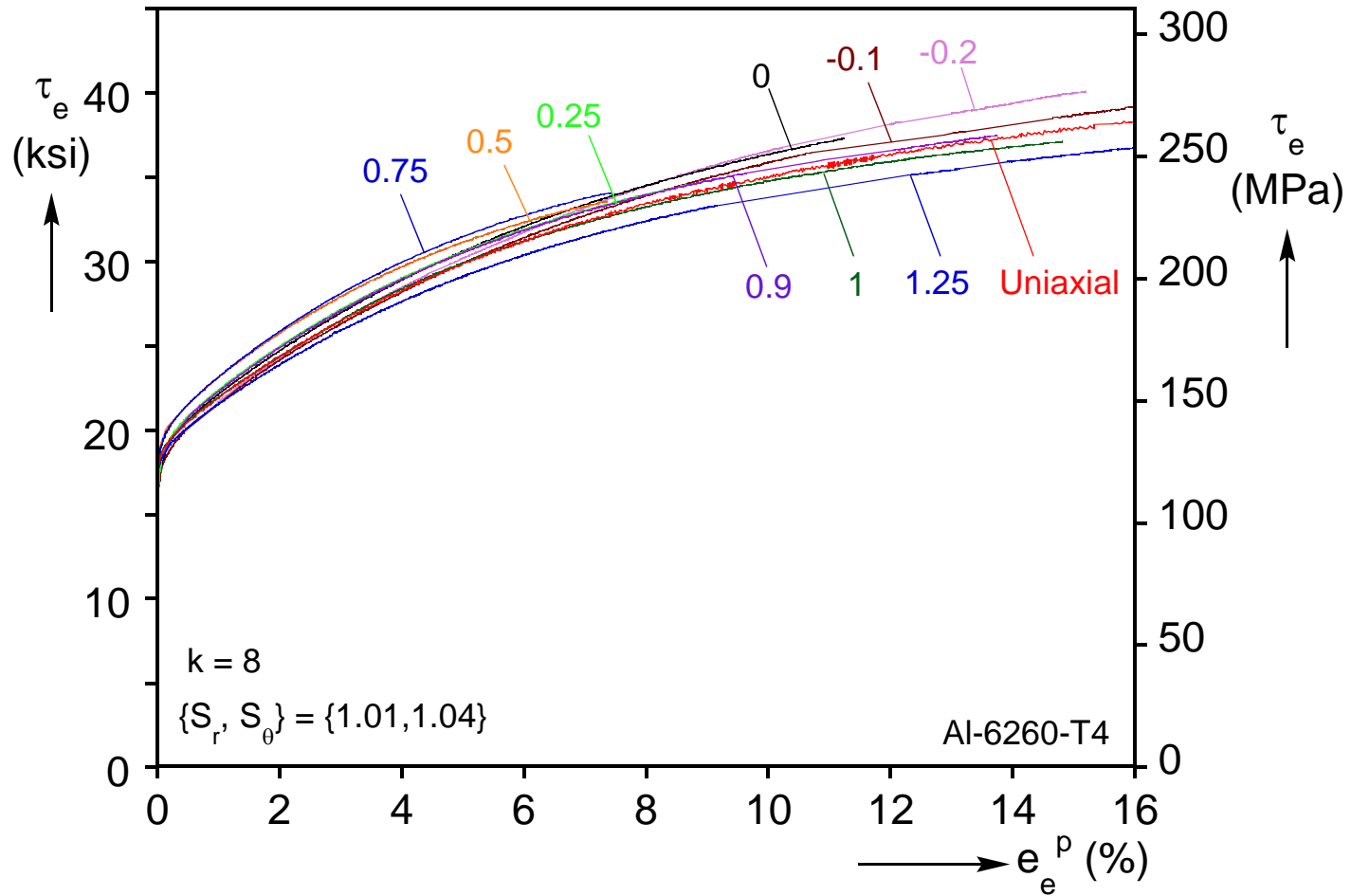


Fig. 4.2 – Experimental data presented in the form of equivalent true stress vs. the work conjugate equivalent logarithmic plastic strain based on Hosford's anisotropic yield function.

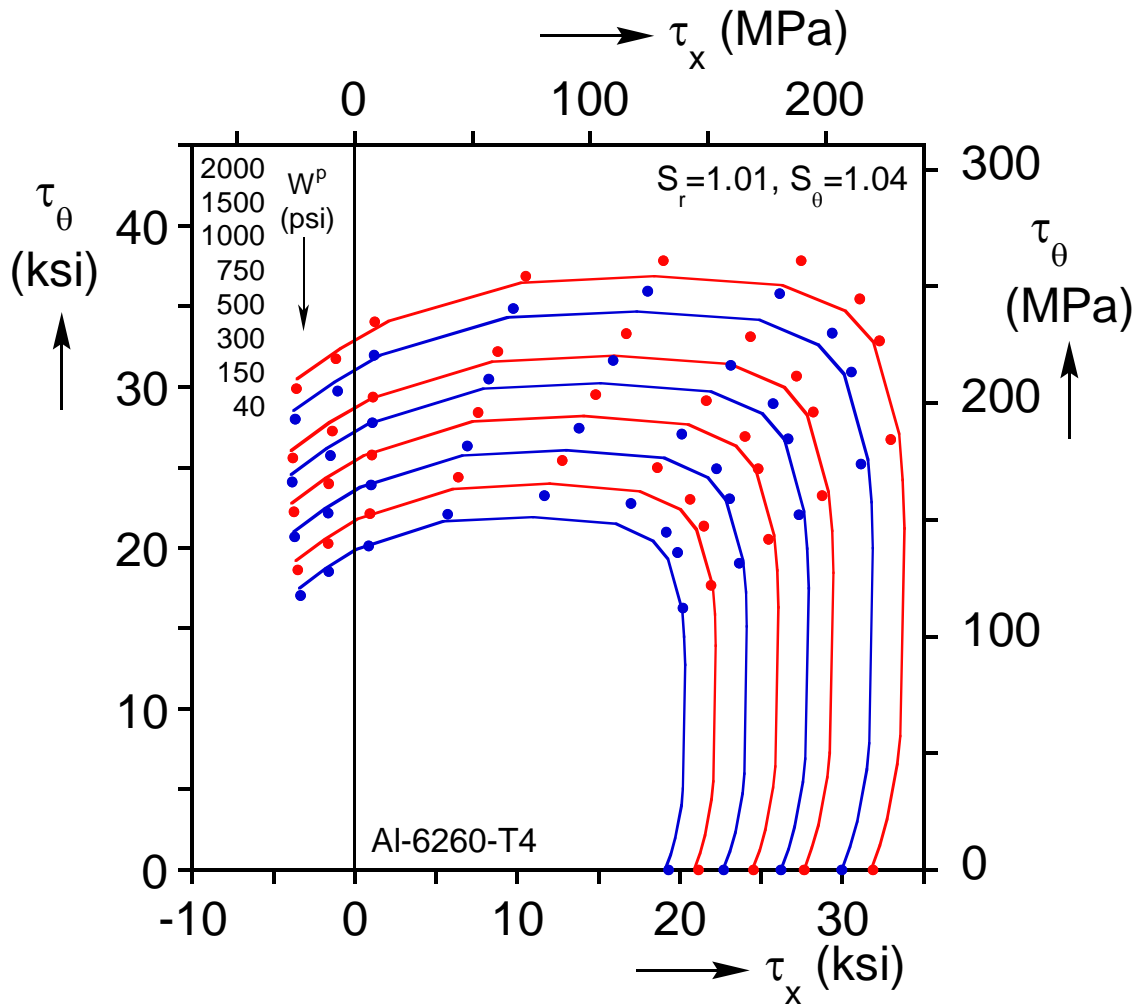


Fig. 4.3 – Loci of experimental points representing various levels of constant plastic work and corresponding contours based on Hosford's anisotropic yield function.

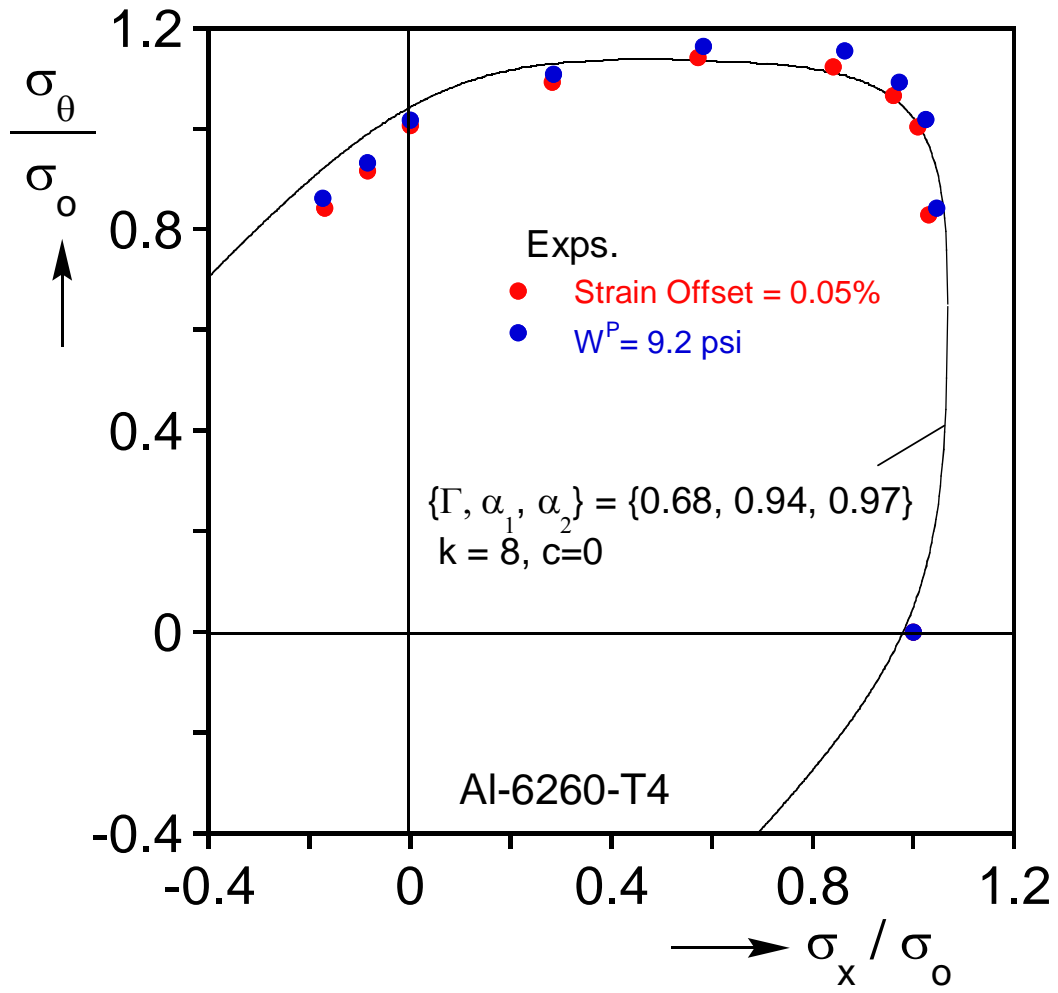


Fig. 4.4 – Experimental data representing the initial yield surface according to two different definitions of yielding and Karafillis – Boyce yield function.

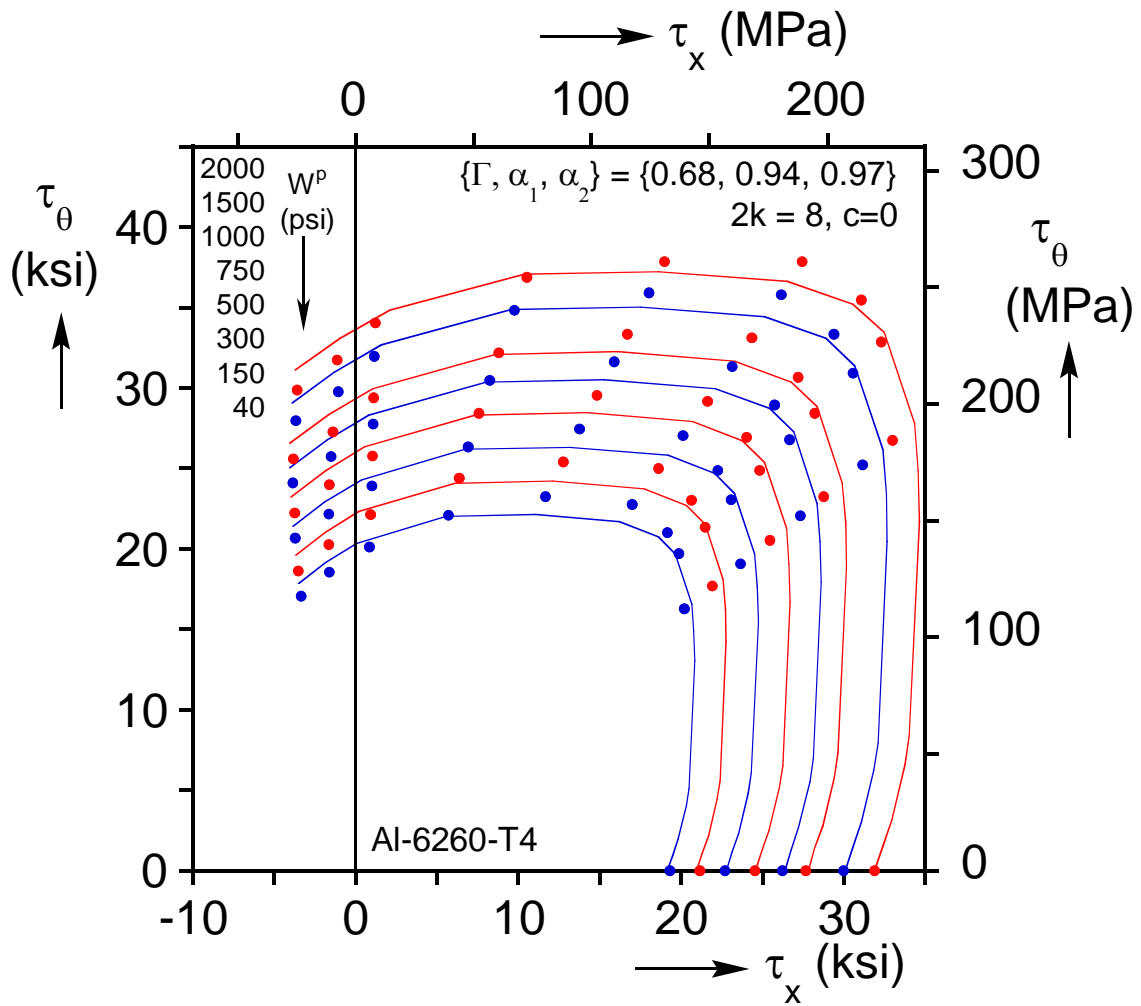


Fig. 4.5 – Loci of experimental points representing various levels of constant plastic work and corresponding contours based on Karafillis - Boyce anisotropic yield function.

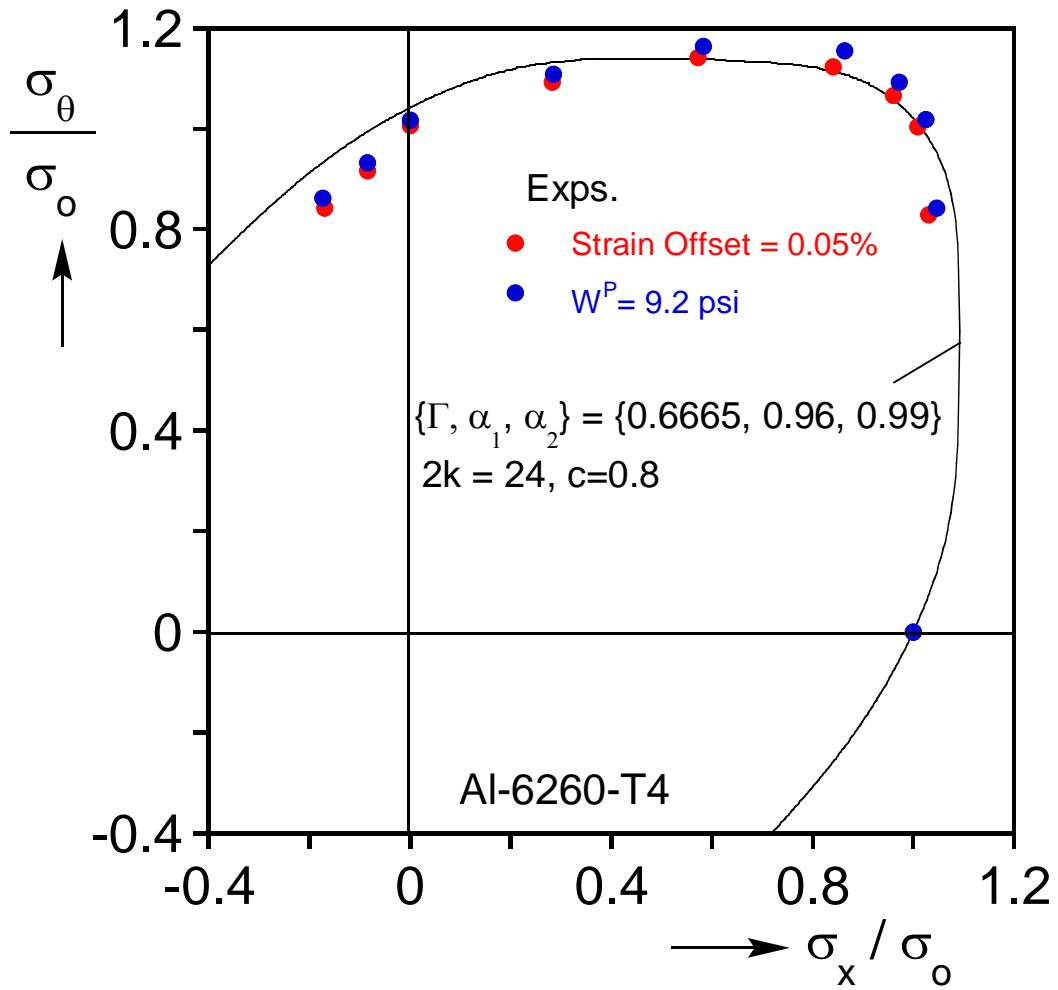


Fig. 4.6 – Experimental data representing the initial yield surface according to two different definitions of yielding and the weighted Karafillis – Boyce yield function.

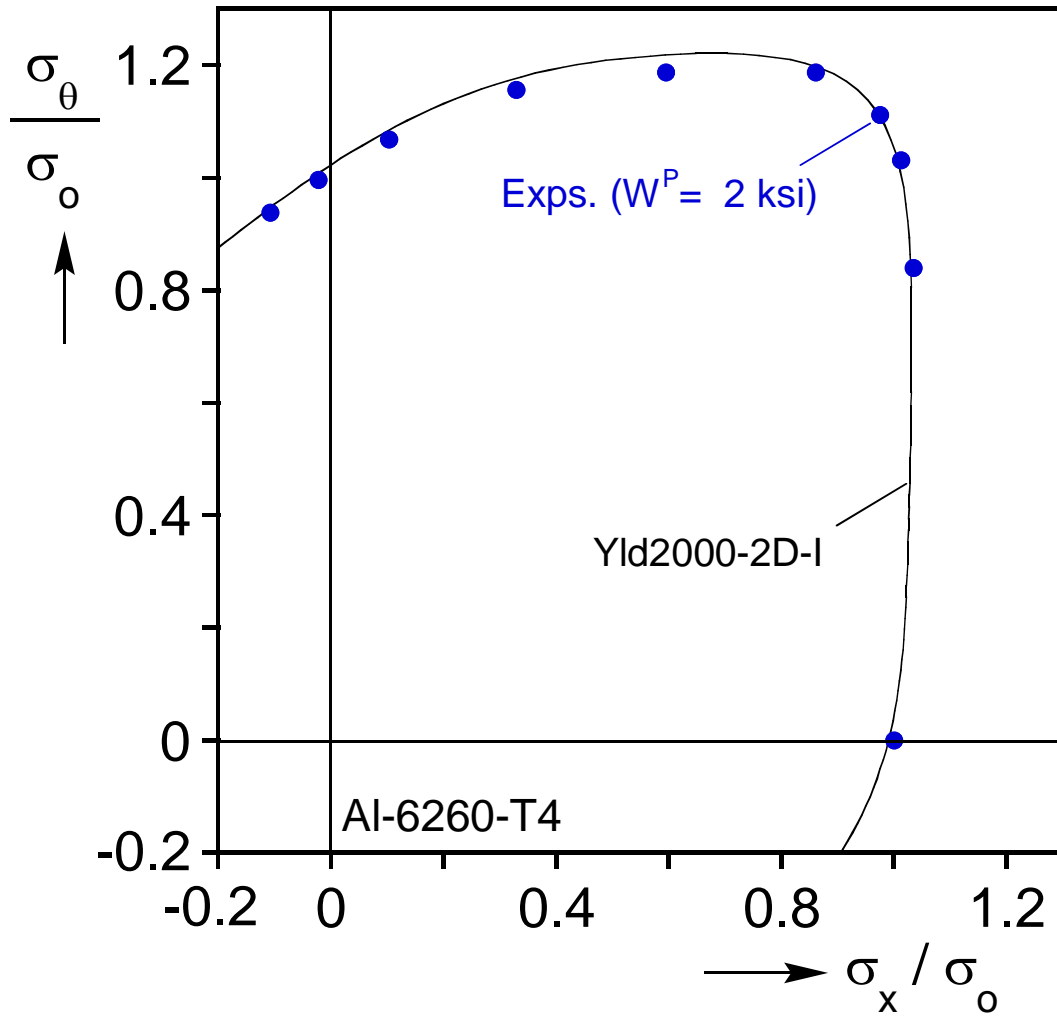


Fig. 4.7 – Experimental data representing the 2 ksi (13.8 MPa) work contour and the Yld2000-2D yield function, Case I.

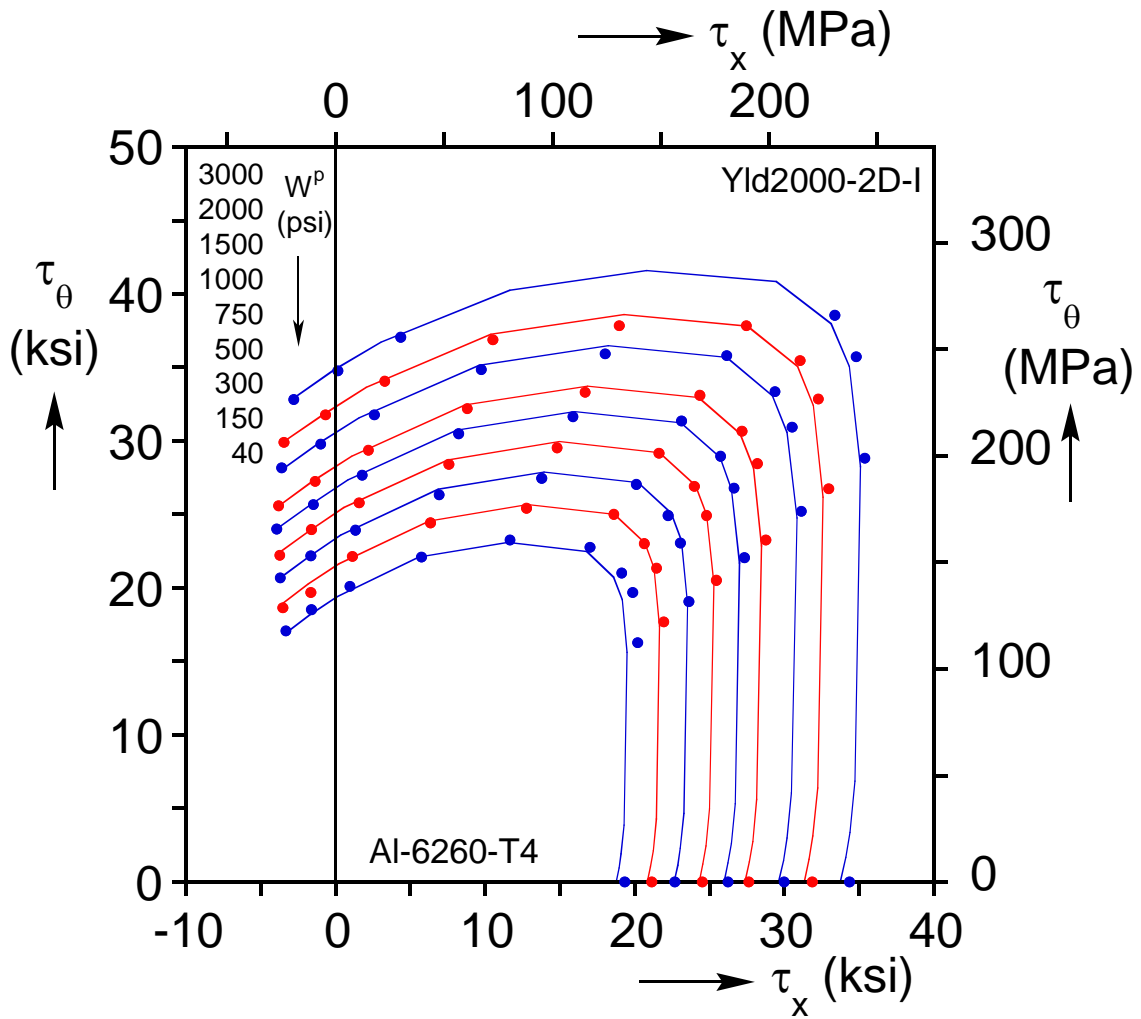


Fig. 4.8 – Loci of experimental points representing various levels of constant plastic work and corresponding contours based on the Yld2000-2D yield function Case I.

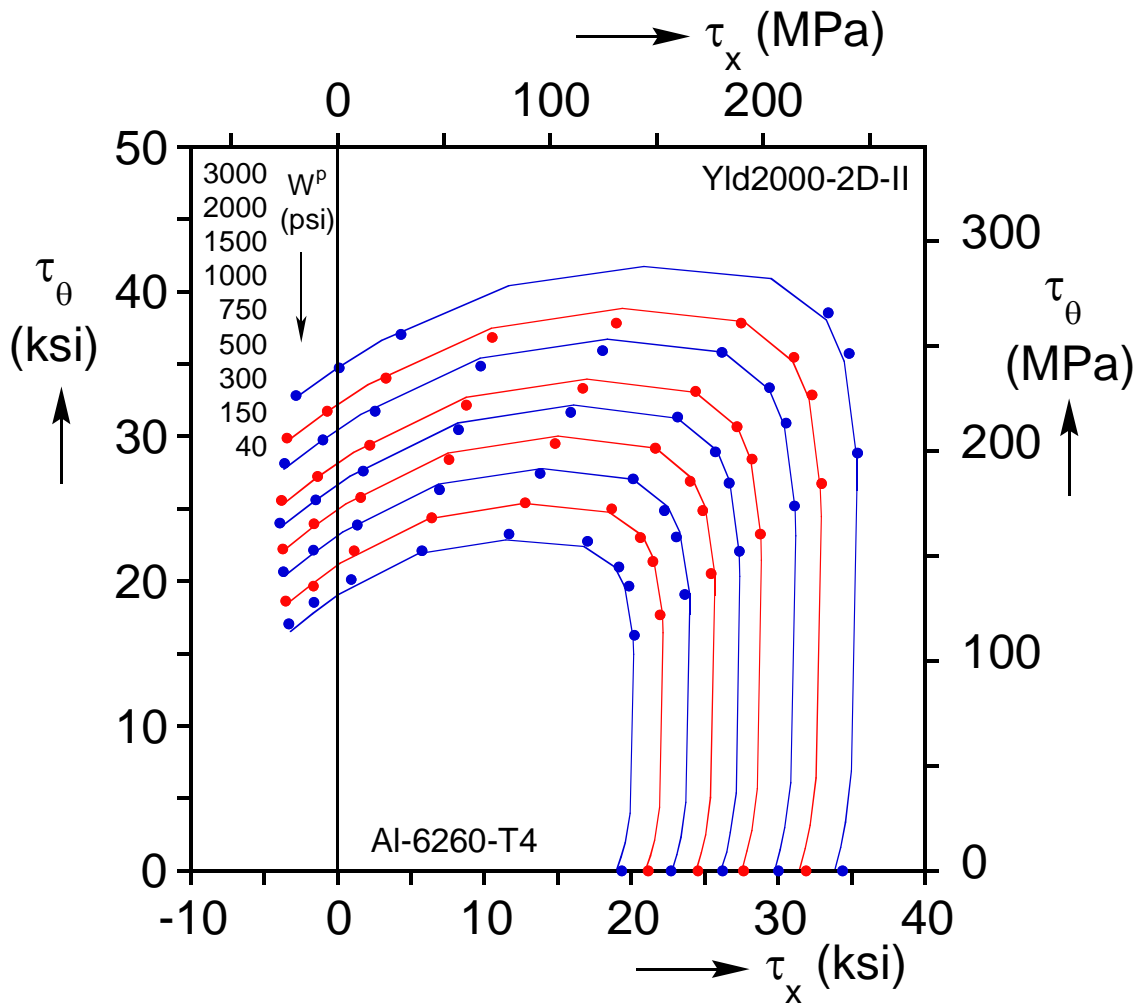


Fig. 4.9 – Loci of experimental points representing various levels of constant plastic work and corresponding contours based on the Yld2000-2D yield function Case II.

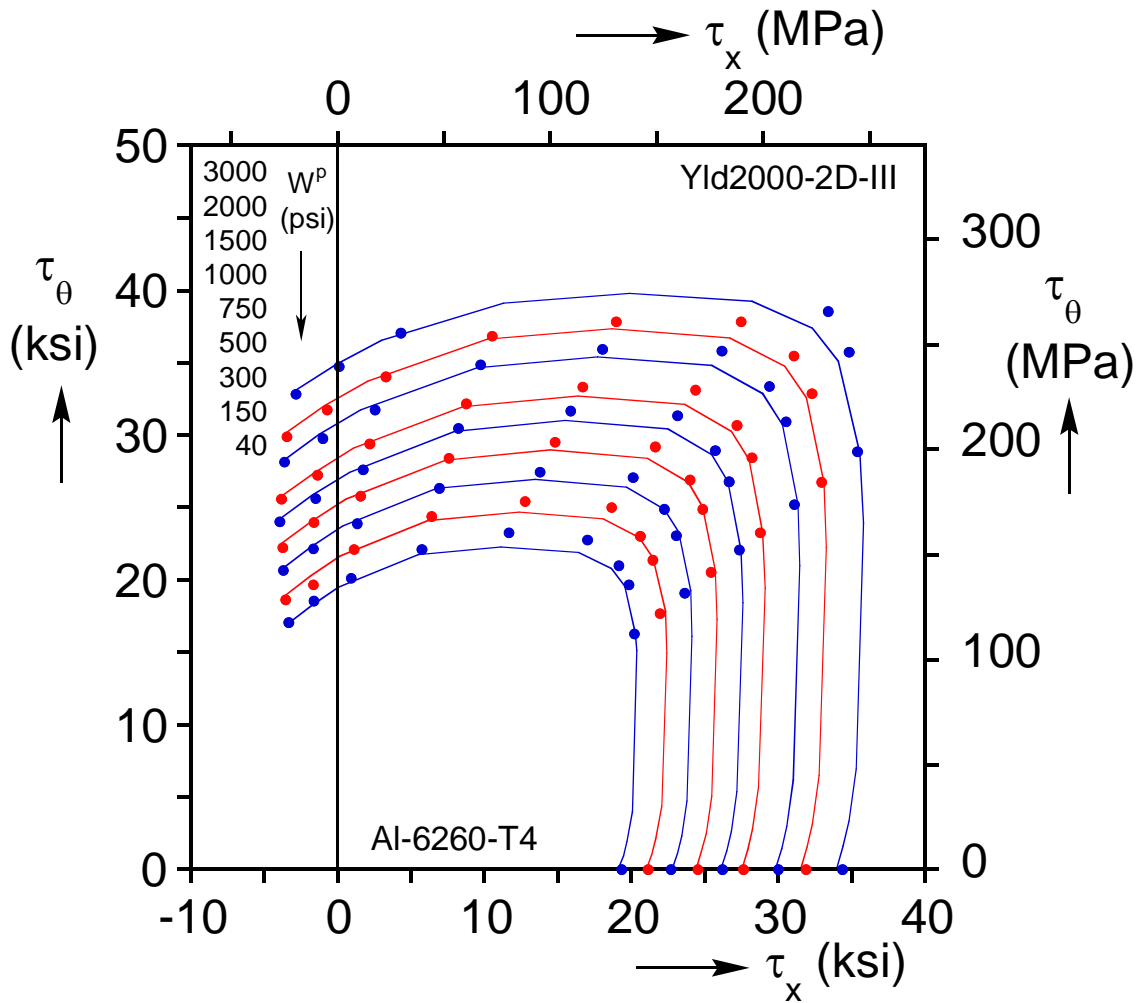


Fig. 4.10 – Loci of experimental points representing various levels of constant plastic work and corresponding contours based on the Yld2000-2D yield function Case III.

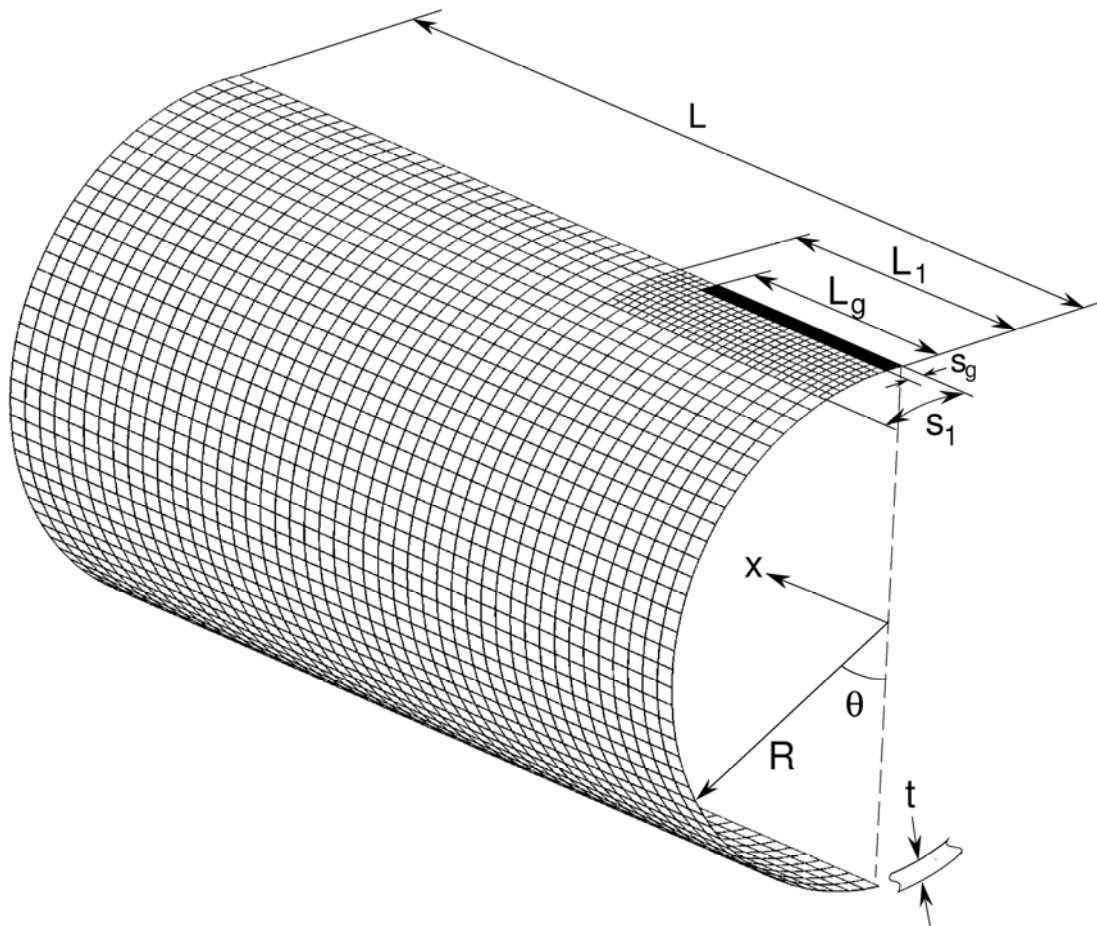


Fig. 4.11 – Model geometry and FE mesh for cases that rupture in the axial direction.

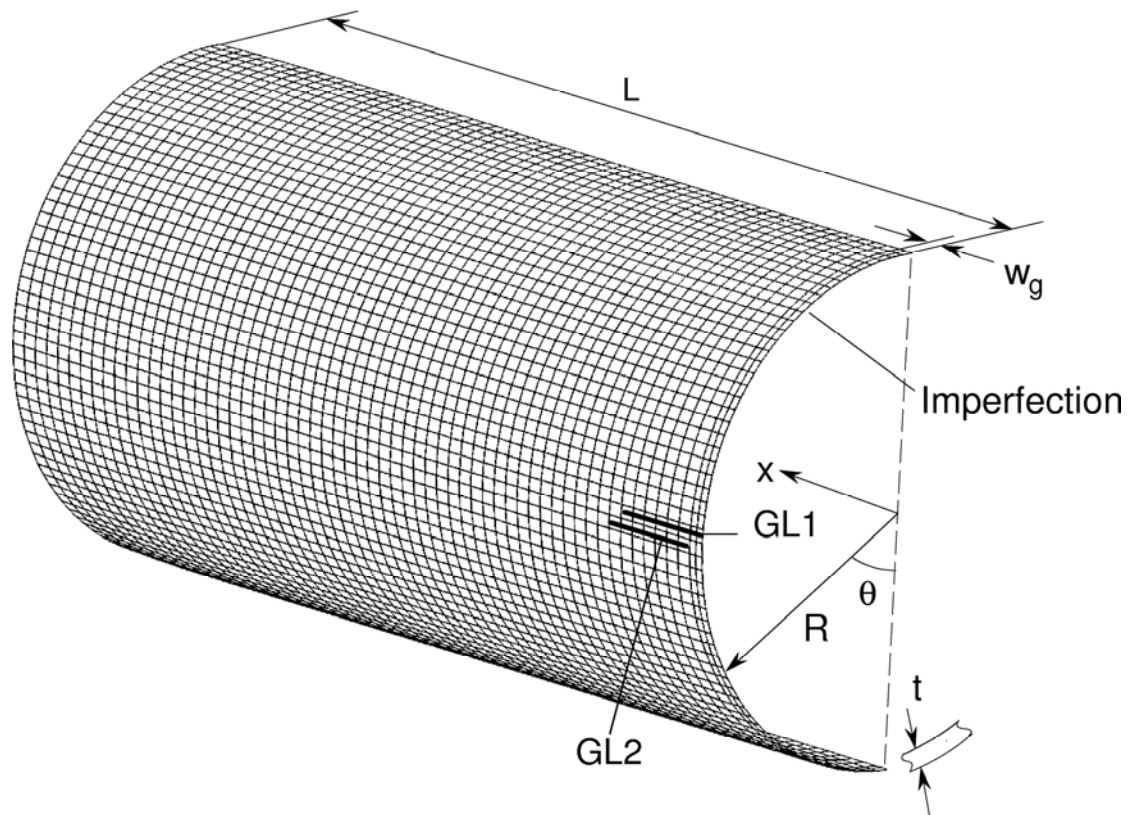
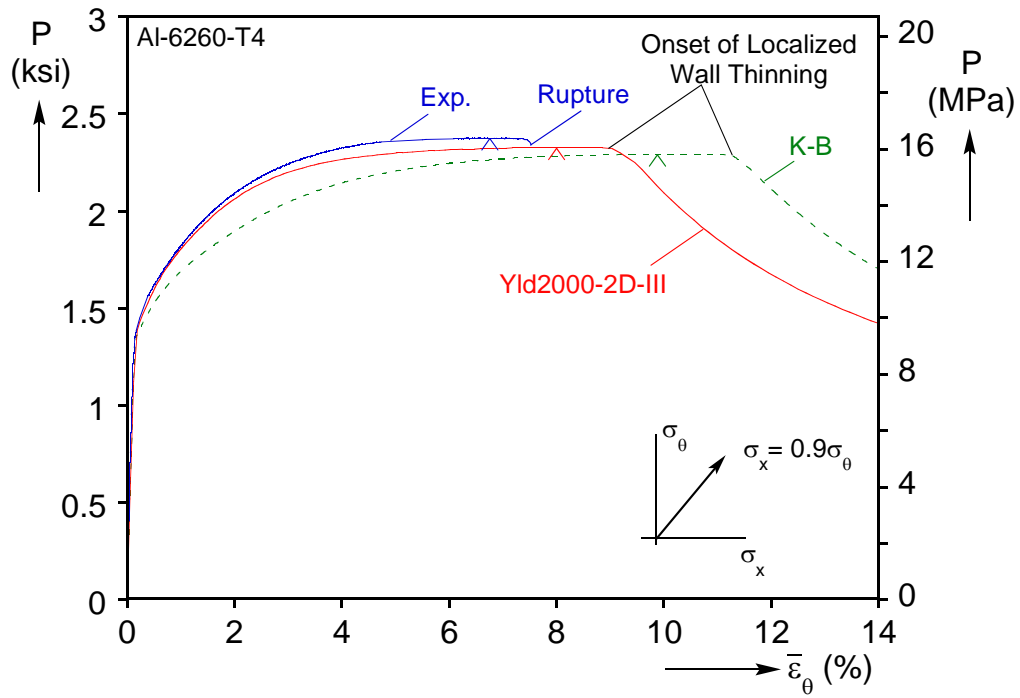
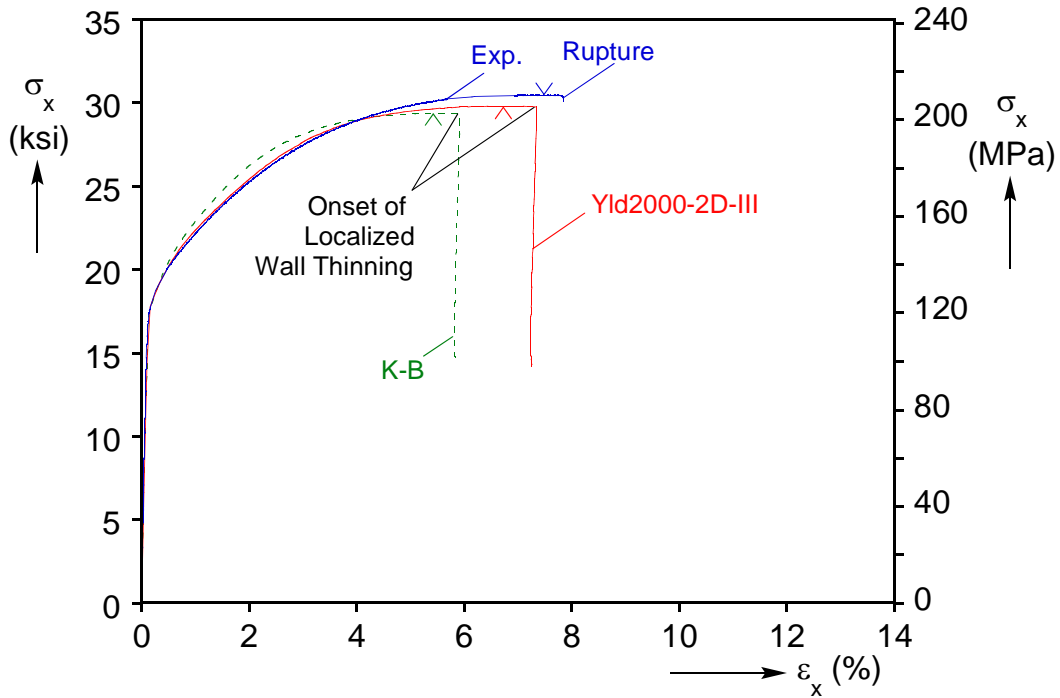


Fig. 4.12 – Model geometry and FE mesh for cases that rupture in the circumferential direction.

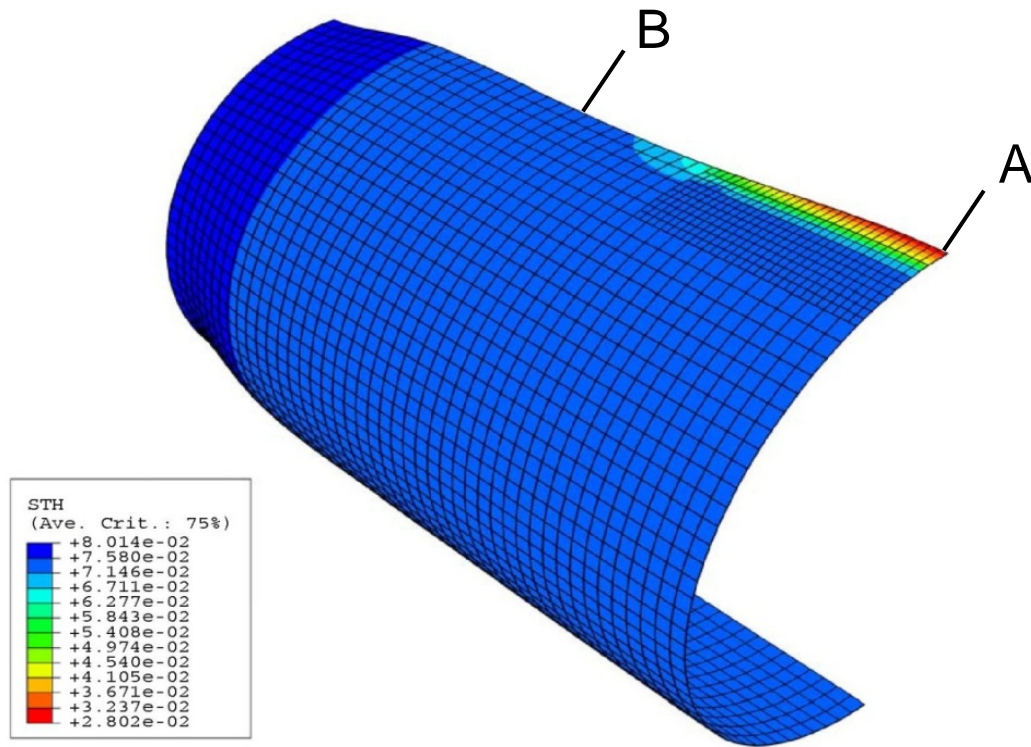


(a)

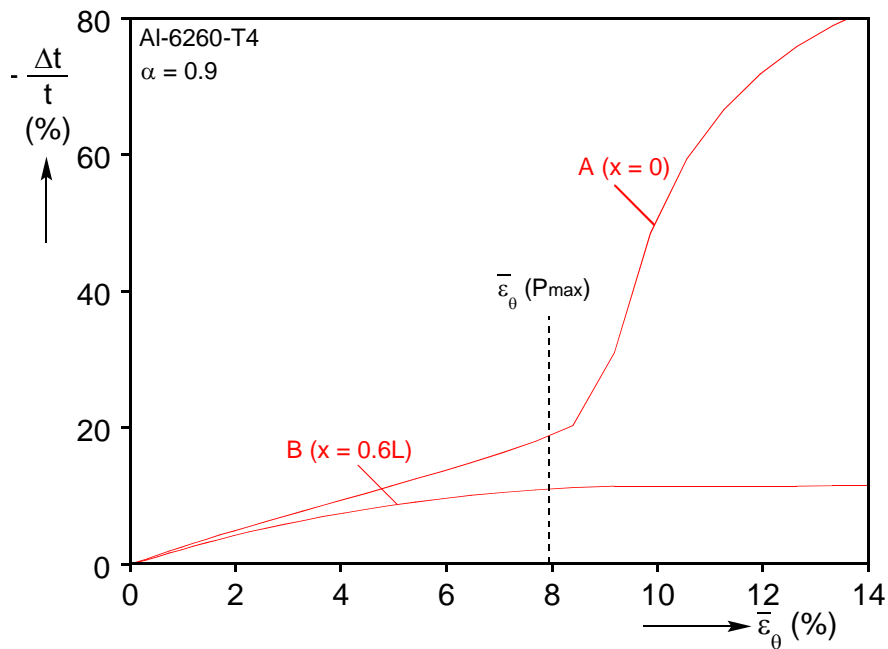


(b)

Fig. 4.13 – Results from numerical simulation of $\alpha = 0.9$ path using two plasticity models, and the corresponding experimental responses. (a) $P - \bar{\epsilon}_\theta$ and (b) $\sigma_x - \epsilon_x$.



(c)



(d)

Fig. 4.13 (cont'd) – (c) Model deformed configuration just after the onset of localization (K-B) and (d) calculated wall thinning at two locations, from Yld2000-2D, Case III.

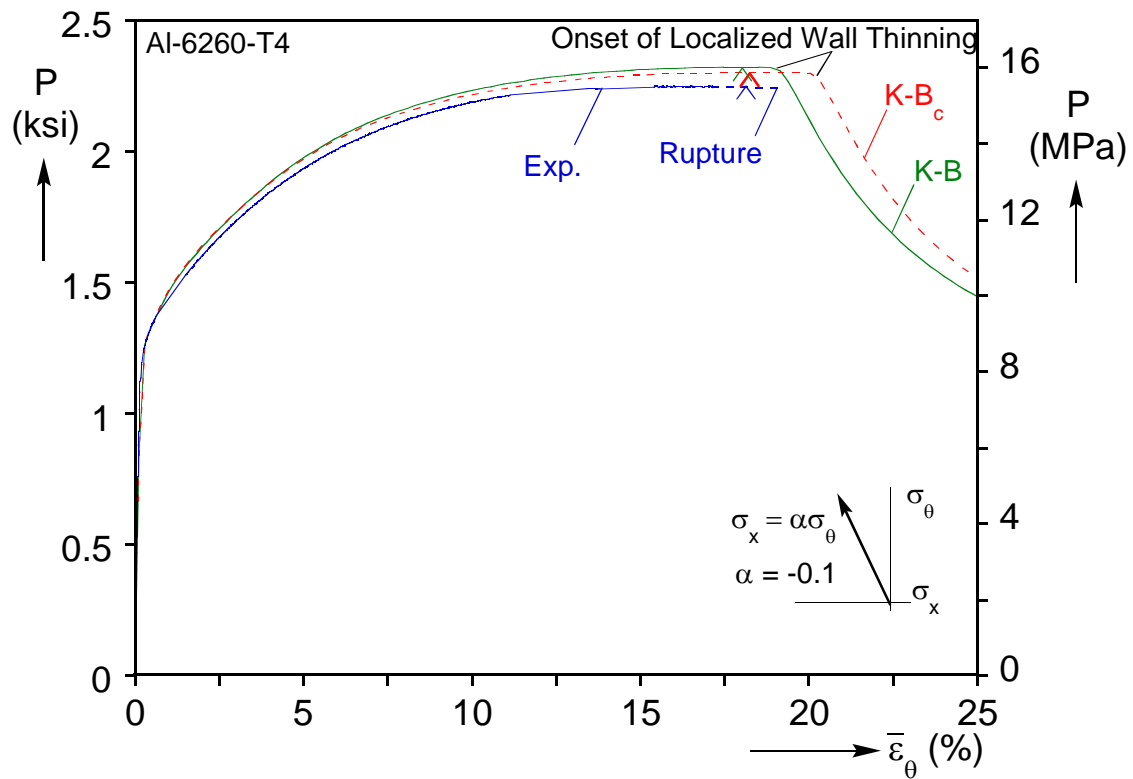


Fig. 4.14 – Comparison of $P - \bar{\epsilon}_\theta$ responses calculated using two Karafillis – Boyce models (reference, K-B, and weighted, K-B_c).

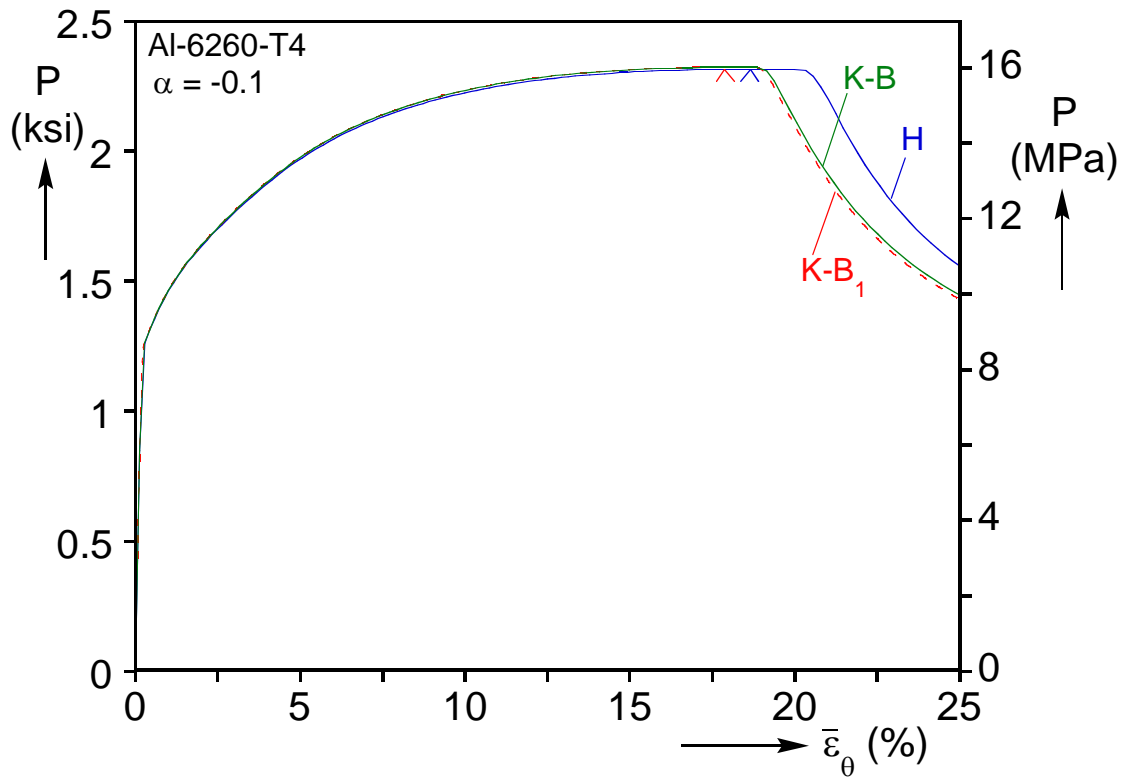
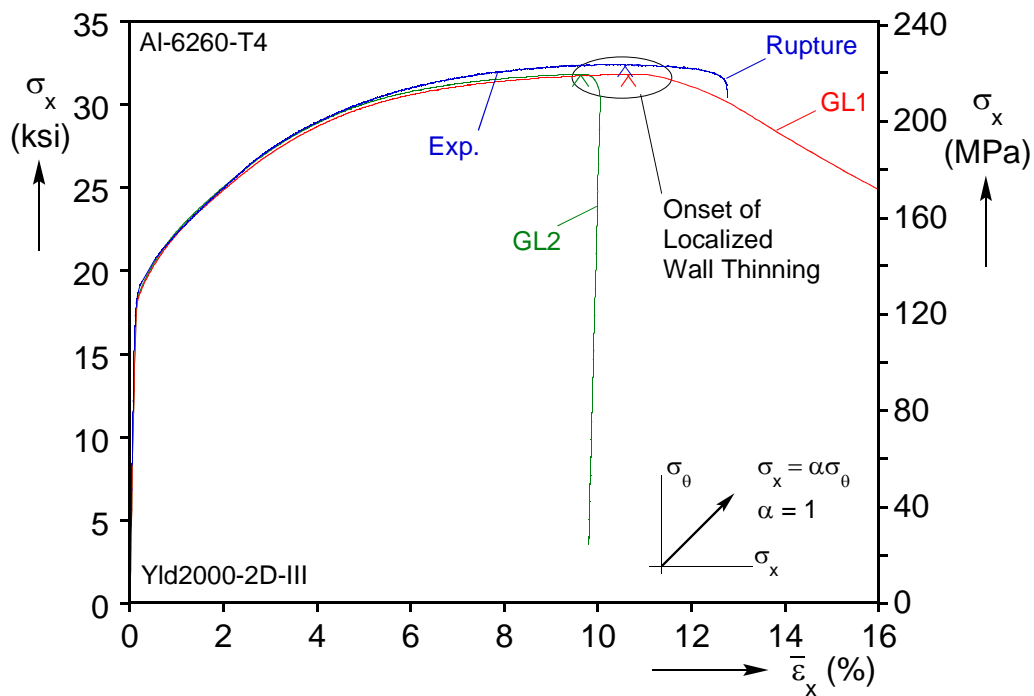
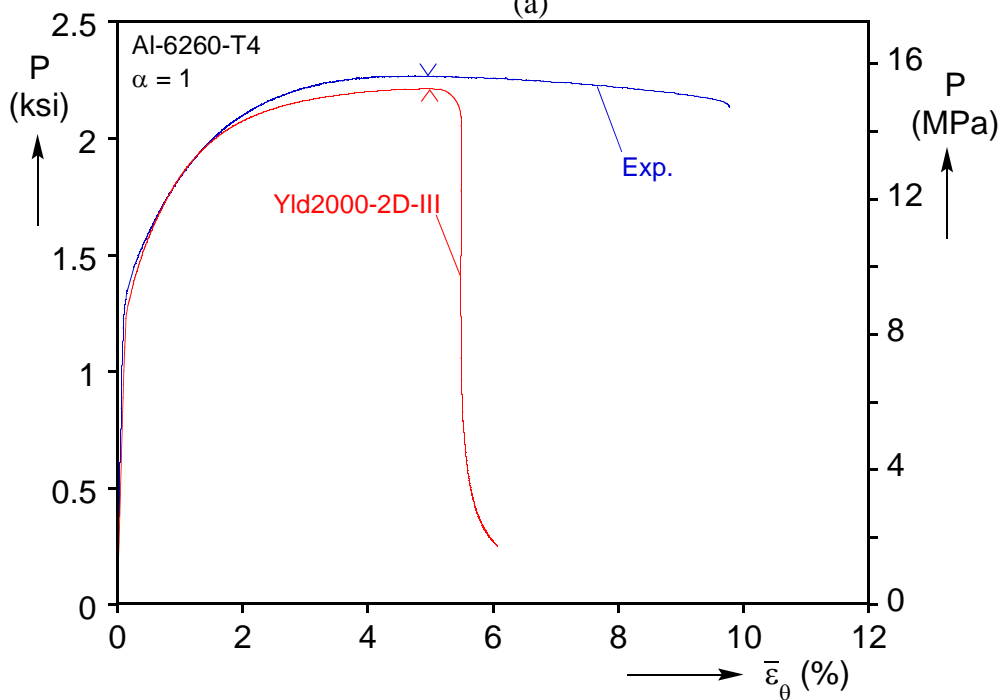


Fig. 4.15 – Comparison of $P - \bar{\epsilon}_\theta$ responses calculated using two Karafillis – Boyce models (K-B₁ includes the shear anisotropy) and anisotropic Hosford's model



(a)



(b)

Fig. 4.16 – Results from numerical simulation of $\alpha = 1.0$ path using the Yld2000-2D, Case III plasticity model, and the experimental responses. (a) $\sigma_x - \varepsilon_x$ and (b) $P - \bar{\varepsilon}_\theta$.

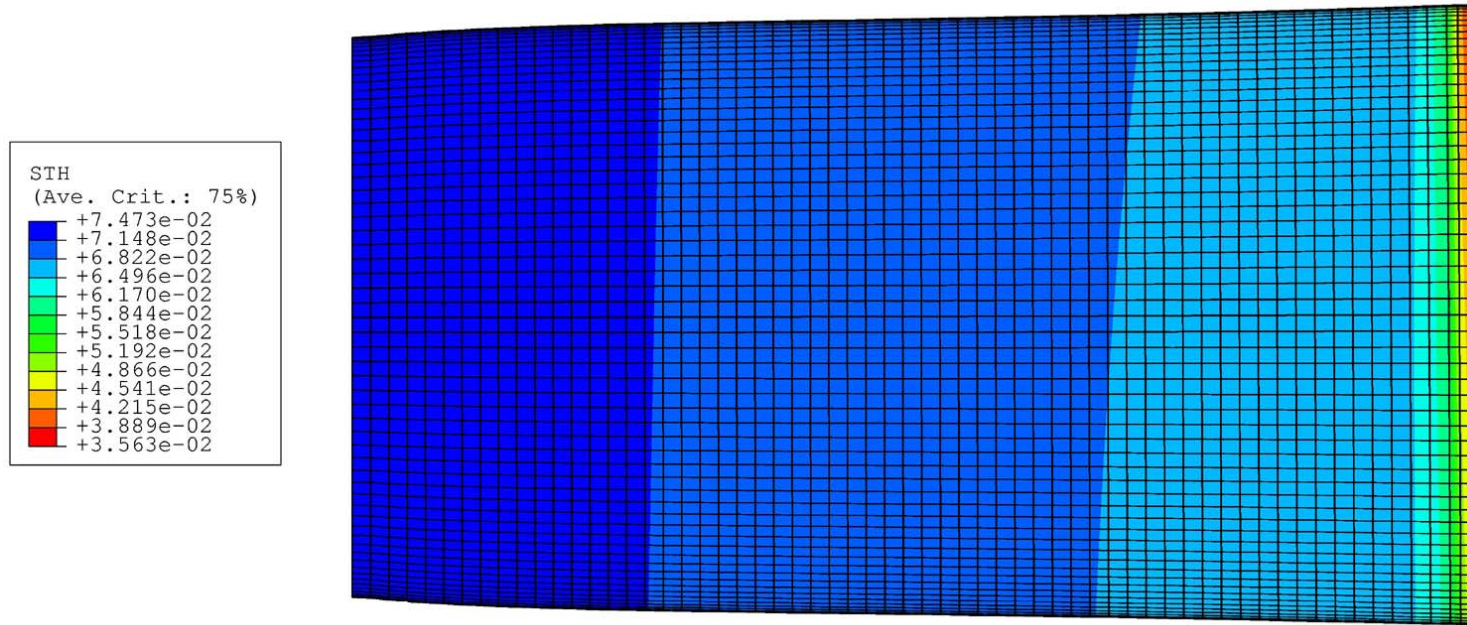
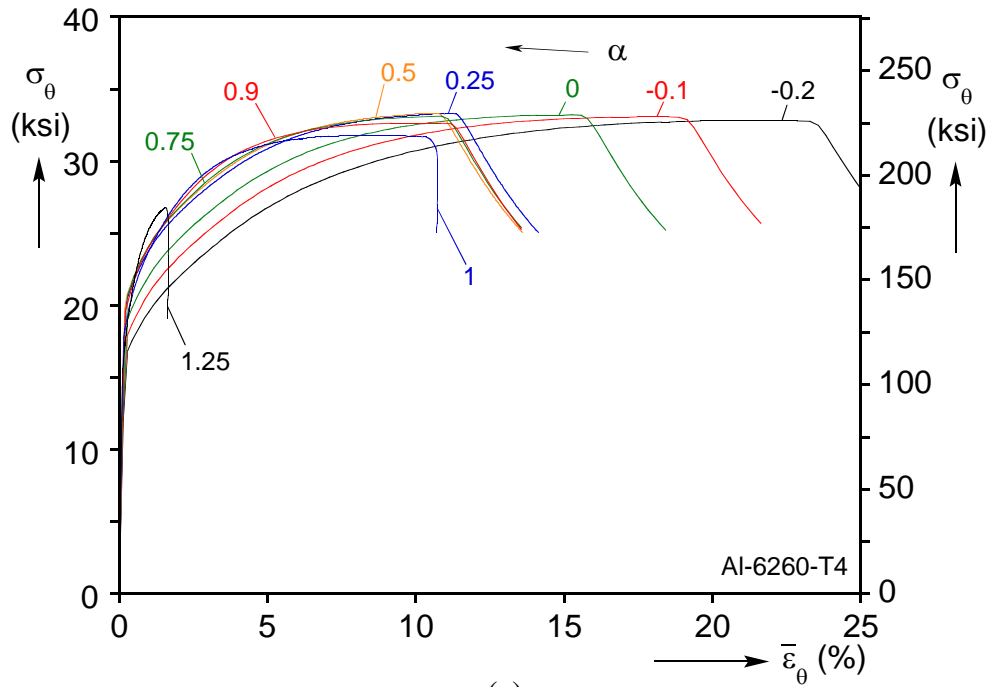
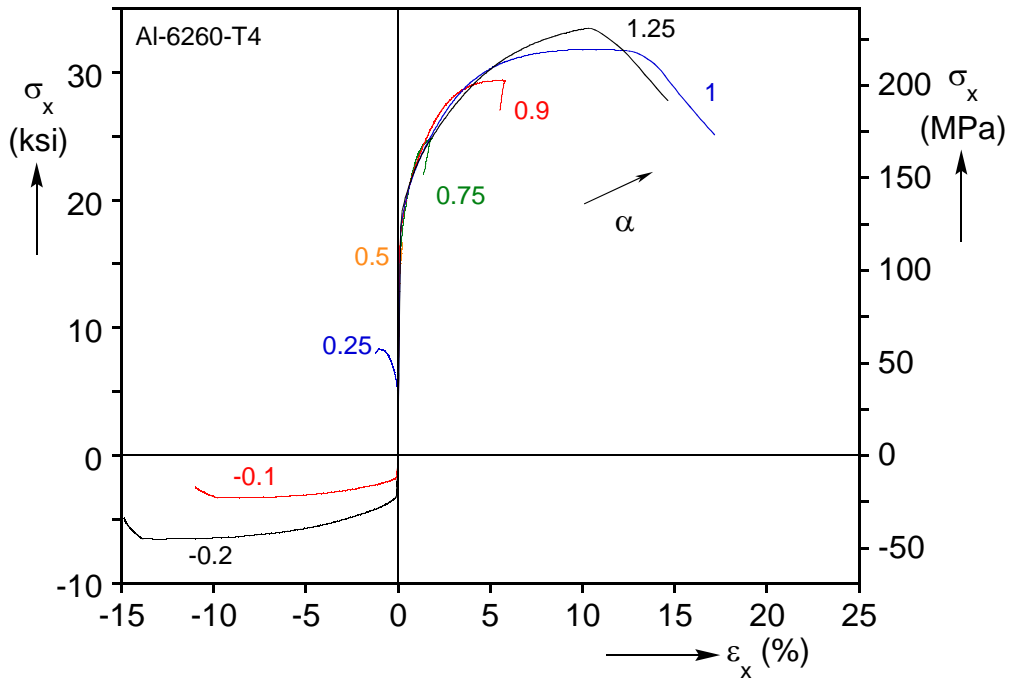


Fig. 4.16 (cont'd) – (c) Model deformed configuration just after the onset of localization (Yld2000-2D, Case III).



(a)



(b)

Fig. 4.17 – Results from numerical simulations of the nine radial experiments, using the K-B plasticity model. (a) $\sigma_\theta - \bar{\epsilon}_\theta$ and (b) $\sigma_x - \epsilon_x$.

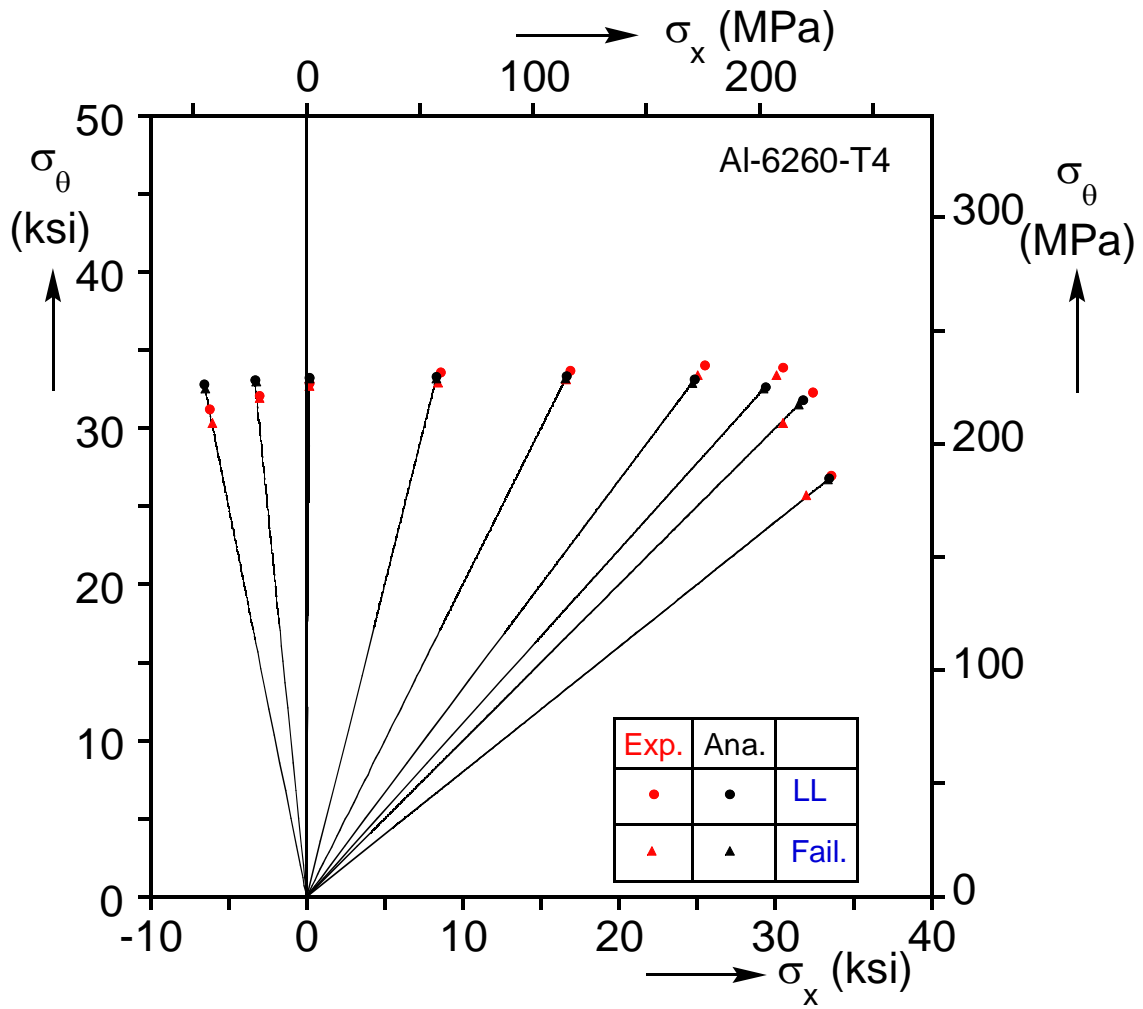


Fig. 4.18 – Engineering stress paths prescribed in the experiments and predicted by the analysis, using the K-B plasticity model. Marked are the stresses at the limit load and at rupture.

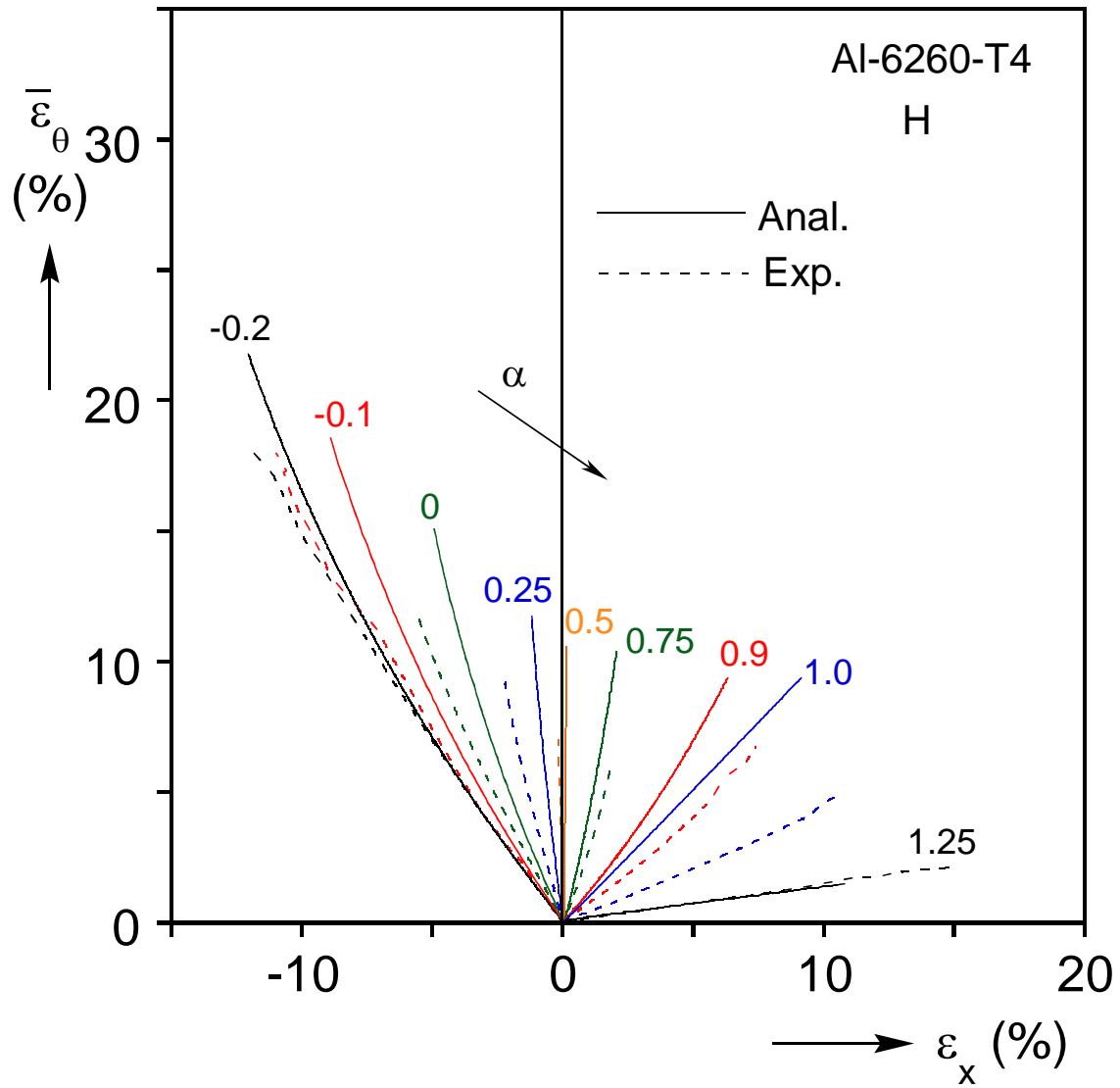


Fig. 4.19 – Comparison of calculated and measured engineering strain paths for nine radial paths using the Hosford yield function.

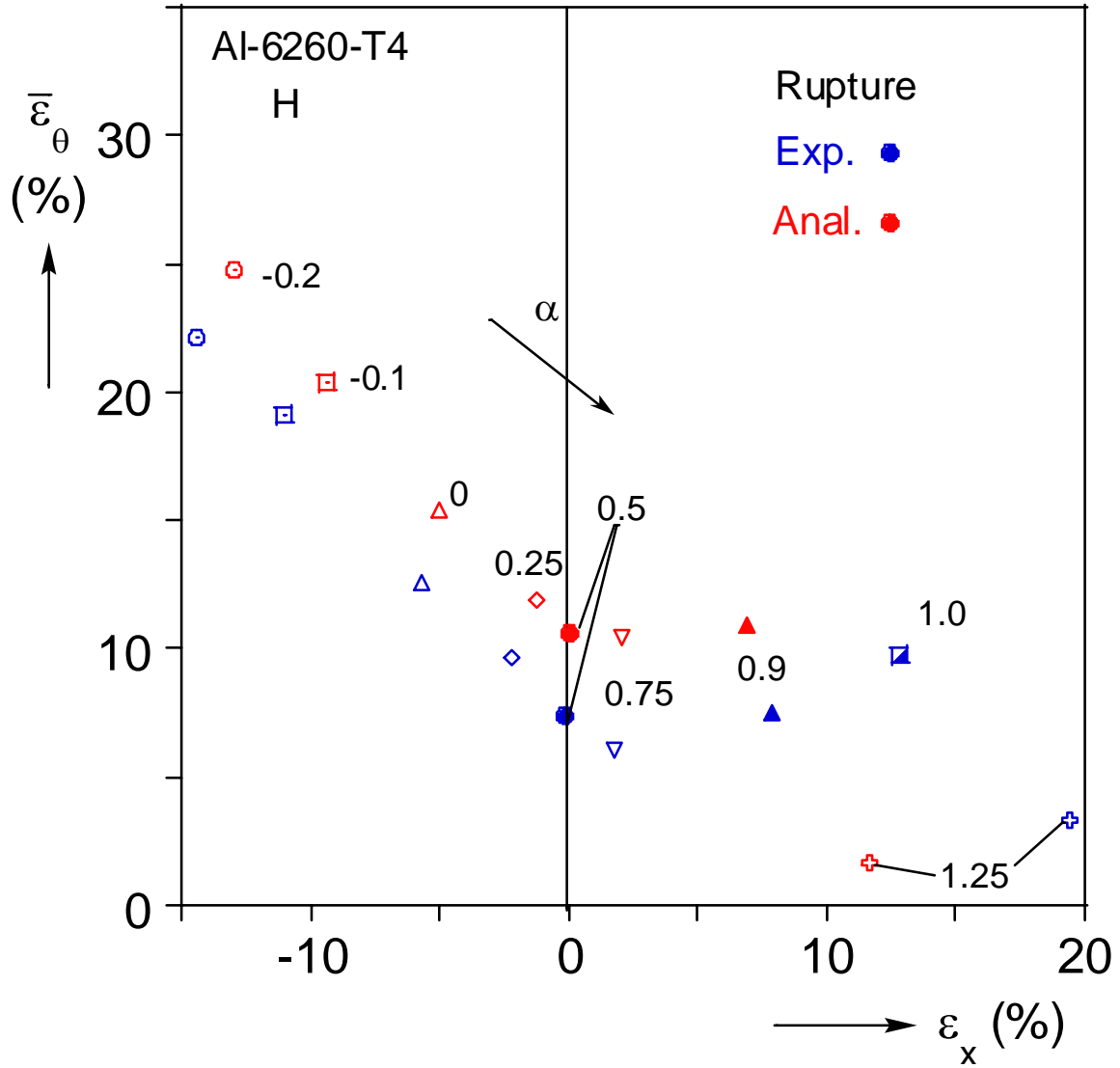


Fig. 4.20 – Comparison of measured and calculated average strains at rupture using the Hosford yield function.

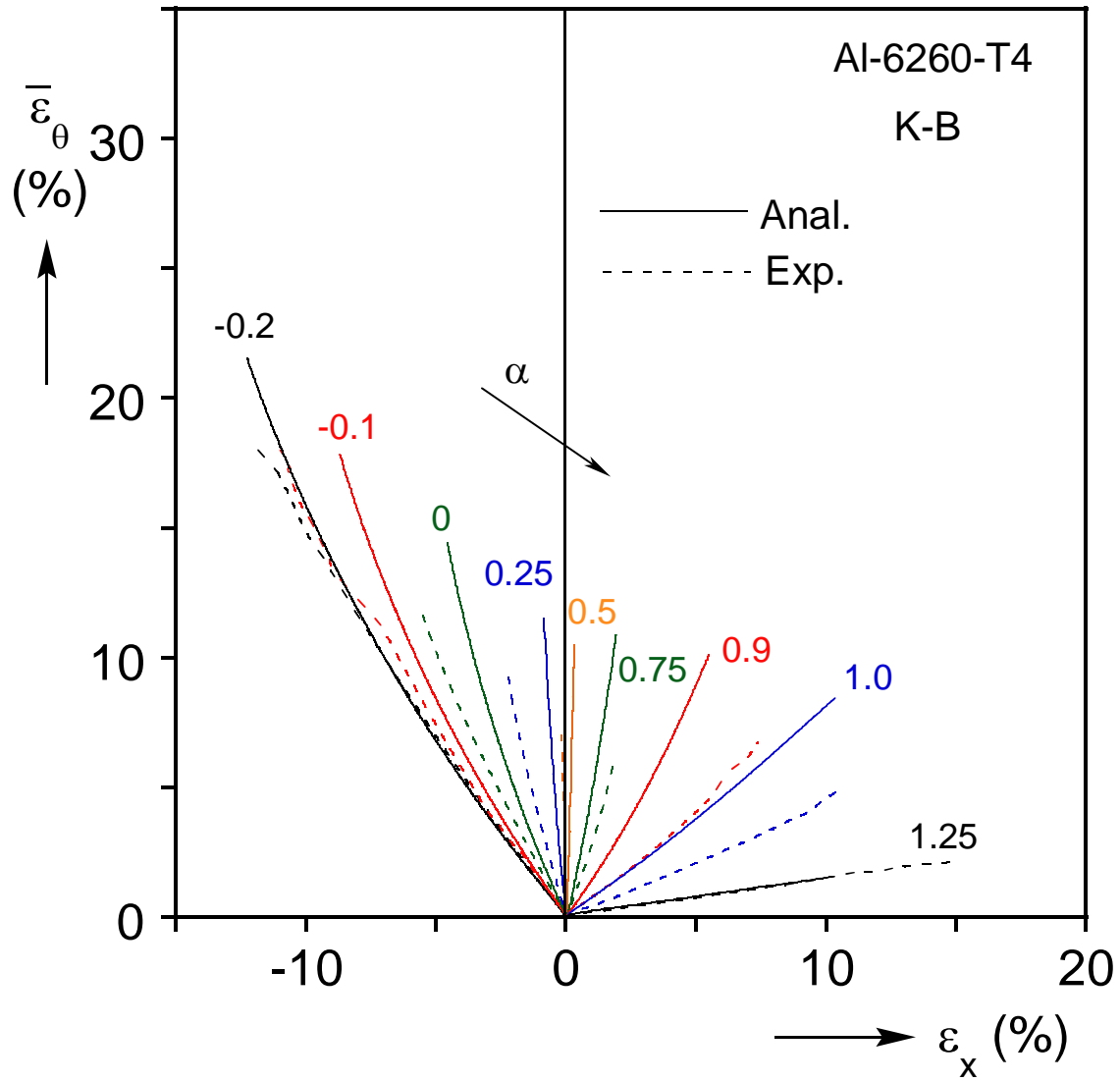


Fig. 4.21 – Comparison of calculated and measured engineering strain paths for nine radial paths using the Karafillis – Boyce yield function.

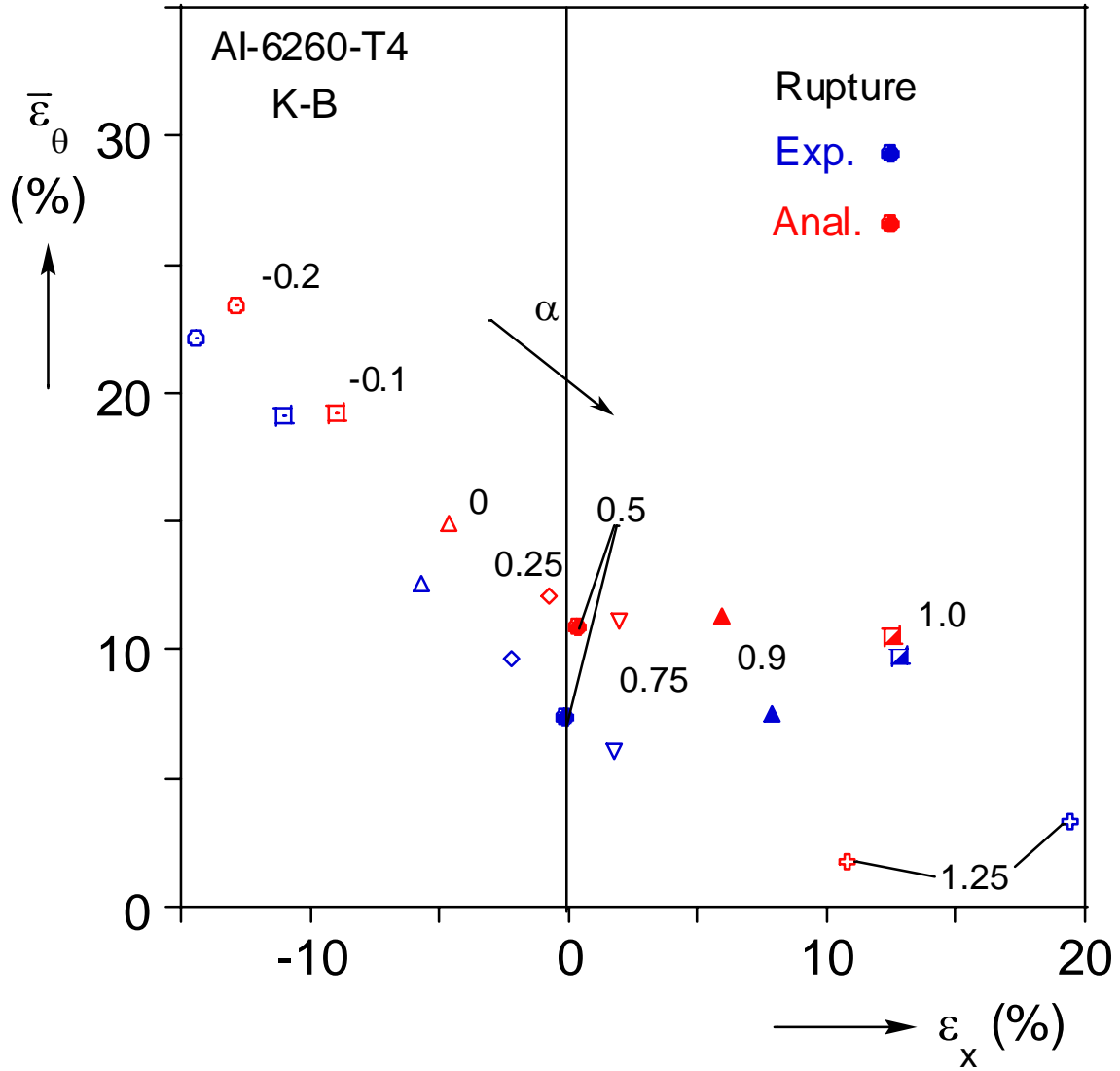


Fig. 4.22 – Comparison of measured and calculated average strains at rupture using the Karafillis – Boyce yield function.

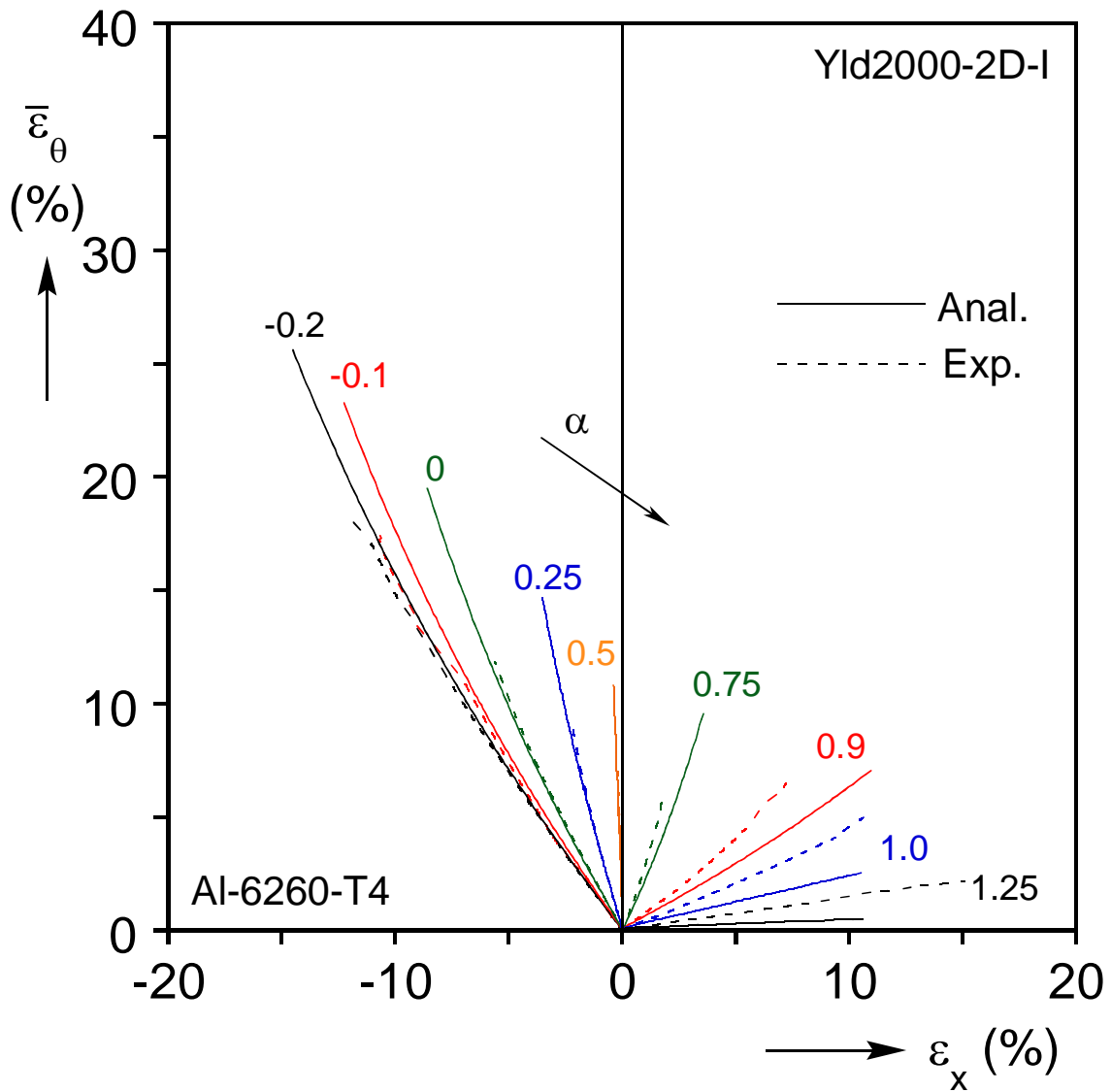


Fig. 4.23 – Comparison of calculated and measured engineering strain paths for nine radial paths using the Yld2000-2D yield function, Case I.

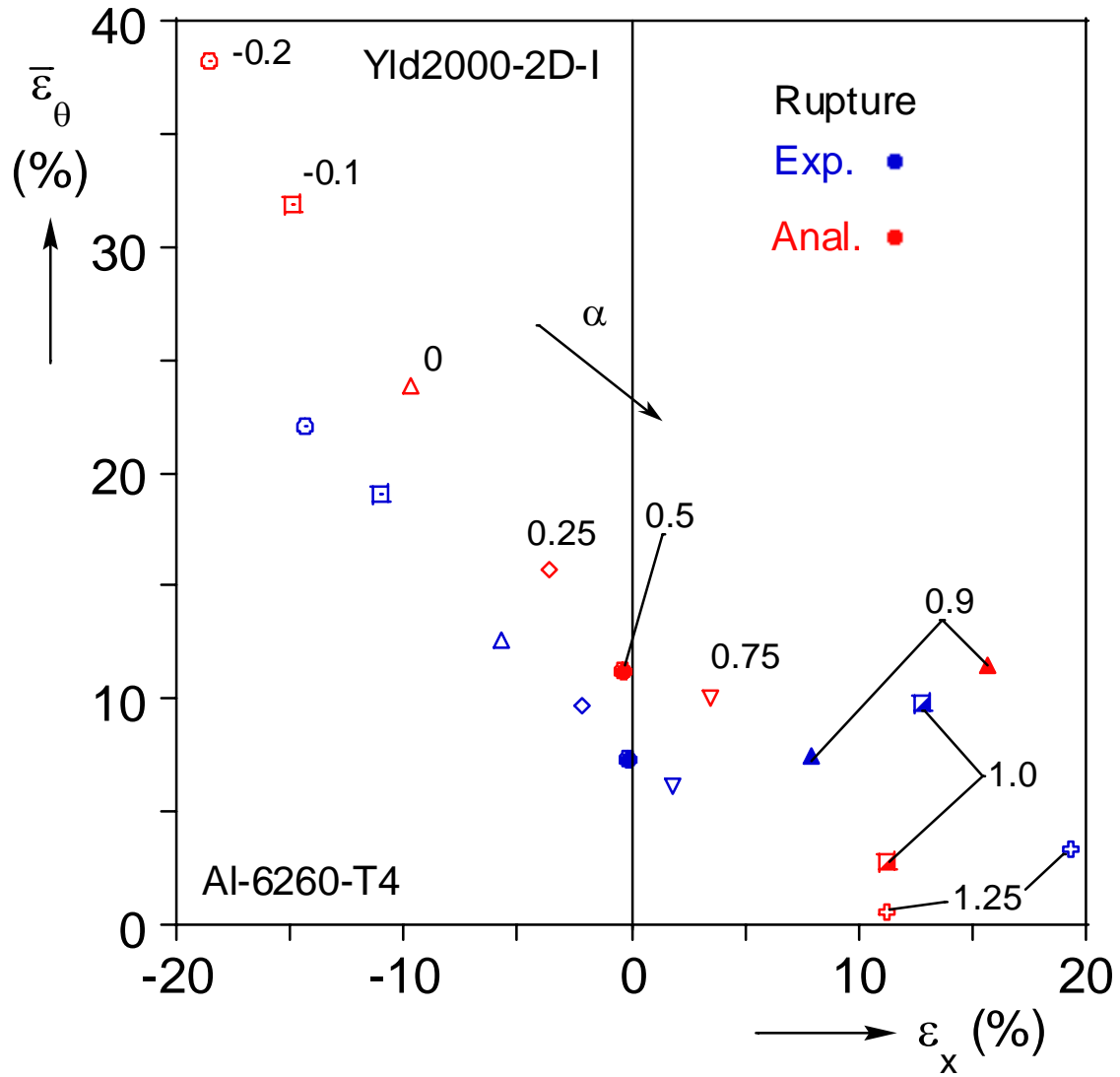


Fig. 4.24 – Comparison of measured and calculated average strains at rupture using the Yld2000-2D yield function Case I.

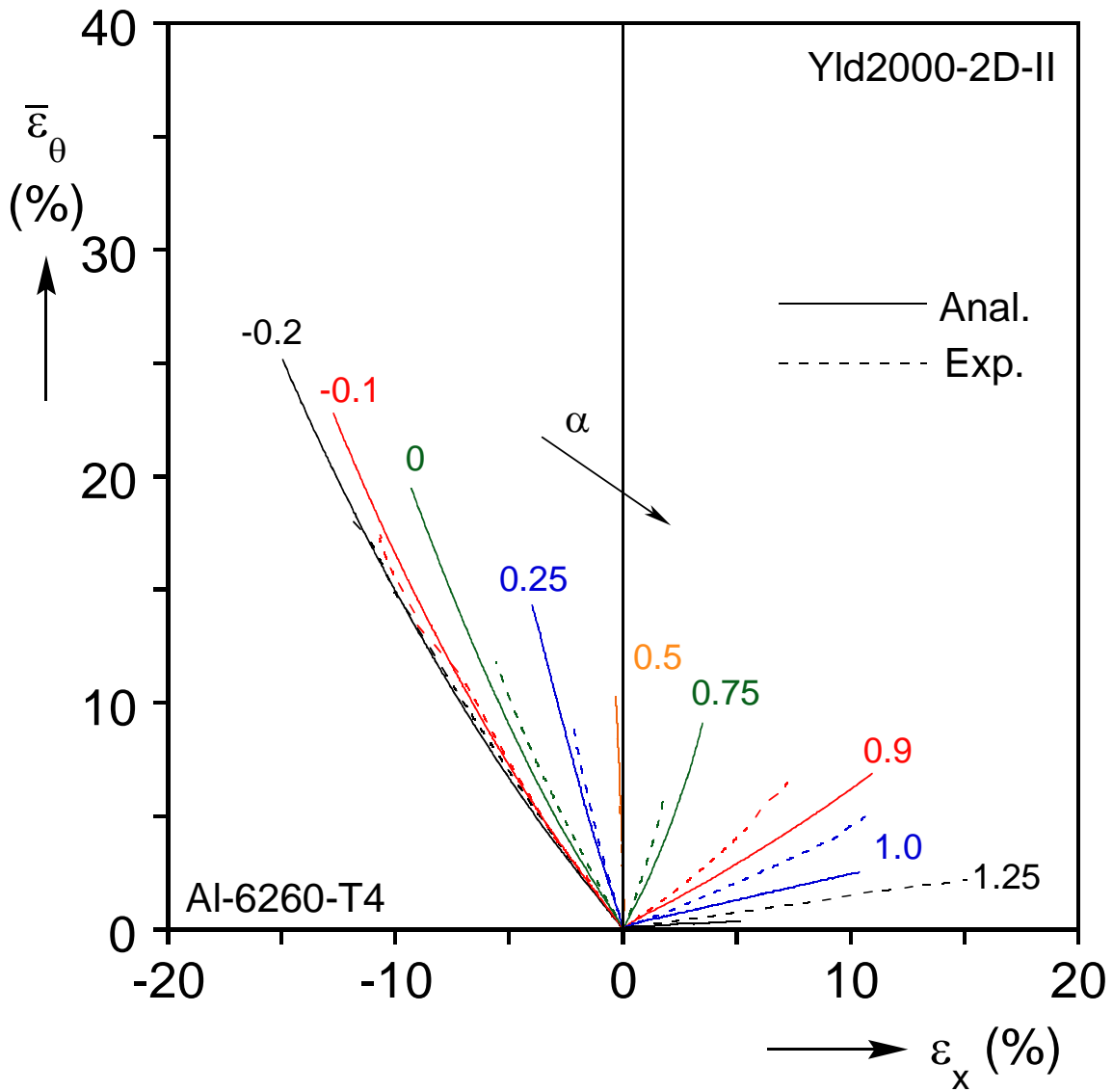


Fig. 4.25 – Comparison of calculated and measured engineering strain paths for nine radial paths using the Yld2000-2D yield function, Case II.

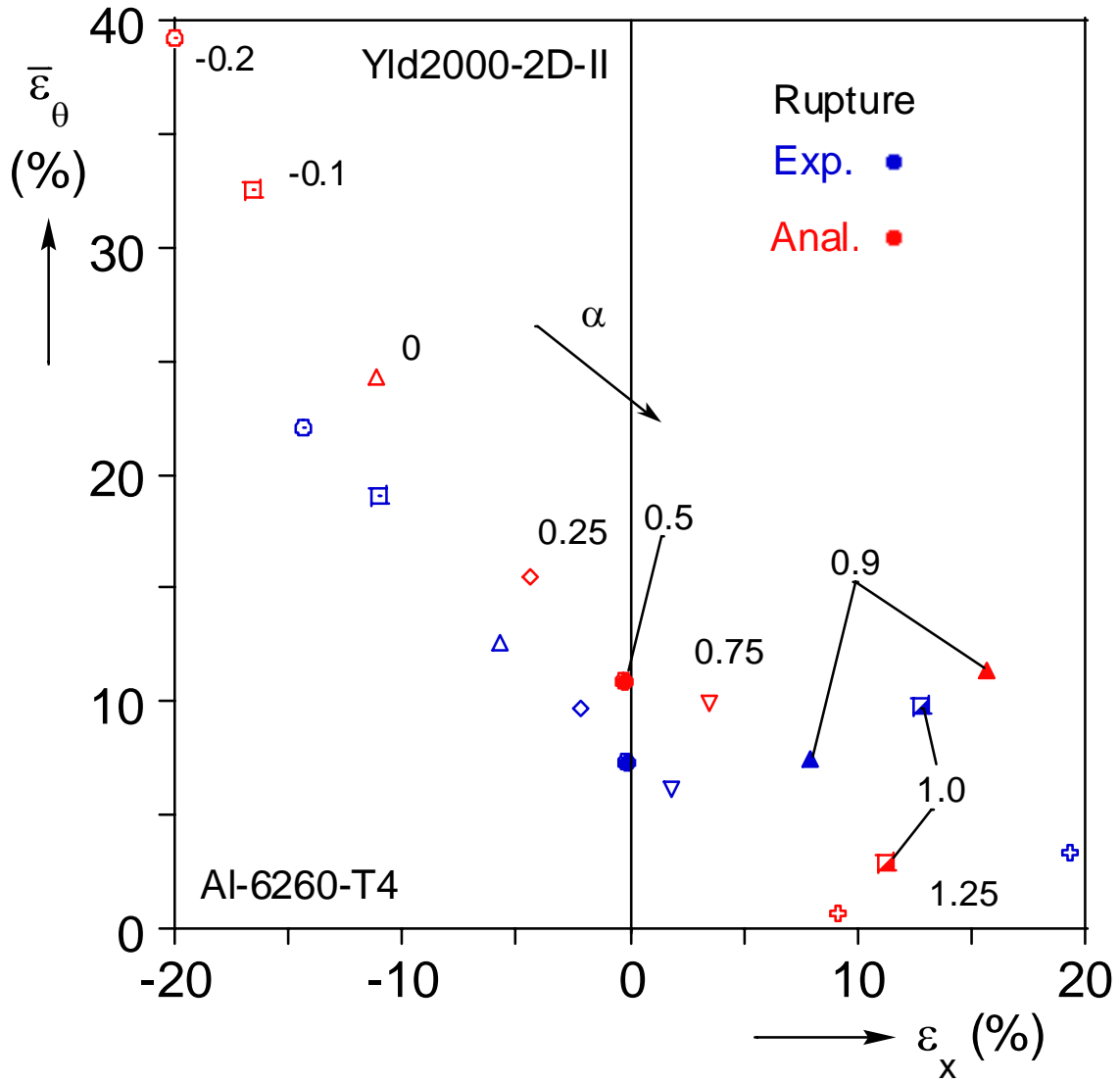
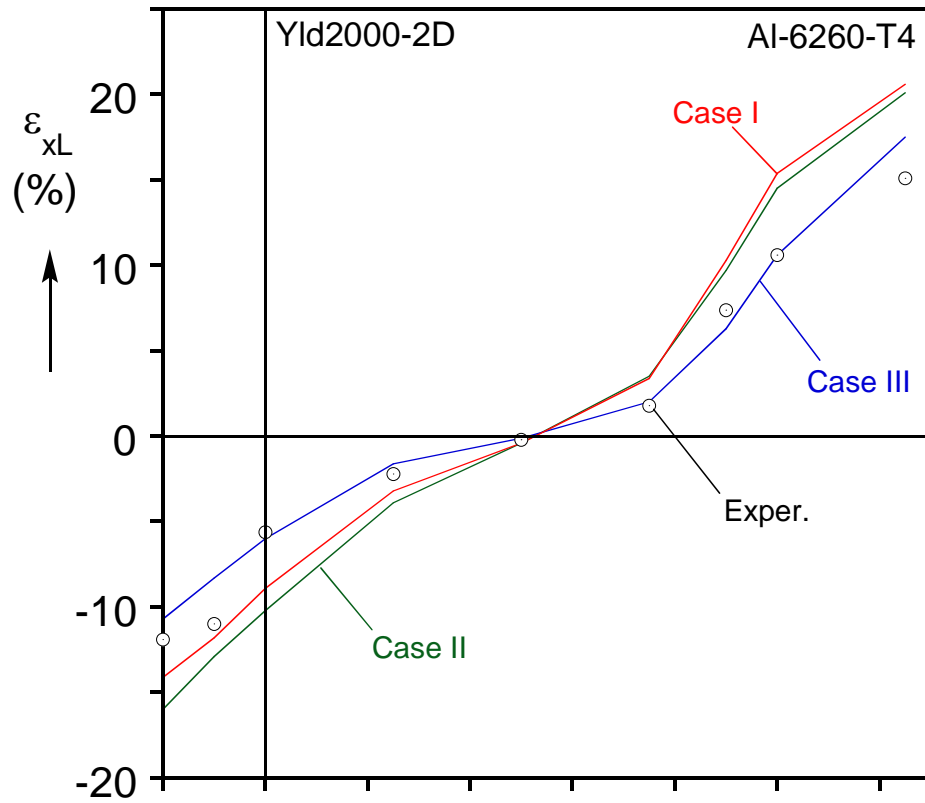
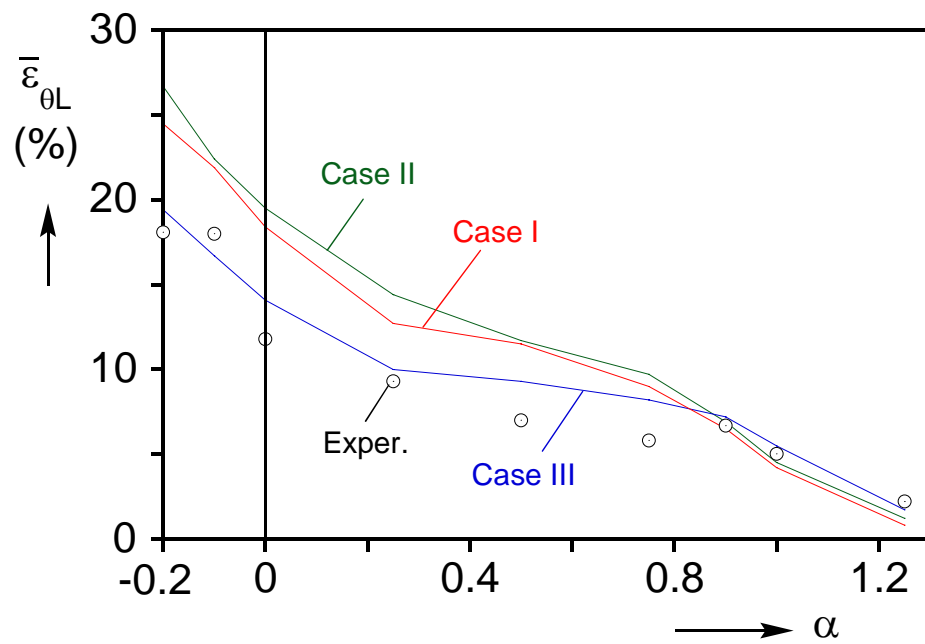


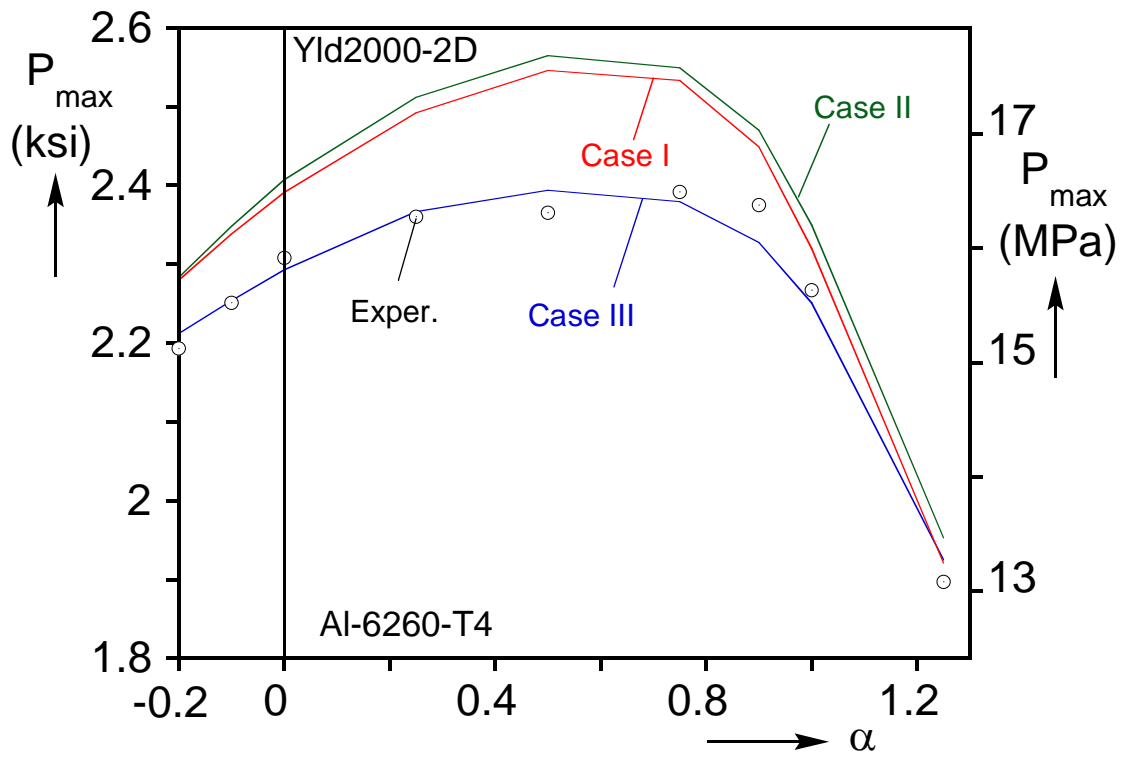
Fig. 4.26 – Comparison of measured and calculated average strains at rupture using the Yld2000-2D yield function Case II.



(a)



(b)



(c)

Fig. 4.27 – Performance of the three constitutive models in predicting the limit load states for each imposed stress ratio α and corresponding experimental data. (a) Axial strain at the limit pressure, (b) hoop strain at the limit pressure, and (c) limit pressure.

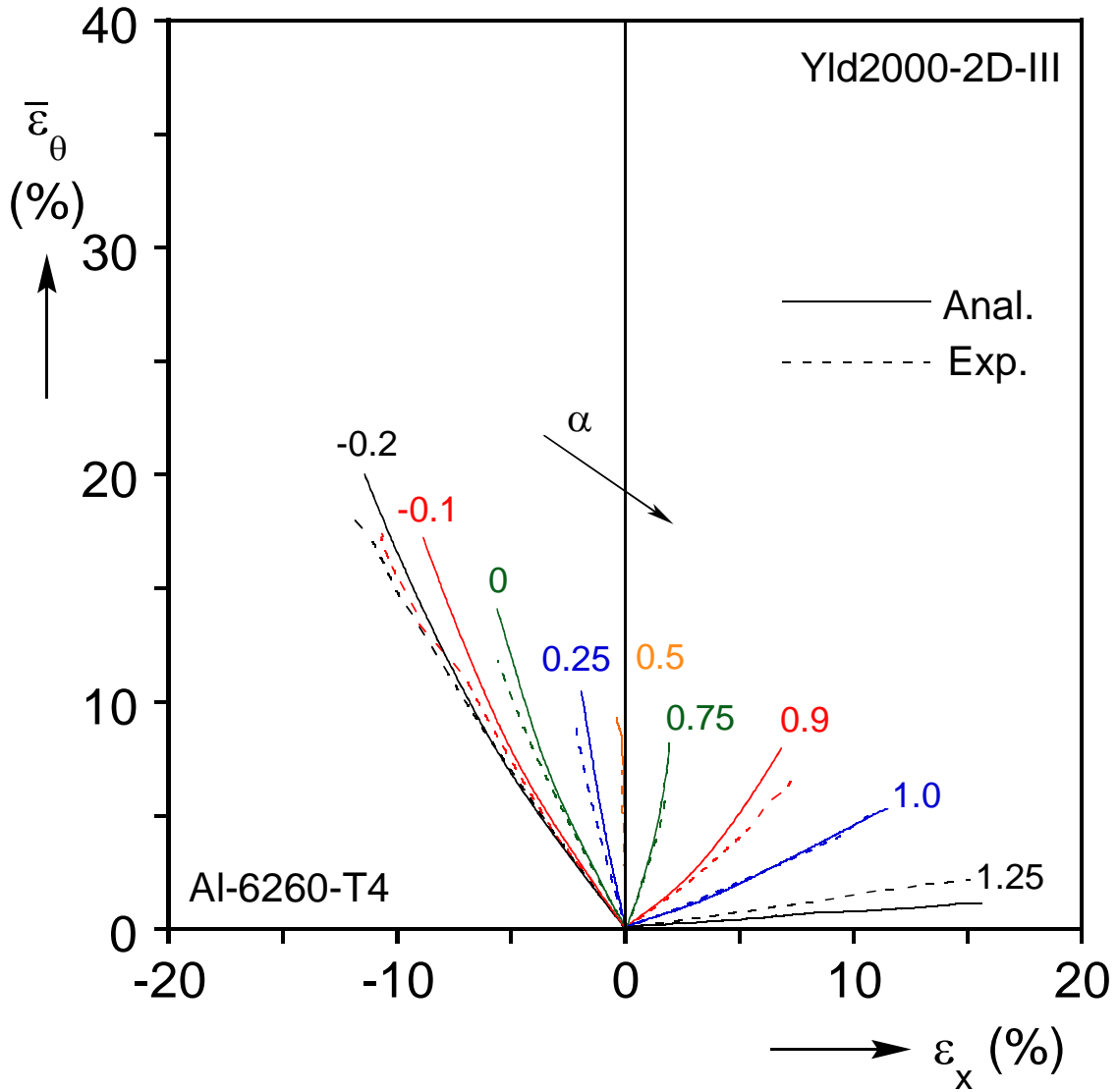


Fig. 4.28 – Comparison of calculated and measured engineering strain paths for nine radial paths using the Yld2000-2D yield function, Case III.

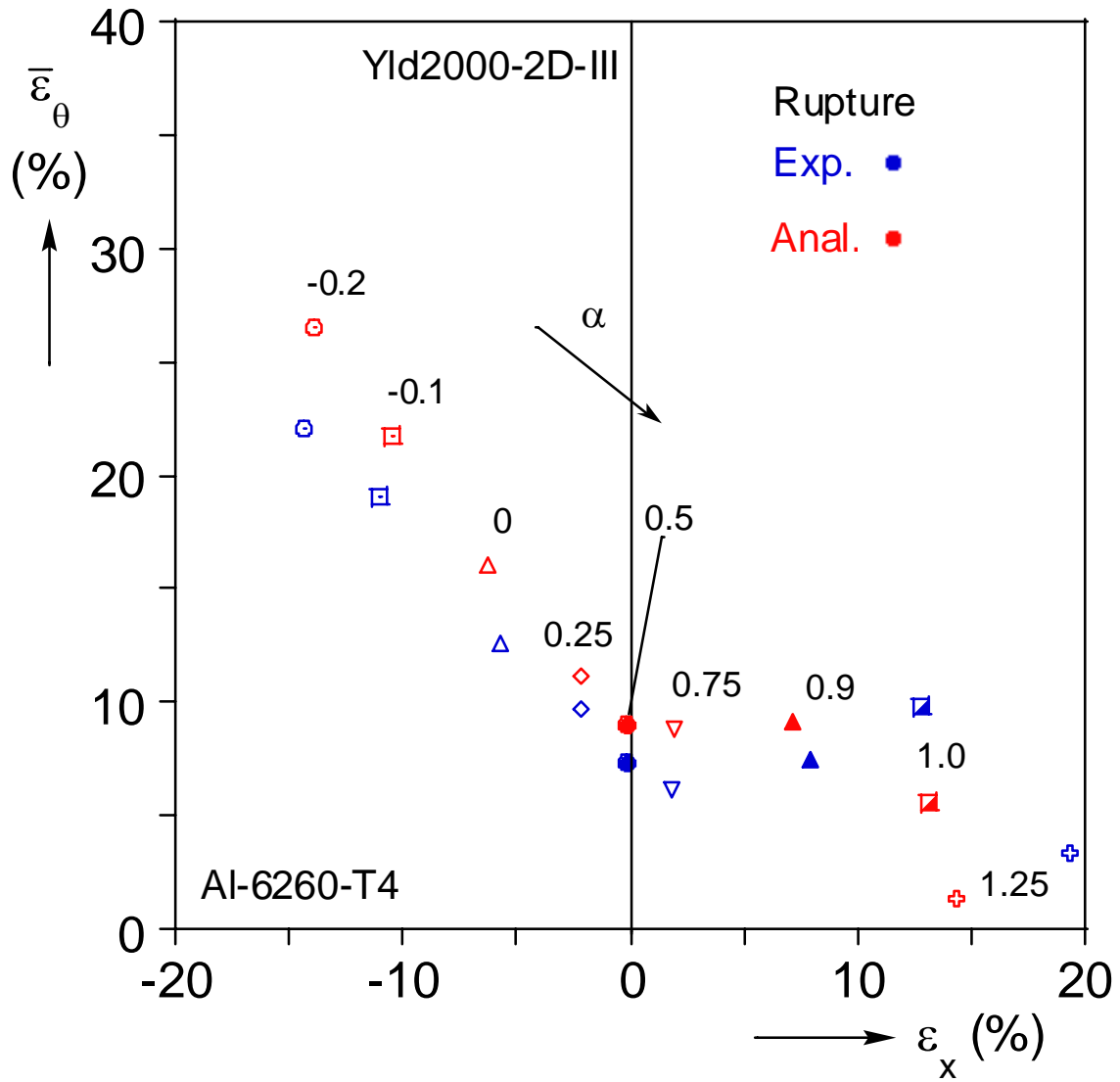


Fig. 4.29 – Comparison of measured and calculated average strains at rupture using the Yld2000-2D yield function Case III.

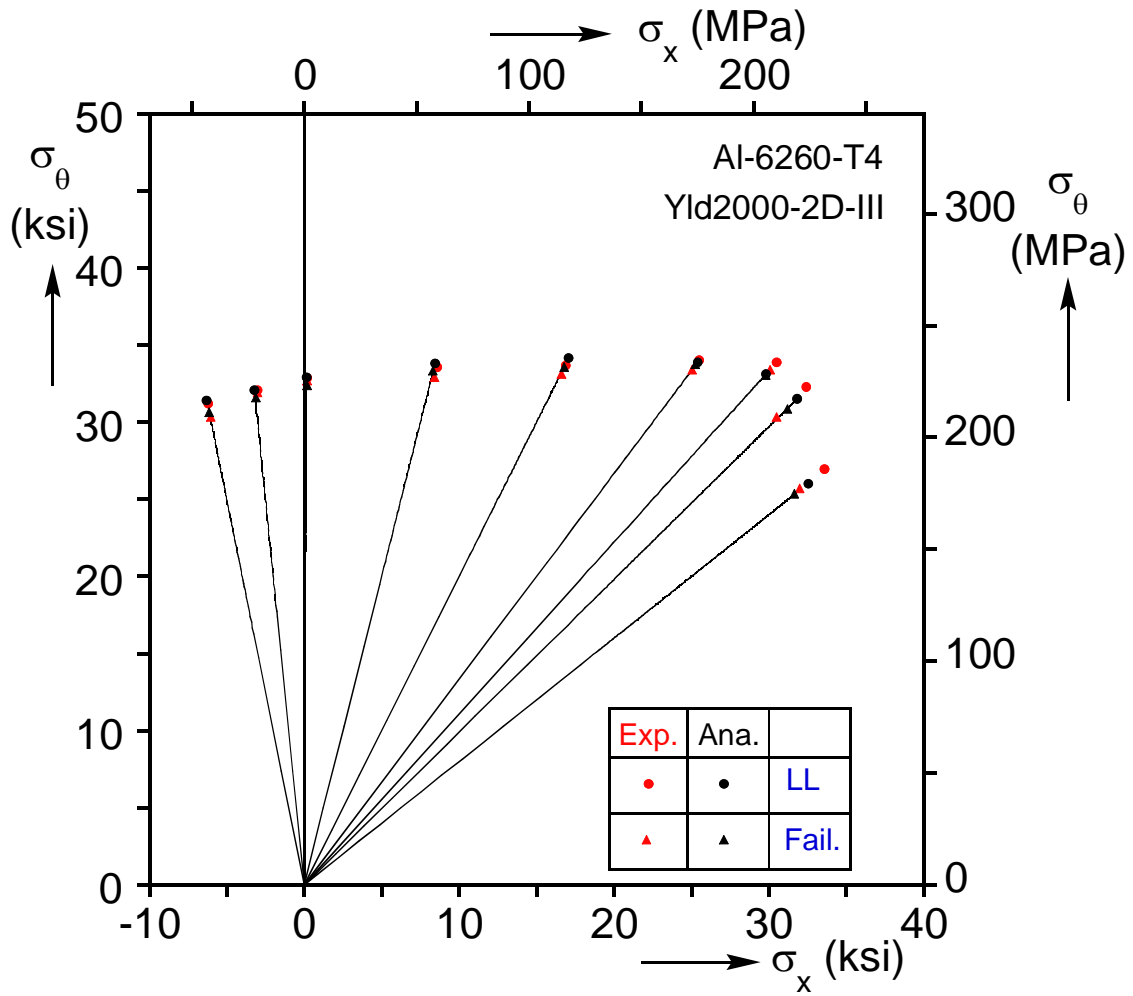
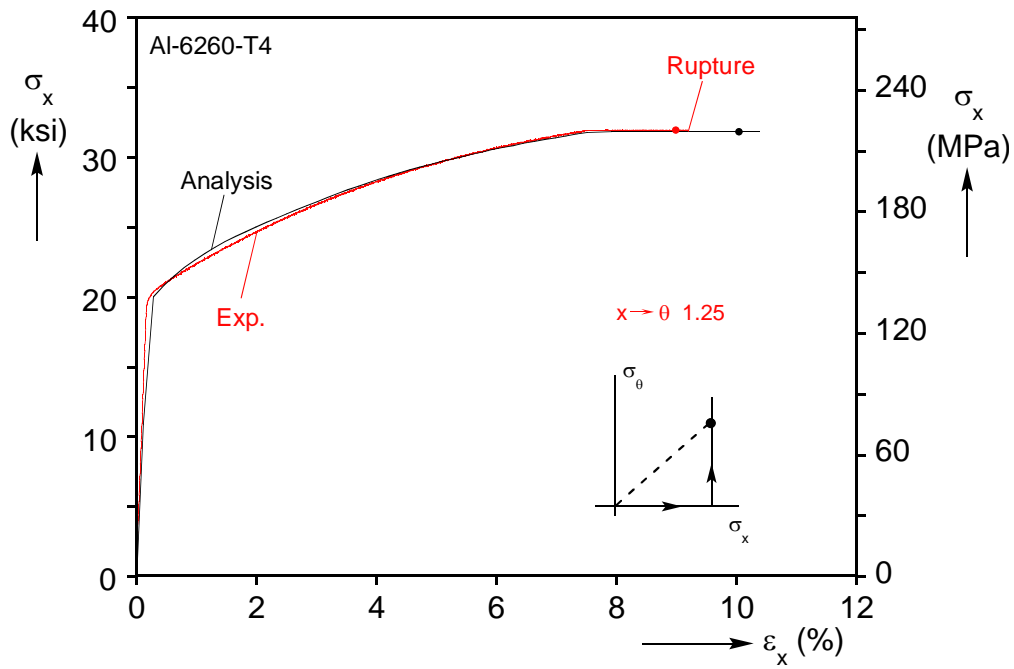
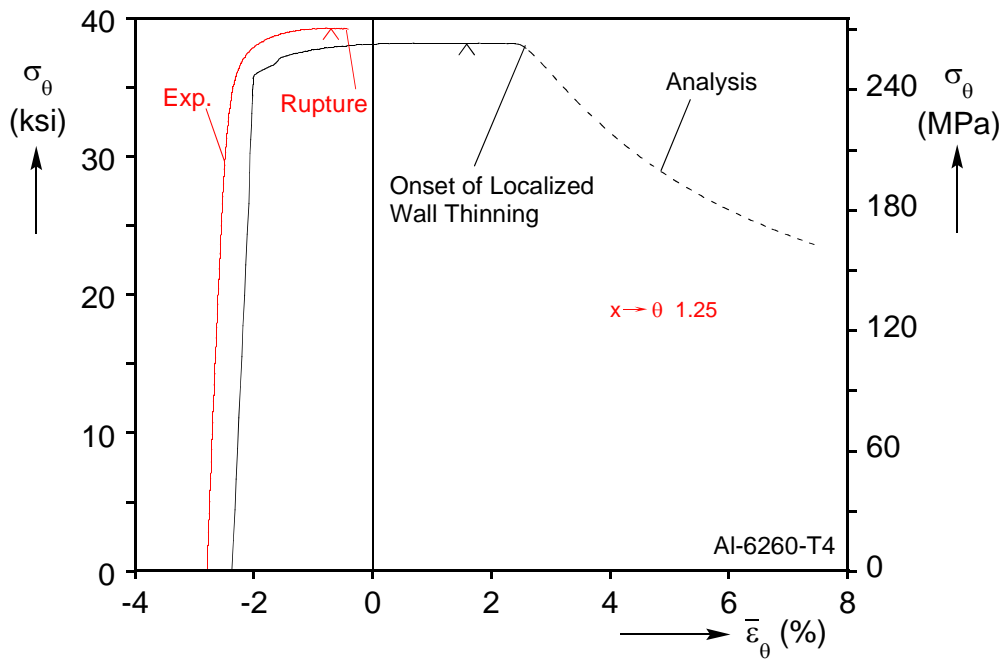


Fig. 4.30 – Engineering stress paths prescribed in the experiments and predicted by the analysis, using the Yld2000-2D-III plasticity model. Marked are the stresses at the limit load and at rupture.



(a)



(b)

Fig. 4.31 –(a) Axial, and (b) circumferential stress-strain responses recorded in the $x \rightarrow \theta$ 1.25 corner path experiment and comparison with the numerical simulation results using the Yld2000-2D-III plasticity model. The symbol (●) in (a) corresponds to the limit pressure marked in (b).

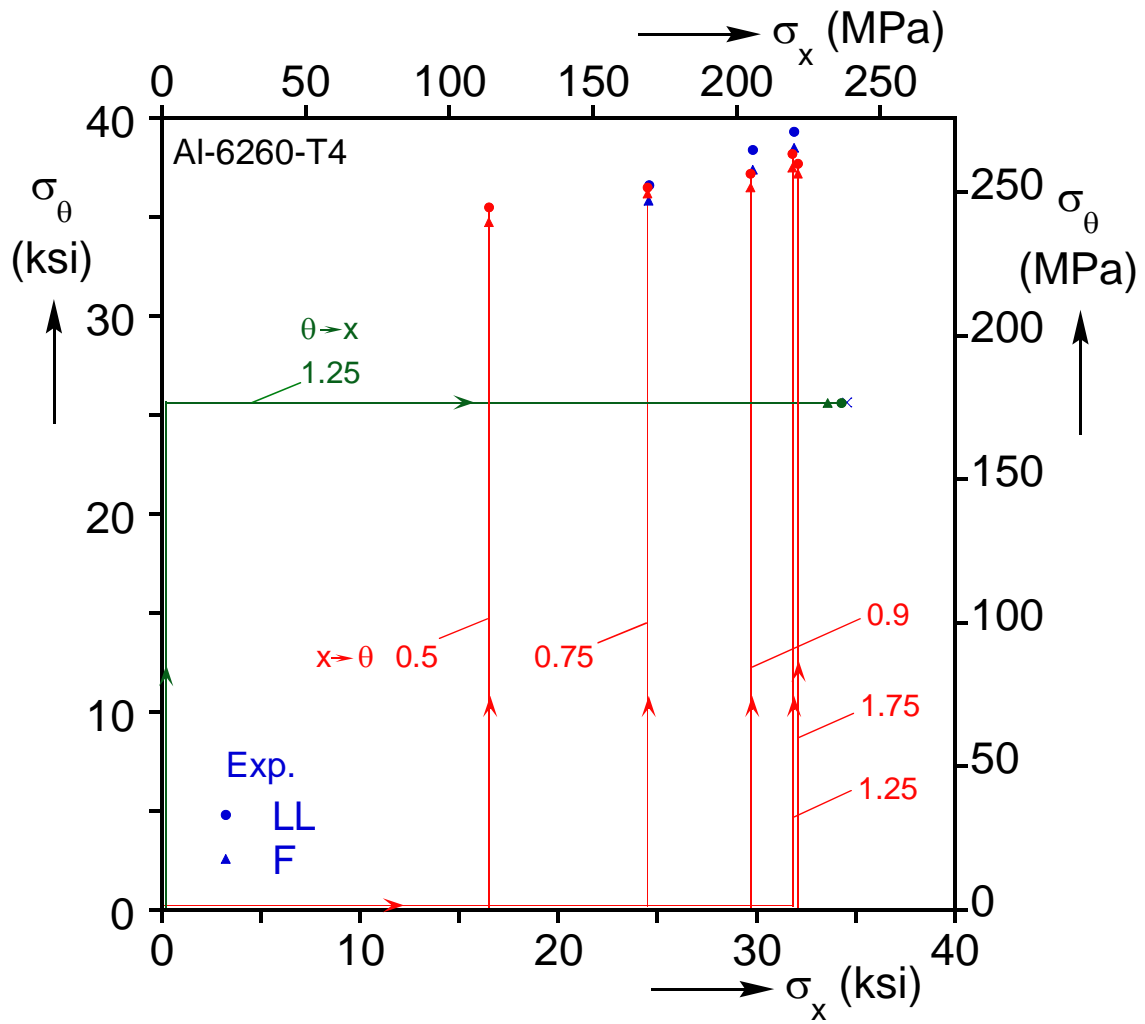


Fig. 4.32 Engineering stress paths prescribed in the experiments and predicted by the analysis, using the Yld2000-2D-III plasticity model. Marked are the stresses at the limit load and at rupture.

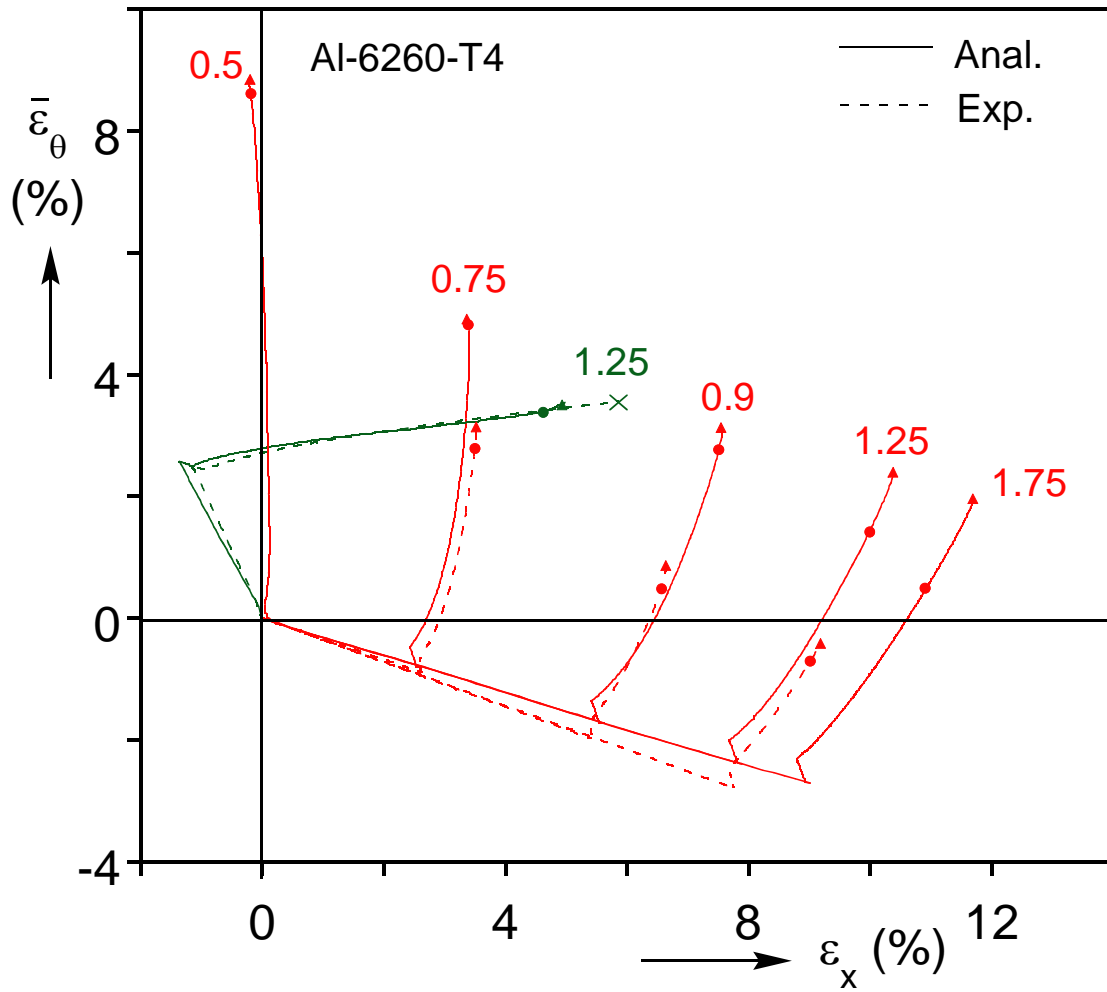
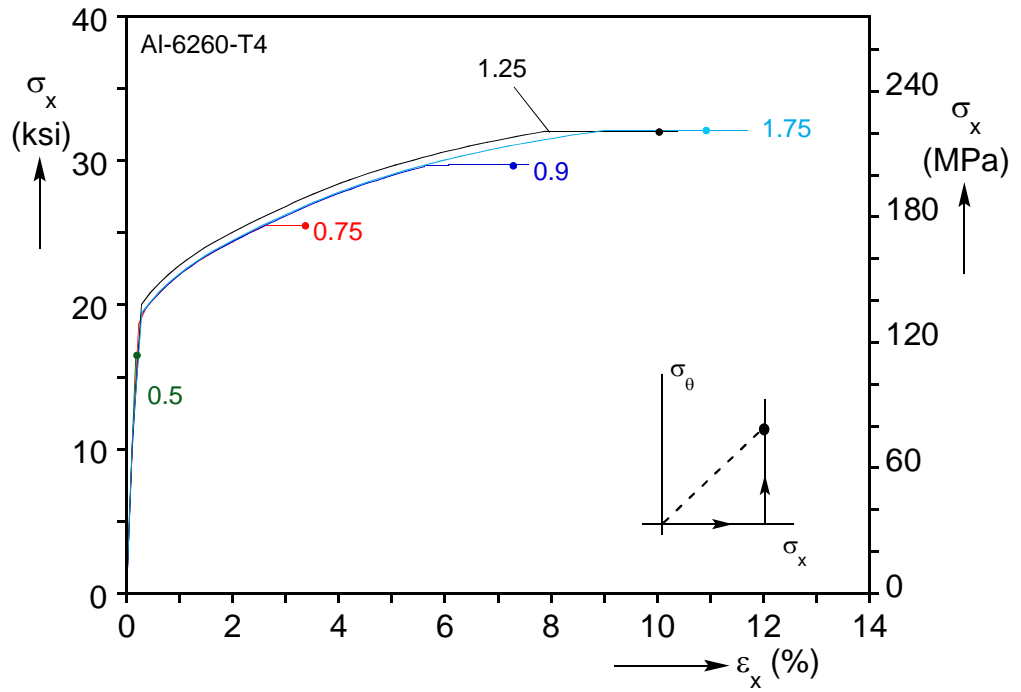
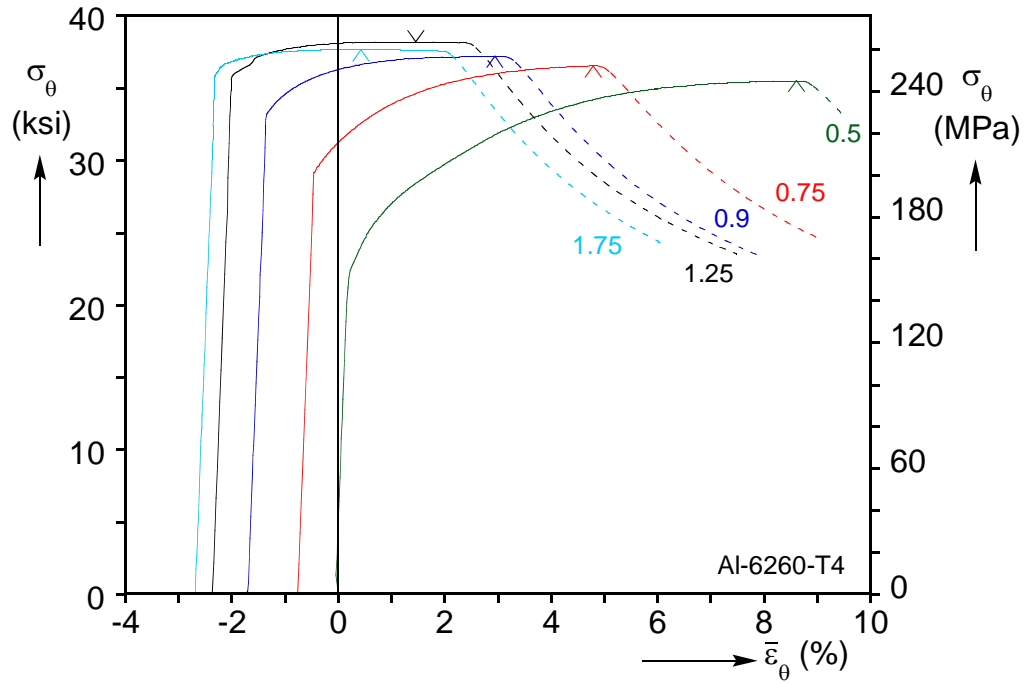


Fig. 4.33 Comparison of measured and calculated engineering strain paths, using the Yld2000-2D-III plasticity model. Marked are the average strains at the limit load and at failure.



(a)



(b)

Fig. 4.34 (a) Axial, and (b) circumferential stress-strain responses from numerical simulations of various $x \rightarrow \theta$ corner paths. The symbol (●) in (a) corresponds to the limit pressure marked in (b).

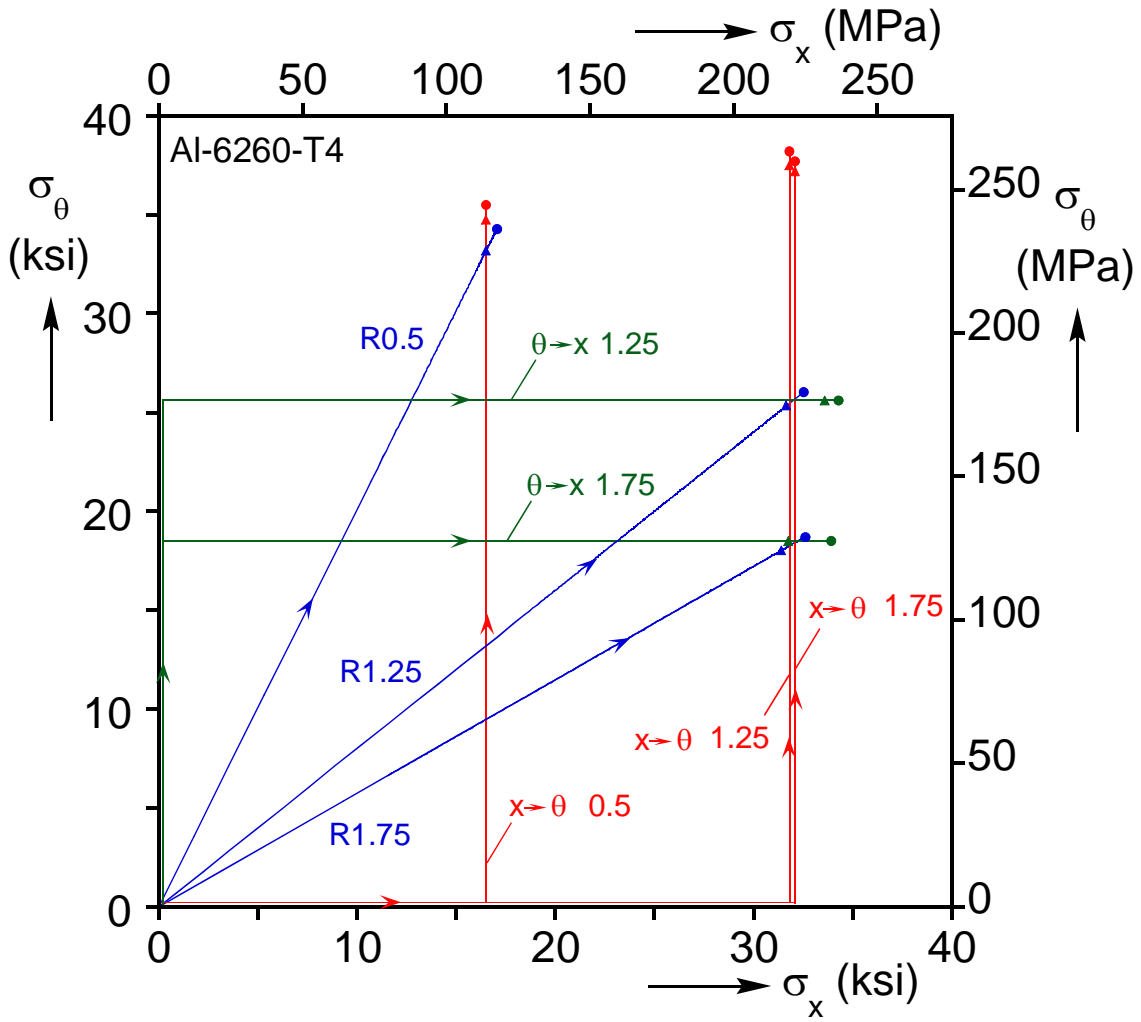


Fig. 4.35 Engineering stress paths prescribed in numerical calculations, using the Yld2000-2D-III plasticity model. Marked are the average strains at the limit load and at failure.

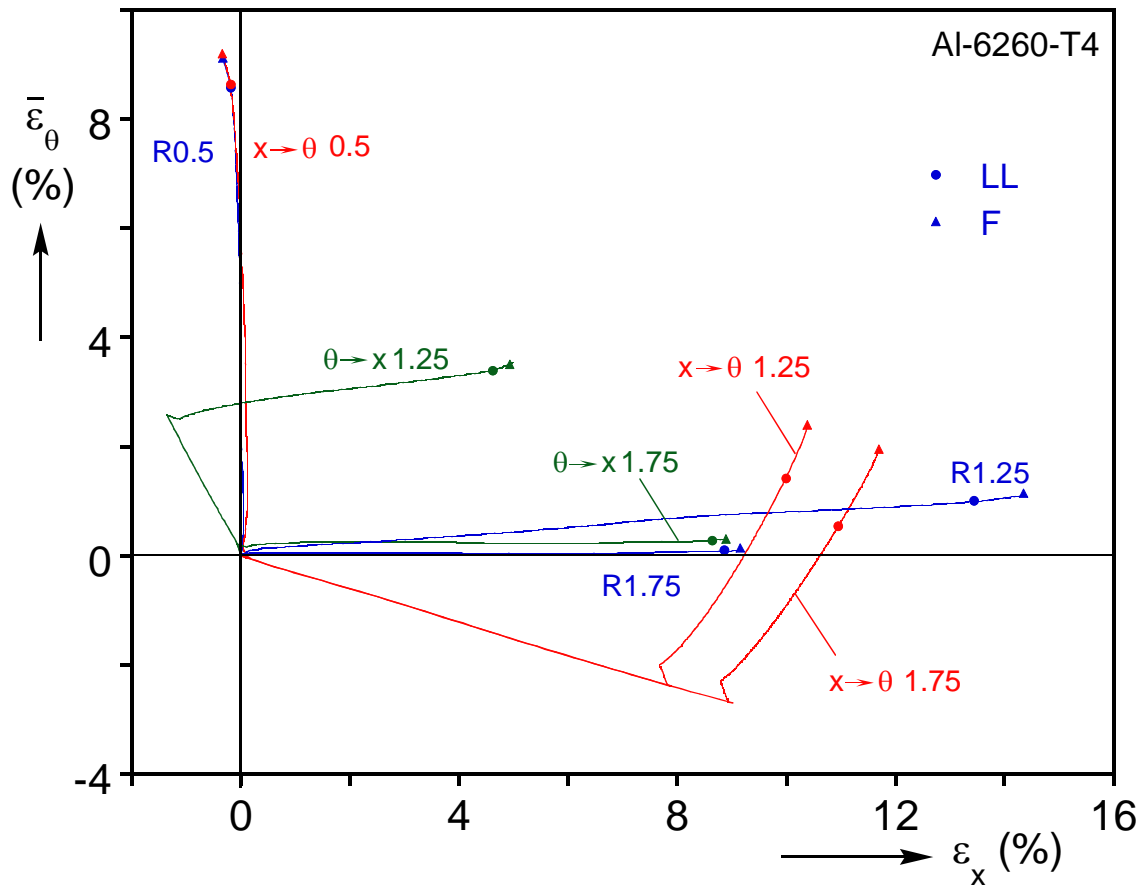
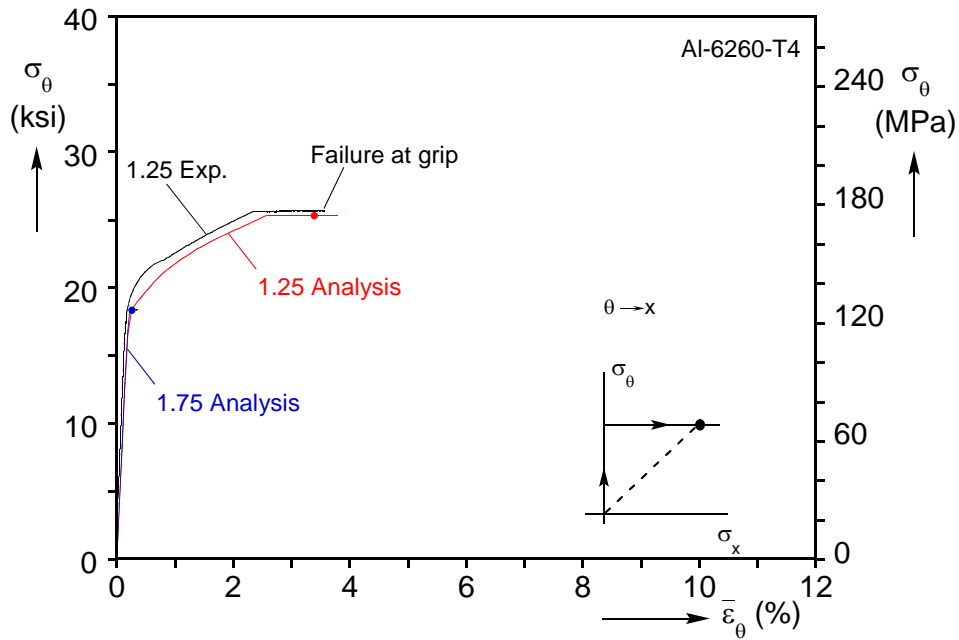
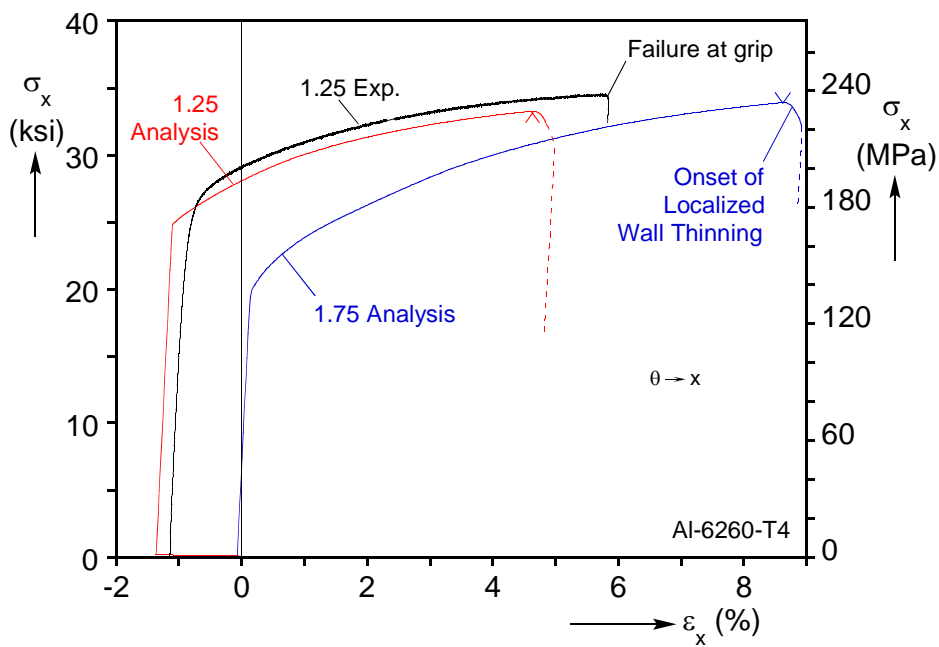


Fig. 4.36 Strain paths corresponding to stress paths in previous figure.



(a)



(b)

Fig. 4.37 (a) Circumferential, and (b) axial stress-strain responses from numerical simulations of various $\theta \rightarrow x$ corner paths. The symbol (●) in (a) corresponds to the limit load marked in (b). Notice that the specimen failed at the grips before a limit load was encountered.

Chapter 5: *Numerical Modeling of Tube Hydroforming*

The present chapter contains the numerical simulations of the tube hydroforming experiments described in Chapter 2. As will be shown shortly, the standard von Mises plasticity does not yield accurate predictions of failure in these experiments. This prompted the formability study described in Chapters 3 and 4. With the constitutive framework developed in this study, we now return to the hydroforming experiments and examine numerically the prediction of the failures encountered. Different numerical models were developed in Abaqus/Standard for this purpose and are described below.

5.1 GENERALIZED PLANE STRAIN MODEL (2D)

5.1.1 Model Set-up

The simplest model that can be used for the geometry at hand is a slice of the tube at mid-span, treated as a 2D problem. Exploiting the symmetries of the setup (see Fig. 2.1), only one fourth of the tube slice needs to be examined, as shown in Fig. 5.1. (Note that the quarter sector was preferred over one-eighth as it allows demonstration of localization of wall thinning.) The model has been meshed with linear, 4-node, generalized plane strain elements with reduced integration (CPEG4R). These elements allow the application of a uniform deformation in the out-of-plane direction, replicating the effect of axial feed in the actual experiments. The use of linear elements is dictated by the presence of contact between the tube and the die. Soft contact is used, where the constraint is enforced by the introduction of non-linear springs on the tube surface nodes. In this case, the contact pressure-overclosure relationship is assumed to have an exponential form. The Coulomb friction coefficient used is $\mu=0.2$ (see Section 5.2.2).

The fluid cavity (see Fig. 5.1) is meshed with hydrostatic elements (F2D2), allowing for either pressure- or volume-controlled inflation. Additionally, this allows for the load on the structure (tube + fluid cavity) rather than on the tube only, to be monitored.

The elements are arranged as 4×98 (thickness \times circumference) for the CPEG4R elements, with 98 matching F2D2 elements in the inner surface of the tube (see Fig. 5.2). This configuration was arrived at after suitable parametric studies, shown in Fig. 5.3. The criterion for mesh convergence is the prediction of the final wall thickness. At least 60 elements are required in the circumferential direction (Fig. 5.3a), whereas at least 4 elements are needed in the thickness direction (Fig. 5.3b). The finding that even 4 elements through the thickness can be sufficient is somewhat surprising, since the bending deformation is significant and reduced integration elements are used. Since the computational time required by any of these models is rather small, we opted to use the 4×98 configuration which uses the most regularly shaped elements.

To gain a better insight into the behavior of the 2D model, a number of additional parametric runs were performed by varying the coefficient of friction and the axial feed. In the first case, shown in Fig. 5.4a, increasing the friction impedes the flow of the material circumferentially and each material point that comes into contact with the die tends to remain where it is. As the internal pressure increases, localized wall thinning in the regions where the tube detaches from the die tends to develop (i.e., at about 25° and 65° in Fig 5.4a). Friction tends to intensify the localization. Recall from Fig. 2.14b that these were exactly the locations of failure in the experiments.

The effect of the axial feed on the final wall thickness is shown in Fig. 5.4b. By increasing the axial feed, the formed tube becomes thinner in the flat regions and thicker in the curved ones. Interestingly, the minimum thickness around the circumference appears to be much less sensitive to the axial feed.

5.1.2 Design of the Hydroforming Experiments

The 2D model was used extensively for the design of the hydroforming experiments described in Chapter 2. Given a tube geometry and a target shape, the computational efficiency of the model allows the user to quickly generate estimates of the required loading parameters. With the benefit of this initial guess, the design can be further evaluated and streamlined with the aid of more detailed but also computationally more intensive 3D simulations.

The philosophy employed in the design of our hydroforming experiments (Chapter 2) is to gradually increase the axial feed and the internal pressure in a manner that avoids load maxima, associated with buckling and wrinkling instabilities. Figure 5.5a shows an axial force-internal pressure-axial feed response from such a process parameter study with the 2D model. Note that the force reported is the one acting on the specimen only and that it increases monotonically. Four deformed configurations in Fig. 5.5b show the evolution of the cross section and correspond to the locations marked in Fig. 5.5a. In configuration ① the tube is in partial contact with the die. Interestingly, as the axial feed is exhausted the tube is still not in full contact with the die, which prompts the further pressurization (calibration phase, see also Sect. 2.2.1). The pressure required for full contact exceeds 5,000 psi: configuration ③ at 5,500 psi is seen to be in full contact with the die.

5.1.3 Numerical Results

Despite its simplicity, the 2D model can provide fairly reasonable estimates for a variety of features of the hydroforming process. The final deformed configuration as predicted by this model for HY5 is shown in Figs. 5.6a (equivalent stress) and 5.6b (equivalent plastic strain). In the flat regions of the tube, the stress contours appear as layers, which is typical of bending dominated problems. In the still curved part, the

contours also appear as layers, which is characteristic of a cylinder under internal pressure. In the boundaries between the flat and the curved parts, the 2D model predicts locally increased plastic deformation. Further localization of the deformation will eventually lead to failure at these locations.

The predicted wall thinning for the HY5 path is compared to the experiment in Fig. 5.7. The model reproduces the average wall thickness of the formed part quite well. However, it fails to capture the intensity of the localized deformation at the two locations where the flat sides meet the curved one. In one of these locations the wall thinning will increase further and will precipitate failure if the loading continues (see Fig. 2.14b). As will be shown later, even a fully 3D model fails to capture this feature when using the von Mises plasticity.

Clearly then, the 2D model offers significant advantages in the preliminary design of a process and in the selection of material, undeformed geometry and loading path to achieve a target shape. However, it is impaired by the use of an unsuitable, for the material at hand, constitutive model and hence the predictions of failure cannot be depended upon. Also, given the high friction encountered in the process, the coefficient of friction and the axial strain that will develop at the tube mid-span (which the 2D model simulates) can only be guessed at this stage. This situation invites the use of more advanced 3D models, which are also capable of including the constitutive framework developed in Chapter 4.

5.2 SHELL ELEMENT MODEL (3D-SH)

The yield functions detailed in Chapter 4 were originally developed to describe the anisotropy of metallic sheets. Hence they are either limited to plane stress (e.g., the Yld2000-2D model) or can be adapted to such states (e.g., the Karafillis – Boyce model). Furthermore, the models were calibrated from experiments on thin-walled tubes under

internal pressure and axial load, i.e., where the through thickness stresses can be neglected. Naturally then, to employ these models as well as to take into account the three-dimensional features of the tube hydroforming process, the next step in the numerical modeling employs shell elements. It should be noted that shell element calculations constitute at the time of the writing of this report the standard industrial practice in sheet and tube forming simulations.

5.2.1 Model Set-up

A schematic of the shell element model is shown in Fig. 5.8. Taking into account the symmetries of the problem (see Fig. 2.1), only one eighth of the actual tube is considered. The model is meshed with linear, reduced integration shell elements (S4R), capable of course for large deformations. The mesh employed features 77×40 (length \times circumference) elements and uses Simpson's rule with 7 integration points for the through-thickness integration of the field equations. This mesh was arrived at after suitable parametric studies, shown in Figs. 5.9 to 5.13. In the order presented in these figures, the performance criteria examined were the final shape at mid-span, $x = 0$ in. (Fig. 5.9), the axial load-feed response (Fig. 5.10), the distribution of axial compressive strain along the tube (Fig. 5.11), and the final wall thickness at mid-span (Figs. 5.12 and 5.13). The variables investigated were the number of elements in the axial direction, in the circumferential direction, and the through-thickness integration rule. The results of the parametric simulations shown in Figs. 5.9 to 5.12, demonstrate that 77 elements along the length and 40 around the circumference of the model are sufficient. Also, the use of the alternate integration rules available in Abaqus did not give different results (see Fig. 5.13), hence the default option is used subsequently (Simpson rule with 7 integration points through the thickness).

It is worth noting that the number of elements in the circumference is less than half of those employed in the 2D model. Interestingly, finer meshes do not result in better performance. This can be explained by considering the aspect ratio of the different element arrangements. For the 77×40 mesh, the in-plane dimensions of each element are 0.206×0.045 in. (length \times circumference) while the undeformed thickness of the tube is 0.080 in. Thus, further refining the mesh in the circumferential direction results in poorly shaped shell elements and should be avoided. In addition, the variations encountered in the axial direction are much milder than those in the circumferential one (see Figs. 2.15a and 2.18) and hence a relatively coarse mesh (axially) is sufficient. For these reasons, a locally refined mesh around the tube mid-span did not yield different results either.

There is a variety of options available in Abaqus for the modeling of contact with shell elements. The default is that the reference surface is the mid-surface of the shell, and contact takes place between this surface and the rigid die. This was chosen because of its simplicity.

5.2.2 Numerical Results

A deformed configuration from the shell element model is shown in Fig. 5.14, for HY5 (the model has been reflected about the $\theta=0$ and $\theta=\pi/2$ planes). The axial non-uniformity of the shape of the formed tubes that is due to the friction (see Figs. 2.14 and 2.15a) is reproduced by the numerical model very well. In fact, the model can be used to accurately calculate the coefficient of friction μ : in Fig. 5.15 the resulting compressive axial strain distributions along the tube for different values of μ are compared to the experimental one for HY8. A value of $\mu=0.2$ provides the best correlation between experiment and analysis and will be used throughout this work.

The shell element model can be used in conjunction with the 2D model (see Section 5.1.2) to design a hydroforming process given the target shape and to predict the

properties of the formed tube. For example, the final thickness distribution of the tube is shown in Fig. 5.16. As a result of the friction, the thickness contours vary along the length of the tube with the most precarious conditions occurring at mid-span ($x = 0$ in.). The localized wall thinning is predicted to occur at the locations where the flat sides meet the curved ones, as in the experiment. The areas of the figure that are colored in gray have become thicker than the undeformed tube (0.080 in.), as a result of the friction encountered in the die. The actual measurements of thickness for the same experiment (HY5) were presented in Fig. 2.18 and confirm the numerical results.

The various constitutive models described and calibrated in Chapter 4 can be straightforwardly used with the shell element model of tube hydroforming. Since this model also includes the 3D geometry and the friction, it is interesting to examine the effect of the yield function on the numerical predictions of failure. In Fig. 5.17, the compressive load on the specimen is plotted with the axial feed for HY8 from the shell elements with the various models employed and is compared to the experiment. It appears that switching to a non-quadratic yield function lowers somewhat the predicted responses, however the details of each yield function do not make much difference. Similarly, the prediction of the axial compressive strain variation along the tube shown in Fig. 5.18 also appears to be insensitive to the model used. These findings are perhaps to be expected since the plotted quantities correspond to the overall structural response of the tube, in the presence of contact and friction. In both figures however, the good agreement between experiment and analysis is noted.

What is more interesting in the context of failure prediction is the performance of the different constitutive models in the neighborhood of failure, i.e., at the tube mid-span. As shown in Fig. 5.19, the final shape of the mid-surface at mid-span is dependent to

some extent on the constitutive model, with the higher exponents leading to more pronounced deformation of the curved part of the cross-section.

The prediction of the final wall thickness by the constitutive models described in Chapter 4 is presented in Figs. 5.20 and 5.21 and is compared to the experiment for the HY5 case. The effect of the anisotropic description is shown in Fig. 5.20. Most of the models considered yield approximately the same results. An exception is the isotropic Hosford with an exponent of 8, which produced more wall thinning and more pronounced localization. This finding is in drastic contrast with the results presented in Chapter 4 for the simulation of the free inflation experiments. In that problem, the details of each constitutive model had a much more profound effect on the prediction of rupture, which actually prompted the examination of additional models until a satisfactory performance was finally achieved.

The effect of the yield function exponent on the predictions of wall-thinning is examined in more detail in Fig. 5.21 using the isotropic Hosford model. It is shown that increasing the exponent intensifies the localization, at the expense however of the quality of the prediction of wall thinning in the rest of the circumference. In addition, there would be no way of deciding on the appropriate exponent to capture the localization if the experimental value had not been available.

In summary, we have seen that switching to a non-quadratic yield function improves the prediction of localization. At the same time, unlike the problem of free inflation, tube hydroforming in the context of a shell element model, is not particularly influenced by the specifics of each description of anisotropy. It will now be shown that these conclusions are not completely true if one switches to a more elaborate numerical model using solid elements.

5.3 SOLID ELEMENT MODEL (3D-SO)

The objective of this model is to reproduce exactly the three-dimensional features of the hydroforming problem, but in contrast to the shell element model described in Section 5.2, to also capture and monitor the evolution of stress triaxiality in the regions of the tube that are in contact with the die and the evolution of localization.

5.3.1 Model Set-up

Once again the symmetries allow only one-eighth of the actual tube to be considered. The model is meshed with linear, 8-node solid elements with full integration (C3D8), arranged as $45 \times 60 \times 3$ (axial \times circumference \times thickness). The model is shown in Fig. 5.22a, with a close up at mid-span given in Fig. 5.22b. As before, the relatively mild variations along the length of the tube in comparison to the circumference has allowed for a mesh with axially elongated elements. The mesh convergence studies are included in Figs. 5.23 to 5.25. As before, we seek the optimal number of elements in the axial, hoop and thickness directions. The axial load-feed response is given in Fig. 5.23, the distribution of axial compressive strain along the tube in Fig. 5.24 and the final wall thickness at mid-span in Fig. 5.25. It can be concluded that at least 3 elements through the thickness, 60 around the circumference and 45 along the length are required for best performance.

5.3.2 Numerical Results

The hydroforming experiments were simulated with the solid element models and the results presented in the following figures. Once again several constitutive frameworks will be considered. Figure 5.26 shows the deformed configuration of the tube. The effect of the coefficient of friction in the non uniform final shape is quite obvious, as was the case with the shell element model in Fig. 5.14. Another rendering of the original and the

deformed configurations is given in Fig. 5.27. The equivalent plastic strain contours are shown in Fig. 5.28 for the isotropic Hosford model with an exponent of 8. It can be seen that there is significant deformation at the feeding end of the tube, which as reported earlier is due to wall thickening. At mid span, the model predicts localized wall thinning at the expected locations. An interesting feature is that in any one quadrant, one of the thickness wells tends to deepen at faster rate than the other (see later discussion). The contact pressure contours between the tube and the die are given in Fig. 5.29. The boundary of contact between the tube and the die is outlined very neatly by the highest pressure contour, as expected.

Quantitative comparisons of the solid element models to the hydroforming experiments is given next. In addition to the constitutive models presented in Chapter 4, here we will also include results based on a more recent 3D extension of the anisotropic Yld2000-2D of Barlat *et al.* designated as Yld2004-3D. The model is outlined in Appendix A while the subroutine used was provided by Yoon (2009). The axial load-feed responses calculated for HY2 with the solid elements using 3 constitutive models appear in Fig. 5.30 along with the corresponding experimental one. The three models yield similar predictions, as noticed earlier from the shell element simulations, while the agreement of all three models with the experiment is very good. Similar is the conclusion from Fig. 5.31 which shows the distribution of axial compressive strain along the formed tube. Figures 5.32 and 5.33 show comparisons of predicted and measured wall thinning for HY6 and HY2 respectively. In these results the three constitutive models yield significantly different predictions. It can be seen that a non-quadratic yield function promotes the localization much more than the von Mises plasticity model does. This is particularly pronounced in the two zones of localized wall thinning at approximately 25° and 65° . It is interesting to also observe that at some stage, one of the sites overtakes the

other one, as is natural in localization problems. Depending on the specifics of each loading path, incorporation of anisotropy may or may not have a noticeable effect on the thinning predictions, at least for the present material (compare Fig. 5.32 for HY6 to Fig. 5.33 for HY2). The present results support the conclusion drawn earlier from the shell element calculations, namely that the specifics of the description of anisotropy appear to be much less crucial in tube hydroforming than they were for the free inflation problem. The difference however between the two sets of results is that in the solid element models, the calculated thickness wells approach the experimental measurements more closely (compare Figs. 5.20 and 5.32 or 5.33).

A set of solid element results that illustrate the effect of the exponent of the yield function on the predicted localized wall thinning at mid-span is shown Fig. 5.34. Notice that despite the thickness being approximately the same in the rest of the tube, increasing the exponent leads to much more intense localization of wall thinning. The evolution of wall thinning with pressure is shown in Fig. 5.35. While the wall thickness is initially uniform, as the deformation progresses and the tube-die contact is established, the friction encountered promotes the development of two wells in the circumferential distribution of the thickness. This deformation pattern is stable up to some pressure, but at higher values the deformation localizes in one of the two wells and grows precipitously leading to failure (not included in the model). Simultaneously the thickness well at the second site stops growing. This “bifurcated” behavior is better illustrated in Fig. 5.36 where the thickness reduction in the two wells is plotted against the pressure. The critical pressure is approximately 4400 psi. Interestingly this is very close to the pressure at which the HY6 tube failed in the experiment.

5.4 DISCUSSION

We now summarize the main findings from the numerical simulations of tube hydroforming. First, a 2D model, although capable of reproducing most of the structural aspects of the process is unsuccessful in capturing localization and by extension, failure. Prompted by the results of the free inflation study, the problem was tackled next with shell elements using increasingly more complex constitutive models. However, this model did not prove to be adequate for hydroforming, either.

The results indicate that correct simulation of the evolution of localized wall thinning requires a fully 3D model using solid elements. This can be attributed to the triaxiality that is associated, first with the contact of the structure with the die and second with the actual necking process. In the regions that are in contact with the die, the tube is acted upon by the internal and contact pressures. Hence, non-negligible through thickness stresses develop. In addition, necking is triggered and regulated by the tube-die contact and by the resulting friction. This causes a relatively stable deformation, with multiple necks forming around the circumference and growing gradually with pressure (see Fig. 2.18 and 5.35). Capturing the stress triaxiality and the growth of the necks, both essential for accurate failure predictions, requires the use of solid elements.

By contrast, in the free inflation problem rupture is precipitated by a structural limit load instability. Failure is once more localized necking but one that occurs soon after the limit load in a sudden and dynamic fashion. Thus the simulation of the problem can be terminated at the onset of localization. In other words, it is not necessary to track the evolution of the localized wall thinning. Since the stress state up to the onset of localization is essentially two-dimensional (negligible through thickness components), it can be adequately represented by a shell element model. This is a crucial difference

between the two problems and the reason behind the requirements for different FE formulations.

Interestingly, Cho *et al.* (2002) observed a similar need for a switch to solid elements in predictions of necking in sheet metal stamping. Despite the thin-walled geometry, the contact with a die can result in triaxial stress states locally that can only be captured by a 3D formulation.

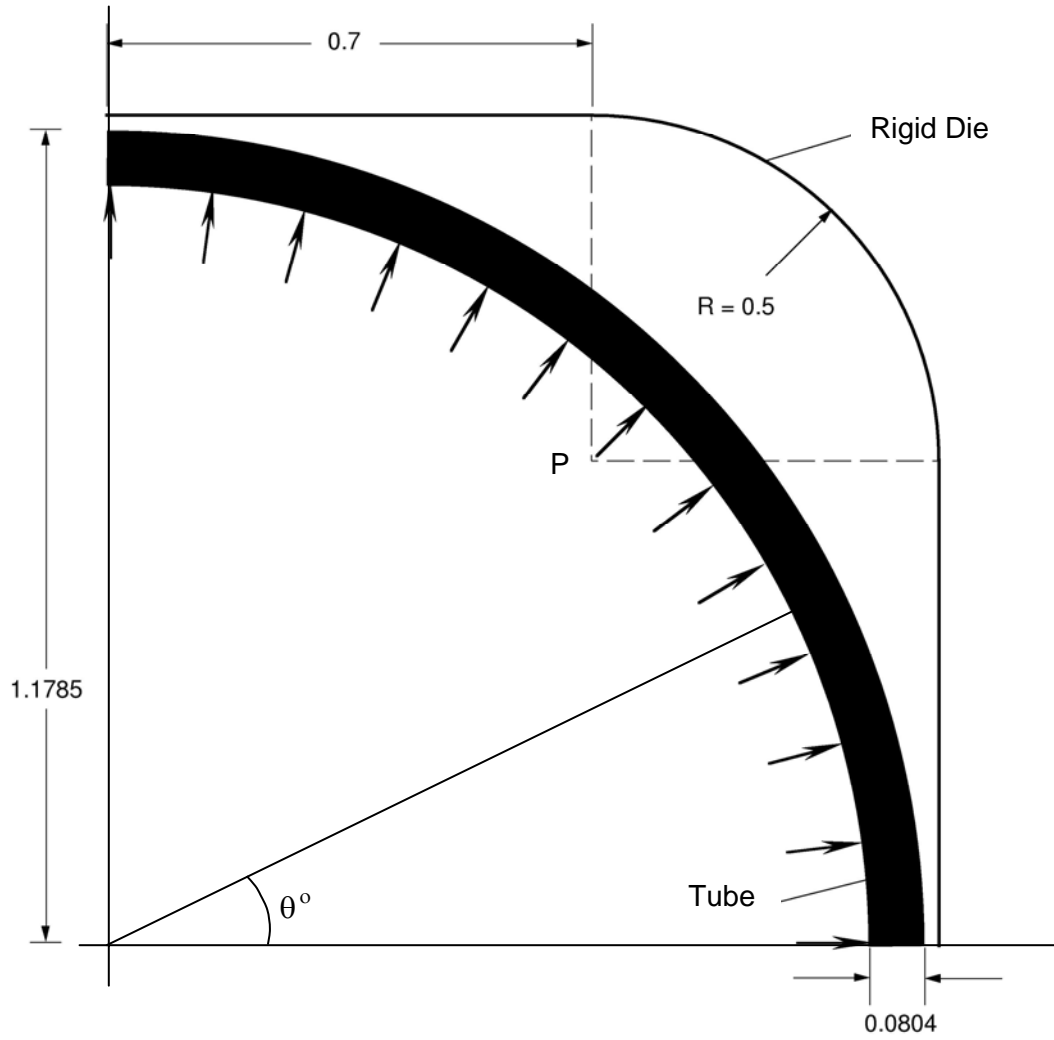


Fig. 5.1 – Problem geometry in 2D: all dimensions in inches. Note the initial gap between the tube and the die.

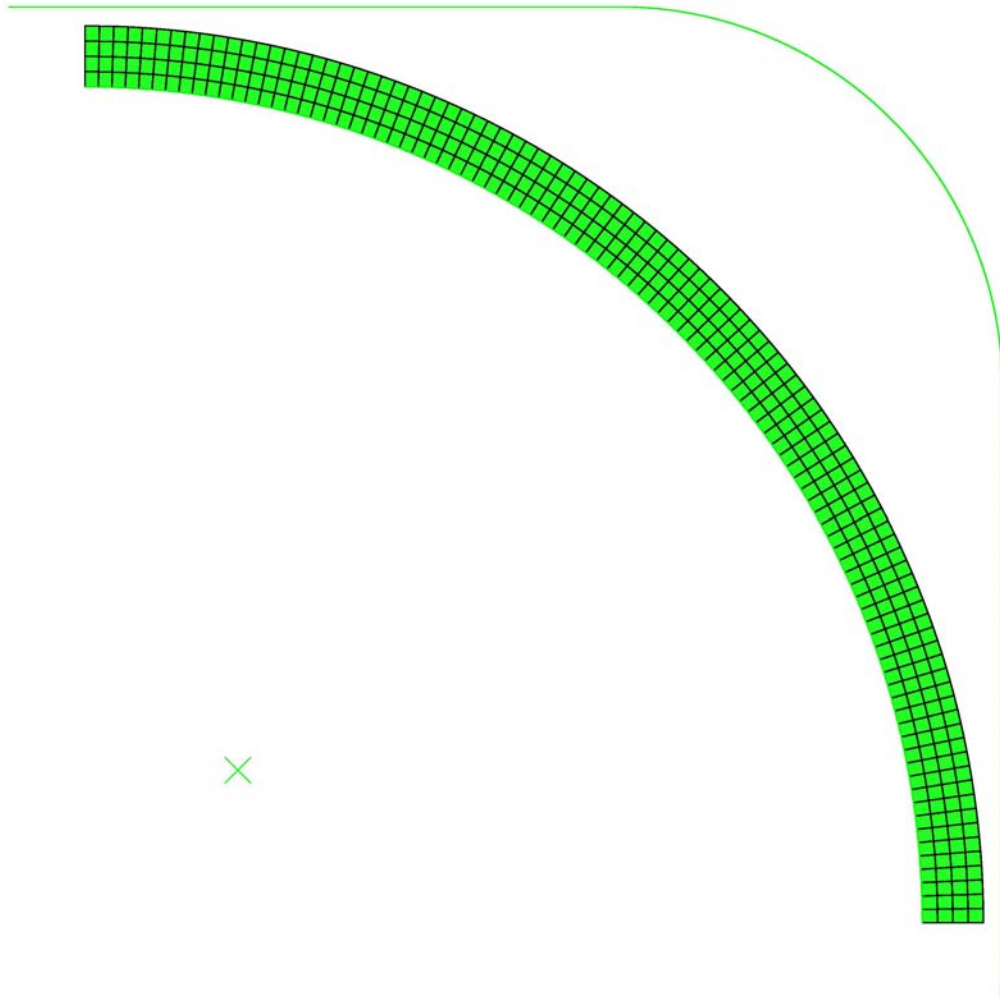
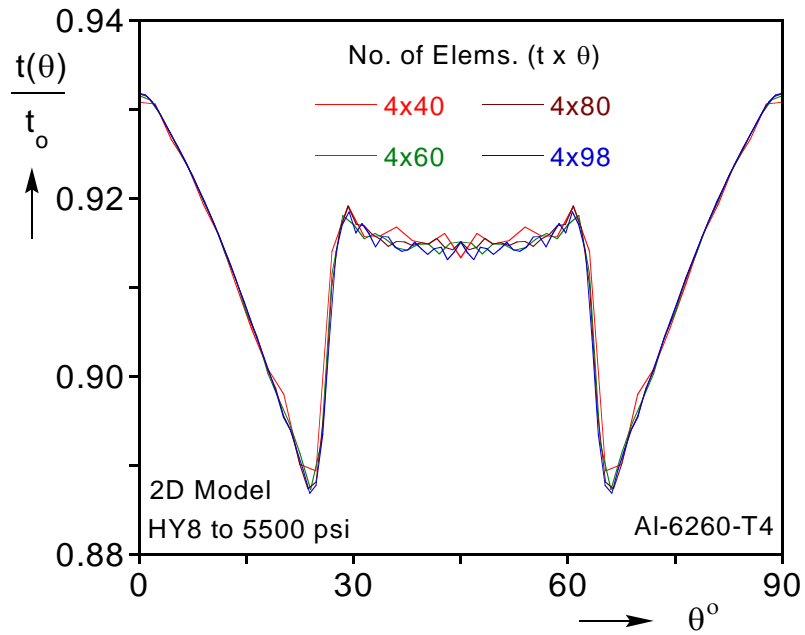
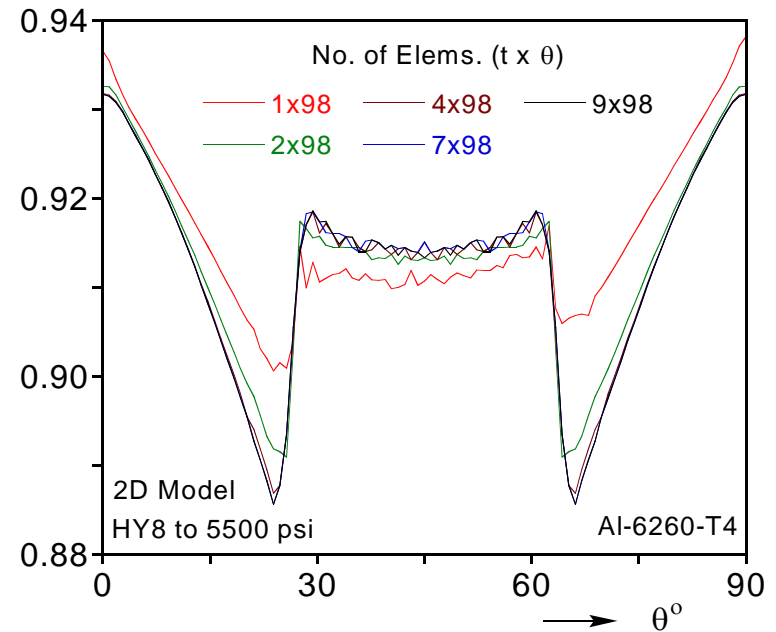


Fig. 5.2 – Finite element mesh used with the generalized plane strain elements (dimensions given in Fig. 5.1).



(a)



(b)

Fig. 5.3 – Convergence study for the effect of number of (a) circumferential and (b) through-thickness elements on the prediction of wall thinning.

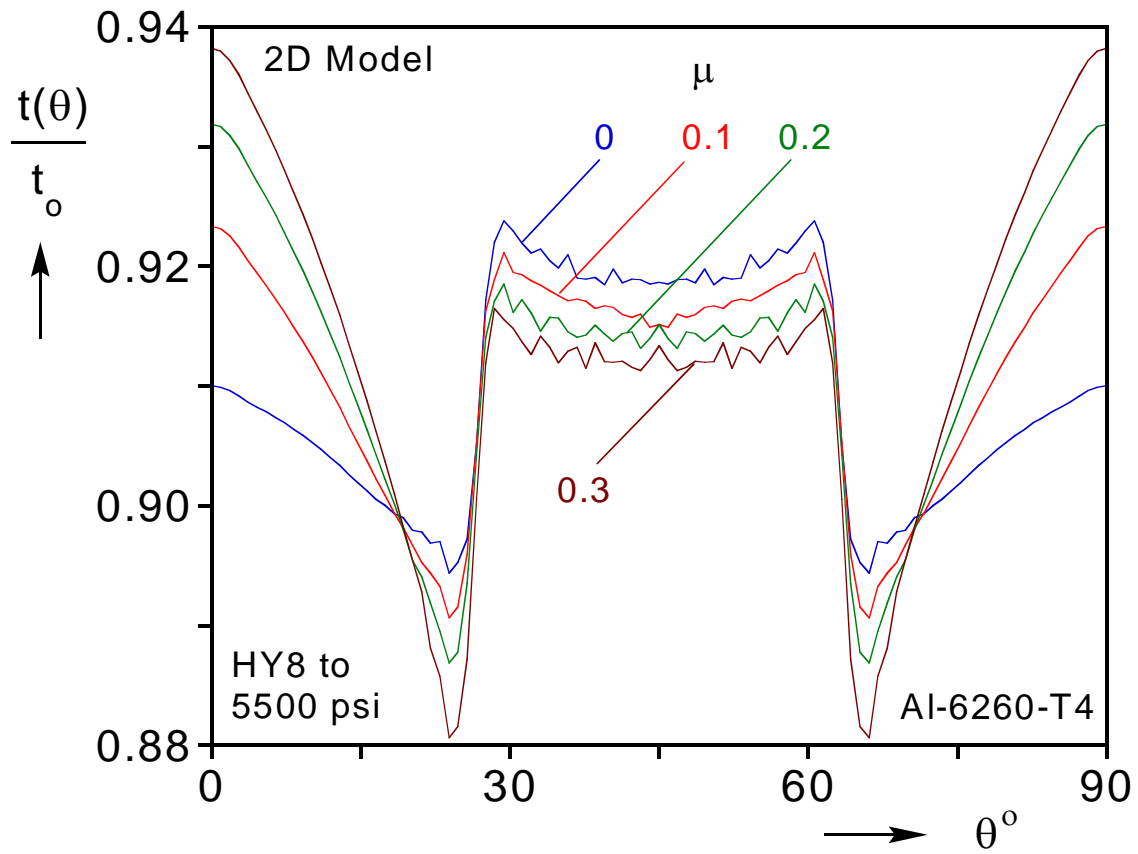


Fig. 5.4(a) – Effect of friction coefficient on the prediction of wall thickness distribution at mid-span

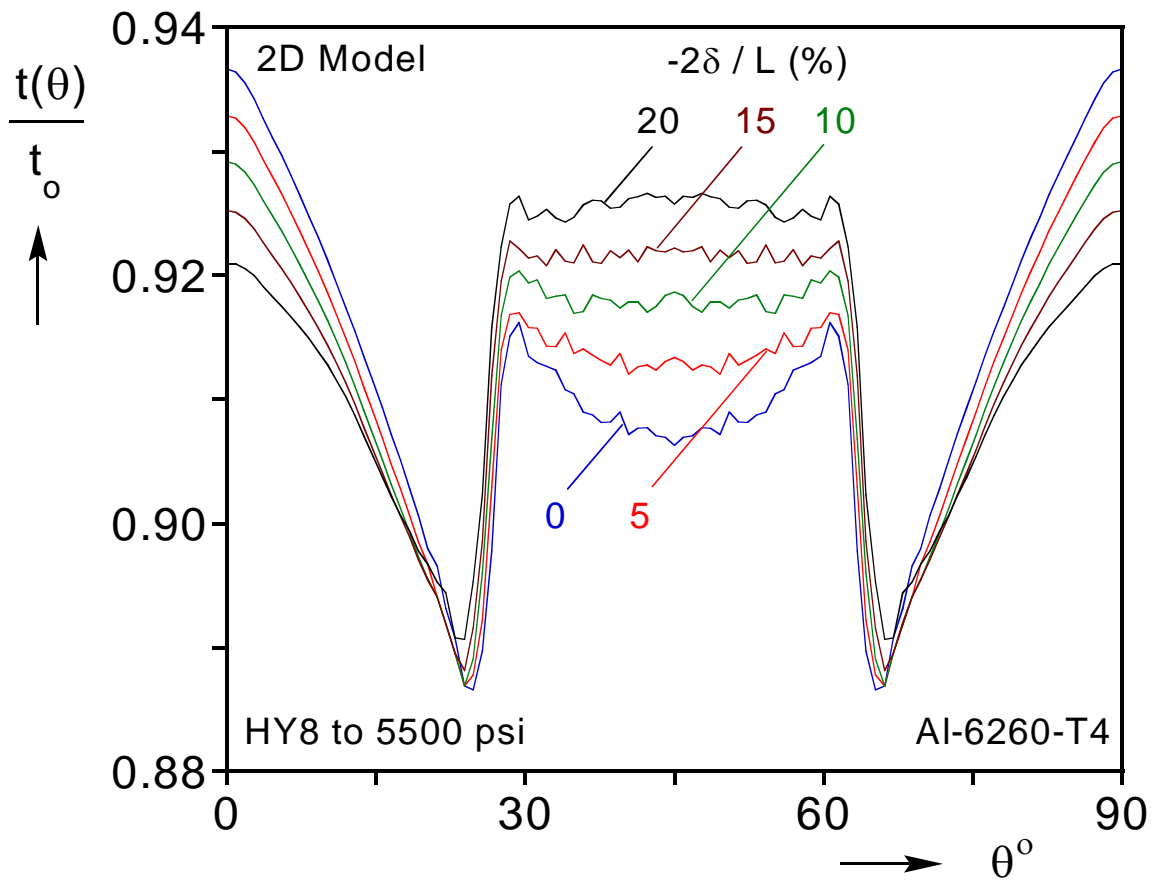
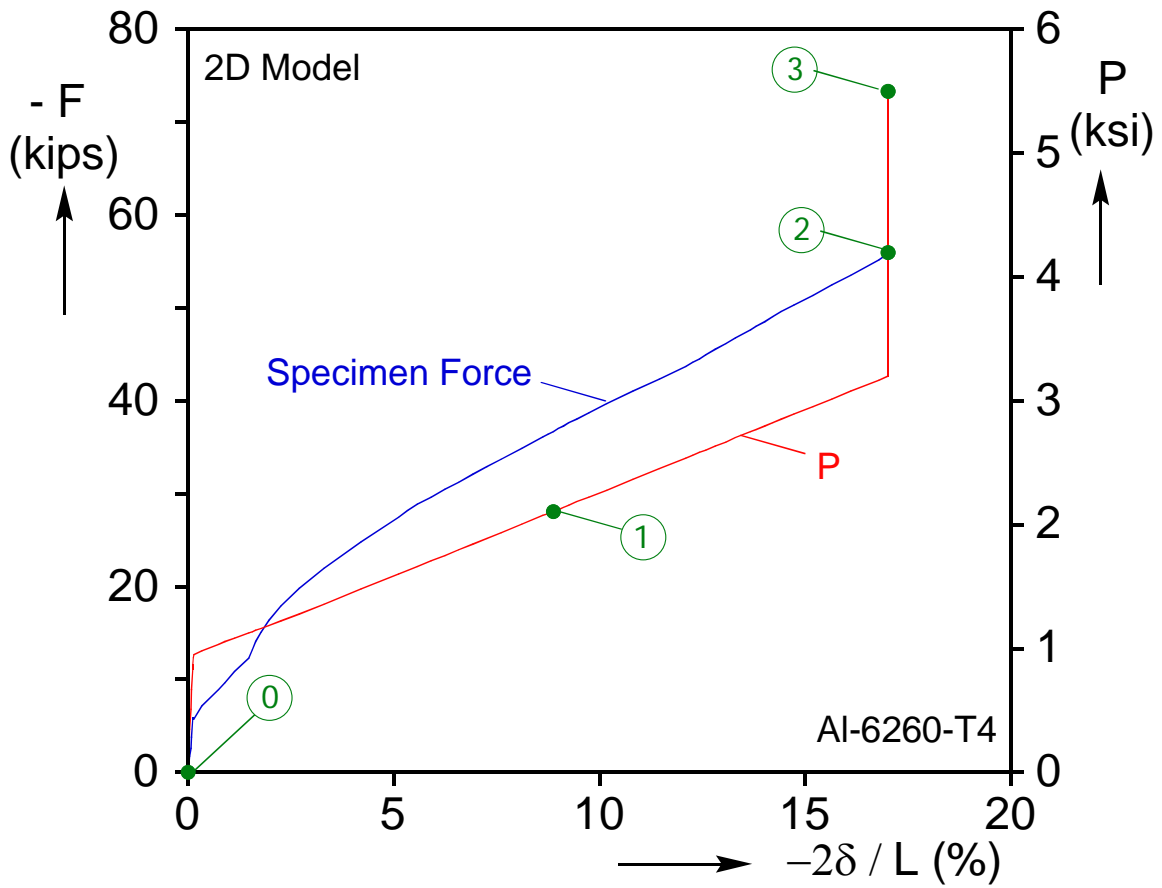
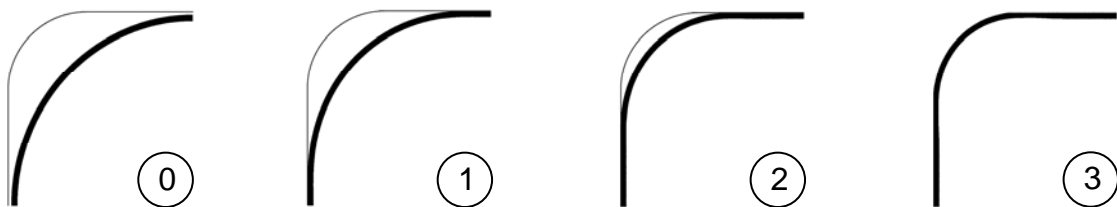


Fig. 5.4(b) – Effect of axial feed on the prediction of wall thickness distribution at mid-span



(a)



(b)

Fig. 5.5 – Results from a 2D simulation used to select hydroforming process parameters. (a) Load – pressure – axial feed history, and (b) predicted cross-section deformed configurations.

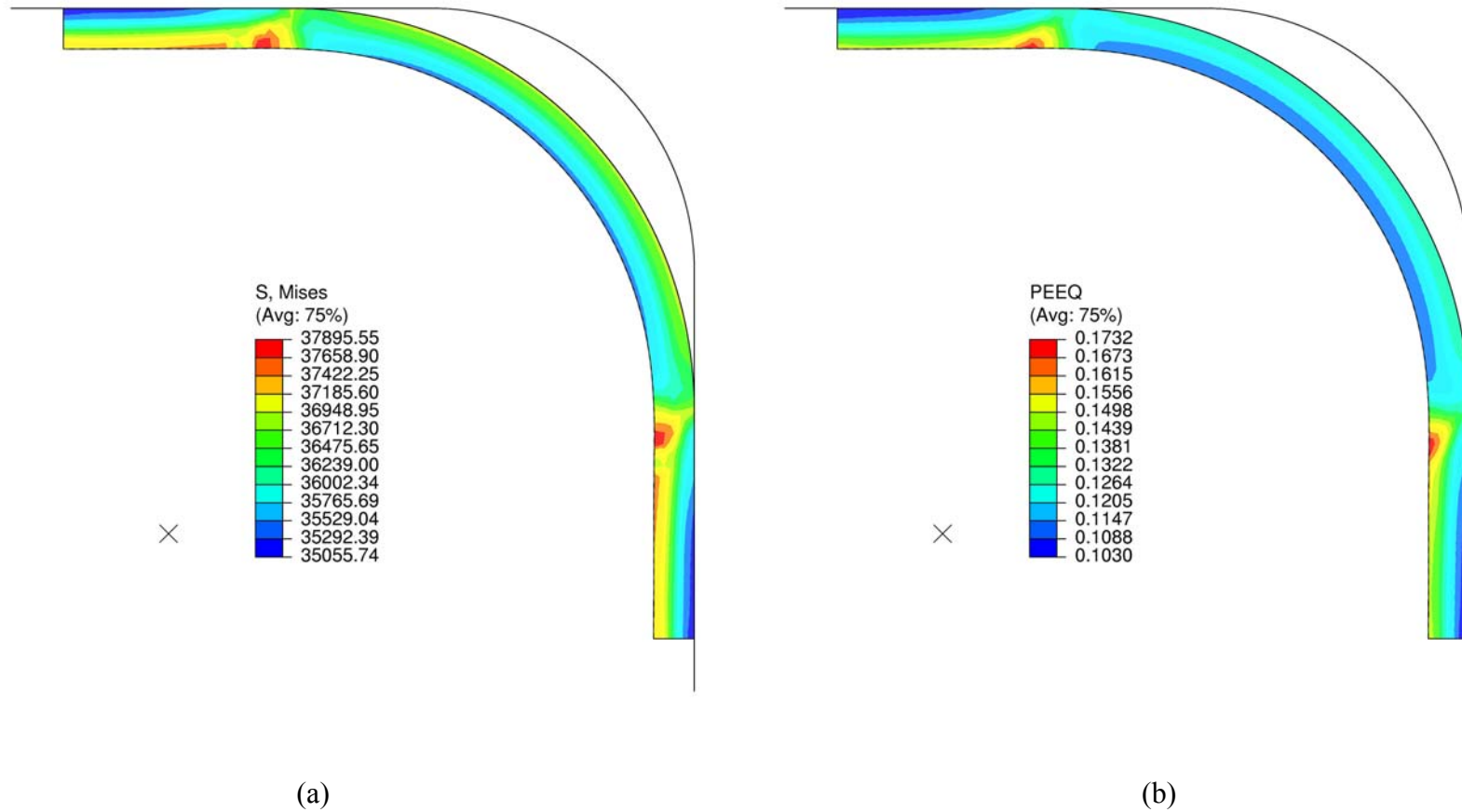


Fig. 5.6 – Results from numerical simulations of experiment HY5 using the 2D model with von Mises plasticity. (a) Equivalent stress, and (b) equivalent plastic strain.

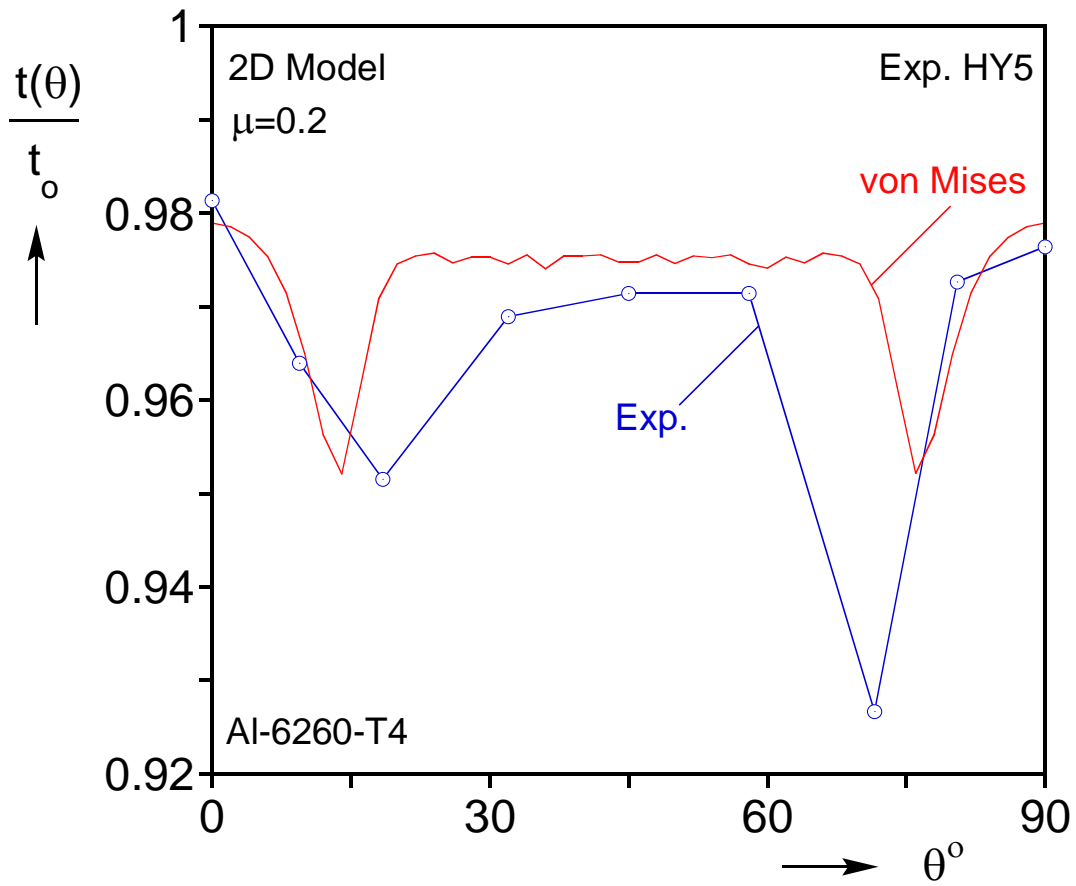


Fig. 5.7 – Experimental and predicted circumferential distribution of wall thickness at mid-span (2D model using von Mises plasticity).

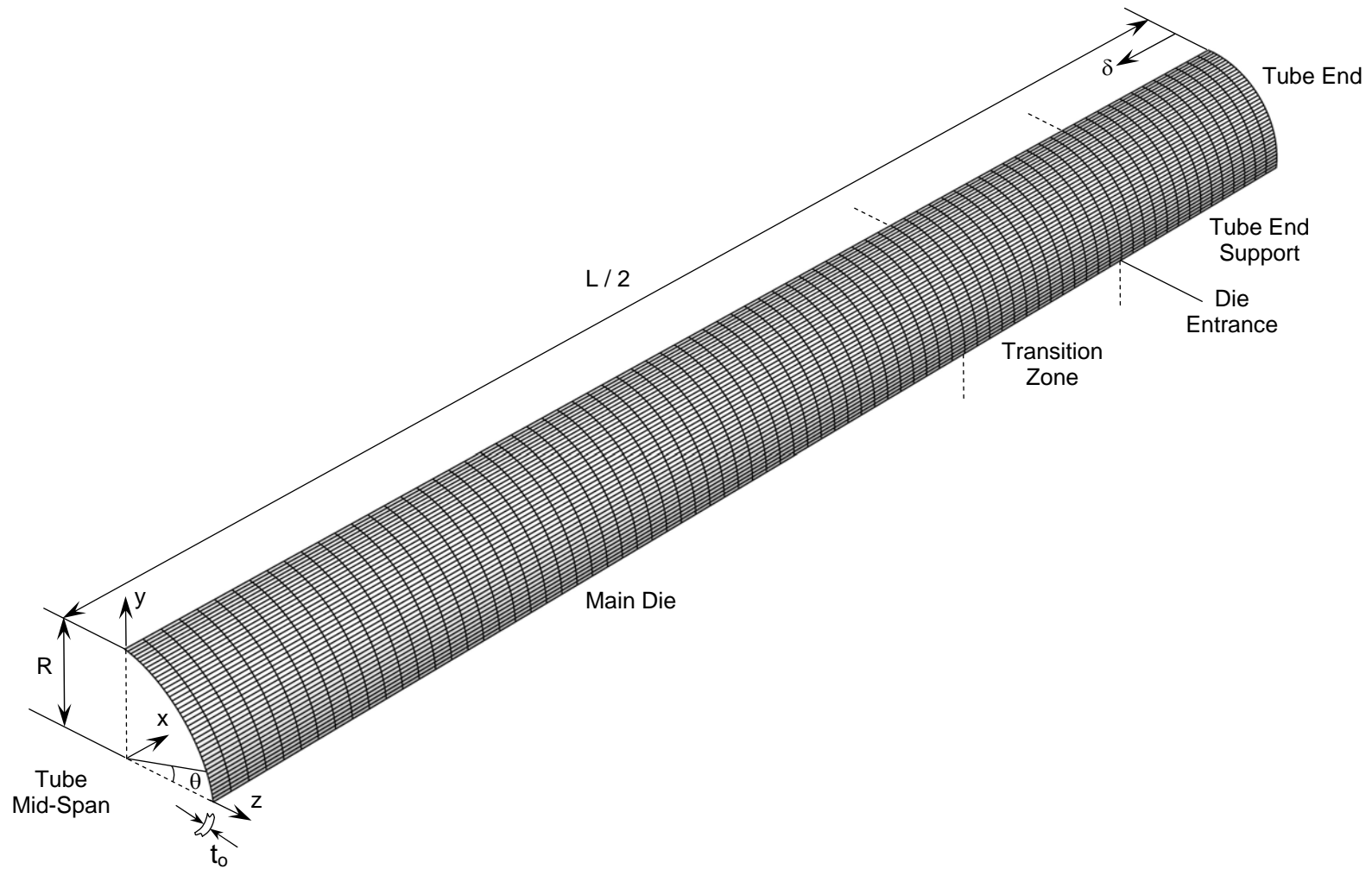
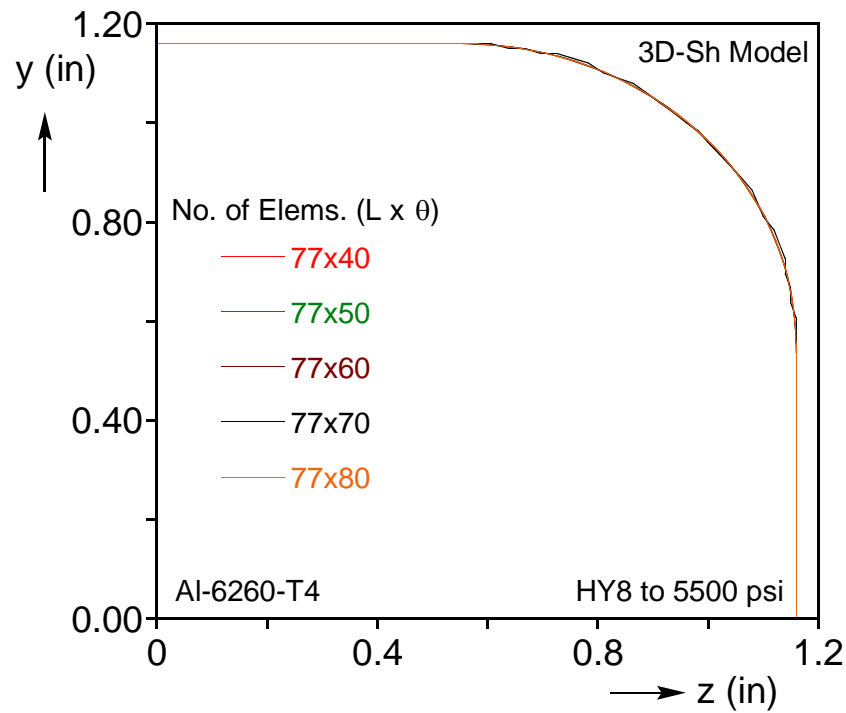
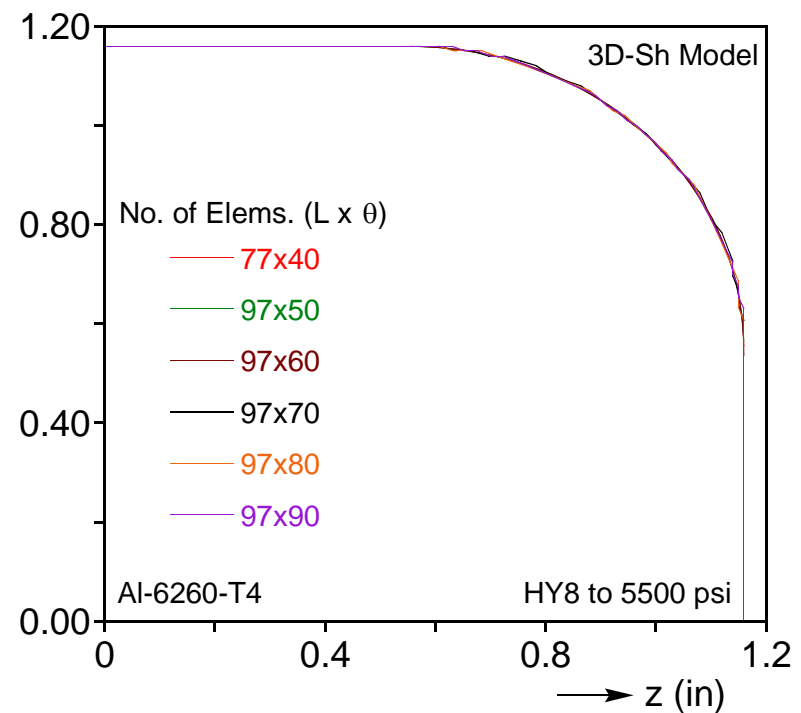


Fig. 5.8 – Undeformed mesh using 77×40 shell elements ($L \times \theta$), showing $1/8^{\text{th}}$ of the tube (surrounding die has been removed for clarity).

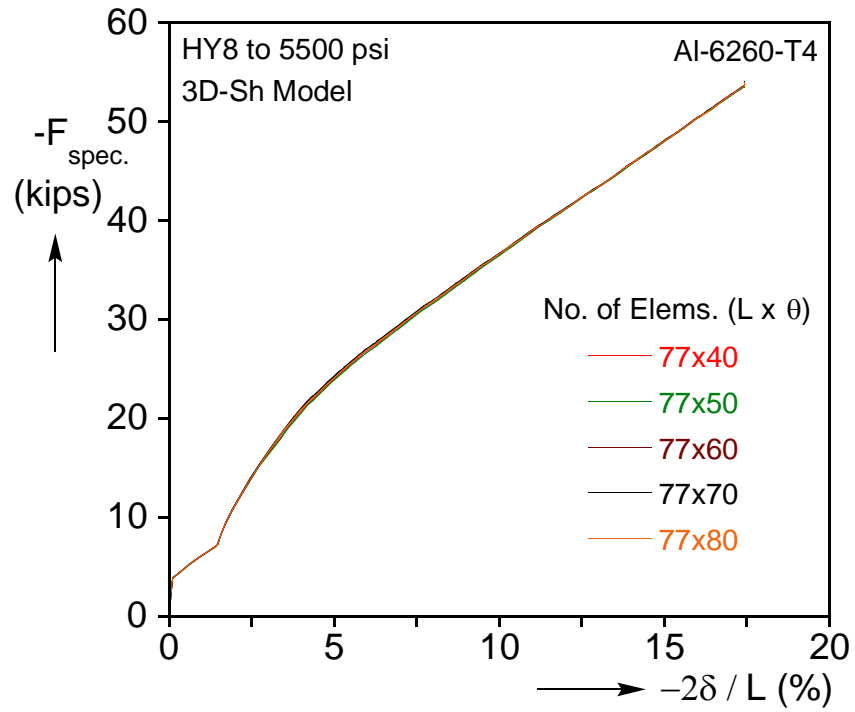


(a)

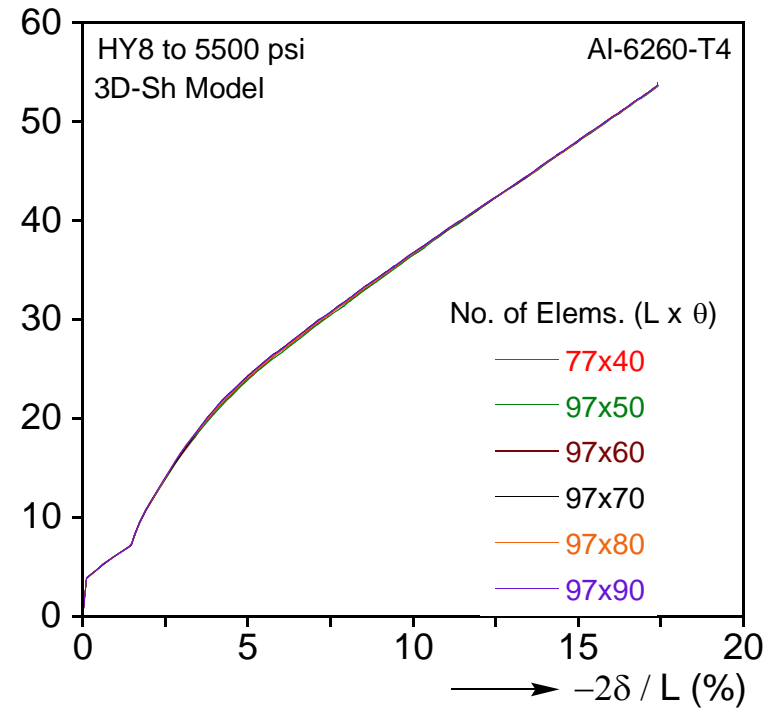


(b)

Fig. 5.9 – Effect of number of elements on the prediction of the mid-surface final shape at mid-span. (a) 77 elements along the tube, and (b) 97 elements.

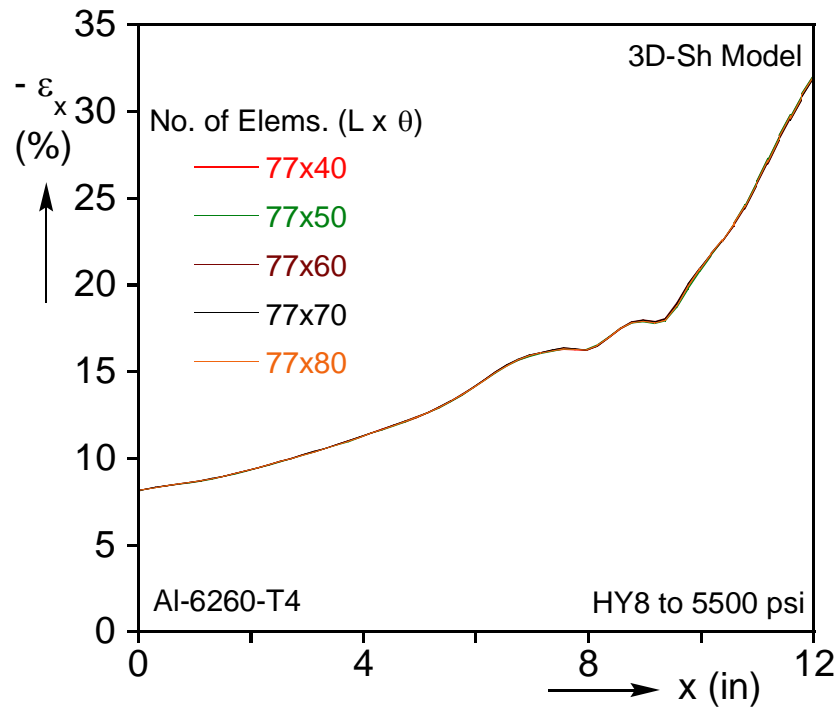


(a)

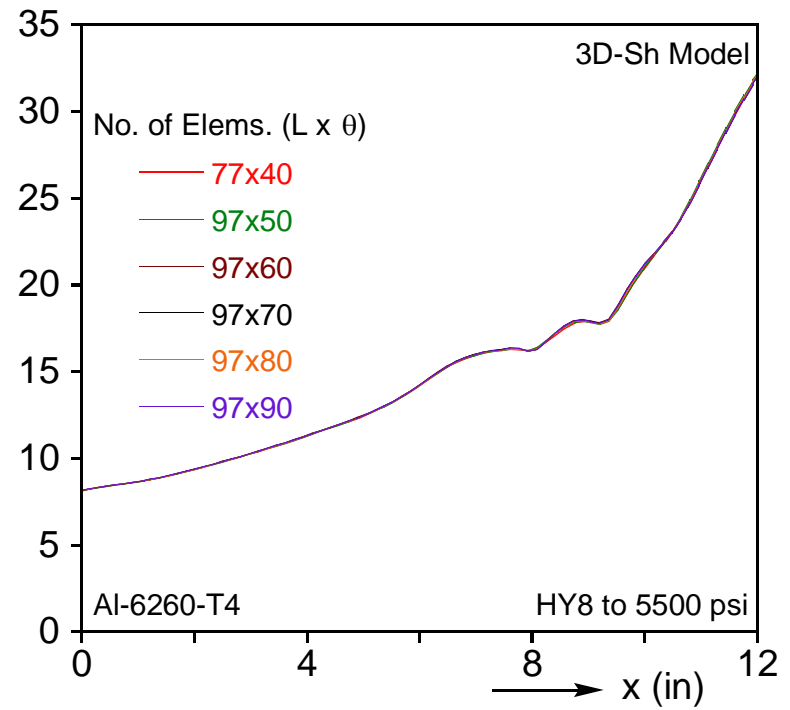


(b)

Fig. 5.10 – Effect of number of elements on the prediction of load on specimen vs. axial feed response. (a) 77 elements along the tube, and (b) 97 elements.



(a)



(b)

Fig. 5.11 – Effect of number of elements on the prediction of axial strain along the formed tube. (a) 77 elements along the tube, and (b) 97 elements.

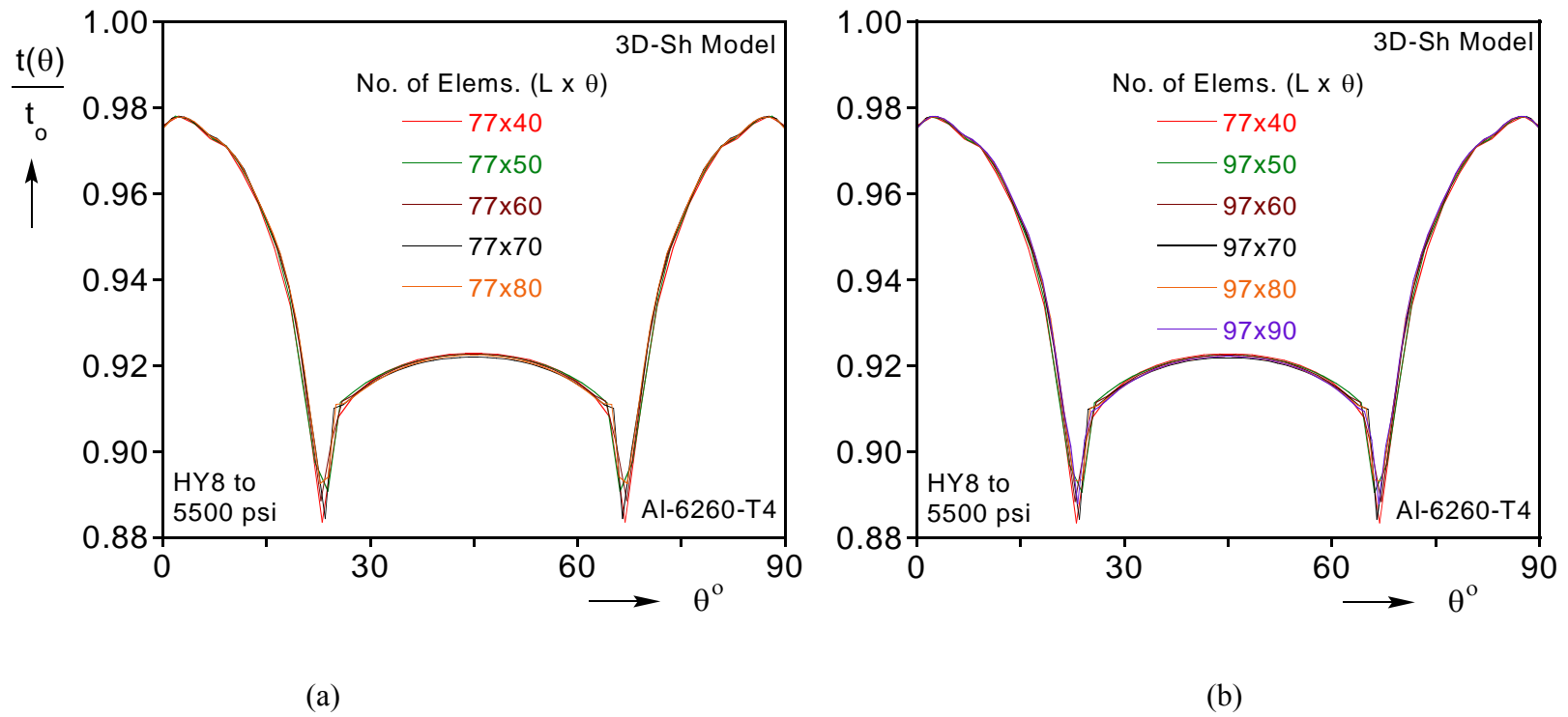


Fig. 5.12 – Effect of number of elements on the prediction of wall thickness distribution at mid-span. (a) 77 elements along the tube, and (b) 97 elements.

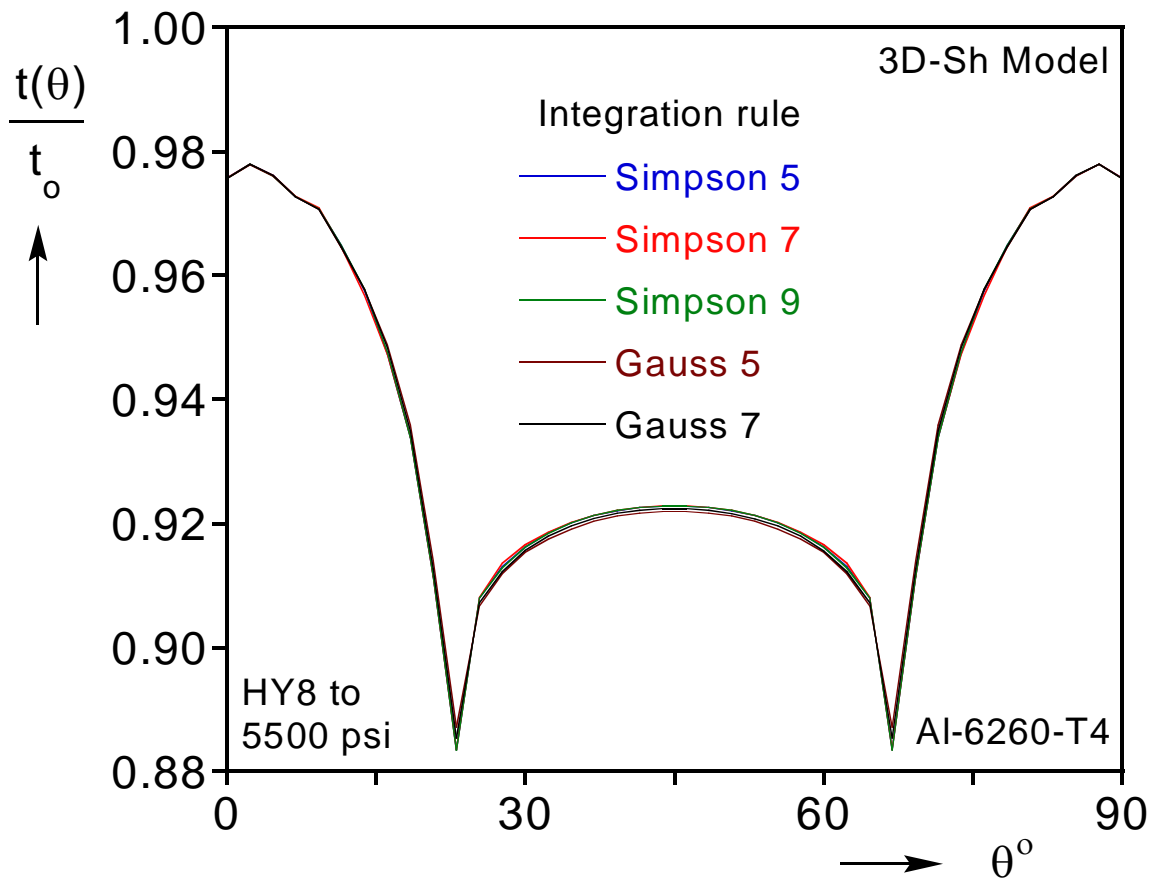


Fig. 5.13 – Effect of type of integration rule on the prediction of wall thickness distribution at mid-span.

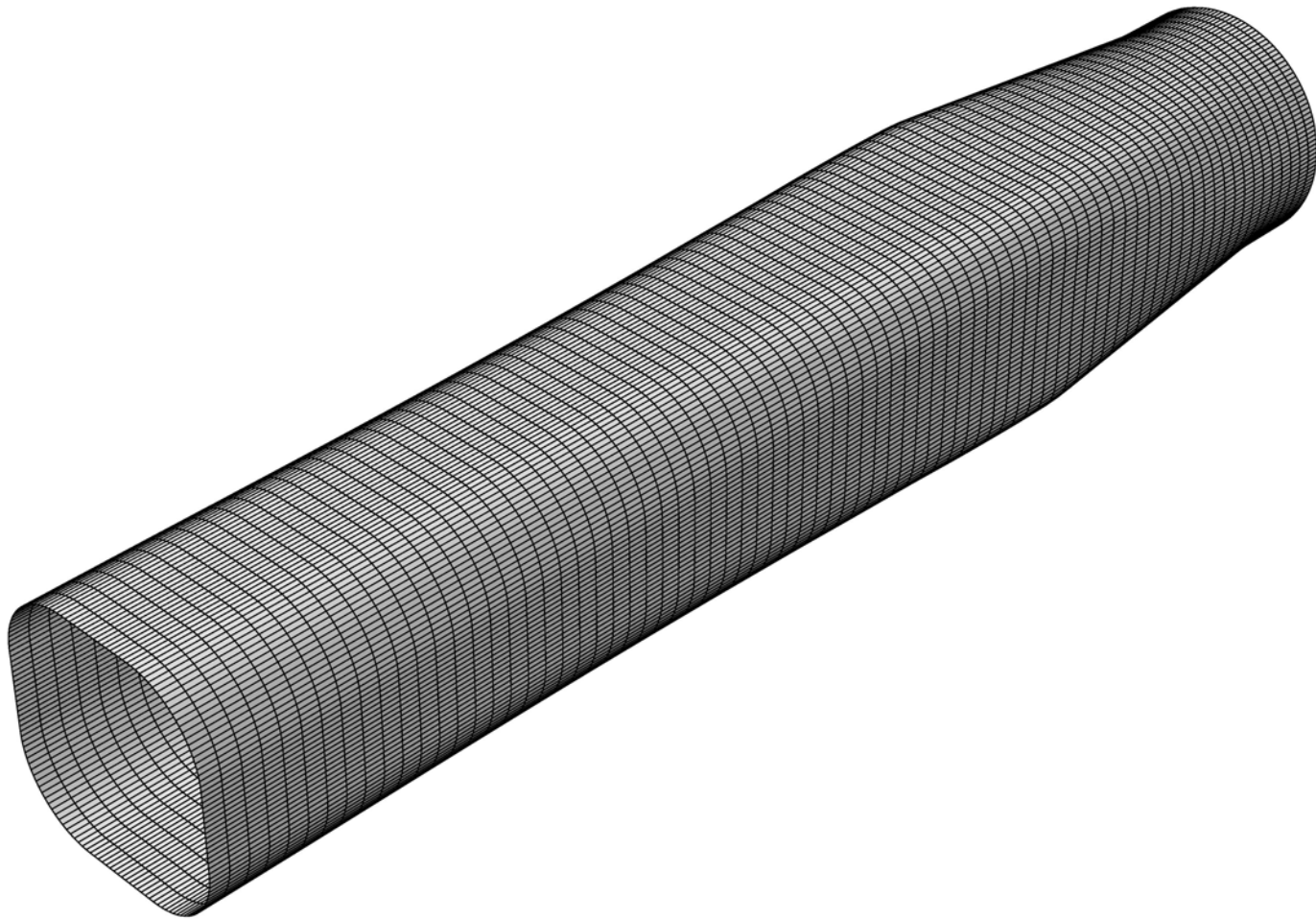


Fig. 5.14 – Deformed configuration for experiment HY5 using shell elements with $\mu = 0.2$ and the Hosford plasticity model (isotropic case, $k=8$). Surrounding die has been removed for clarity and the model has been reflected about the $\theta = 0$ and $\theta = \pi/2$ planes. Notice the variation of shape along the length and compare with the experiment in Fig. 2.14a.

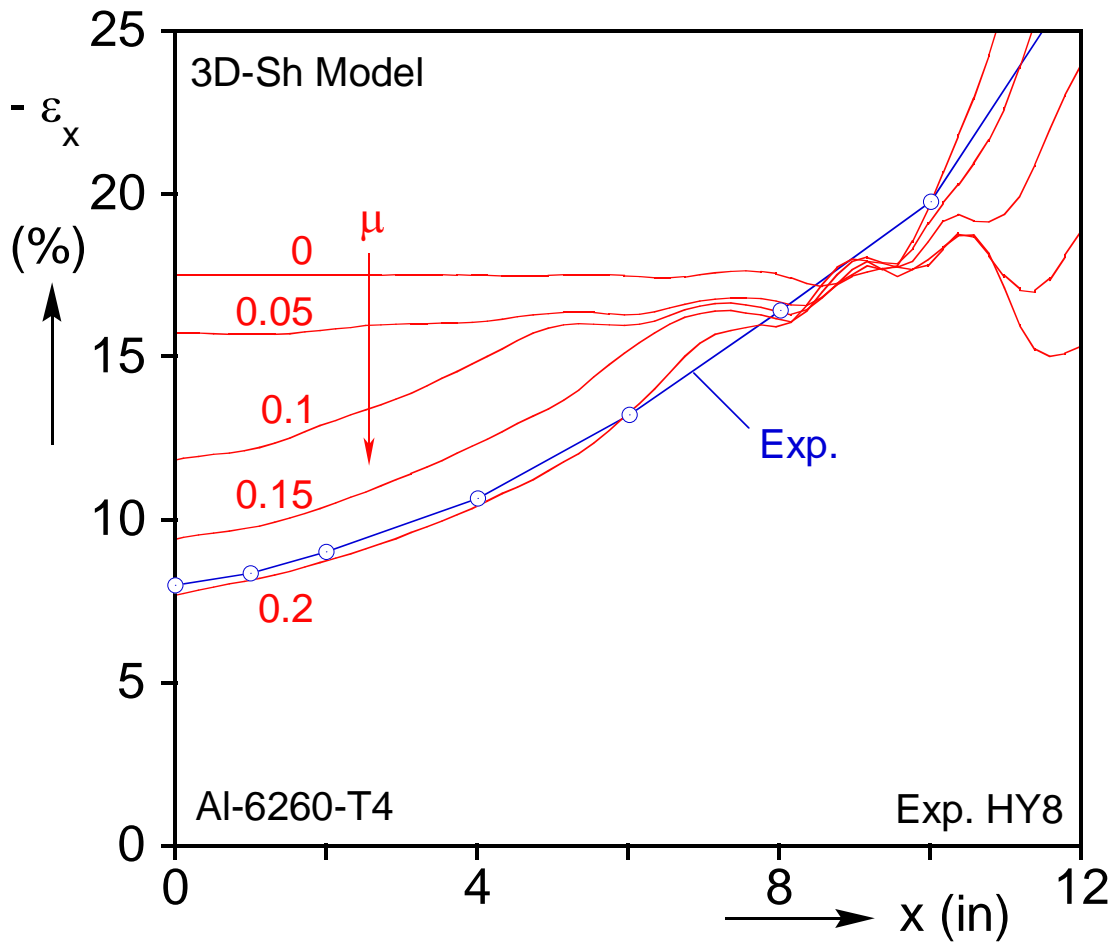


Fig. 5.15 – Predictions of the axial strain variation along the formed tube for different coefficients of friction and comparison to experiment, using von Mises plasticity.

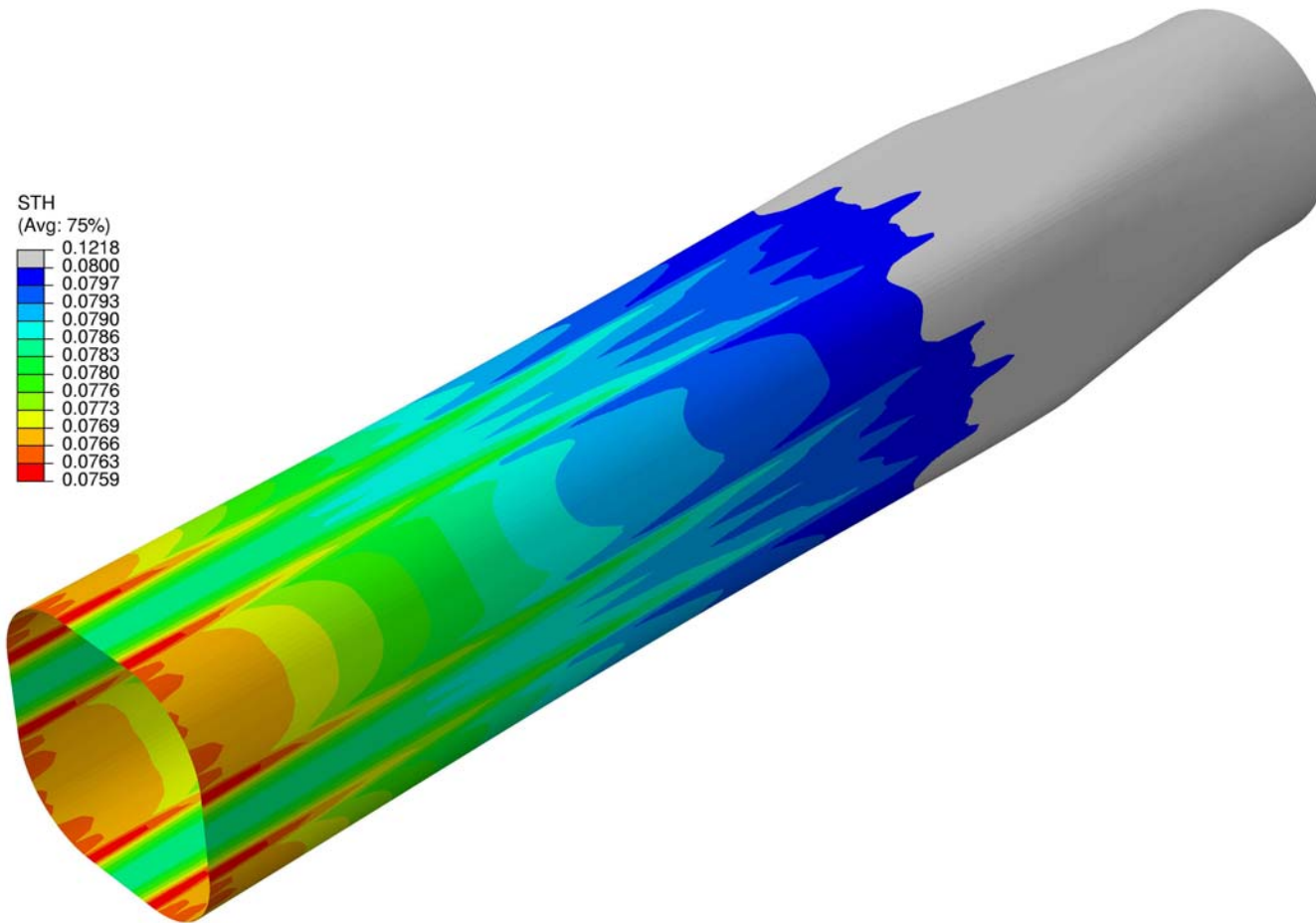


Fig. 5.16 – Predicted thickness reduction contours for the shell element model ($\mu = 0.2$) for experiment HY5, using the Hosford plasticity model (isotropic case, $k=8$). In the grey areas the formed tube is thicker than the undeformed one (compare to Fig. 2.18).

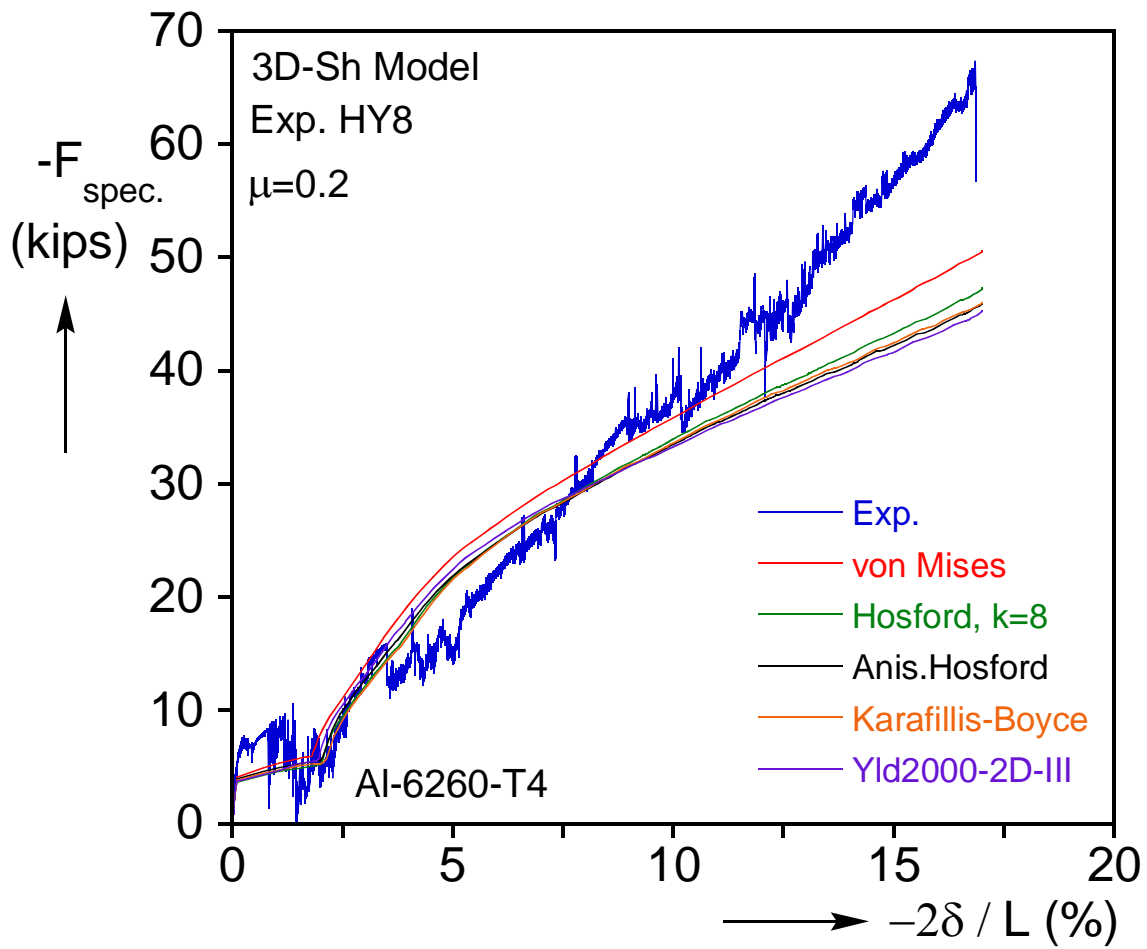


Fig. 5.17 – Predictions of axial load on the tube specimen against the axial end feed for HY8, with different plasticity models. Also included is the experiment.

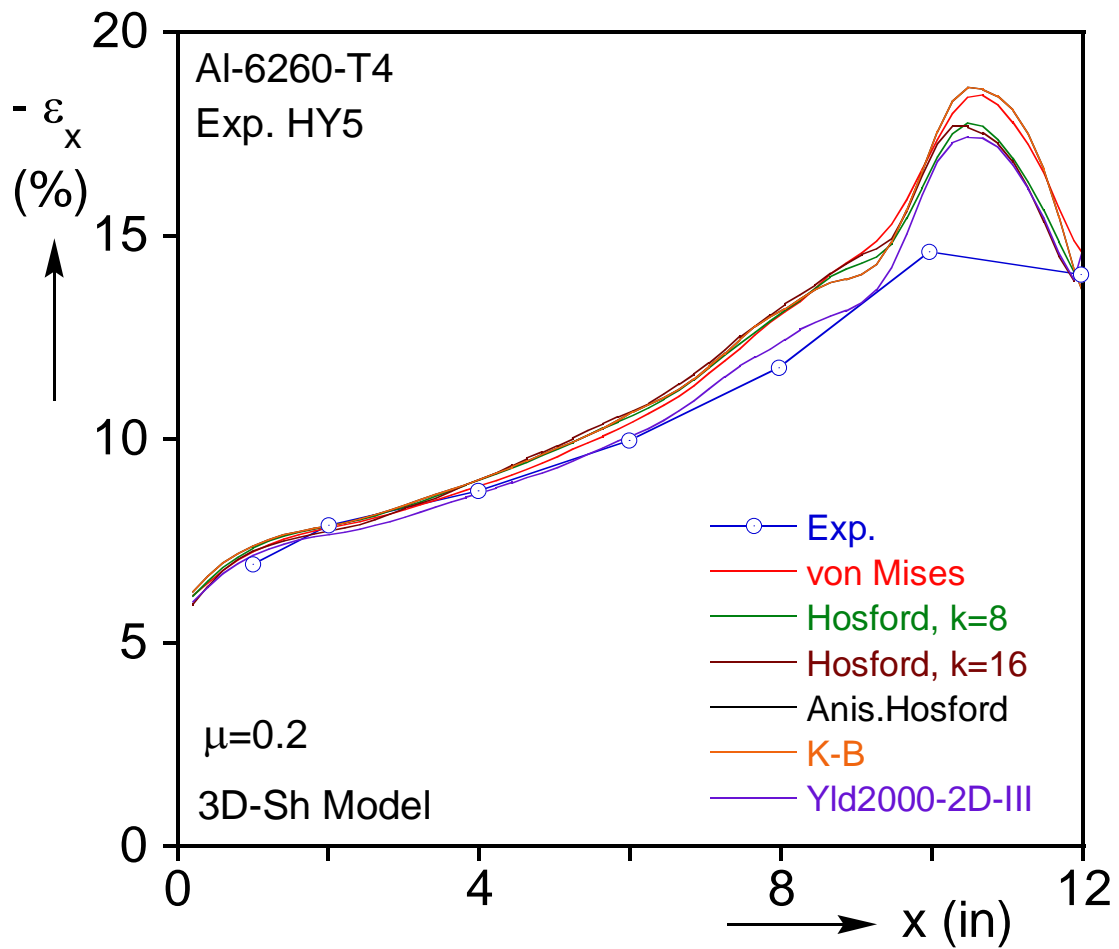


Fig. 5.18– Effect of constitutive model on predicted axial strain distribution along the formed tube for HY5, and comparison to experiment.

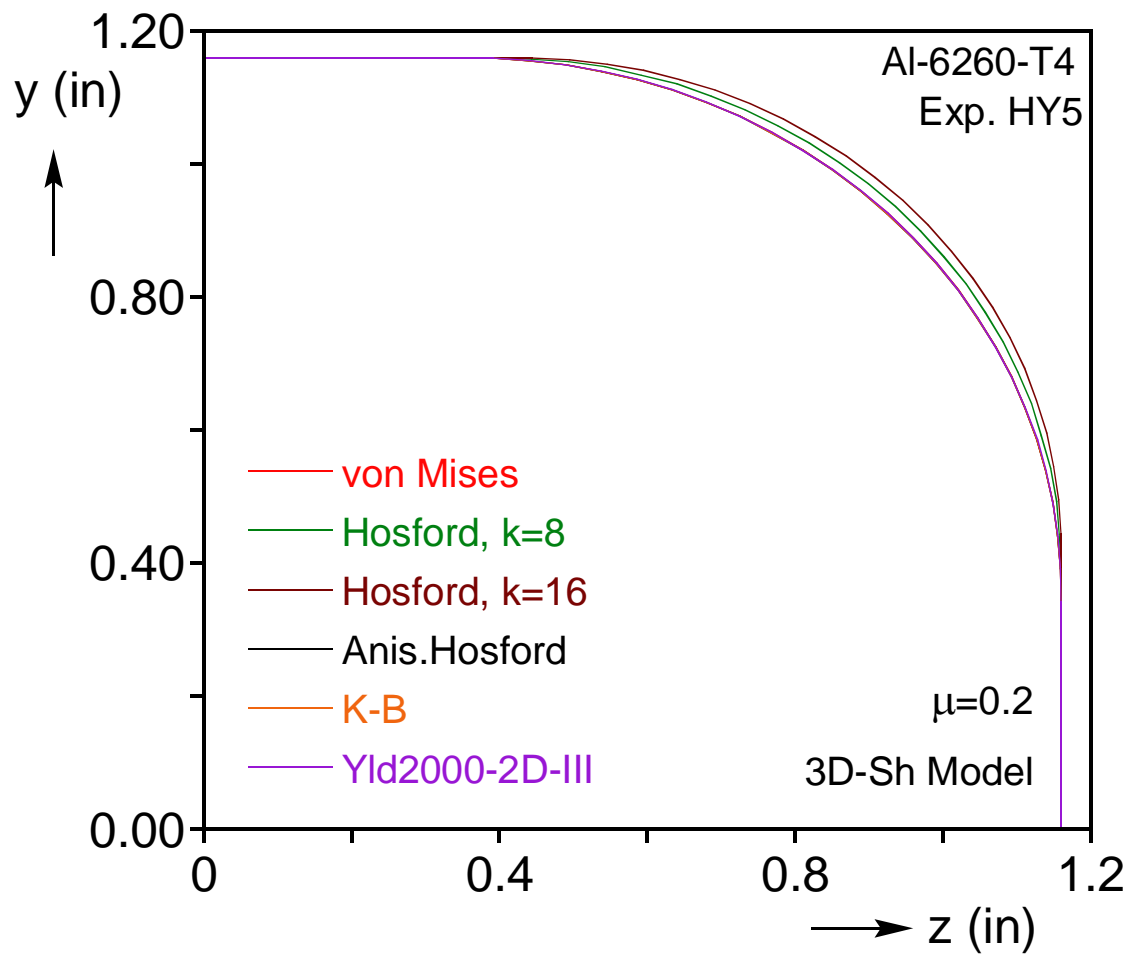


Fig. 5.19– Effect of constitutive model on predicted final shape of the mid-surface at mid-span for HY5.

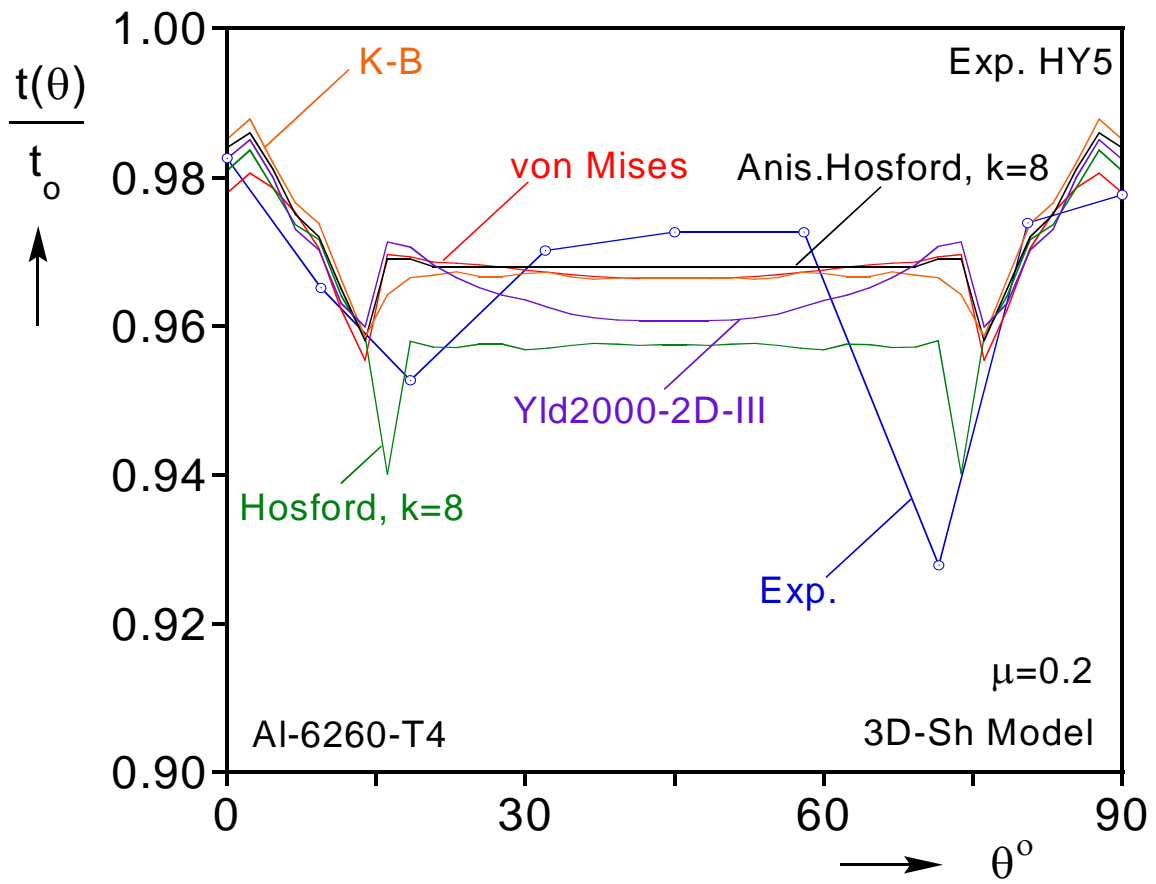


Fig. 5.20 – Effect of the yield function employed on the prediction of wall thinning at mid-span for HY5. The constitutive models have been calibrated in Chapter 4.

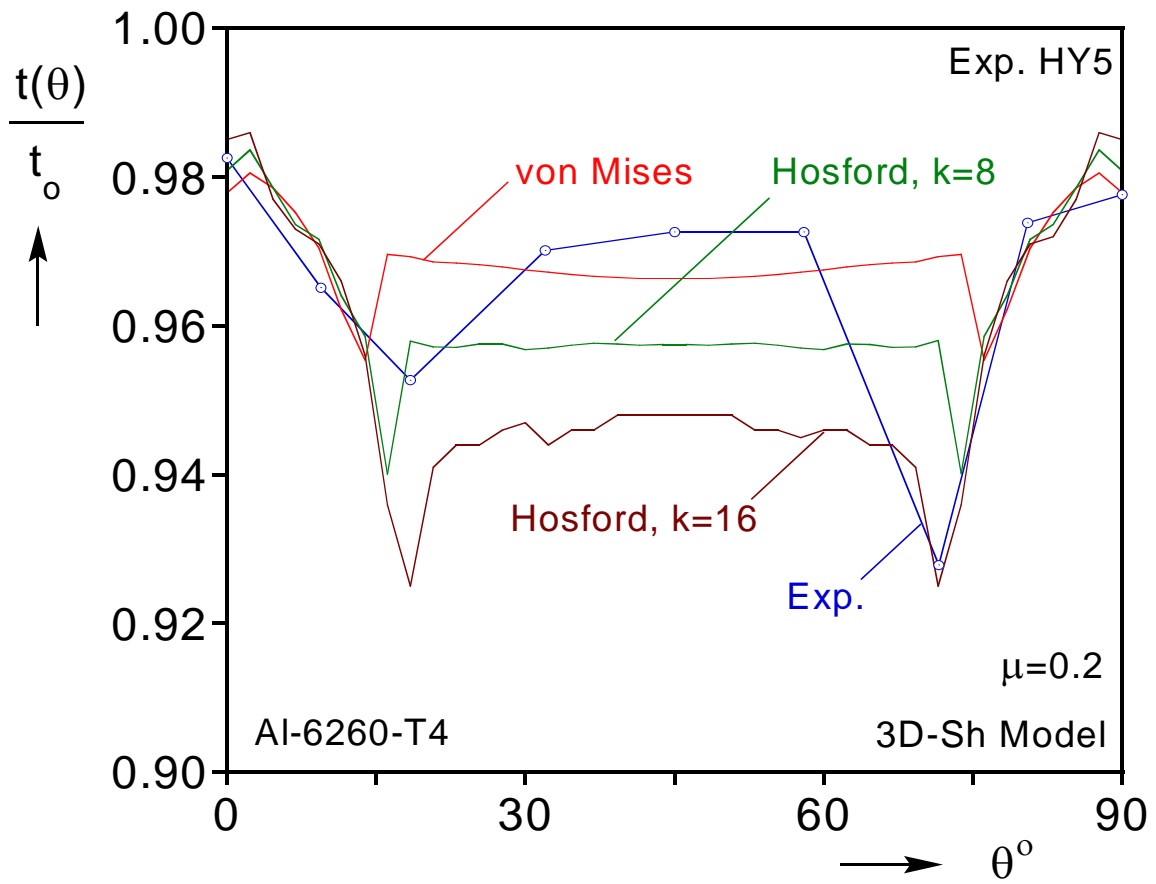


Fig. 5.21 – Effect of the exponent of Hosford’s yield function (isotropic case) on the prediction of wall thinning at mid-span for HY5.

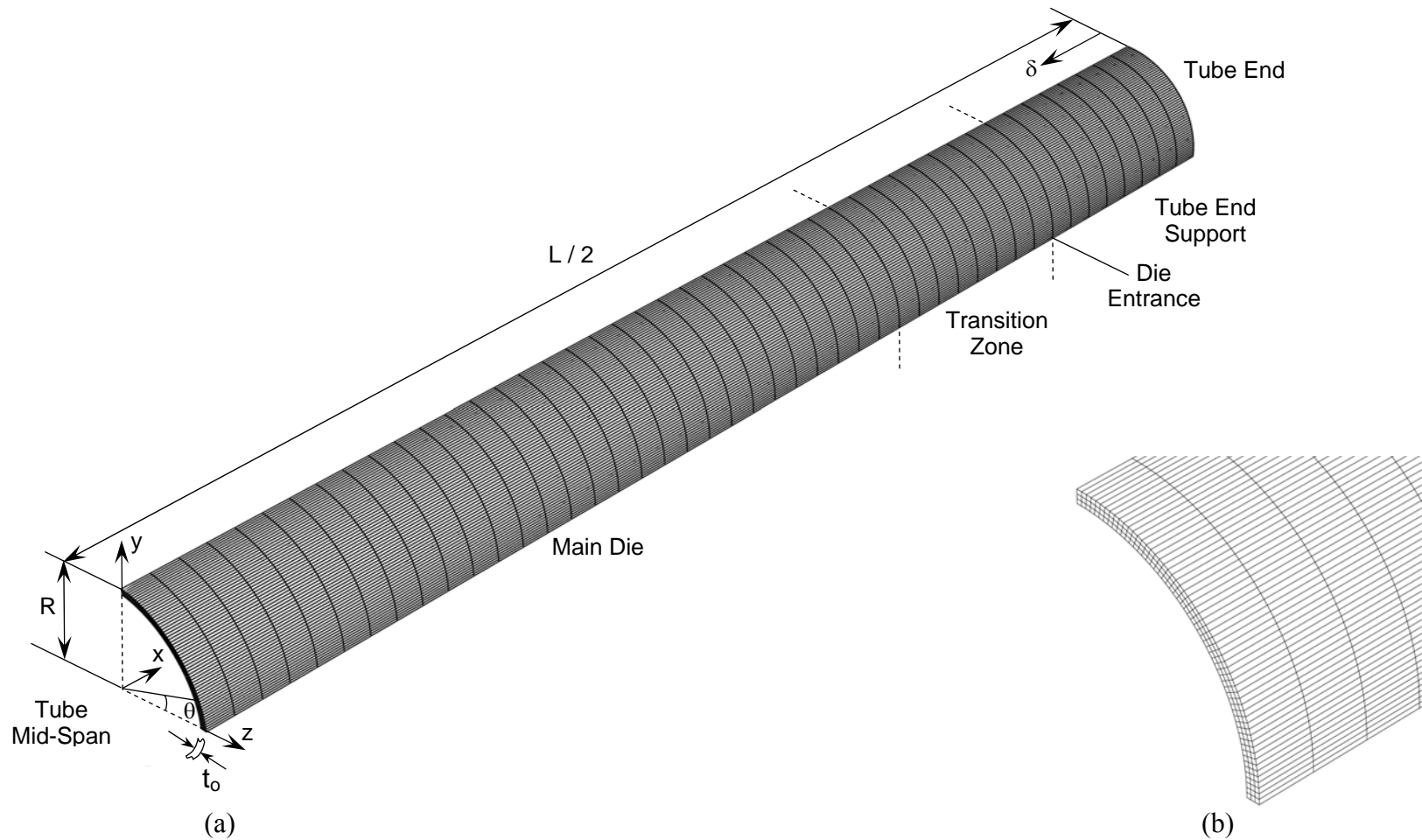
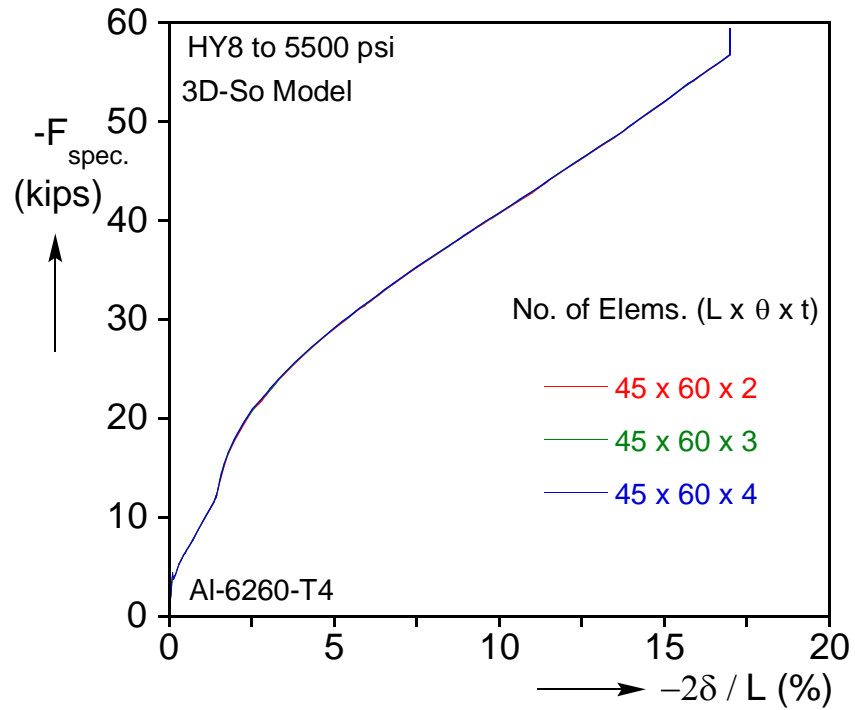
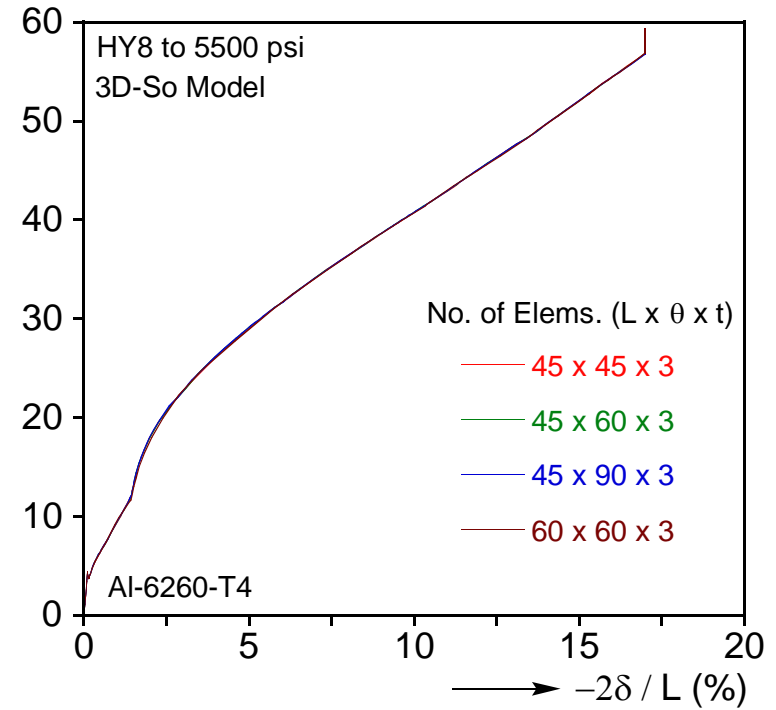


Fig. 5.22 – (a) Undeformed mesh using $45 \times 60 \times 3$ shell elements ($L \times \theta \times t$) continuum (solid) elements, showing $1/8^{\text{th}}$ of the tube, and (b) close-up of the model at mid-span, showing the arrangement of the elements. Surrounding die has been removed for clarity.



(a)



(b)

Fig. 5.23 – Effect of number of (a) through-thickness and (b) axial and circumferential elements on the prediction of load on specimen vs. axial feed response.

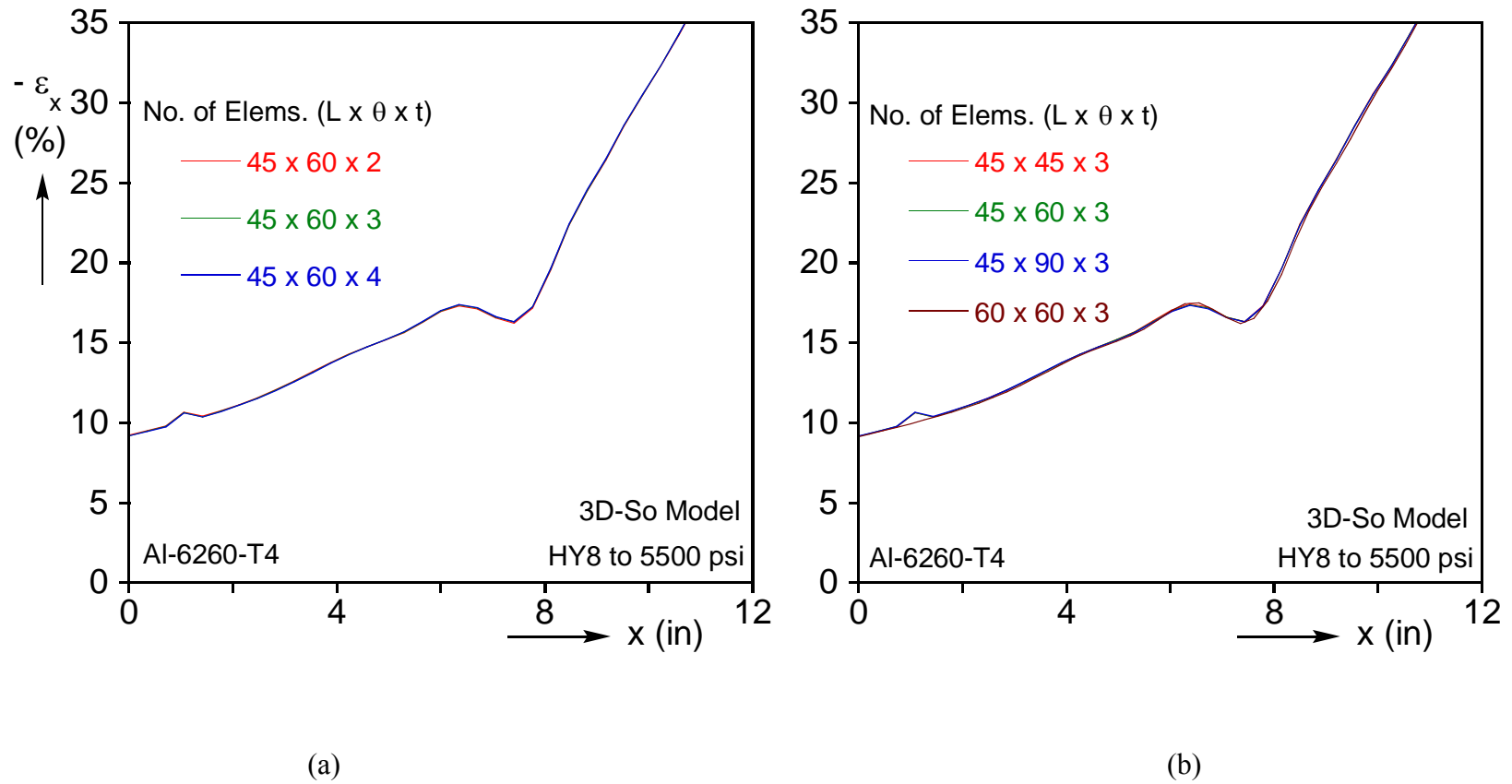
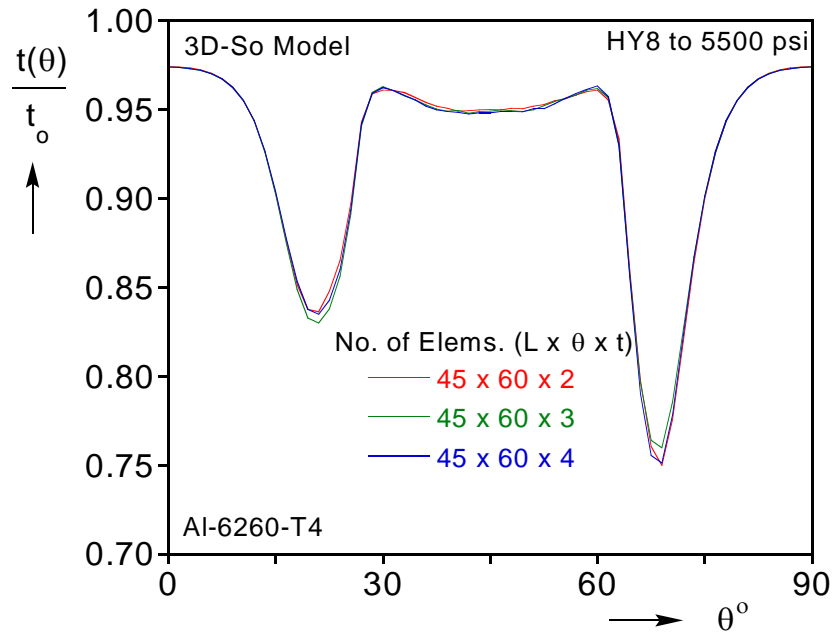
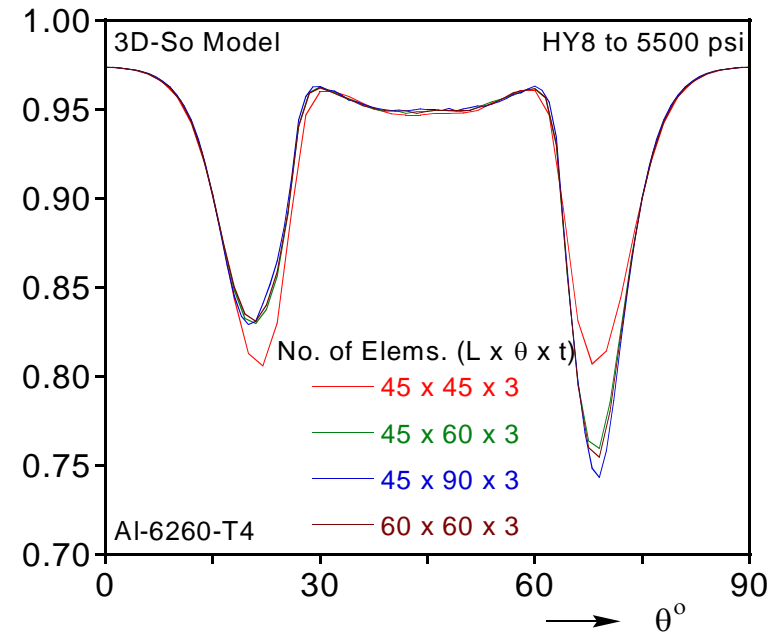


Fig. 5.24 – Effect of number of (a) through-thickness and (b) axial and circumferential elements on the prediction of axial strain along the formed tube.



(a)



(b)

Fig. 5.25 – Effect of number of (a) through-thickness and (b) axial and circumferential elements on the prediction of wall thickness distribution at mid-span.

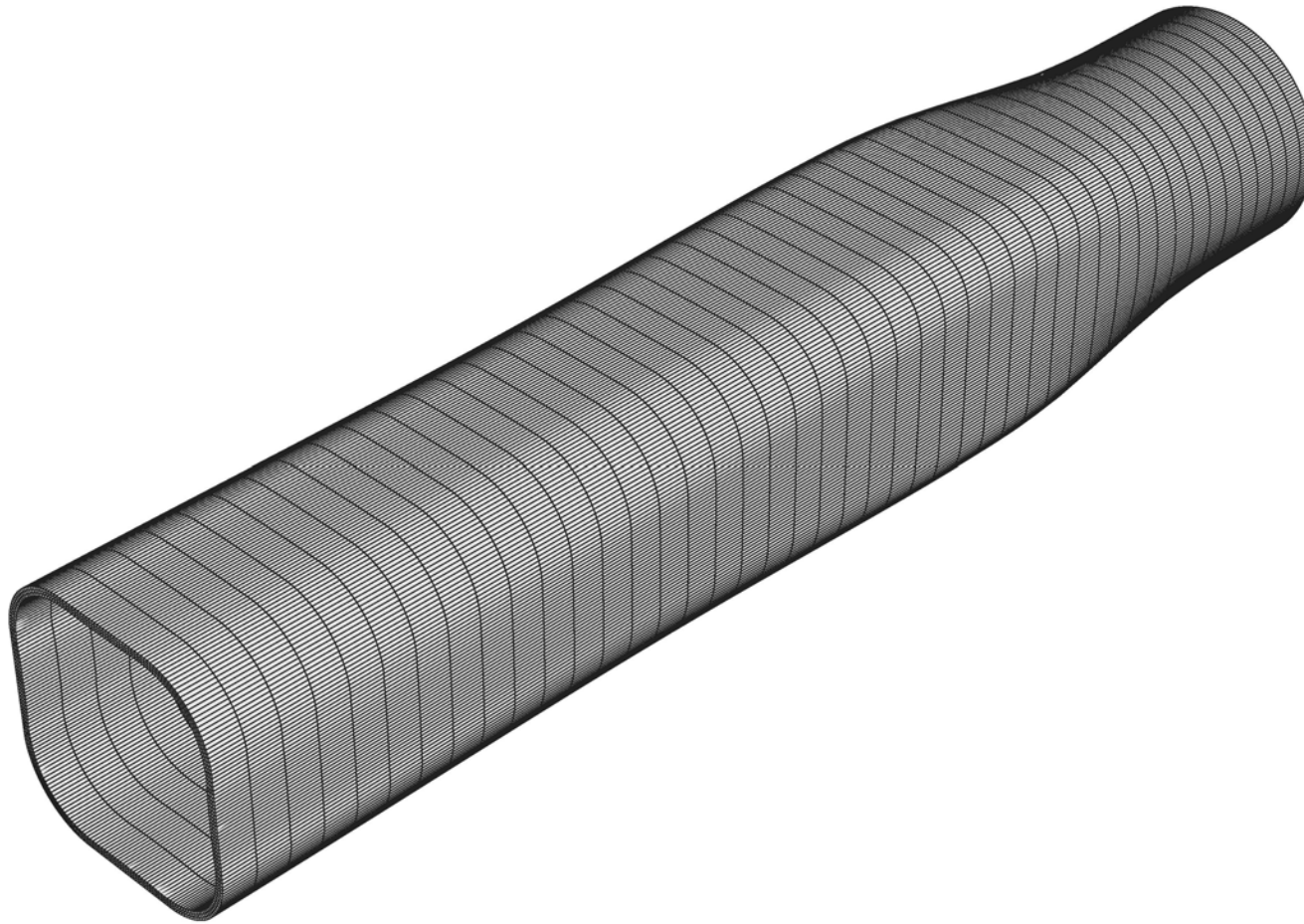
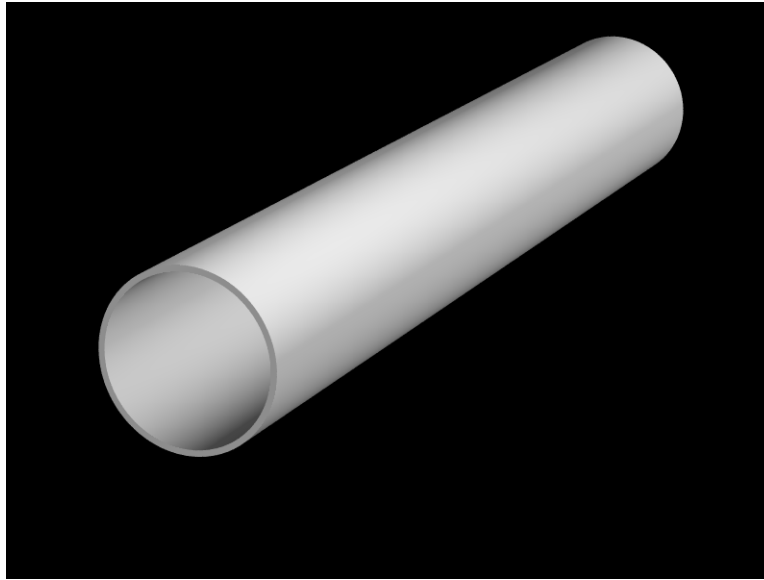
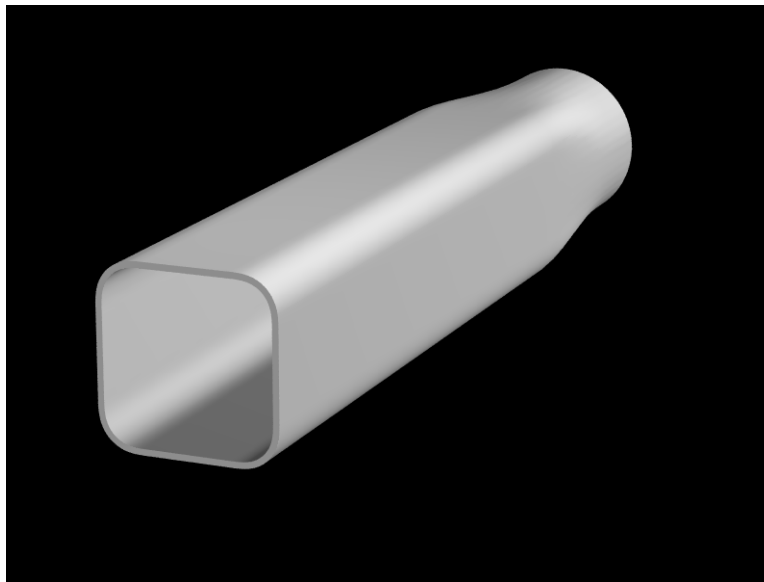


Fig. 5.26 – Deformed configuration for experiment HY6 using solid elements ($\mu = 0.2$, Hosford, isotropic, $k=8$). Notice the variation of shape along the length and compare with the experiment in Fig. 2.14a



(a)



(b)

Fig. 5.27 – Renderings of (a) initial, and (b) deformed configuration using solid elements. Surrounding die has been removed for clarity.

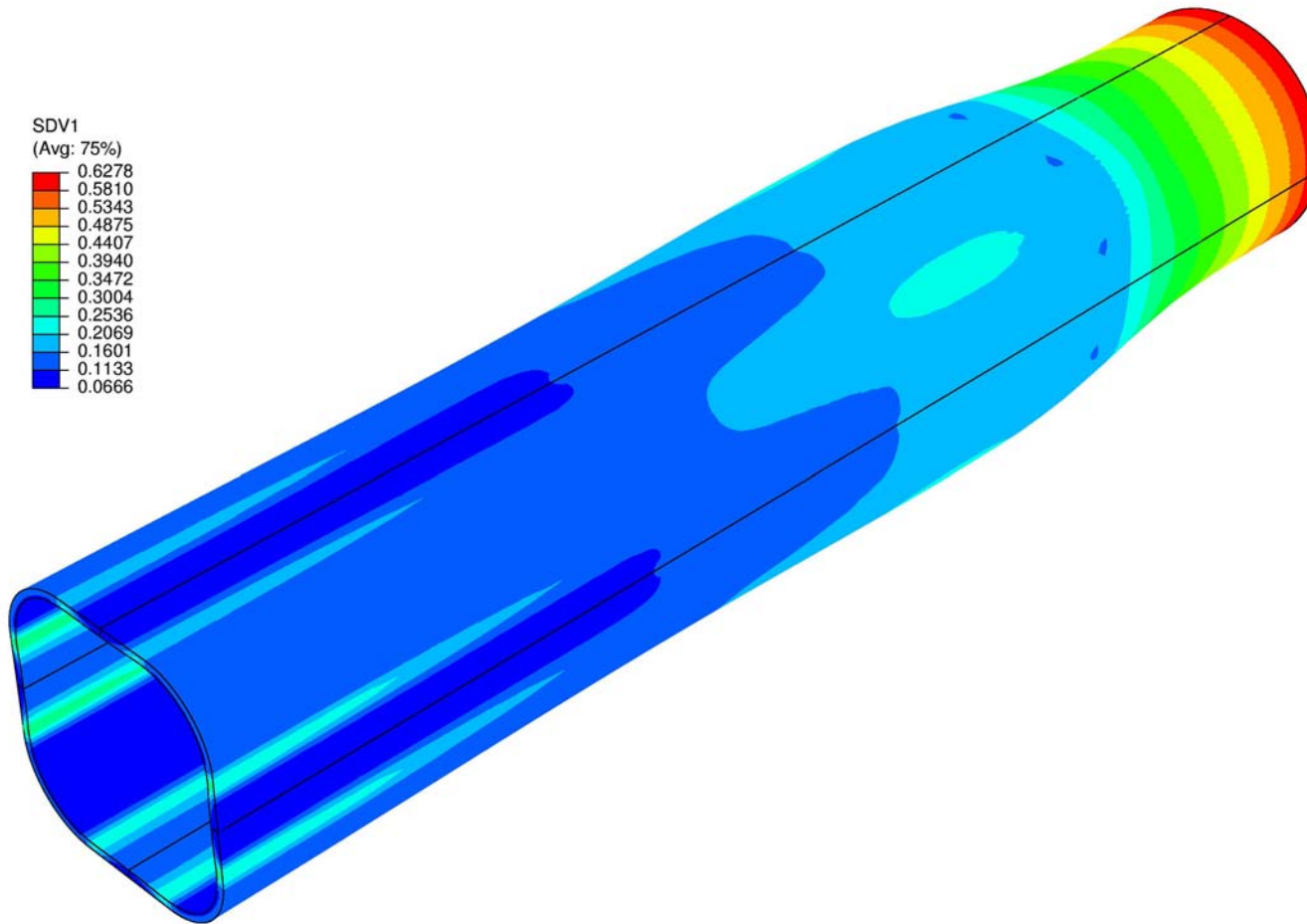


Fig. 5.28 – Prediction of equivalent plastic strain of the formed tube for experiment HY6, using the solid elements ($\mu = 0.2$, Hosford, isotropic, $k=8$). Note the large deformation at the feeding end of the tube.

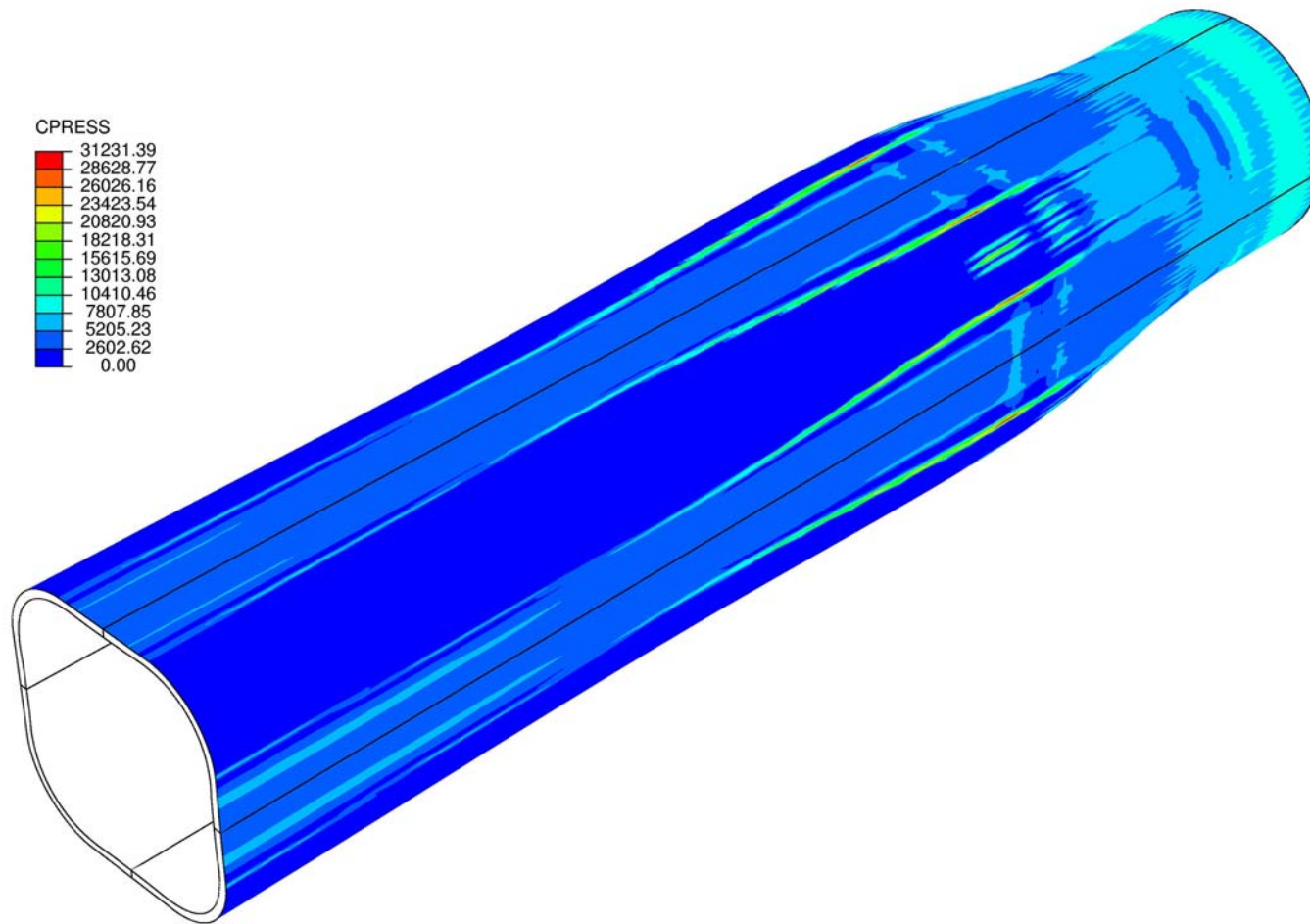


Fig. 5.29 – Prediction of the contact pressure between the formed tube and the die for experiment HY6, using the solid elements ($\mu = 0.2$, Hosford, isotropic, $k=8$). The contours outline the boundaries of contact between the tube and the die (compare with the experiment at Fig. 2.14a).

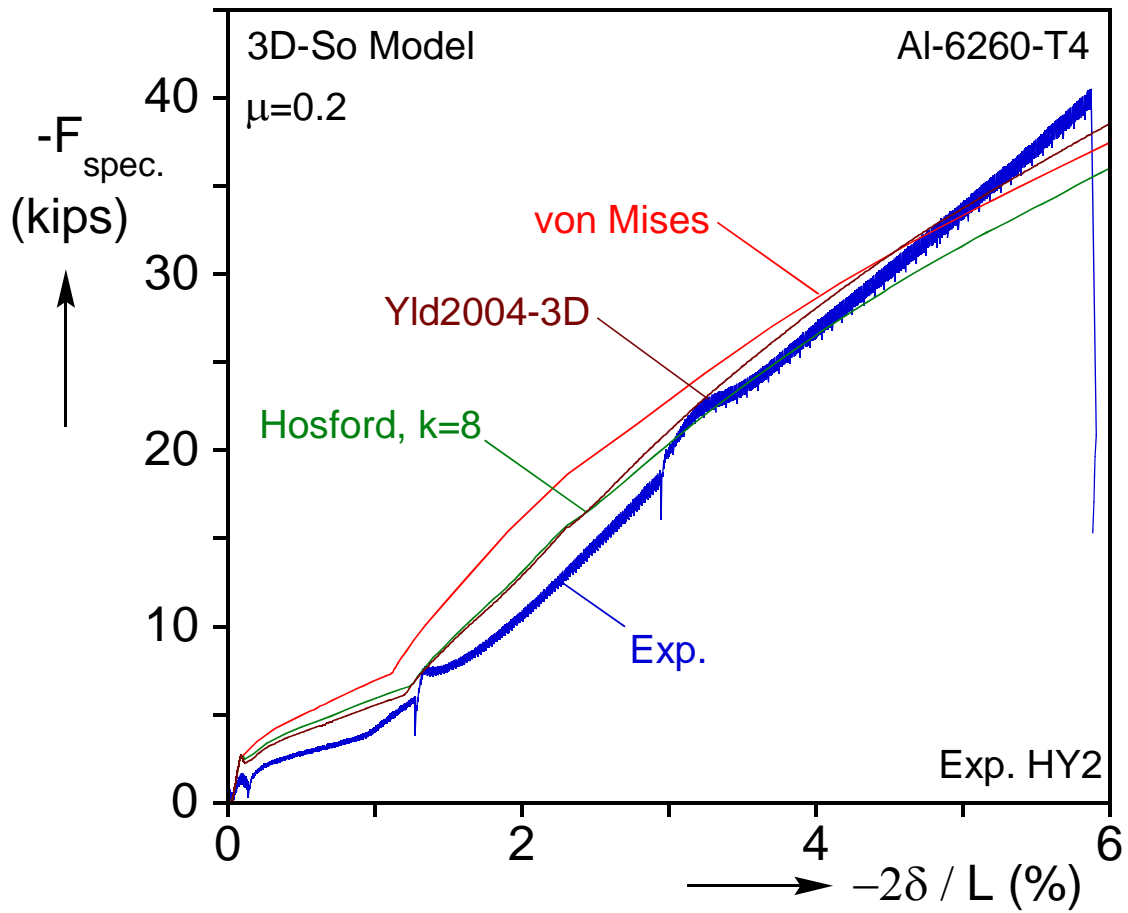


Fig. 5.30 – Predictions of axial load on the tube specimen against the axial end feed for HY2, using solid elements with different plasticity models. Also included is the experiment.

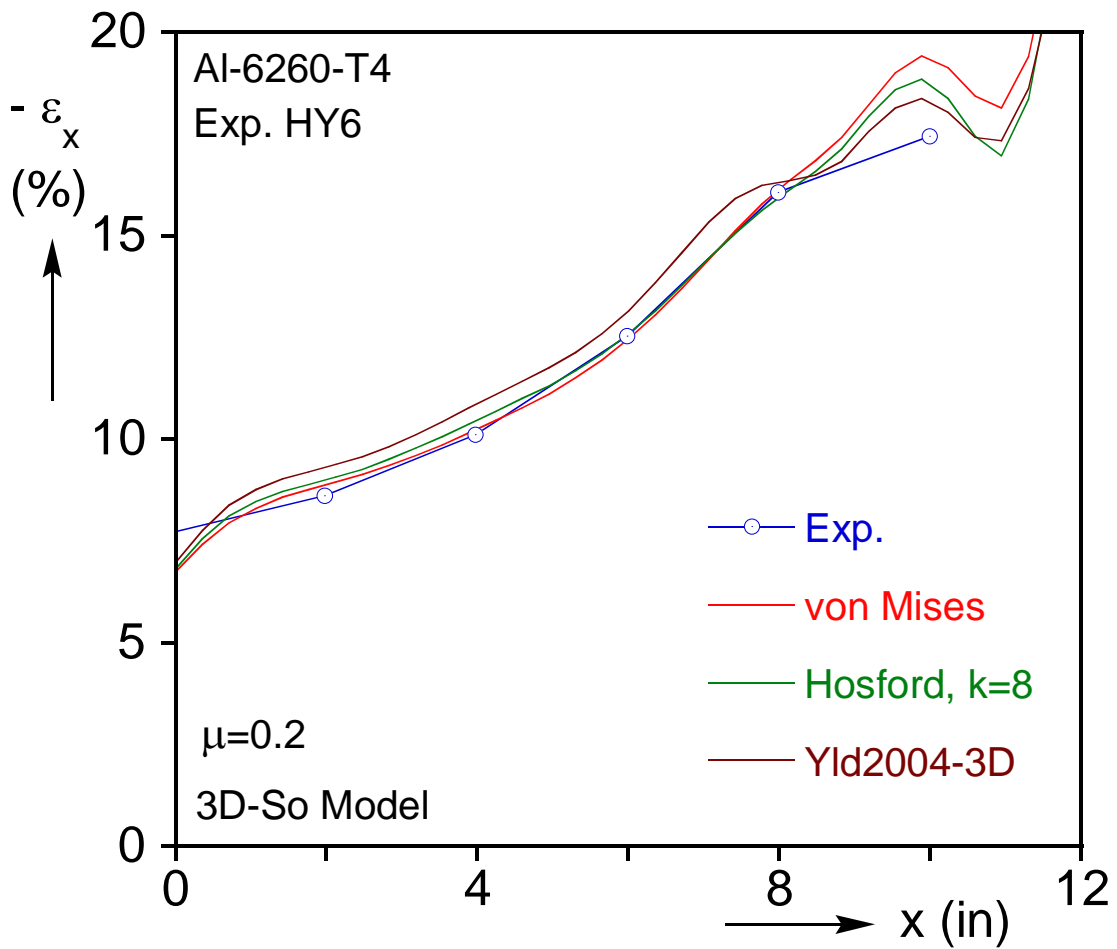


Fig. 5.31– Effect of constitutive model on predicted axial strain distribution along the formed tube for HY6, and comparison to experiment.

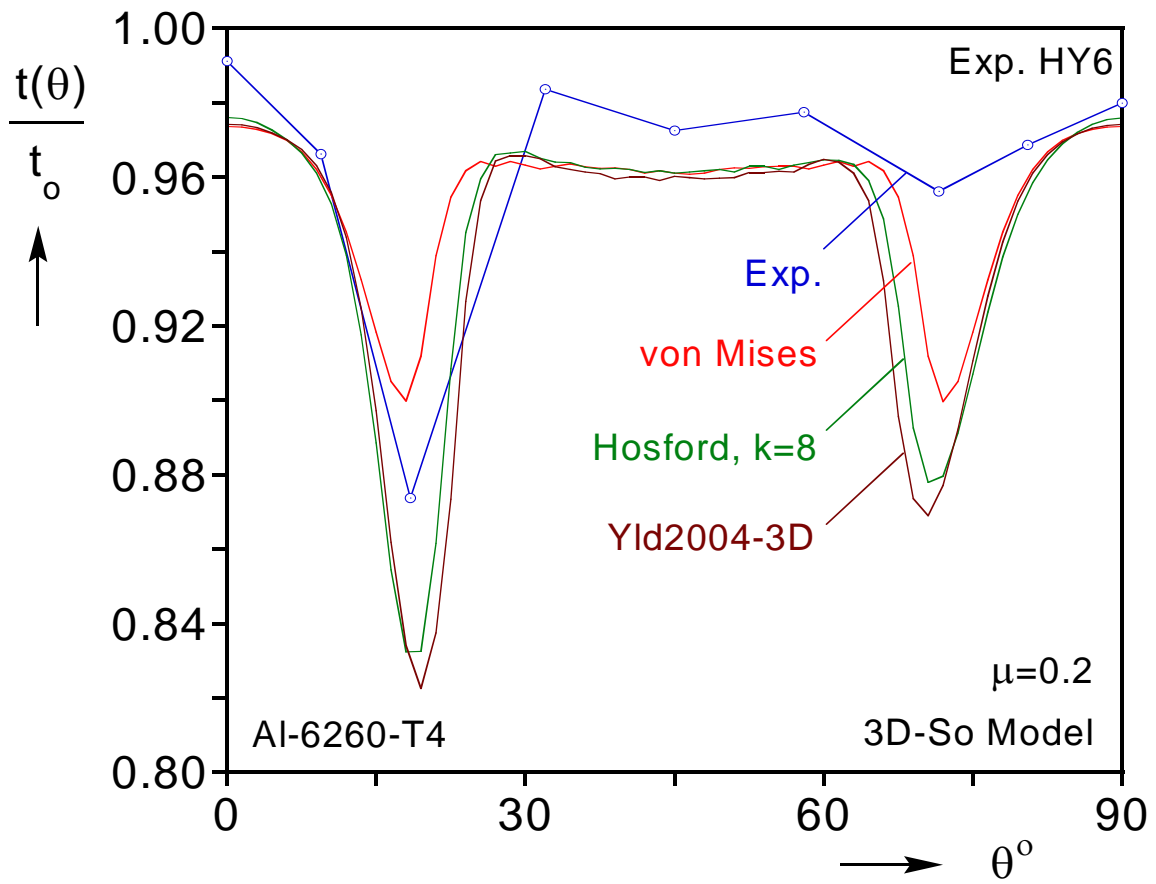


Fig. 5.32 – Predictions of wall thinning for HY6 using solid elements with $\mu = 0.2$ and different plasticity models. Also included is the experiment.

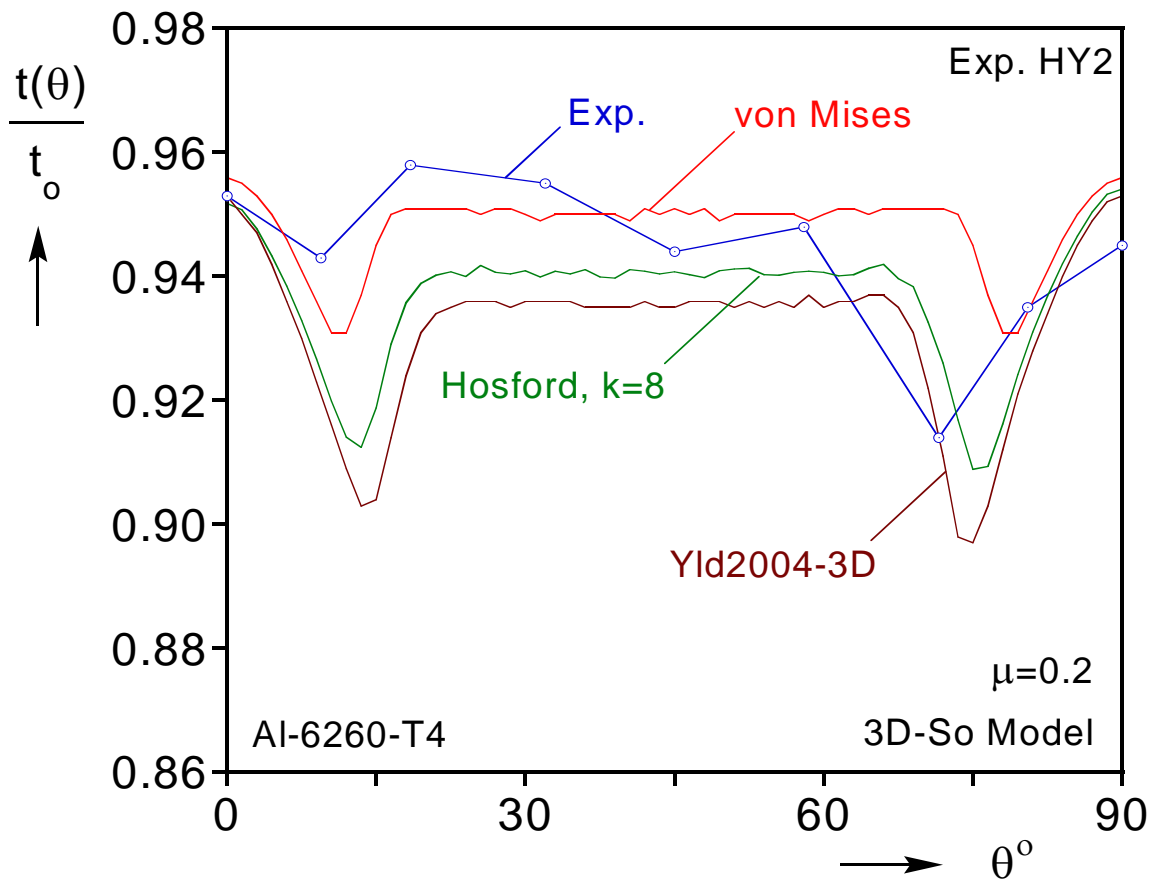


Fig. 5.33 –Predictions of wall thinning for HY2 using solid elements with $\mu = 0.2$ and different plasticity models. Also included is the experiment.

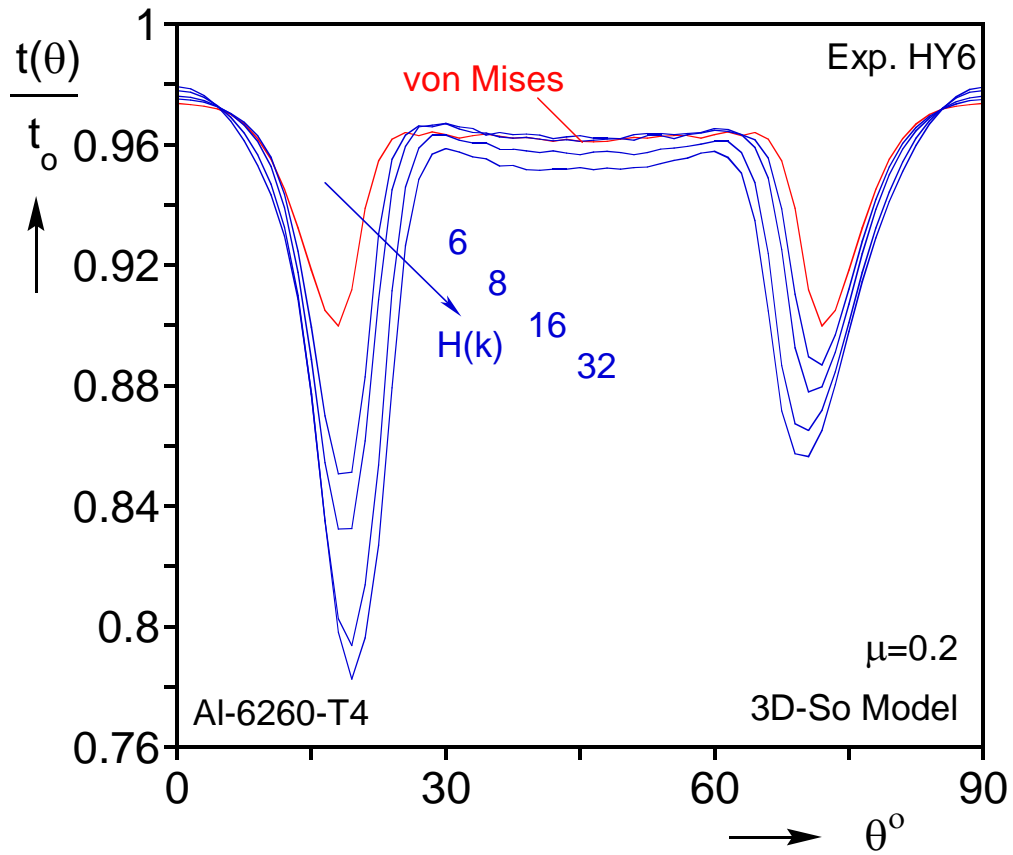


Fig. 5.34 – Effect of exponent of Hosford's yield function (isotropic case) on the prediction of wall thinning at mid-span.

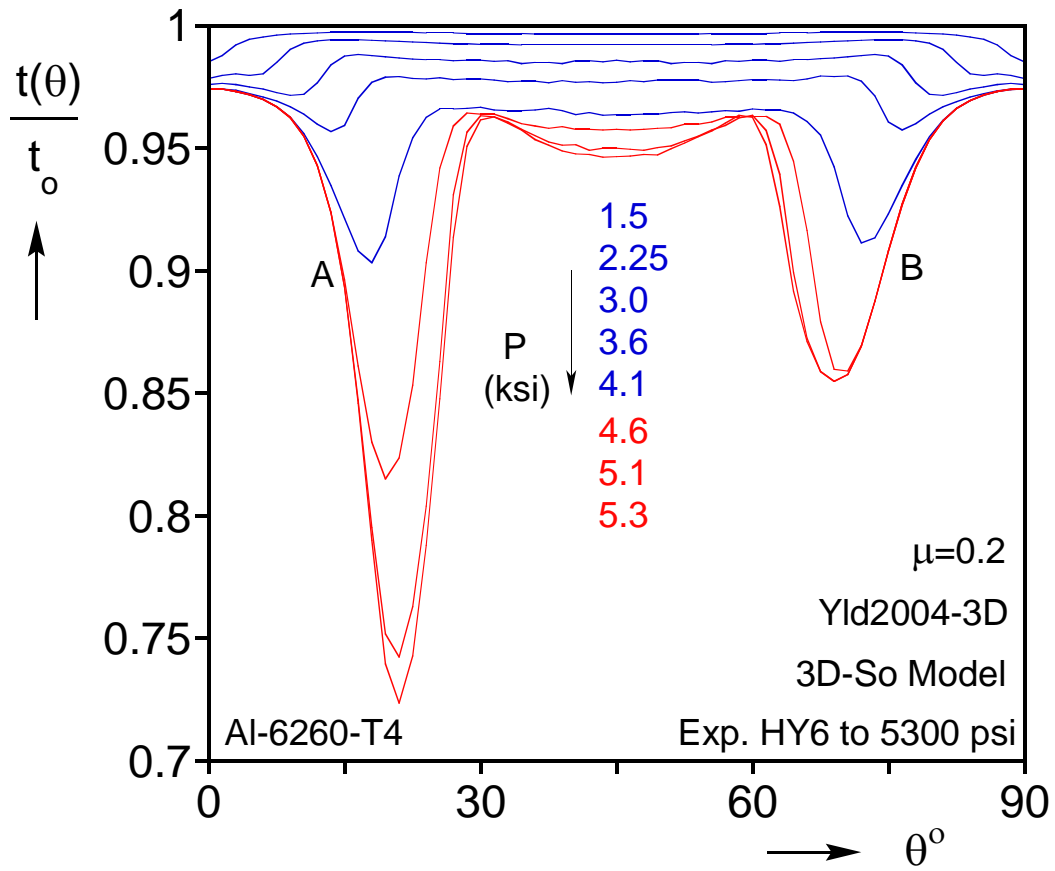


Fig. 5.35 – Evolution of the localization of plastic deformation, using the solid element model and the Yld2004-3D yield function.

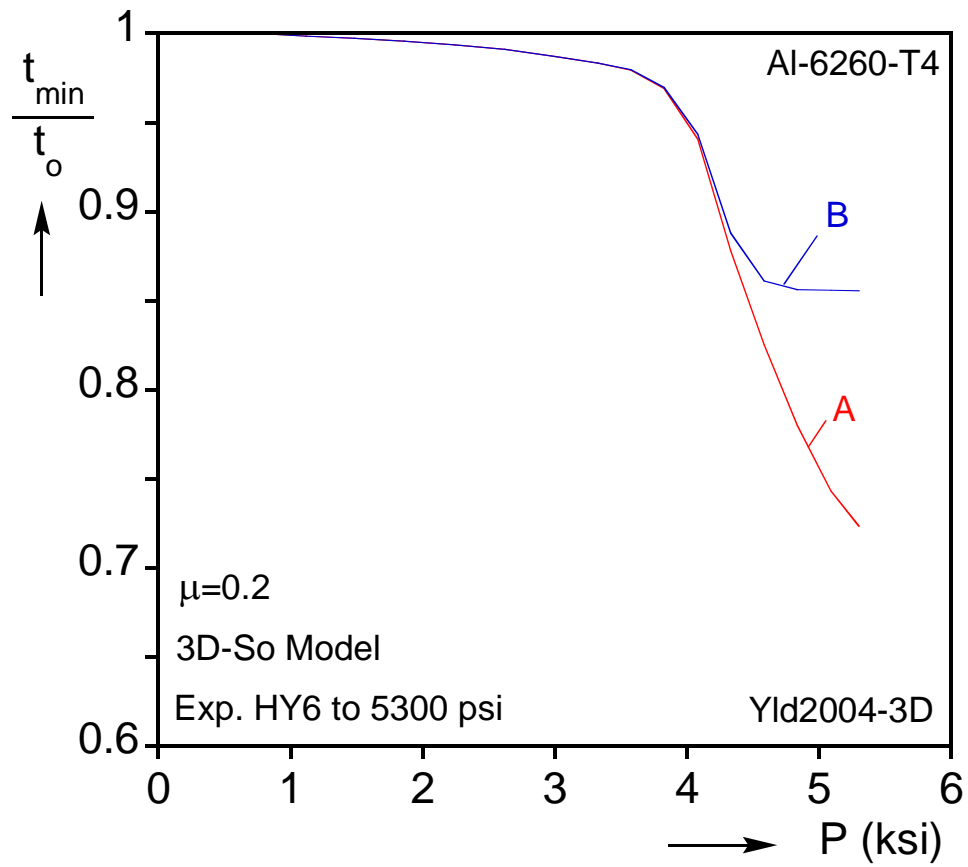


Fig. 5.36 – Evolution of wall thinning at the two thickness depressions (see Fig. 5.35) using the solid element model and the Yld2004-3D yield function.

Chapter 6: *Conclusions*

This dissertation uses experiments and analyses to study aluminum tube hydroforming. The study includes the design and fabrication of a custom hydroforming testing facility, the design and conduct of hydroforming experiments and investigation of bursting failures that were found to be a limit state of the process. Following are the major conclusions drawn from these efforts.

6.1 HYDROFORMING EXPERIMENTS

The hydroforming experiments were performed in a dedicated facility, designed and fabricated for the purposes of this study. The specimens tested were Al-6260-T4 seamless tubes with diameters of approximately 2.36 in and wall thickness of 0.080 in. The circular tubes started with a length of about 32 in and they were formed into a rounded square cross section with a side of 2.4 in. The major points to be made from the experimental investigation of the THF process are:

- (a) The loading paths were selected so as to avoid maxima in the axial load, so that overall bucking and wrinkling were not encountered in our experiments.
- (b) Because of the relatively large aspect ratio of the test specimens chosen, friction between the tube and the die prevented the complete filling of the die and yielded products with a non-uniform axial shape. The tubes thickened close to the feeding end, while they developed non-uniform wall thinning around mid-span.
- (c) The amount of wall thinning was affected by the friction, and typically involved two thickness wells at each quadrant of the rounded square cross-section.

(d) As a result of (b) and (c), burst was a major limiting factor in the experimental work prompting an extensive independent investigation of bursting under biaxial loading states of this alloy tubes.

6.2 TUBE FORMABILITY STUDY

This study was dictated by the need to understand and model bursting as a major limit state in hydroforming. The study involved loading of Al-6260-T4 tubes to failure under selected biaxial stress states and calibration and evaluation of constitutive models for the prediction of the induced strain paths and failures. The main conclusions from the experimental study are the following:

- (a) Tubes were tested to failure under radial and corner paths in the engineering stress space. Depending on whether the axial or the hoop stress was dominant, the tubes failed in different modes (circumferential or axial rupture, respectively).
- (b) For some paths, significant deformation followed the limit load. This dictates the use of volume instead of pressure control when inflating the specimens.
- (c) The failure strains are influenced by the cylindrical geometry of the test specimens. Thus, for example, for the uniaxial hoop stress state (until bulging develops) the limit hoop strain was 11.8%, which compares with a 19.5% strain measured in a uniaxial tension test on an axial strip. Hence the formability investigation needs to be performed on tubes directly, rather than extrapolated from studies on sheets.
- (d) The shape of the initial yield surface for Al-6260-T4 lies between that of the Tresca and von Mises yield surfaces, as indeed has been observed previously for many aluminum alloys. Thus, a non-quadratic yield criterion is required for the present material.

- (e) The material exhibited some initial anisotropy that appears to be different from that observed in aluminum alloy sheets. In addition, the constant plastic work contours indicate that the anisotropy evolved to some degree with deformation.
- (f) The corner path tests verified that the failure strains are distinctly path-dependent, as expected. However, it was discovered that the failure stresses can be path-dependent as well, especially as the prestrain increases. This was at least partly attributed to the fact that the corner paths chosen introduced significant prestraining to the specimens, something that is not sufficiently investigated in the literature. For the specific material, this tended to expand the yield surface, which in turn delayed re-yielding during the second branches of the corner paths.

The following conclusions can be drawn from the numerical investigation.

- (a) The initial yield surface was fitted quite well using Hosford's principal stress anisotropic yield function and two versions of the K-B yield function with exponents of 8. The more powerful yield function examined subsequently (Yld2000-2D) captured the experimental work contours even better.
- (b) Strains from the radial paths calculated with the H and K-B models differed from measured ones, in particular in the neighborhood of equibiaxial tension, where the yield surface has the highest curvature. On the other hand, the use of Yld2000-2D captured the experimental strain paths very well.
- (c) The influence on burst of the sizeable shear anisotropy present in the tubes tested was found to be small.
- (d) The stresses corresponding to the limit load instabilities were generally well captured by the simulations. The corresponding strains and those at the onset of rupture were very sensitive to the constitutive model used. A properly calibrated Yld2000-2D model gave the best predictions of the onset of failure. The same function was very

satisfactory in predicting failure not only for the radial, but for the corner paths as well.

- (e) The hybrid calibration procedure used for the best performing Yld2000-2D model is too cumbersome to be used in more complicated settings.

6.3 HYDROFORMING SIMULATIONS

Several levels of modeling were performed for the simulation of the hydroforming experiments. These include 2D models used primarily for the preliminary design of the experiments and 3D shell and solid element models that are more appropriate for capturing the effects of friction and the axial variation of deformation. These simulations led to the following observations:

- (a) A 2D model using generalized plane strain elements can reproduce quite well the main structural features of the THF process. Hence it can be profitably used to generate estimates of the initial cross sectional geometry, material specification and loading path to obtain a given target shape. On the other hand, it is deficient in predicting failure.
- (b) The next level of analysis involves a 3D FE model that uses shell elements. Such a model is capable of incorporating the yield functions calibrated and evaluated in the formability study (Chapters 3 and 4). The model includes friction and reproduces the axial variation of the shape of the formed tube, as well as a variety of structural features of the problem (e.g., axial load-feed response, distribution of axial strain along the tube, etc.). However, the shell elements fail to capture the localized wall thinning to the extent and intensity that it was observed experimentally, and hence the failure predictions also fall short of the experiments. This is true despite the use of the various constitutive models that were calibrated in Chapter 4 to give excellent predictions of failure in the free inflation case.

- (c) The deficiency of the shell element model was traced to the stress triaxiality that develops during hydroforming, both due to the tube-die contact and to the necking itself. To capture this, a discretization of the problem using solid elements is required. In conjunction with a non-quadratic yield function, this model yielded failure predictions much more in concert with the experiments. Traditionally sheet metal forming processes have been modeled using formulations based on thin-walled assumptions (i.e., shell elements). The present results demonstrate that localized wall thinning in the presence of contact is a fully 3D process, requiring appropriate modeling with solid elements, if tracking of its evolution is necessary for predicting failure.
- (d) Using the solid element model, the details of the anisotropic description appear to be less crucial in hydroforming, than they were in the free inflation. This is due to the different stress states and paths involved and to other factors active in hydroforming and not present in the free inflation case such as geometrical constraints, friction, etc.

Appendix: Yld2004-3D Anisotropic Yield Function

The Yld2004-3D constitutive model suggested by Barlat *et al.* (2005) follows the lines of their earlier Yld2000-2D function (see Chapter 4) but affords a fully three-dimensional description of anisotropy. Two linear transformations are used here as well, operating on the deviatoric stress tensor and offering a total of eighteen parameters for the description of anisotropy (compares with the eight parameters of Yld2000-2D). Despite the popularity of the plane stress models, especially for sheet metal forming applications, the three-dimensional nature of necking and localization even in a thin sheet may necessitate the use of this more complete model.

The starting point is again the non-quadratic isotropic yield function of Hosford (1972) which in terms of the principal values of the stress deviator is written as:

$$|s_1 - s_2|^k + |s_2 - s_3|^k + |s_3 - s_1|^k = 2\sigma_o^k \quad (\text{A.1})$$

Anisotropy is now introduced by two linear transformations, which are used to construct the tensors S' , S'' from the actual stress tensor as follows:

$$S' = C's = C'T\sigma = L'\sigma \quad \text{and} \quad S'' = C''s = C''T\sigma = L''\sigma \quad (\text{A.2})$$

where C' , C'' , T , L' and L'' are appropriate transformation matrices that allow introduction of the anisotropy.

Naturally, the deviator is obtained from the stress tensor with the transformation matrix T :

$$\mathbf{T} = \frac{1}{3} \begin{bmatrix} 2 & -1 & -1 & 0 & 0 & 0 \\ -1 & 2 & -1 & 0 & 0 & 0 \\ -1 & -1 & 2 & 0 & 0 & 0 \\ 0 & 0 & 0 & 3 & 0 & 0 \\ 0 & 0 & 0 & 0 & 3 & 0 \\ 0 & 0 & 0 & 0 & 0 & 3 \end{bmatrix} \quad (\text{A.3})$$

while the transformation matrices \mathbf{C}' and \mathbf{C}'' contain the 18 anisotropy parameters:

$$\mathbf{C}' = \begin{bmatrix} 0 & -c'_{12} & -c'_{13} & 0 & 0 & 0 \\ -c'_{21} & 0 & -c'_{23} & 0 & 0 & 0 \\ -c'_{31} & -c'_{32} & 0 & 0 & 0 & 0 \\ 0 & 0 & 0 & c'_{44} & 0 & 0 \\ 0 & 0 & 0 & 0 & c'_{55} & 0 \\ 0 & 0 & 0 & 0 & 0 & c'_{66} \end{bmatrix} \quad (\text{A.4a})$$

and

$$\mathbf{C}'' = \begin{bmatrix} 0 & -c''_{12} & -c''_{13} & 0 & 0 & 0 \\ -c''_{21} & 0 & -c''_{23} & 0 & 0 & 0 \\ -c''_{31} & -c''_{32} & 0 & 0 & 0 & 0 \\ 0 & 0 & 0 & c''_{44} & 0 & 0 \\ 0 & 0 & 0 & 0 & c''_{55} & 0 \\ 0 & 0 & 0 & 0 & 0 & c''_{66} \end{bmatrix} \quad (\text{A.4b})$$

Writing now the principal values of the linearly transformed stress tensors \mathbf{S}' and \mathbf{S}'' as (S'_1, S'_2, S'_3) and (S''_1, S''_2, S''_3) , respectively, the Yld2004-3D yield function is:

$$\begin{aligned} \phi = & |S'_1 - S''_1|^k + |S'_1 - S''_2|^k + |S'_1 - S''_3|^k + |S'_2 - S''_1|^k + \\ & |S'_2 - S''_2|^k + |S'_2 - S''_3|^k + |S'_3 - S''_1|^k + |S'_3 - S''_2|^k + |S'_3 - S''_3|^k = 4\sigma_o^k \end{aligned} \quad (\text{A.5})$$

The analytical solution for the principal stresses (S'_1, S'_2, S'_3) and (S''_1, S''_2, S''_3) using Cardan's method, as well as the first and second derivatives of the yield function with

respect to the stress components, which are required for the flow rule and the consistent tangent modulus, are given in Barlat *et al.* (2005).

In concert with the rest of our work, the exponent k is again assigned the value of 8, typical for aluminum alloys. The model is then calibrated by fitting the twelve parameters c'_{ij} and c''_{ij} ($i, j = 1, 3$) to the 2 ksi plane stress work contour. These parameters are associated with normal stresses. The remaining six parameters, c'_{ii} and c''_{ii} ($i = 4, 5, 6$, no sum on i) which are associated with shear stresses are set equal to 1, since it was demonstrated that shear anisotropy does not affect the failure predictions (see Section 4.2.2). The set of eighteen parameters thus arrived at is given in Table A.1 and the resulting plane stress work contour is shown in Fig. A.1. Notice that the agreement between the predicted and the experimental contour is excellent, except perhaps for the uniaxial loading path. This state of stress however lies quite different from the stress states encountered in tube hydroforming. The performance of the constitutive model in the 3D simulations of tube hydroforming is included in Chapter 5 (see Figs. 5.30 to 5.36).

Table A.1 Anisotropy parameters for Yld2004-3D ($k=8$)

W^p	c'_{12}	c'_{13}	c'_{21}	c'_{23}	c'_{31}	c'_{32}	c'_{44}	c'_{55}	c'_{66}
2 ksi	1.02	1.21	1.14	0.91	0.64	0.73	1.0	1.0	1.0
	c''_{12}	c''_{13}	c''_{21}	c''_{23}	c''_{31}	c''_{32}	c''_{44}	c''_{55}	c''_{66}
	1.01	0.85	0.82	1.0	1.03	0.98	1.0	1.0	1.0

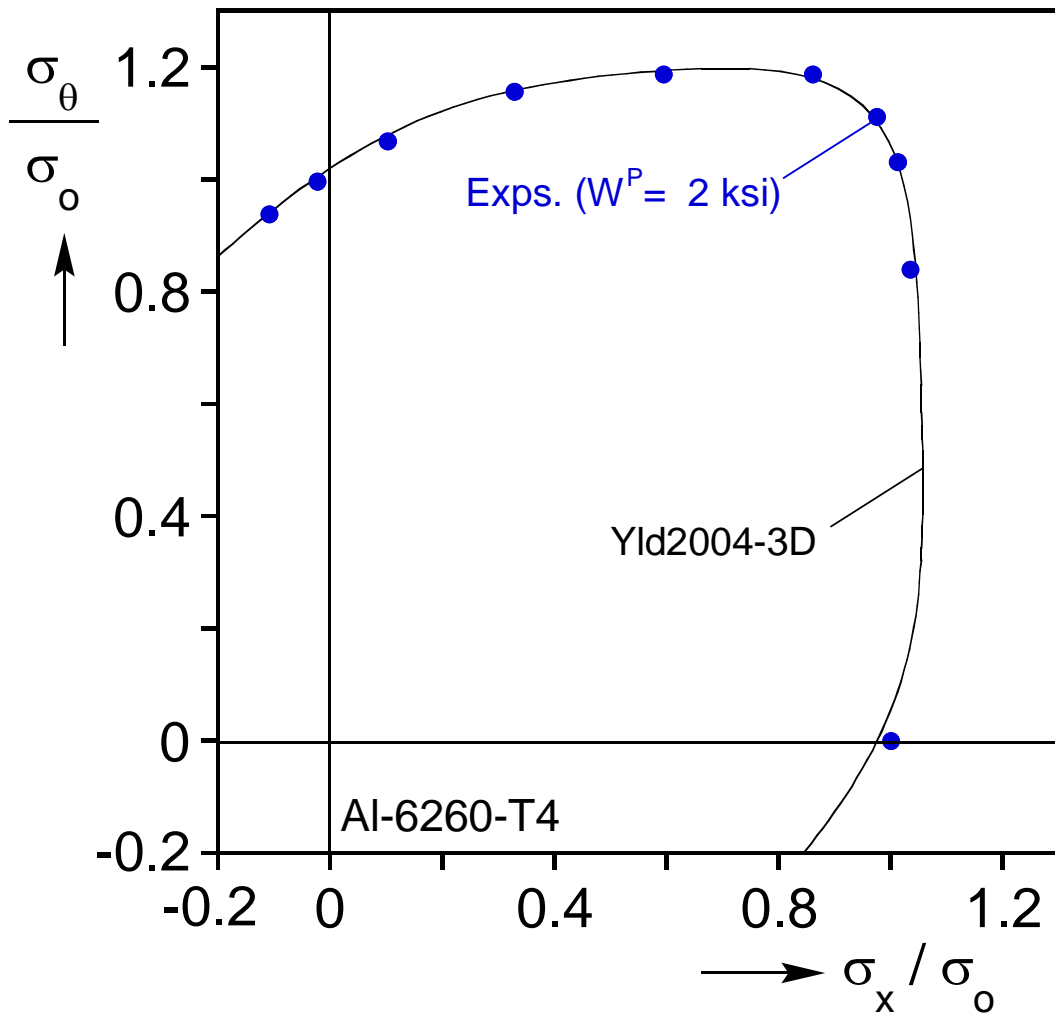


Fig. A.1 – Experimental data representing the 2 ksi (13.8 MPa) work contour and the Yld2004-3D yield function.

References

- Asnafi, N. and Skogsgardh, A. (2000). Theoretical and experimental analysis of stroke-controlled tube hydroforming, *Mat. Sci. Eng. A*. **279**, 95–110.
- Barlat, F., Lian, J. (1989). Plastic behavior and stretchability of sheet metals. Part I. A yield function for orthotropic sheets under plane stress conditions. *Int'l J. Plasticity* **5**, 51–66.
- Barlat, F., Lege, D.J., Brem, J.C. (1991). A six component yield function for anisotropic materials. *Int'l J. Plasticity* **7**, 693–712.
- Barlat, F., Maeda, Y., Chung, K., Yanagawa, M., Brem, J.C., Hayashida, Y., Lege, D.J., Matsui, K., Murtha, S.J., Hattori, S., Becker, R.C., Makosey, S. (1997). Yield function development for aluminum alloy sheets. *J. Mechanics and Physics of Solids* **45** (11/12), 1727–1763.
- Barlat, F., Brem, J.C., Yoon, J.W., Chung, K., Dick, R.E., Lege, D.J., Pourboghrat, F., Choi, S.-H. and Chu, E. (2003). Plane stress function for aluminum alloy sheets-part I: theory. *Int'l J. Plasticity* **19**, 1297-1319.
- Cho, J.W., Yang, D.Y. and Chung, W.J. (2002). A simplified approach for incorporating thickness stress in the analysis of sheet metal forming using shell elements. *Int'l J. Num. Meth. Eng.* **53**, 2311-2327.
- Capeto, J. (2003). On the design of a hydroforming machine for extruded tubes. *MS Thesis, MSS&M Report 03/2*, UT-Austin, May 2003
- Davies, C.H. (1932). Method of making artificial limbs. U.S. Patent 1,884,589
- Davies, R., Grant, G., Herling, D., Smith, M., Evert, B., Nykerk, S. and Shoup, J. (2000). Formability investigation of aluminum extrusions under hydroforming conditions. *SAE Paper 2000-01-2675*.
- Davies, G. (2007). *Materials for automobile bodies*. Elsevier, Oxford, UK
- Eckermann, E. (2001). *World history of the automobile*. Society of Automotive Engineers, Warrendale, PA
- Fenton, J. (1980). *Vehicle body layout and analysis*. Mechanical Engineering Publications, London, UK

- Field, F.R. and Clark, J. (1997). A practical road to lightweight cars. *Technology Review*, 100, 1, 28-36.
- Foster, E.L. (1917). Process of calibrating and justifying parts of wind musical instruments. U.S. Patent 1,210,629
- Garvin, M.M. (1959). Method for making cam shafts. U.S. Patent 2,892,254
- Gray, J.E. (1940). Apparatus for making wrought metal Ts. U.S. Patent 2,203,868
- Hill, R. (1948). A theory of the yielding and plastic flow of anisotropic metals, *Proc. R. Soc. Lond.* **193A**, 281–297.
- Hill, R. (1979). Theoretical plasticity of textured aggregates. *Mathematical Proc. Cambridge Philosophical Society* **85**, 179-191.
- Hill, R. (1990). Constitutive modeling of orthotropic plasticity in sheet metals. *J. Mechanics and Physics of Solids* **38**, 405–417.
- Hill, R. (1991). A theoretical perspective on in-plane forming of sheet metal. *J. Mechanics and Physics of Solids* **39**, 295–307.
- Hill, R. and Hutchinson, J.W. (1992). Differential hardening in sheet metal under biaxial loading: A theoretical framework. *ASME J. Applied Mechanics* **59**, 1-9.
- Hill, R., Hecker, S.S. and Stout, M.G. (1994). An investigation of plastic flow and differential work hardening in orthotropic brass tubes under fluid pressure and axial load. *Int'l J. Solids & Structures* **21**, 2999-3021.
- Hosford, W.F. (1972). A generalized isotropic yield criterion. *ASME J. Applied Mechanics* **309**, 607-609.
- Hosford, W.F. (1979). On yield loci of anisotropic cubic metals. *Proc. 7th North Amer. Metalworking Research Conf., Society of Manufacturing Engineers, Dearborn, MI*, 191-96.
- Hosford, W.F. and Caddell, R.M. (1993). *Metal forming: mechanics and metallurgy*, 2nd Ed., Prentice Hall, Englewood Cliffs, NJ
- Karafillis, A.P. and Boyce, M.C. (1993). A general anisotropic yield criterion using bounds and a transformation weighting tensor. *J. Mechanics and Physics of Solids* **41**, 1859-1886.
- Kearns, G.T. (1950). Hollow propeller blade with bulbed core. U.S. Patent 2,652,121

- Koc, M. (Ed., 2008). Hydroforming for advanced manufacturing, CRC Press, Boca Raton, FL
- Korkolis, Y.P. and Kyriakides, S. (2008a). Inflation and burst of anisotropic aluminum tubes for hydroforming applications. *Int'l J. Plasticity* **24**, 509-543.
- Korkolis, Y.P. and Kyriakides, S. (2008b). Inflation and Burst of Anisotropic Aluminum Tubes Part II: An advanced yield function including deformation-induced anisotropy. *Int'l J. Plasticity* **24**, 1625-1637.
- Korkolis, Y.P. and Kyriakides, S. (2009). Path dependent failure of anisotropic aluminum tubes. *Int'l J. Plasticity* (in press).
- Kuwabara, T., Yoshida, K., Narihara, K. and Takahashi, S. (2005). Anisotropic plastic deformation of extruded aluminum alloy tube under axial forces and internal pressure. *Int'l J. Plasticity* **21**, 101-117.
- Kyriakides, S., Corona, E. and Miller, J.E. (2004). Effect of yield surface evolution on bending induced cross sectional deformation of thin-walled sections. *Int'l J. Plasticity* **20**, 607-618.
- Logan, R.W., Hosford, W.F. (1980). Upper-bound anisotropic yield locus calculations assuming $\langle 111 \rangle$ -pencil glide. *Int'l J. Mechanical Sciences* **22**, 419-430.
- Ludke, B. (1999). Functional design of a lightweight body-in-white taking the new BMW generation as an example. *Stahl und Eisen*, **119**, 123-128
- Marciniak Z. and Kuczynki, K. (1967). Limit strains in the processes of stretch-forming sheet metal. *Int'l J. Mechanical Sciences* **9**, 609.
- Mendelson, A. (1968). Plasticity: Theory and Application. Macmillan, NY.
- Miller, J.E., Kyriakides, S. (2003). Three-dimensional effects of the bend-stretch forming of aluminum tubes. *Int'l J. Mechanical Sciences* **45**, 115-140.
- Ogura, T. and Ueda T. (1968), Liquid bulge forming. *Metalworking Prod.* **24**, 4, 73-81.
- Park, K. (1903). Apparatus for forming serpentine hollow bodies. U.S. Patent 731,124
- Plunkett, B., Lebensohn, R.A., Cazacu, O. and Barlat, F. (2006). Anisotropic yield function of hexagonal materials taking into account texture development and anisotropic hardening. *Acta Mater.* **54**, 4159-4169.
- Sachs, G. (1950). Principles and methods of sheet-metal fabricating. Reinhold Publ. Corp, NY

- Singh, H. (2003). Fundamentals of hydroforming. Society of Manufacturing Engineers, Dearborn, MI
- Stout, M.G., Hecker, S.S. (1983). Role of geometry in plastic instability and fracture of tubes and sheet. *Mechanics of Materials* **2**, 23–31.
- Wu, P.D, Graf, A., MacEwan, S.R, Lloyd, D.J, Jain, M. and Neale, K.W. (2005). On forming limit stress diagram analysis. *Int'l J. Solids & Structures* **42**, 2225-2241.
- Yoon, J.W., Barlat, F., Dick, R.E., Chung, K. and Kang, T.J. (2004). Plane stress function for aluminum alloy sheets-part II: FE formulation and its implementation. *Int'l J. Plasticity* **20**, 495-522.
- Yoon, J.W. (2009). Private communication.
- Yoshida, K., Kuwabara, T., Narihara, K. and Takahashi, S. (2005). Experimental verification of the path-independence of forming limit stresses. *Int'l J. Forming Proc.* **8**, 283-298.
- Yoshida, K., and Kuwabara, T. (2006). Experimental verification of path-dependence of forming limit stress for a steel tube. *Proc. Plasticity '06, Halifax, Canada*, 106-108.
- Yoshida, K., and Kuwabara, T. (2007). Effect of strain hardening behavior on forming limit stresses of steel tube subjected to nonproportional loading paths. *Int'l J. Plasticity* **23**, 1260-1284.

Vita

Yannis Korkolis was born in Athens, Greece in 1976. He entered the National Technical University of Athens in 1993 and graduated in 1998 with a 5-year Diploma in Mechanical Engineering, placing at the top 5% of his class. After 2 years in the industry and the military, he returned to the National Technical University for a Master's degree in Computational Mechanics. In August 2001 he entered the Graduate School of The University of Texas at Austin to pursue a Ph.D. degree in Engineering Mechanics. Following graduation he will begin working as an Assistant Professor at the Department of Mechanical Engineering at the University of New Hampshire.

He has co-authored a number of conference and the following journal publications:

Y.P. Korkolis and S. Kyriakides, "Inflation and burst of anisotropic aluminum tubes for hydroforming applications", *International Journal of Plasticity*, 24/3 (2008) 509-543

Y.P. Korkolis and S. Kyriakides, "Inflation and burst of anisotropic aluminum tubes, part II: an advanced yield function including deformation-induced anisotropy", *International Journal of Plasticity*, 24/9 (2008) 1625-1637

Y.P. Korkolis and S. Kyriakides, "Path-dependent failure of inflated aluminum tubes", (*in press, International Journal of Plasticity*)

Y.P. Korkolis and S. Kyriakides, "Hydroforming of anisotropic aluminum tubes. Part I: experiments & analysis", (*in preparation*)

Y.P. Korkolis and S. Kyriakides, "Hydroforming of anisotropic aluminum tubes. Part II: advanced constitutive models", (*in preparation*)

Permanent Address: Polytechniou 12, Neo Irakleio Attikis, Athens, 141 22, Greece

This dissertation was typed by the author.